Alternative cathode catalysts for PEM fuel cells

Andrew John Dixon

Submitted in accordance with the requirements for the degree of

Doctor of Philosophy

As part of the integrated MSc/PhD in Low Carbon Technologies

The University of Leeds

Energy Research Institute

School of Chemical and Process Engineering

Doctoral Training Centre in Low Carbon Technologies

November, 2015

The candidate confirms that the work submitted is his own and that appropriate credit has been given where reference has been made to the work of others.

This copy has been supplied on the understanding that it is copyright material and that no quotation from the thesis may be published without proper acknowledgement. The right of Andrew J. Dixon to be identified as author of this work has been asserted by him in accordance with the Copyright, Designs and Patents Act 1988.

Acknowledgements

I would like to thank my supervisors, Prof. Mohammed Pourkashanian and Dr. Kevin Hughes, for the help and support they have offered during this PhD. I would also like to thank Prof. Derek Ingham for the generous donation of his time and effort in assisting me with the completion of this thesis, and for being incredibly supportive and approachable when things have seemed somewhat difficult.

This process would have been considerably more difficult without the distractions offered by my colleagues within the DTC for Low Carbon Technologies. Thank you all for never letting me get ideas above my station and occasionally laughing at my jokes.

To Dean, Nicola, Garry, Charlotte, Guy and Francesca; you told me you wanted a direct mention in the acknowledgements, will this do? And finally to Mum, Dad, Stu and my wife, Fi; none of this would have been possible without your support. I also expect you all to use my full title in all forms of formal and informal discussion.

Abstract

Proton exchange membrane fuel cells, PEMFC's, offer a clean, flexible mode of energy generation, though efficiency improvements are required before they can become commercially viable. While platinum is currently the most commonly used cathode catalyst, a large overpotential exists for the oxygen reduction reaction, ORR, limiting the effective potential of a fuel cell to approximately 0.9 V.

Efforts have been made within the literature to develop a low cost, efficient and durable alternative cathode catalyst for use within a PEMFC though at present no viable alternative has been found. However, M-Nx/C active sites, consisting of a central metal atom co-ordinated to two or four nitrogen atoms embedded within a carbon support, show great promise as possible replacements to platinum. While advances have been made in the identification of possible active sites, no study yet exists that examines the influence of each active site component on the overall activity.

In this thesis the influence of each component is examined, and in doing so a highly active site is predicted. The efficacy of the model is first proven by a simultaneous computational and experimental study of the activity of both platinum and Fe/Co-porphyrins, which are commonly used as precursors in the development of highly active M-N$_x$/C catalysts. 16 active sites are modelled using graphene and amorphous carbon-like ligands embedded with two or four nitrogen atoms and co-ordinated to either a cobalt or iron centre. The activity of each active site towards the ORR is assessed by the calculation of redox potentials, and by modelling 20 different elementary reactions which collectively form a comprehensive reduction mechanism.

By direct comparison between each active site, utilising natural population, bond orbital and localised molecular orbital analysis along with electrostatic potential maps, the influence of each constituent part is quantified. Finally, it is predicted that active sites consisting of a disrupted graphene ligand, embedded with four nitrogen atoms co-ordinated to either an iron or cobalt centre, would demonstrate the highest activity towards the ORR, and that such an active site is responsible for the activities reported within the literature.

Table of Contents

List of Tables

List of Figures

Glossary

Active site - The location within a heterogenous catalyst that is directly involved in the reaction being catalysed.

Electrostatic potential - The electric potential energy of an electron located at any point in space.

Endergonic - A process with an associated positive change in Gibbs free energy.

Endothermic - A process with an associated positive change in enthalpy.

Equilibrium - The point at which forward and reverse reactions occur at the same rate, with no associated energy change for either reaction.

Exergonic - A process with and associated negative change in Gibbs free energy.

Exothermic - A process with and associated negative change in enthalpy.

Overpotential - The difference between the theoretical maximum potential of a process, and the experimentally observed potential.

Reversible potential - The equilibrium point for an electrochemical reaction.

Redox potential - The equilibrium point for the reduction and oxidation of an electron transfer reaction.

Abbreviations

AFC: Alkaline fuel cell

CPCM: Conductor-like polarizable continuum model

CV: Cyclic voltammetry

DFT: Density functional theory

ESP: Electrostatic potential

GDL: Gas diffusion layer

MCFC: Molten carbonate fuel cell

MEA: Membrane electrode assembly

NBO: Natural bond orbital

NLMO: Natural localised molecular orbital

NPA: Natural population analysis

ORR: Oxygen reduction reaction

PAFC: Phosphoric acid fuel cell

PEMFC: Proton exchange membrane fuel cell

RDE: Rotating disk electrode

SCF: Self-consistent field

SHE: Standard hydrogen electrode

SOFC: Solid oxide fuel cell

Chapter 1 - Introduction

1.1 - Introduction

In order to meet the targets set out by the Kyoto protocol (UN, 1998), the emissions from both energy and transport sectors must be tackled and heavily reduced. There are a number of technologies that can be adopted to address this problem but only one that can be used both in the energy and transport sectors: hydrogen fuel. Hydrogen technologies can potentially offer clean and sustainable energy, provided the hydrogen fuel is sustainably sourced. Depending on the systems implemented, the only product from hydrogen technologies is water. The notion of using hydrogen as a fuel source is not new, in 1839 Sir William Grove discovered that hydrogen and oxygen gases, when exposed to each other over platinum, generate a current, some heat, and water (Barbir, 2012; Hoogers, 2002; Larminie et al., 2003). While hydrogen can be burnt in air to form water, it is considerably more efficient to directly convert the chemical potential energy of hydrogen and oxygen into an electrical current. Energy conversion will always result in energy loss and so this one step conversion will have fewer losses than a two-step process; chemical potential is converted to heat which is subsequently converted to an electrical current. Despite this early finding the technology remained an academic curiosity alone for almost a century. To this day the principles of fuel cells haven't changed dramatically; while improvements have been made to various components of the cell, essentially todays technologies still require only a fuel source, a semi-permeable membrane, a catalyst and two electrodes, one positive and one negative (Barbir, 2012; Hoogers, 2002; Larminie et al., 2003). There are many types of fuel cells actively being researched and used today with their components designed to suit the fuel type and operating temperatures.

1.2 - Type of fuel cells

With an operating temperature of 800-1100 $^{\circ}$C, the solid oxide fuel cell, SOFC, is the highest temperature fuel cell available. It derives its name from the solid, oxide ion conducting electrolyte at its heart and actually represents the simplest structural design

of fuel cell. The solid oxide fuel cell consists only of an anode, a cathode, and the solid electrolyte[1] (Barbir, 2012; Hoogers, 2002; Larminie et al., 2003). The electrolyte within the SOFC is traditionally zirconia, ZrO_2, stabilised with small amounts of yttria, Y_2O_3. At temperatures over 800 °C, the zirconia is able to conduct O^{2-} ions (Barbir, 2012; Hoogers, 2002; Larminie et al., 2003). One of the major advantages of using SOFC's is their fuel flexibility. As none of the components of the fuel cell are adversely affected by the presence of fuel contaminants such as carbon monoxide, CO, and carbon dioxide, CO_2, there is no need to highly refine the fuel[2]. However, despite the efficiency and fuel flexibility of SOFC's, their uptake is hindered somewhat by long start-up times and the stability of ancillary components at such high temperatures (Barbir, 2012; Hoogers, 2002; Larminie et al., 2003).

Like SOFC's, molten carbonate fuel cells, MCFC's, have a high tolerance for fuel contaminants. Indeed for MCFC's to function, CO_2 is needed as a fuel source. However, unlike SOFC's, the electrolyte is a molten salt electrolyte, either Li/Na or Li/K carbonates, held in a solid lithium aluminate, $LiAlO_2$, ceramic matrix (Barbir, 2012; Hoogers, 2002; Larminie et al., 2003). Again for these fuel cells to operate they must be kept at high temperatures of between 600 °C and 700 °C. At these temperatures the alkali carbonate electrolyte forms a molten salt, which is highly conductive of CO_3^{2-} ions. To form these ions, O_2 and CO_2 must be present at the cathode, while H_2 is present at the anode (Barbir, 2012; Hoogers, 2002; Larminie et al., 2003). At the anode, the H_2 reacts with the CO_3^{2-} ions to form water and carbon dioxide. In an ideal system the CO_2 generated at the anode can be recirculated to the cathode, thus removing the need for an external CO_2 source. However, this is difficult to achieve in a real world scenario, and so ancillary equipment is utilised. If a non-purified H_2 fuel source is used, the anodic gas can be post-combusted. This post-combustion process converts any un-reacted H_2 to H_2O, while generating CO_2 from CO and any unreacted hydrocarbons (Barbir, 2012; Hoogers, 2002;

---

[1] An electrolyte is a conductive media, typically a solution that allows the movement of charged ions.

[2] Hydrogen fuel is typically generated from the steam reformation of hydrocarbons which results in a mixture of CO, CO_2, H_2 and H_2O.

Larminie et al., 2003). The resultant gas feed is then recirculated to the cathode for the regeneration of CO_3^{2-} ions within the electrolyte. While this fuel flexibility is an obviously desirable characteristic of fuel cells, it is unfortunately a feature of high temperature fuel cells which are somewhat hostile environments and thus have short life-spans due to the corrosive nature of the electrolytes (Hoogers, 2002; Larminie et al., 2003).

Phosphoric acid fuel cells (PAFC's) have a considerably lower operating temperature than either MCFC's or SOFC's, but are still considered to be high temperature with an operating temperature range of 180-200 ^{o}C (Barbir, 2012; Hoogers, 2002; Larminie et al., 2003). Phosphoric acid is uniquely suited for use as an electrolyte, as it is the only common inorganic acid with high enough stability and low volatility to survive prolonged use in a fuel cell (Hoogers, 2002). While sulphuric acid would theoretically be able to survive in the fuel cell, its chemical activity is hindered in the presence of platinum, which is used as the catalyst (Larminie et al., 2003). The electrolyte is held in the pores of silicon carbide/PTFE[3] matrix by capillary forces but over time can be lost from the system, as a result replenishment of phosphoric acid is usually required (Larminie et al., 2003). The use of platinum as the catalyst on both the anode and cathode sides of the cell results in much lower tolerance for fuel contaminants, such as carbon monoxide (Barbir, 2012; Hoogers, 2002; Larminie et al., 2003). CO competitively adsorbs to the surface of platinum, thus reducing its catalytic activity towards oxygen reduction and hydrogen oxidation. While PAFC's have a high efficiency they exhibit a low power density, and the use of an aggressive acid results in corrosion of fuel cell components. This, coupled with the need for electrolyte replenishment, means that there is a high maintenance requirement when using PAFC's (Larminie et al., 2003).

Alkaline fuel cells (AFC's) are one of the more versatile fuel cells available, and have been used by NASA to power both Apollo rockets and space shuttles (Barbir, 2012; Hoogers, 2002; Larminie et al., 2003). Their popularity stems from both their versatility and their low cost; the most common component is the potassium hydroxide electrolyte, one of the cheapest standard chemicals available (Barbir, 2012; Hoogers,

---

[3] Polytetraflouroethylene, PTFE, is a hydrophobic polymer commonly used within hydrogen fuel cells.

2002; Larminie et al., 2003). The nature of the electrolyte results in a considerably lower tolerance for contaminants within the hydrogen supply, the presence of CO_2 results in the formation of carbonate ions within the electrolyte which causes a significant drop in the fuel cell performance (Larminie et al., 2003). This can be somewhat offset due to the need to pump the electrolyte around the system, thus allowing a clean KOH supply to be used. However, doing so will only extend the lifespan of the KOH batch, and so eventually replenishment will be needed (Larminie et al., 2003). This pumping also serves to cool the system, allowing temperatures conducive to maximum efficiency to be maintained (Hoogers, 2002; Larminie et al., 2003). AFC's utilise a wide range of catalysts depending on the operating conditions, such as temperature, which typically range from 65-200 ^{o}C, and gas pressures. While it is possible to use platinum within an AFC, it is more common to utilise non-precious catalysts such as nickel, silver, metal oxides or noble metals (Barbir, 2012).

1.3 - Proton exchange membrane (PEM) fuel cells

Proton exchange membranes represent one of the largest areas of research and development within the field of fuel cells (Barbir, 2012). The low operating temperatures and the lack of an aggressive electrolyte result in a low maintenance, relatively high efficiency fuel cell. However they are far from perfect and there are still many problems to overcome before they will achieve full commercialisation. Chief among these is the need to develop a highly efficient, cheap catalyst. Currently, fuel cells utilise platinum as a catalyst, and while the use of nanoparticles as a way of decreasing the platinum loading has helped to reduce the cost, the catalyst itself isn't particularly efficient; the theoretical maximum voltage that can be achieved from a hydrogen fuel cell is 1.2 V, but even the most efficient PEMFC's struggle to sustain voltages over 0.8 V (Barbir, 2012; Hoogers, 2002; Larminie et al., 2003). As the focus of this work is in developing new catalysts for PEMFC's, it seems prudent to cover their structure and function in more detail. Figure 1.1 gives a basic view of the principles of PEM fuel cell operation – hydrogen and oxygen flow on opposite sides of the membrane, which is sandwiched between two electrodes. At the boundary between the electrodes and the membrane, a thin catalyst layer exists that typically consists of platinum on a carbon support, Pt/C.

The purpose of the catalyst is to facilitate the reduction of oxygen by lowering of the activation barriers for the elementary reduction reactions.
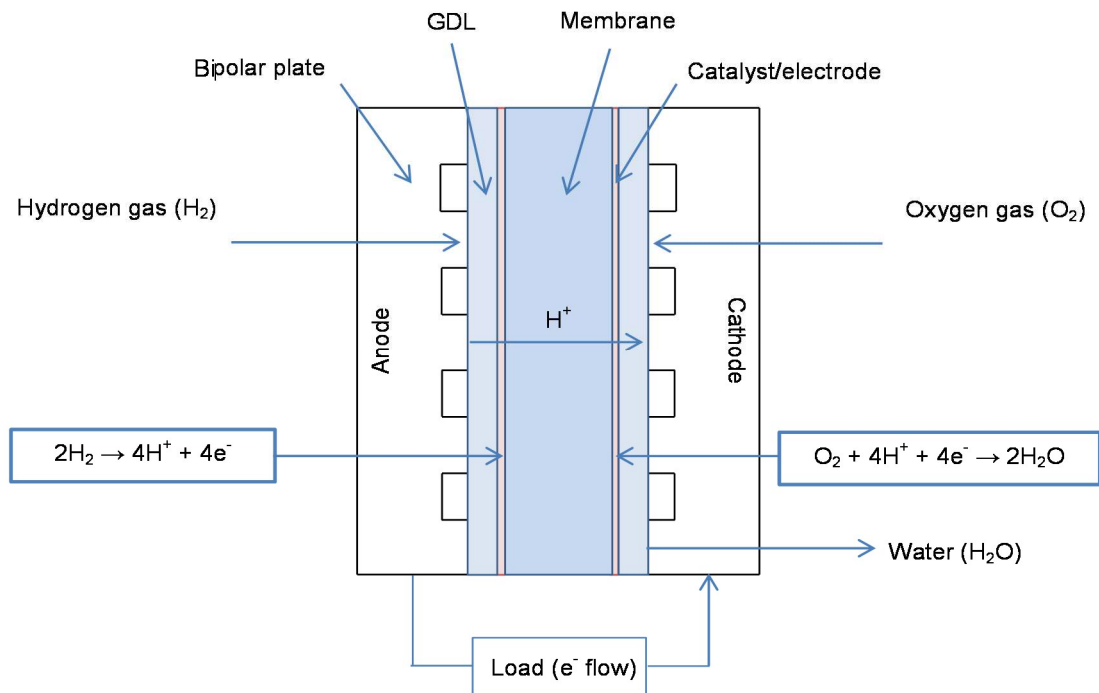
Figure 1.1 - Basic schematic of a PEM fuel cell showing anodic and cathodic reactions.

1.4- Bipolar plates

As a single fuel cell is typically only able to provide 0.8 V, it is common for multiple cells to be connected together to form a stack. Within a fuel cell stack, the bipolar plate serves as both a means to electrically connect two cells and also to provide structural support. The name bipolar plate is derived from the fact that, when connected in a stack, a single plate will serve as the anode for one cell, and the cathode for a second (Barbir, 2012; Larminie et al., 2003). As can also be seen from Figure 1.1, the bipolar plates house grooves, or flow channels, which serve to deliver reactant gas to the cells. As the bipolar plates comprise almost 80% of the stack volume, and a large proportion of the manufacturing costs, it is desirable for them to be comprised of cheap, lightweight, electrically conductive materials. While bipolar plates can be made from a variety of materials, graphite, being both thermally and electrically conductive, is currently one of the more popular materials (Barbir, 2012; Hoogers, 2002; Larminie et al., 2003).

One of the challenges with flow channel design is to provide a means to both allow gas to enter the cell and to provide an effective path for the removal of water. Early bipolar plate designs utilised parallel flow fields but this resulted in water accumulation at the cathode which prevented even gas distribution and thus performance drops within the cell (Vielstich et al., 2003). To combat this, more intricate designs were utilised such as serpentine and interdigited flow fields, as shown in Figure 1.2. Serpentine flow fields reduce the effects of water accumulation by allowing reactant gas to circumvent blockages by way of transport through the gas diffusion layers. If serpentine fields are too intricate, i.e. if they consist of a large number of bends, pressure differentials can occur which lead to the 'short circuiting' of some channels (Vielstich et al., 2003). However, sufficiently straight flow field designs have been shown to reduce these pressure differentials, and so water accumulation in blocked channels is drastically reduced (Vielstich et al., 2003). Interdigited flow fields use dead-end inlet and outlet channels, forcing reactant gas to travel through the gas diffusion layer. Water removal from the cathode is substantially increased by the pressure differential between inlet and outlet channels, and as a result it has been shown that the use of interdigited flow fields can increase the performance of a fuel cell by 50-100 % over serpentine or parallel designs (Vielstich et al., 2003).

The maximum performance increase is typically found with higher numbers of channels and with shorter shoulder widths, i.e. smaller gaps between channels (Vielstich et al., 2003). However, it should be noted that as the bipolar plate also performs a structural and electrical function, that decreases in contact area between the plate and the gas diffusion layer can cause performance loss. Thus a balance should be struck between gas flow, water removal and contact area to find the optimal flow field design.
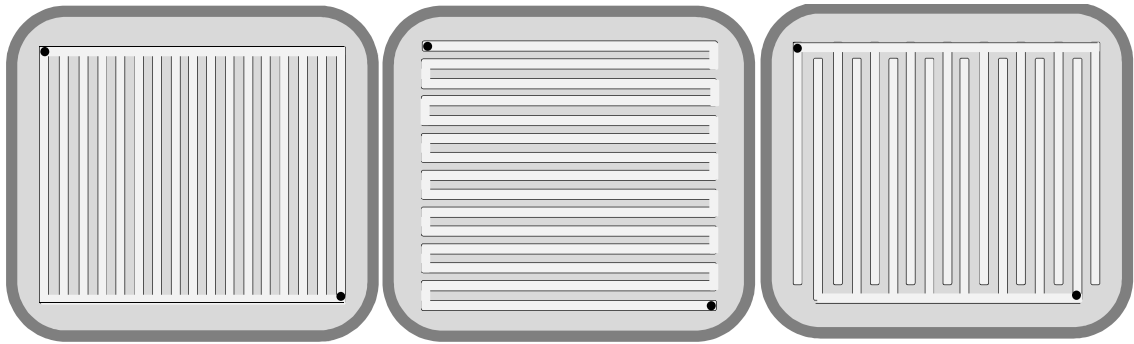
Figure 1.2 - From left to right; parallel, serpentine and interdigited flow field designs. The inlet is a black dot in the top left with the outlet shown as a black dot in the bottom right.

1.5 - Gas diffusion layer

While the gas diffusion layer, GDL, is not directly involved in the chemical reaction at the heart of the cell, it is still essential to the cell. The GDL performs a number of functions; it facilitates the removal of water from the catalyst layer to the flow channels, provides a diffusion pathway for reactant gas to the catalyst layer and provides an electrical connection between the catalyst and the bipolar plates (Barbir, 2012). Water is formed on the catalyst surface at the cathode, and so to avoid saturation it is essential that the layer is suitably porous (Barbir, 2012; Hoogers, 2002; Larminie et al., 2003). It is important that the pore size is large enough to allow the removal of water, but small enough to support the catalyst particles next to the membrane. Both through-plane and in-plane permeability are essential characteristics of GDL materials, as both facilitate the removal of water and the introduction of gas to the membrane electrode assembly, MEA[4].

The GDL also performs a structural role in the cell, and so it must be both flexible enough to ensure good electrical connections between the MEA and the bipolar plate, and rigid enough to support the membrane and catalyst layers (Barbir, 2012; Hoogers, 2002; Larminie et al., 2003). Carbon cloths/papers display these characteristics and so are typically used for the GDL. Carbon papers are thinner than cloths and are commonly used when the cell is to be made to be extremely thin (Larminie et al., 2003). Carbon

---

[4] The MEA is the collective name for the GDL, membrane and electrode layers.

cloths are slightly thicker and are therefore able to absorb more water thus provide a greater performance (Barbir, 2012; Hoogers, 2002; Larminie et al., 2003). Cloths are also able to provide better electrical connections to the bipolar plate as they can fill any surface irregularities although in plates with shallow flow channels this can present an issue (Larminie et al., 2003).

The GDL is usually coated with PTFE in order to ensure the layer is hydrophobic but 'these properties are often tailored to a specific cell design, and must be measured and correlated to the cell performance' (Barbir, 2012). Hydrophobicity is essential to facilitate the removal of water from the layer, as waterlogging of the fuel cell causes a dramatic reduction in the performance. The porosity of the GDL media is another important property to be taken into consideration when designing a fuel cell. GDL media typically show bulk diffusion, as the pores are usually much larger than the surface area of the diffusing gas. As a result, in large pores, the diffusing gas is not hindered by the pore size and can diffuse through the GDL with ease. Knudsen diffusion, i.e. diffusion through long, small pores where gas molecules typically collide with pore walls, is thought to be prevalent as the pore size decreases, for example, in microporous layers supporting the catalyst (Barbir, 2012).

1.6 - Membrane

The membrane within a PEM fuel cell is analogous to the electrolyte layer in other, higher temperature fuel cells. However, while other fuel cells have fully mobile electrolytes to transport ions from one electrode to another the PEM membrane is dependent on absorbed water for proton transport. While the membrane must facilitate proton transport, it must also be electrically insulative and provide an effective barrier to gas transport to prevent the mixing of hydrogen and oxygen gases while at the same time remaining both mechanically and chemically stable (Barbir, 2012). These characteristic can be fulfilled by using materials composed of long chain, polar molecules such as those used by DuPont in the manufacture of Nafion^{TM} (Barbir, 2012). The backbone of Nafion^{TM} is a flouro-carbon chain to which side chains of perflourinated vinyl polyethers are added (see Figure 1.3). At the end of these side chains are sulphonic acid residues which cluster to form highly hydrophilic regions resulting in the uptake of
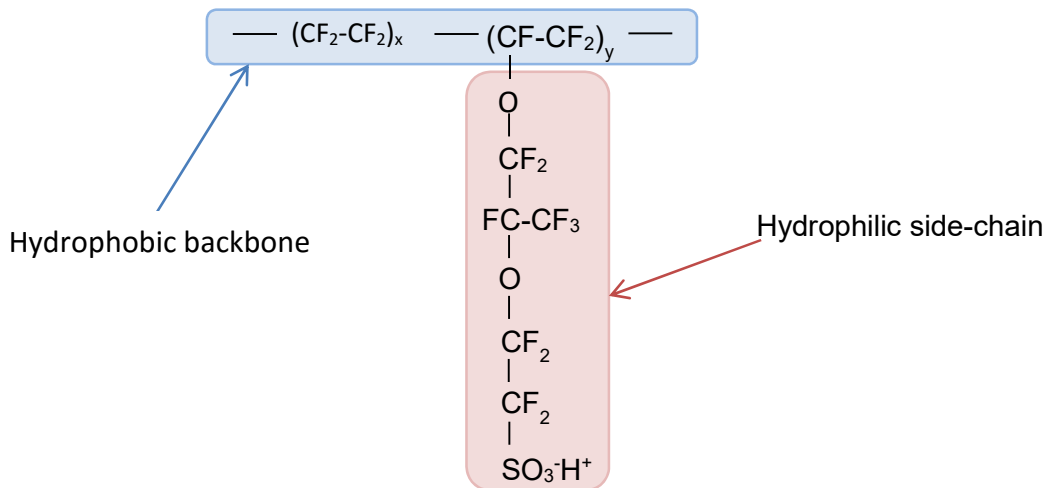
Figure 1.3 - Chemical structure of Nafion™.

large amounts of water (Barbir, 2012; Hoogers, 2002; Larminie et al., 2003). The exact volume of water and the rate by which it absorbs into the membrane are strongly affected by the temperature. As proton mobility is considerably higher in hydrated membranes than in dry conditions, there is an obvious desire to keep the membrane well hydrated, and as such it is not uncommon for reactant gases, i.e. H_2 and O_2, to be humidified (Barbir, 2012). Indeed such is Nafions' capability for proton transport that when fully hydrated, proton mobility is only one order of magnitude less than in aqueous sulphuric acid (Barbir, 2012). This difference in proton mobility can be understood by investigating how protons are transported across the membrane when dry and when hydrated. In a dry membrane, protons transfer from side-chain to side-chain by 'hopping' between sulfonic acid groups. In a well hydrated membrane the ion-dipole interactions of the side chains are 'shielded' by the presence of excess water thus allowing the free movement of protons, according to their concentration gradient, and towards the cathode (Barbir, 2012). However, when protons transfer in such a way they are typically co-ordinated to a number of water molecules. It is stated within the literature that a solvated proton would be stable in the form of $H_9O_4^+$, where a central H_3O^+ ion hydrogen bonds to three water molecules (Ishikawa et al., 2007). This stable form of a solvated proton gives rise to electro-osmotic drag, a process by which water is literally dragged across the membrane with the H^+ ion. Electro-osmotic drag can result

in the anode side of thicker membranes drying out, although this can be combatted by using thinner membranes and humidifying the H_2 feed.

1.7 - Electrode

The electrode is essentially a thin catalyst layer sandwiched between the membrane and the GDL at which all chemical reactions take place (Barbir, 2012). There are two catalyst layers in a PEM fuel cell, one anodic and one cathodic, and both are typically carbon supported platinum nanoparticles[5]. Platinum has been utilised in fuel cells since 1839 and while this has historically been one of the most expensive components of a fuel cell, the use of carbon supported nanoparticles has drastically reduced the amount of platinum needed, and thus the associated cost, without sacrificing catalytic activity (Barbir, 2012). The electrode functions as a 3-phase boundary within the cell; the area at which gas phase reactants, solvated protons and solid-conducted electrons meet and react (Barbir, 2012). As this three-phase boundary is the electrochemically active site within the cell, efforts have been made to increase the surface area and as such it is not uncommon to incorporate membrane treatments such as PTFE within the catalyst layer (Barbir, 2012). As catalytic reactions occur on the surface of the metal, and not in the bulk, high surface area to weight ratios are achieved by using nanoparticles supported on carbon. However, if nanoparticles are not well dispersed, the overall surface area available for reactions is reduced due to adjacent nanoparticles 'blocking' active areas, and as such smaller, well dispersed particles are desirable (Barbir, 2012). Indeed activity decreases significantly if Pt/C ratios of more than 40 wt.% are used (Barbir, 2012). However, the catalyst layer should also be thin to reduce losses associated with proton transport and gas permeation to the catalyst active area, and so the amount of carbon should be reduced (Barbir, 2012). Significant reduction in catalyst layer thickness can be achieved by using loadings above 40 wt.% Pt/C but, as mentioned, this can cause significant reductions in catalytic activity, and so a balance between catalyst layer thickness and active area should be sought in order to find a loading of equal

---

[5] Platinum is supported on larger carbon particles to prevent the nanoparticles from 'falling' into the pores of the GDL

compromise; one thin enough that losses due to gas diffusion/proton transport are minimised, while at the same time not compromising on the active area of the platinum (Barbir, 2012).

1.8 - Thesis overview

As mentioned in Section 1.7, platinum is still the best catalyst for the oxygen reduction reaction, capable of achieving higher potentials and current density than other metals within acidic media (Anderson et al., 2012; Antoine et al., 2001; Michaelides & Hu, 2001; Nørskov & Rossmeisl, 2004; Sidik & Anderson, 2002; Yang et al., 2010), though issues that hinder the commercialisation of PEMFC's remain (Nilekar & Mavrikakis, 2008; Shi et al., 2006). While the kinetics of the platinum catalysed anodic reaction, $H_2 \rightleftharpoons 2H^+ + 2e^-$, do not need vast improvement (Anderson et al., 2012), the platinum catalysed cathodic reaction, $O_2 + 4H^+ + 4e^- \rightleftharpoons 2H_2O$, is hindered by a large overpotential loss, limiting the effective potential of the fuel cell to 0.8-0.9 V (Anderson, 2002; Anderson & Albu, 1999; Ford et al., 2010; Nilekar & Mavrikakis, 2008; Shi et al., 2006; Tian & Anderson, 2011; Walch et al., 2008).

This thesis aims to explore source of the overpotential exhibited by platinum and use this knowledge to ascertain the viability of other, non-precious metal based catalysts. Relevant literature pertaining to the ORR catalysed by platinum and non-platinum catalysts is reviewed in Chapter 2, along with a summary of computational and experimental methodologies that are used to explore such electrochemically active species. In Chapter 3 the platinum catalysed and porphyrin catalysed ORR is explored, both experimentally and computationally, to ascertain the suitability of computational techniques to describe catalytic activity. Chapter 4 details the computational investigation of the ORR by non-precious metal containing $M-N_x/C$ active sites that are prepared via the pyrolysis of porphyrins but cannot be experimentally isolated. Chapter 5 compares the activity of these proposed active sites with that of porphyrins, thereby allowing for a direct assessment as to the influence of heat treatment on the catalytic activity of porphyrins. Chapter 6 then assesses how these findings build upon the current knowledge base, and what future steps could be taken to progress towards the generation of highly active PEM cathode catalysts.

Chapter 2 - Literature Review

2.1 - Introduction

While the cost of platinum is an oft quoted barrier to fuel cell commercialisation (Anderson et al., 2012; Maruyama & Abe, 2003; Shi et al., 2006), it is something of a misnomer. Recent work focussed on the reduction of platinum loading by reducing platinum particle size (Maruyama & Abe, 2003; Yang et al., 2012), by doing so the surface area to volume ratio, and thus the number of catalytically active surface sites, is increased. While the reduction in particle size is shown to decrease the costs, there is a point at which decreasing particle size serves to reduce the activity and even shift the reaction to one which favours the production of hydrogen peroxide (Yang et al., 2012). In addition to nano-particle size, the distribution is shown to affect both the activity and preferred reaction pathway (Yang et al., 2012). Thus despite a significant reduction in the costs associated with the use of platinum in recent years, the overpotential associated with the cathodic reaction persists and remains an obstacle to fuel cell commercialisation. Minimisation of this is considered one of the primary aims for PEMFC catalysis studies (Anderson & Albu, 1999; Nørskov & Rossmeisl, 2004; Wang & Balbuena, 2004). The kinetics of the cathodic reaction are considerably slower than that of its anodic counterpart; while increased catalyst loading on the cathode layer is able to offset some losses (Barbir, 2012), the primary loss is due to poor reaction kinetics (Tripković et al., 2010). A deep understanding of the structure/electronic factors that control the kinetics of the oxygen reduction reaction, ORR, is essential if the activity of ORR catalysts is to be improved (Anderson & Albu, 1999). While efforts to alloy platinum have shown some promise, the stability and reactivity of platinum are hard to replicate (Anderson et al., 2012; Ford et al., 2010) and even the best performing alloys are only capable of producing cell potentials in the region of 0.7 V (Anderson et al., 2012). Recent efforts have sought not to improve the performance of platinum, but to seek alternative, non-precious metal catalysts that offer comparative performance at a fraction of the price of platinum.

Along with a review of thermodynamic and kinetic principles pertaining to the catalysed ORR and detailed explanations of the computational and experimental techniques, a thorough yet concise review of available literature pertaining to both the platinum catalysed ORR and non-precious metal containing catalysts is herein presented. In brief, one finds that that the mechanisms present on all catalysts are significantly more complex than the overall reaction would suggest and that changes in the mechanism result from the imposition of a potential at the electrode surface. In addition, it is found that while some non-precious metal containing catalysts show good activity towards the ORR, uncertainty about the nature of the active site is hindering the development of highly active catalysts.

2.2 - Thermodynamic and kinetic principles

In PEMFC's, the oxygen reduction is a multi-step mechanism involving four electrons and four protons. The mechanism can be either direct, indirect or terminate at the production of hydrogen peroxide as detailed in Figure 2.1 below.
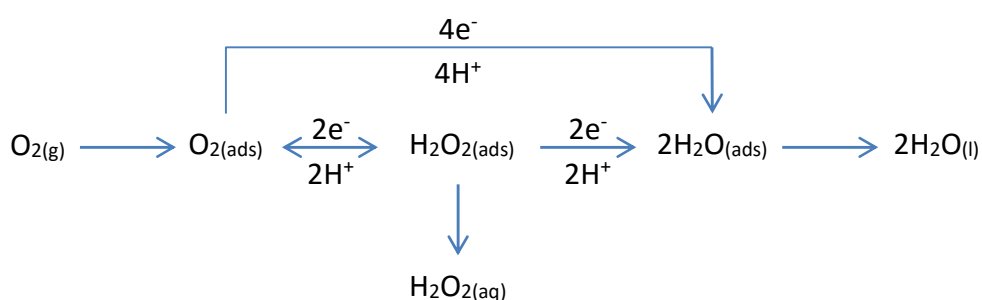
Figure 2.1 - Oxygen reduction pathways.

The direct pathway is the most desirable, having the highest reversible potential of 1.229 V. In this pathway the O-O bond of either $O_{2(ads)}$ or $OOH_{(ads)}$ is broken prior to reduction to H_2O_2(ads). The indirect and peroxide pathways form H_2O_2 as either an intermediate or final product with a reversible potential of 0.7 V, while its reduction has a reversible potential of 1.76 V, the average of these two values being the reversible potential for the reduction of O_2 to $2H_2O$, 1.23 V.

The reversible potential of a reaction is linked directly to the associated Gibbs free energy change by Equation 2.1:

$$\Delta G = -nFU$$

Equation 2.1 - Relationship between Gibbs free energy and reversible potential.

where ΔG is the Gibbs free energy change of the reaction, n is the number of electron transferred, F is the Faraday constant and U is the reversible potential. From this it can be seen that the formation of peroxide results in an overall loss in the system and as such is undesirable. The Gibbs free energy change is a function of both the enthalpy and entropy change of a reaction:

$$\Delta G = \Delta H - T\Delta S$$

Equation 2.2 - Relationship between Gibbs free energy, enthalpy and entropy.

where ΔH is the enthalpy, T is the temperature and ΔS is the entropy change of the reaction.

The effect of an electric field on the ORR must also be considered. In a fuel cell, an electron is transferred independently of the proton through an external circuit, the energy of said electron is a function of the electric field resulting from the potential difference between the anode and cathode. At a given potential (U), the Gibbs free energy of a proton/electron pair, i.e. $H^+ + e^-$, is given by:

$$G_{\left(H^+_{(aq)} + e^-_{(aq)}\right)} = \frac{1}{2}G_{(H_{2(g)})} - eU$$

Equation 2.3 - Gibbs free energy of a solvated proton/electron pair.

Where $G_{\left(H^+_{(aq)} + e^-_{(aq)}\right)}$ represents the Gibbs free energy of a proton-electron pair, $G_{(H_{2(g)})}$ is the Gibbs free energy of a gas phase H_2 molecule and eU is the energy of a proton at potential U. Thus at a potential of 0 V relative to the standard hydrogen electrode, a molar equivalent proton/electron pair has a Gibbs free energy equal to exactly half a mole of hydrogen gas. At higher potentials one can thus model the influence of a potential on electrochemical reactions by simply adding to the reactant side of a balanced equation the operating potential of the cell in electron volts; for example at 0.5 V the electron has an extra 0.5 eV, or 48.243 kJmol^{-1}, of Gibbs free energy.

As the Gibbs free energy change for a reaction is directly related to the reversible potential, the four electron reduction of O_2 to $2H_2O$, having a reversible potential of 1.229 V, must have an associated Gibbs free energy change of 474.154 kJmol^{-1} which correlates to the transfer of four electrons, each with a Gibbs free energy of 118.539 kJmol^{-1}. An ideal catalyst would allow for all of this Gibbs free energy to be converted to electrical potential energy. However, chemical reactions with an associated Gibbs free energy cost decrease the available Gibbs free energy available for conversion and thus reduce the operating potential of the cell (Anderson, 2012), thus the effective potential of a cell is found using:

$$E_{eff} = \frac{\Delta G_{max} - \Delta G_{chem}}{nF}$$

Equation 2.4 - Effective potential of electrochemical reaction involving chemical steps.

Where ΔG_{max} is the maximum Gibbs free energy change of the reaction, n is the number of electrons transferred, ΔG_{chem} is the Gibbs free energy consumed in chemical reactions and F is the Faraday constant, 96485.333 Cmol^{-1}.

2.2.1 - Effect of a catalyst on a reaction

While an ideal catalyst would allow the reaction to proceed via a pathway that involves no chemical steps one must also consider the U_{rev} of these electrochemical steps; at potentials higher than U_{rev} a reaction is no longer spontaneous, thus requiring work to be input to the system, and the reaction will either proceed via an alternative pathway, if one is available, or simply not occur.

Take, for example, the non-catalysed ORR in acidic media. This reaction consists of four successive proton/electron transfer reactions:

$$O_{2(g)} + H^+ + e^- \rightleftharpoons OOH_{(aq)} \;(U_{rev} = \text{-0.125 V}) \tag{2.1}$$

$$OOH_{(g)} + H^+ + e^- \rightleftharpoons H_2O_{2\,(aq)} \;(U_{rev} = \text{1.515 V}) \tag{2.2}$$

$$H_2O_{2\,(g)} + H^+ + e^- \rightleftharpoons OH_{(aq)} + H_2O_{(l)} \;(U_{rev} = \text{0.806 V}) \tag{2.3}$$

$$OH_{(aq)} + H^+ + e^- \rightleftharpoons H_2O_{(l)} \;(U_{rev} = \text{2.720 V}) \tag{2.4}$$
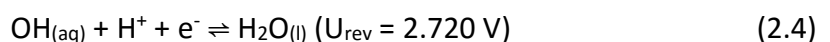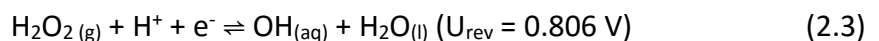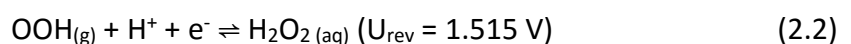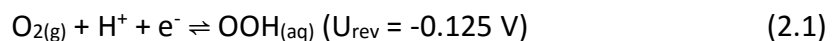
As can be seen, while U_{rev} of the overall reaction is 1.229 V, only two of the four reduction steps are plausible at this potential, the reduction of $OOH_{(aq)}$ and the reduction of $OH_{(aq)}$. The first step of the reaction, the formation of $OOH_{(aq)}$, has a reversible potential of -0.125 V meaning that at 0 V vs. SHE the reaction is endergonic by 12.061 $kJmol^{-1}$, non-spontaneous, and highly unlikely to proceed without external intervention. Thus, we find another key characteristic of an ideal catalyst: the ability to shift the reversible potentials of each individual reaction to 1.229 V.

A catalyst must, by definition, be unchanged by a reaction, thus for a complete reaction cycle, i.e. the complete reduction of O_2, the Gibbs free energy change must be -474.154 $kJmol^{-1}$; any deviation from this implies that the catalyst is at least partially consumed by the reaction. However, individual steps can be affected by the presence of a catalyst; by providing a surface on which intermediates can bind the catalyst serves to shift the reversible potentials (Anderson, 2012):

$$U_{surf}^{rev} = U^0 + \frac{\Delta_{ads}G_{(Ox)} - \Delta_{ads}G_{(Red)}}{-nF}$$

Equation 2.5 - Relationship between the reversible potential, standard potential and adsorption energies of intermediates for a catalysed electrochemical reaction.

where U_{surf}^{rev} is the reversible potential of the catalysed reaction, U^0 is the standard reversible potential, $\Delta_{ads}G_{(Ox)}$ is the Gibbs free energy of adsorption of the oxidised species, $\Delta_{ads}G_{(Red)}$ is the Gibbs free energy of the reduced species, n is the number of electron transferred and F is the Faraday constant. We can adapt Equation 2.5 to extend to chemical reactions by simply multiplying by $-nF$, giving (Anderson, 2012):

$$\Delta G_{surf} = \Delta G^0 + \Delta_{ads}G_{(Ox)} - \Delta_{ads}G_{(Red)}$$

Equation 2.6 - Gibbs free energy change of a catalysed reaction.

Thus, by calculating ΔG^0 for each possible reaction and the $\Delta_{ads}G$ of each intermediate, one is able to characterise the efficacy of a particular catalyst in a fuel cell environment.

2.3 - Computational techniques

It is difficult to ascertain detailed thermodynamic information about intermediate reactions and short lived intermediates using experimental techniques. While one can ascertain the overpotential of a reaction on a particular catalyst using electrochemical characterisation, it is impossible to measure directly the adsorption energy of highly reactive species, such as OH^-, or ascertain how the local electronic environment of a catalyst affects the interaction with substrates on an atomic scale. Over the past 20 years computational chemistry has developed from a curiosity into a well-developed tool, used for a wide range of research purposes. However, software packages developed for such in depth study are never 'black boxes', where one simply asks a question and is given a straight answer, instead one must appreciate the fundamentals behind the software and the limitations associated with different methodologies.

2.3.1 - The Schrödinger equation

In 1924, Louis de Broglie showed that matter, like light, has wave-like properties and that any particle with linear momentum has a wavelength directly related to its momentum (Broglie, 1924). This concept might seem strange in the macro-world, where the mass of an object is so great that the associated wavelengths are undetectably short, but for sub-atomic particles these wavelengths are such an integral part of their character that they are said to have wave-particle duality (Atkins & De Paula, 2012). Such is the magnitude of this wave-like behaviour that these sub-atomic particles do not follow well-defined paths at constant speed, like a particle, but are instead spread across space as a wave, this wavelike trajectory is referred to as the wavefunction, Ψ, of a particle. In 1926 Erwin Schrödinger presented his eponymous equation (Atkins & De Paula, 2012):

$$E\Psi = V(x)\Psi - \frac{\hbar^2}{2m}\frac{d^2\Psi}{dx^2}$$

Equation 2.7 - Time-independent Schrödinger equation.

which states that the total energy of a wavefunction is equal to the sum of potential energy, $V(x)\Psi$, and kinetic energy, $-\frac{\hbar^2}{2m}\frac{d^2\Psi}{dx^2}$. This kinetic energy term can then be

broken into two components, one a modification of Planck's constant, $-\frac{\hbar^2}{2m}$ where $\hbar$ is the reduced Planck constants and m is the mass of the particle, the other a description of the curvature of the wavefunction, $\frac{d^2\Psi}{dx^2}$. This is commonly presented in an abbreviated form (Atkins & De Paula, 2012):

$$E\Psi = \hat{H}\Psi$$

Equation 2.8 - Abbreviated time-independent Schrödinger equation.

where $\hat{H}$ is known as the Hamiltonian operator, containing all the kinetic and potential energy terms of the wavefunction.

Classical models state that electrons orbit the nucleus of an atom, typically treated as a static point charge with an associated mass, in well-defined spherical orbits. However, this classical view cannot be reconciled with the wave-particle duality model of particles such as electrons due to the Heisenberg uncertainty principle. This principle states that it is impossible to know exactly the position and momentum of an electron (Atkins & de Paula, 2009). Moreover, this principle states that the more we know about the position of an electron, the less we know about the momentum and vice versa. In order to obtain a strict path for an electron around a nucleus one must know both the position and momentum of an electron at all points on said path, information which cannot be obtained. Instead, one finds that Schrodinger's equation for a single electron can be solved, producing orbits that are instead probability densities - that is to say that an electron of particular energy will be found within a particular orbital but that the exact position within the orbital cannot be known exactly. Collectively the multiple Schrödinger solutions for a single electron result in the atomic orbitals shown in Figure 2.2 (Atkins & de Paula, 2009). Within computational chemistry software, such as Gaussian09, these orbitals are described by basis-sets, with larger basis sets able to more accurately describe not only the orbital shape, but also their overlap to form hybrid orbitals which are described in section 2.3.3.
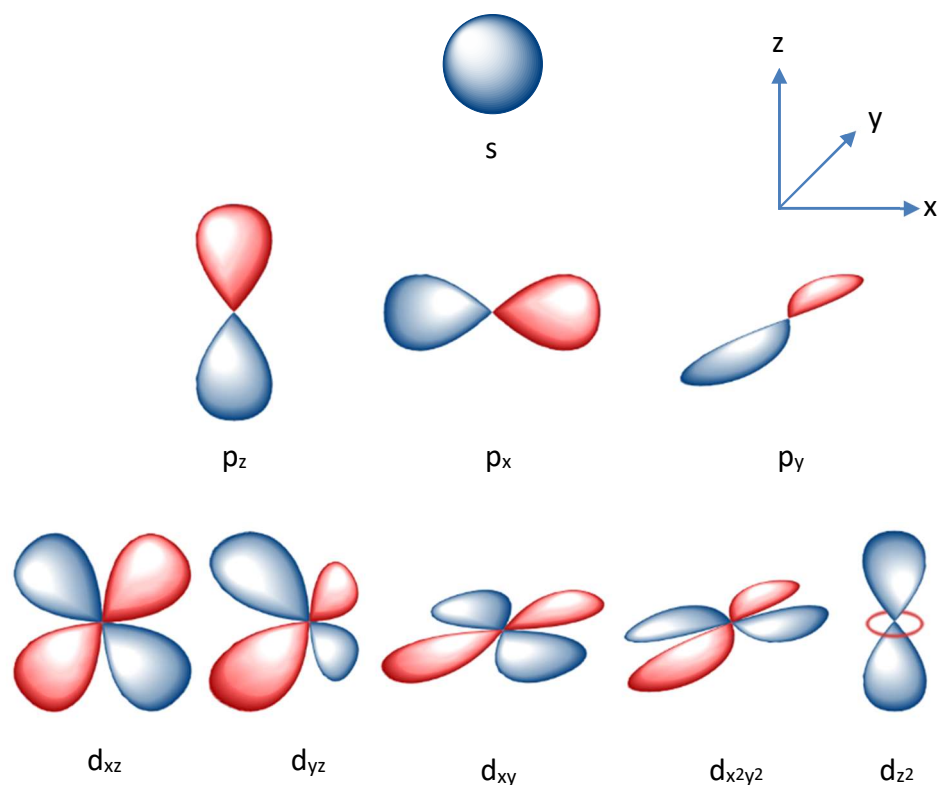
Figure 2.2 – 's', 'p' and 'd' molecular orbitals as predicted by the Schrödinger equation.

Thus far orbitals have been described exclusively with the time-independent Schrödinger equation, albeit on a simplistic level, but to accurately describe a dynamic system we must include momentum, in doing do we find the time-dependent Schrödinger equation (Atkins & de Paula, 2009):

$$i\hbar\frac{\delta}{\delta t}\Psi = \hat{H}\Psi$$

Equation 2.9 - Abbreviated time-dependent Schrödinger equation.

The Hamiltonian within this time-dependent Schrödinger equation includes a multitude of terms that allow for the description of the energy of a particle while taking into account the momentum of said particle. For ease and brevity the derivation of this Hamiltonian will not be detailed here, instead some of the more interesting implications will be discussed.

When we apply this time dependent equation we find that the description of a single electron must include a way to describe the momentum of an electron within an

orbital. Overall the description of an electron can be made using four 'quantum numbers' (Atkins & De Paula, 2012):

1. The principle quantum number - i.e. the 'shell' of an atom being occupied
2. The azimuthal quantum number - i.e. the subshell 'type', be that 's', 'p', 'd', 'f'' or 'g'
3. The magnetic quantum number - i.e. the specific orbital within the subshell, such as p_x, p_y or p_z
4. The spin quantum number - i.e. the angular momentum of the electron, this can either be 0.5 or -0.5, commonly referred to as α and ß electrons, respectively.

These four quantum numbers show that a single orbital, i.e. the $2p_x$ orbital, can be occupied by up to two electrons but that these electrons must have opposing spin. The notion of electron spin is incredibly important within computational chemistry and is found to influence not only the electronic structure of an atom but also the reactivity of a system.

2.3.2 - Self-consistent field and density functional theory methods

Self-consistent field, SCF, methods such as Hartree-Fock consider the Hamiltonian of a multi-particle, time-dependent Schrödinger equation as the sum of multiple single-particle Hamiltonians, plus terms for their interaction (Koch & Holthausen, 2001a). Consider two electrons in separate orbitals, one electron feels electron-electron-repulsion from the other and thus moves to reduce the energy of the system, distorting the probability density and thus the orbital shape. In a multi-particle system, each electron feels repulsion from all other electrons, and moves to reduce this repulsion, and so the location of one electron affects the location of all others. Additionally, each electron feels an attraction towards each nucleus, and each nucleus feels repulsion against all other nuclei. Thus, the position and momentum of a particle is a function of the position and momentum of all other particles within a system, quantities which cannot be known precisely (Koch & Holthausen, 2001b). For Hartree-Fock methods, the most important of these multi-particle interactions is electron-electron repulsion (Leach, 2001). Approximations for these inter-particle interactions must be introduced, the extent of which makes an SCF method either more or less accurate and the speed of

calculation either slower or faster; in general the more accurate a method, the slower the calculation.

Density functional theory methods, such as B3LYP, instead consider the Hamiltonian as a function of electron density (Koch & Holthausen, 2001b). According to the Hohenburg-Kohn theorem, the density of a system allows for the determination of all ground state properties (Koch & Holthausen, 2001b). By focussing on the density of a system, the number of variables is considerably reduced; while SCF methods contain 3N special variables, where N is the number of particles within the system, DFT minimises this to 3 spacial variables regardless of system size. This has the obvious effect of speeding up the calculations considerably.

This inevitably has the effect of changing the form of the Hamiltonian and removes the need to create additional terms for electron-electron repulsion making calculations of comparative accuracy faster. DFT is also especially useful when considering d-block elements such as platinum, where it produces better agreement with experiment than other methods (Atkins & De Paula, 2012).

2.3.3 - Basis sets and hybridization

The accuracy of both SCF and DFT methods are dependent on the selection of a suitable basis set. A basis set is comprised of a number of basis functions[6]; it provides a description of the molecular orbitals within a complex and thus how orbitals and electrons can interact (Leach, 2001). The most simple basis sets have very restricted orbitals due to the low number of basis functions, offering the least accurate view of bonding but the shortest computation times (Foresman & Frisch, 1996). By increasing the number of basis functions, one is able to more accurately describe the atomic and molecular orbitals.

Split-valence basis sets describe valence orbitals with multiple basis functions, allowing valence orbitals to change size depending on the local electronic environment, i.e. the proximity of neighbouring electrons (Foresman & Frisch, 1996). As bonding

---

[6] A basis function is the mathematical representation of a single hydrogen atomic orbtial

principally involves valence orbitals, these split-valence basis sets provide a considerably more accurate view of atomic orbital overlap and thus bonding.

The accuracy of a basis set is also increased by including polarization and diffuse functions (Foresman & Frisch, 1996). As atoms interact their orbitals may shift position either as a result of repulsion or overlap, polarisation functions allow for this shifting of position, and thus a distortion from the classical orbital shapes shown in Figure 2.2, by mixing orbitals, resulting in hybrid orbitals. The inclusion of polarization functions is also crucial to the accurate description of weak van der Waals interactions in systems including hydrogen atoms, as well as the interaction of 'p' and 'd' orbitals between carbon, nitrogen and transition metal atoms (Leach, 2001). Diffuse functions allow for a more precise description of anions and lone pairs by including larger 's' and 'p' orbitals (Leach, 2001). For systems involving anions and hydrogen bonding, such as the interaction of oxygen reduction intermediates with a catalyst, both polarization and diffuse functions are essential components of a basis set. All the calculations presented herein utilise either the 6-311g++(d,p) basis set[7] or the LANL2DZ basis set[8]. These basis sets has been used extensively in similar work and has been shown to produce accurate and reliable results (Anderson, 2002; Anderson, 2010; Anderson et al., 2005; Asiri & Anderson, 2013; Aydin, 2013; Bikiel et al., 2008; Kieber-Emmons et al., 2011; Tian & Anderson, 2011; Zhang et al., 2005).

2.3.4 - Natural population, natural bond orbital and natural localised molecular bond orbital analyses

By performing natural population and natural bond orbital analyses it is possible to marry up theory and experiment. As described in the previous sections, computational chemistry methods allow for the wavefunction of a complex system to be resolved albeit to varying, method dependant, degrees of accuracy. In doing so, the orbital occupations

---

[7] A split-valence basis set with polarization and diffuse functions included on atoms H through to Zn

[8] A split valence basis set that uses an approximation for core electrons and multiple basis sets for valence electrons. This allows for a significant reduction in computation times for systems involving heavy transition elements such as platinum.

of each atom can be calculated. There are three strands to an in-depth investigation of orbital occupation, the natural population analysis, NPA, natural bond orbital, NBO, and natural localised molecular orbital, NLMO, analyses. NPA simply prints the calculated occupation of each sub-orbital which is a function of its maximum occupation and the probability of finding an electron within said sub-orbital at any given time, effectively a breakdown of the self-consistent wavefunction. Comparing the natural populations of the stable structures within a reaction mechanism allows one to ascertain the movement of electrons and infer their relative reactivity. However, a natural population analysis does not offer any information regarding the nature of bonding within a stable structure.

NBO analysis allows one to ascertain short-range interactions between neighbouring atoms via traditional covalent bonds. NBO analyses are somewhat more complex than the output for an NPA as it includes hybridization between sub-orbitals and the polarization of a bond between two atomic centres. From this, one can ascertain both the extent of a bond dipole and the stability of a bond under particular conditions.

NLMO analysis is more involved still than NBO analysis, containing detailed information not only about the nature of a single bond, but how bonds and lone pairs interact with anti-bonding and excited orbitals. The output from an NLMO analysis is incredibly complex but, if performed correctly, gives perhaps the most detail regarding the likely direction and lability of a particular reaction.

These techniques form the backbone of the majority of the computational analysis presented herein but the outputs from such reactions are too large and complex to include at a suitable level of detail; for example the smallest catalysed system has an abridged population output of over 200,000 words. Instead it is thought more useful to present how these results are interpreted for a simple molecule; O_2.

Molecular oxygen is known to exist in a triplet state, with electron pairs occupying all p-bonding orbitals and partial electron occupation of anti-bonding p-orbitals, as shown in Figure 2.3. From Figure 2.3 we can see that both oxygen atoms in O_2 have 8
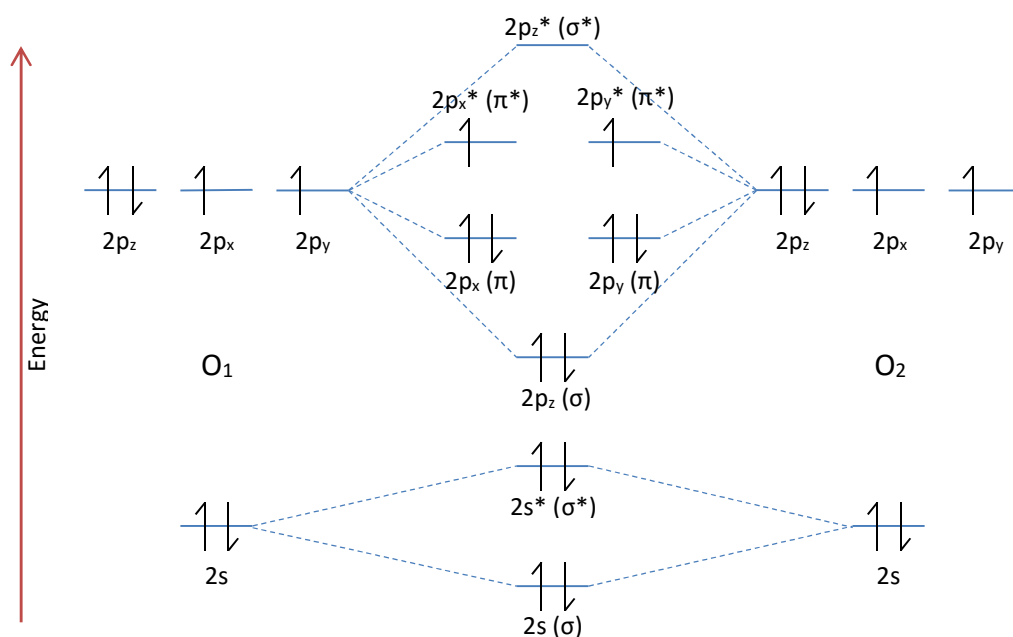
Figure 2.3 - The molecular orbital diagram of O_2.

electrons, the 1s orbital being lowest in energy, the 2s higher and the $2p_x$, $2p_y$ and $2p_z$ orbitals higher still but approximately degenerate with each other. We can also see that the 1s, 2s and $2p_x$, $2p_y$ and $2p_z$ bonding orbitals are all doubly occupied while the $2p_x$ and $2p_y$ anti-bonding orbitals are both singly occupied. Table 2.1 shows the orbital occupation of molecular oxygen as calculated by Gaussian09[TM].

Overall there are four electrons occupying the 1s level and approximately 3 electrons occupying the $2p_x$ and $2p_y$ orbitals. The 2s and 2pz orbitals present what appears to be a somewhat impossible scenario, one where a fraction of an electron occupies an orbital. In such a case it is essential that one remembers that any orbital analysis is not treating an electron as a particle, but rather as the probability of an electron occupying a space at any given moment, thus it can be said that at any one moment in time there is an average of 3.576 electrons in the 2s orbital and 2.384 electrons in the $2p_z$ orbital. Also in Figure 2.3 it can be seen that while the 2s bonding orbital of O_2 is significantly lower in energy than the $2p_z$, the 2s anti-bonding orbital, 2s*, lies between them. Thus if these two orbitals are relatively close in energy an electron could occupy both. It is also of interest to see how these electrons organise themselves within the atomic orbitals. Table 2.1 also shows that for both oxygen

Table 2.1 - Orbital occupation of molecular oxygen.

			1s	2s	2px	2py	2pz	Rydberg	Charge
O_2	O_1	α	0.999	0.901	0.998	0.998	0.590	0.015	-0.50
		ß	1.000	0.888	0.500	0.500	0.602	0.011	0.50
		tot	1.999	1.788	1.497	1.497	1.192	0.025	0.00
	O_2	α	0.999	0.901	0.998	0.998	0.590	0.015	-0.50
		ß	1.000	0.888	0.500	0.500	0.602	0.011	0.50
		tot	1.999	1.788	1.497	1.497	1.192	0.025	0.00
	Total		3.999	3.576	2.995	2.995	2.384	0.050	0.00

atoms the $2p_x$ and $2p_y$ orbitals have a single alpha electron each and a shared beta electron. Overall the oxygen molecule is not charged and a dipole does not exist as the total charges on both atoms are equal to zero.

The NBO analysis allows for a further insight into how these simple atomic orbitals overlap to form bonding orbitals. For O_2 it is common to refer to an oxygen double bond though this is something of a misnomer. If one were to consider the O_2^{2+} molecule, in which the $2p_x*$ and $2p_y*$ orbitals were unoccupied, one would find three doubly occupied bonding orbitals. There are two possible ways for the neutral system to be arranged; either the $2p_x$ or $2p_y$ orbitals are double occupied, or both are singly occupied. Given the energy degeneracy of these two orbitals, it is more feasible that the latter scenario is true, as this reduces electron-electron repulsion within the same orbital, and so the system is instead described as having one and two 'one-half' bonds.

From the NBO output, shown in Figure 2.4, it can be seen that this single alpha NBO is completely occupied, is a single bond, exists between oxygen atoms numbers 1 and 2, has equal contribution from each atom and is non-polarized due to identical polarization coefficients. The data highlighted by light brown and grey boxes in Figure 2.4 give information regarding the hybridization of the NBO. The light brown box gives the hybridization of the contributing orbitals, 15.28 %/84.72 % 's' and 'p' character respectively, while the grey box highlights information regarding exactly which sub-orbitals are involved, in this case the 2s and $2p_z$ orbitals on both atoms 1 and 2. While the latter of these two seems convoluted, a key is given earlier in the output file that allows for the elucidation of orbital contribution. The annotated alpha NBO list has a

Type of orbital (BD
= bond, CR = core,
LP = lone pair, RY
= Rydberg)

Serial number (i.e.
single, double, triple
bond etc)

Alpha NBO list

Atoms involved (i.e. Oxygen
#1 and oxygen #2)

Atomic orbital
contribution to
NBO

```
         (Occupancy)    Bond orbital/ Coefficients/ Hybrids
   -------------------------------------------------------------------------
     1.  (1.00000)  BD ( 1) O    1 - O    2
             ( 50.00%)    0.7071* O    1 s( 15.28%)p 5.54( 84.72%)
                                         0.0000 -0.3789  0.0964  0.0000  0.0000
                                         0.0000  0.0000  0.0000  0.0000  0.0000
                                         0.9184 -0.0601 -0.0025
             ( 50.00%)    0.7071* O    2 s( 15.28%)p 5.54( 84.72%)
                                         0.0000 -0.3789  0.0964  0.0000  0.0000
                                         0.0000  0.0000  0.0000  0.0000  0.0000
                                        -0.9184  0.0601  0.0025
```

No. of electrons
in orbital

% contribution to
NBO

Polarization
coefficients

Sub-orbital contribution to NBO
(the key to this list is found
elsewhere in the output file)

Beta NBO list

```
         (Occupancy)    Bond orbital/ Coefficients/ Hybrids
   -------------------------------------------------------------------------
     1.  (1.00000)  BD ( 1) O    1 - O    2
             ( 50.00%)    0.7071* O    1 s( 17.42%)p 4.74( 82.58%)
                                         0.0000 -0.4074  0.0906  0.0001  0.0000
                                         0.0000  0.0000  0.0000  0.0000  0.0000
                                         0.9071 -0.0539 -0.0048
             ( 50.00%)    0.7071* O    2 s( 17.42%)p 4.74( 82.58%)
                                         0.0000 -0.4074  0.0906  0.0001  0.0000
                                         0.0000  0.0000  0.0000  0.0000  0.0000
                                        -0.9071  0.0539  0.0048
     2.  (1.00000)  BD ( 2) O    1 - O    2
             ( 50.00%)    0.7071* O    1 s(  0.00%)p 1.00(100.00%)
                                         0.0000  0.0000  0.0000  0.0000  0.9996
                                         0.0292 -0.0028  0.0000  0.0000  0.0000
                                         0.0000  0.0000  0.0000
             ( 50.00%)    0.7071* O    2 s(  0.00%)p 1.00(100.00%)
                                         0.0000  0.0000  0.0000  0.0000  0.9996
                                         0.0292 -0.0028  0.0000  0.0000  0.0000
                                         0.0000  0.0000  0.0000
     3.  (1.00000)  BD ( 3) O    1 - O    2
             ( 50.00%)    0.7071* O    1 s(  0.00%)p 1.00(100.00%)
                                         0.0000  0.0000  0.0000  0.0000  0.0000
                                         0.0000  0.0000  0.9996  0.0292 -0.0028
                                         0.0000  0.0000  0.0000
             ( 50.00%)    0.7071* O    2 s(  0.00%)p 1.00(100.00%)
                                         0.0000  0.0000  0.0000  0.0000  0.0000
                                         0.0000  0.0000  0.9996  0.0292 -0.0028
                                         0.0000  0.0000  0.0000
```

Figure 2.4 - Annotated output from NBO analysis of O_2.

a function of orbital energy. The more complicated a system is, however, the more
bonding and atomic orbitals there are that are likely to be degenerate in terms of energy
and the less intuitive a molecular orbital appears. Thus in this study NLMO's are single

26

entry due to the dual occupation of the alpha $2p_x/2p_x*$ and $2p_y/2p_y*$ orbital pairs, resulting in the 'cancelling out' of the alpha component of the $2p_x$ and $2p_y$ bonds, while the lack of occupation in the beta $2p_x*$ and $2p_y*$ orbitals effectively results in the two 'one-half' bonds predicted earlier. From the beta NBO list in Figure 2.4, it can be seen that these two 'one-half' bonds are again homogenous, as indicated by identical atomic contributions and polarizations, and are exclusively of 'p' character from the $2p_x$ and $2p_y$ orbitals for NBO 2 and 3 respectively.

Finally, one should attempt to resolve the conclusions drawn from the NPA and NBO analysis with the molecular orbital analysis. The molecular orbital analysis allows for a graphical representation of the probability of electron location within a system as investigated, which take into account the influence of energy degenerate orbitals within close proximity to the bond orbitals of interest, and thus provide a more intuitive representation of the molecular orbitals.

Figure 2.5 shows the energy of the molecular orbitals of O_2 and their associated wave functions. As can be seen the 1s, 1s*, 2s, $2p_x$, $2p_y$ and $2p_z$ orbitals are all doubly occupied, the $2p_x*$ and $2p_y*$ orbitals are occupied by a single alpha electron, and the $2p_z*$ and 2s* orbitals are both unoccupied. These results fully support the findings of the NPA and NBO analysis. Overall the combined use of NPA, NBO and NLMO analysis allows for an in-depth investigation as to the electron configuration and bonding of systems under investigation. By comparing the reactant and product of a reaction, one can gain detailed knowledge of the nature of reactions and ascertain exactly how additions to a system, such as a catalyst, are able to influence the reactions under investigation.

2.4 - Electrochemical techniques

The typical experimental set-up is simple; one needs a working electrode onto which the catalyst is deposited, a reference electrode against which the potential can be measured, a counter electrode to provide current and a suitable electrolyte containing an electro-active species, such as $K_3[Fe(CN)_6]$ or O_2. Using this three electrode system, one is able to measure the interaction between the working electrode and the electro-active species of interest across a range of potentials and
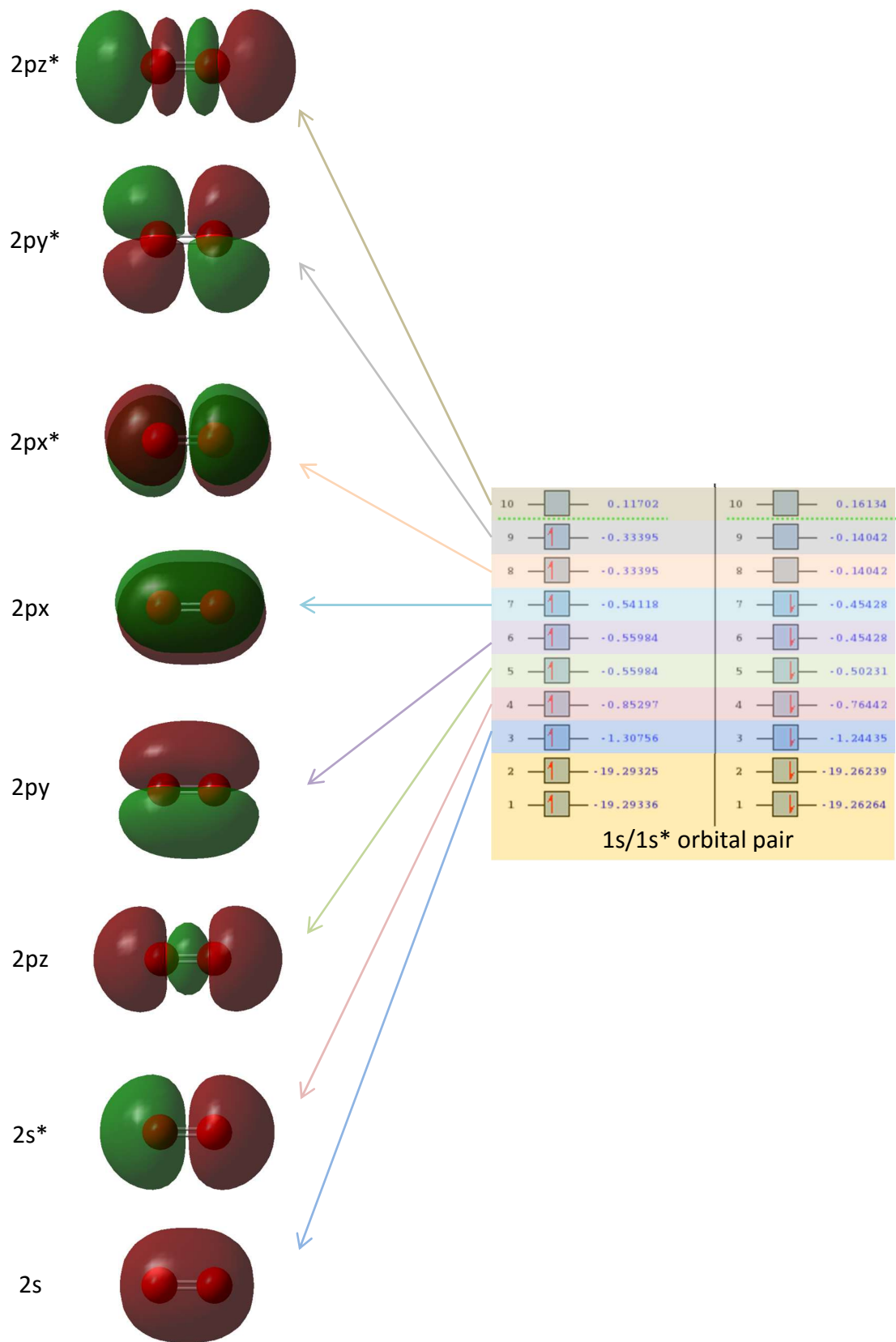
Figure 2.5 - MO analysis of O₂, note the energy degeneracy of the 2pₓ/2pᵧ and 2pₓ*/2pᵧ* orbital pairs.

currents. Techniques such as cyclic voltammetry and rotating ring-disk electrode analysis are able to provide a wealth of information regarding the activity of a catalyst; from ORR onset potentials, to the reversibility of a reaction, to the number of electrodes transferred at a given potential.

2.4.1 - Cyclic voltammetry

Cyclic voltammetry, CV, sweeps the potential between the reference electrode and the working electrode forwards and backwards across a potential range while monitoring the current flowing between the working electrode and the counter electrode. By sweeping the potential at a constant rate, the scan rate, and measuring the current response, one is able to ascertain the potential at which electro-active species within the electrolyte are oxidized/reduced. Figure 2.6 shows the CV of 10 mM $K_3[Fe(CN_6)]$, the active species, in 1 M KNO_3, the electrolyte, when using a glassy carbon disk working electrode, a standard hydrogen reference electrode and a platinum wire counter electrode. During this experiment the potential was repeatedly cycled between 1.0-0.0 V as it is known that the redox potential of the ferricyanide couple lies within this range. During the initial sweep no discernible current increase is seen until the reduction reaction occurs, $[Fe(CN_6)]^{3-} + e^- \rightarrow [Fe(CN_6)]^{4-}$, at which point a large peak appears, with the current going through a peak potential, and then decreasing. During the reverse sweep a similar behaviour is seen, with an ideally equal and opposite current occurring due to the oxidation reaction, $[Fe(CN_6)]^{4-} \rightarrow [Fe(CN_6)]^{3-} + e^-$. In this example the reaction is perfectly reversible, that is to say that all the $[Fe(CN_6)]^{4-}$ ions generated during the forward sweep can be oxidised during the reverse sweep and vice versa.

However, when assessing the performance of a catalyst towards the ORR, the resultant voltammograms are somewhat more complex. Figure 2.7 shows the CV of a platinum catalyst in O_2 saturated 0.5 M H_2SO_4 in which the potential cycles between 0.05-1.20 V. During the forward sweep (red), species from the electrolyte adsorb to the platinum surface and oxidise. During the reverse peak (blue) reduction reactions occur on the surface of the electrode, in this case including the reduction of solvated O_2 within the electrolyte. The highlighted peak in Figure 2.7 is attributed to the
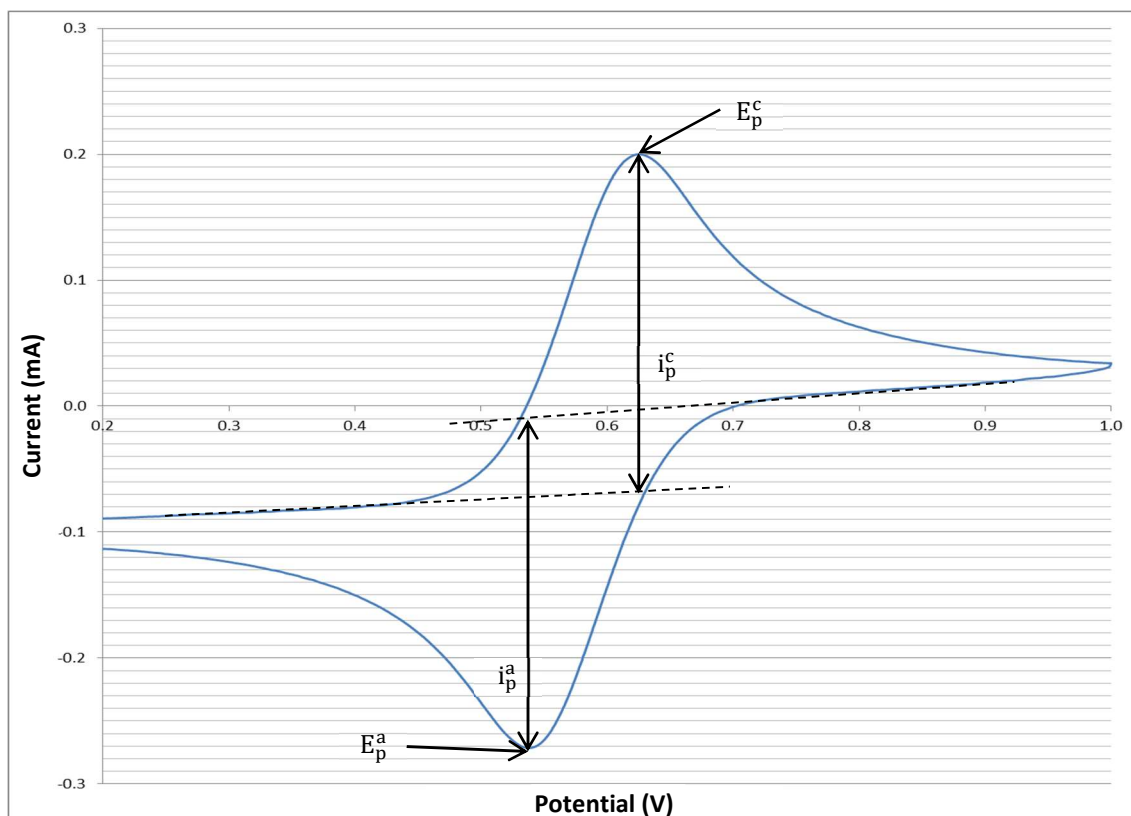
Figure 2.6 - Cyclic voltammogram of 10 mM K$_3$[Fe(CN$_6$)] in 1 M KNO$_3$ (30 mVs^{-1} scan rate) using a glassy carbon disk as the working electrode. Labelled are the cathodic/anodic peak potentials, E_p^c and E_p^a respectively, and peak currents, i_p^a and i_p^c respectively.
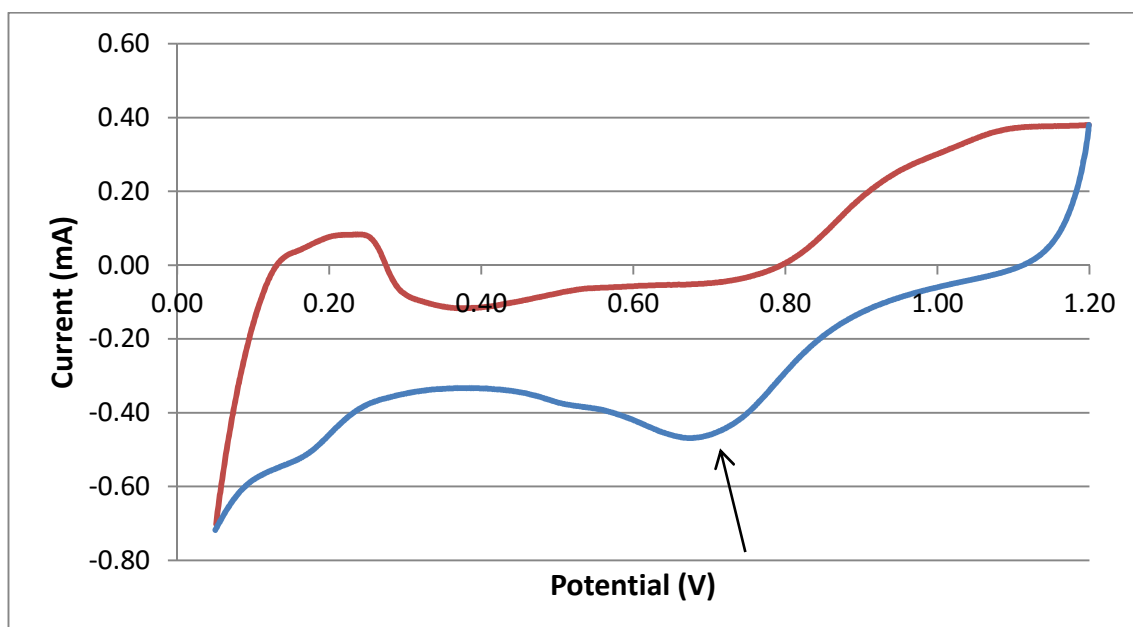
Figure 2.7 – Cyclic voltammogram of 20 wt.% Pt on carbon in O$_2$ saturated 0.5 M H$_2$SO$_4$, the O$_2$ reduction peak is highlighted by a black arrow.

reduction of O_2. By comparing the onset potential of this peak, the potential of peak current and the absolute peak current of various catalysts, one can ascertain their electrocatalytic activity; the higher these values the more active the catalyst.

2.4.2 - Rotating disk and rotating ring-disk electrodes

By rotating the working electrode in the electrolyte, typically between 1-3000 rpm (Compton & Banks, 2007), a constant flow of analyte from the bulk solution to the electrode tip is induced. Unlike with the CV shown in Figure 2.6, well defined peaks are not seen, instead at potentials below the reduction potential a plateau current is seen, called the limiting current, due to the constant flux of reactive species to theelectrode surface. This limiting current is therefore a function of both the kinetics of the surface reaction and the diffusion of analyte from the solution, through the diffusion layer, to the surface of the electrode. The size of this diffusion layer is dependent on the rotation rate of the electrode, with a faster rotation rate resulting in a faster flow of electrolyte and thus a smaller diffusion layer. The relationship between the rotation rate, the kinetic reaction rate and the limiting current is given by the Koutecky-Levich equation:

$$\frac{1}{i_{lim}} = \frac{1}{i_k} + \frac{1}{0.62nFC_0AD_0^{2/3}v^{-1/6}\omega^{1/2}}$$

Equation 2.10 - Koutecky-Levich equation.

where i_{lim} is the limiting current, i_k is the kinetic-limited current, n is the number of electrons transferred, F is the Faraday constant, A is the surface area of the electrode, C_0 is the concentration of analyte, D_0 is the diffusion coefficient, v is the kinematic viscosity and ω is the rotation rate. A plot of i_0^{-1} against $\omega^{-1/2}$ thus produces a gradient of $(0.62nFC_0AD_0^{2/3}v^{-1/6})^{-1}$ and an intercept of $(nFAkC_0)^{-1}$. From the gradient and intercept of a Koutecky-Levich plot one can therefore ascertain the number of electrons transferred and the rate constant of the surface reaction.

Rotating ring-disk electrodes incorporate a second working electrode to allow for the detection of reaction intermediates, this is particularly useful when investigating the ORR as hydrogen peroxide generated on the catalyst surface can be detected. In such an electrode the central disk is separated by a small non-conductive polymer from a

platinum ring. The ring is held at a potential high enough to oxidise formed intermediates and the current mapped as a function of the disk potential. Figure 2.8 shows the RRDE voltammogram of 10 mM $K_3[Fe(CN)_6]$ in 1 M KNO_3 using a glassy carbon disk as the working electrode at 1200 rpm. $[Fe(CN)_6]^{4-}$ ions formed on the disk electrode are oxidised to $[Fe(CN)_6]^{3-}$ on the ring, thus one would expect near-identical currents on the two electrodes. The disparity between the measured currents is due to both the difference in surface areas between the two electrodes and the percentage of reduced ions that come into contact with the ring electrode. Using a single electron redox couple (e.g. $[Fe(CN)_6]^{3-}/[Fe(CN)_6]^{4-}$) one can find the collection efficiency, N, from the ring current, i_R, and disk current, i_D, via Equation 2.11.

$$N = \frac{-i_R}{i_D}$$

Equation 2.11 - Collection efficiency of RRDE.

As the current observed on both the disk and ring electrodes are functions of the diffusion layer thickness, and thus the rotation rate, all peroxide calculations were performed at 1200 rpm, at this rotation rate the collection efficiency was found to be 24.57 %. With the collection efficiency known, one can thus calculate the amount of peroxide generated using Equation 2.12:

$$\%H_2O_2 = \frac{2i_R/N}{i_D + i_R/N}$$

Equation 2.12 - Peroxide yield calculation from ring and disk currents
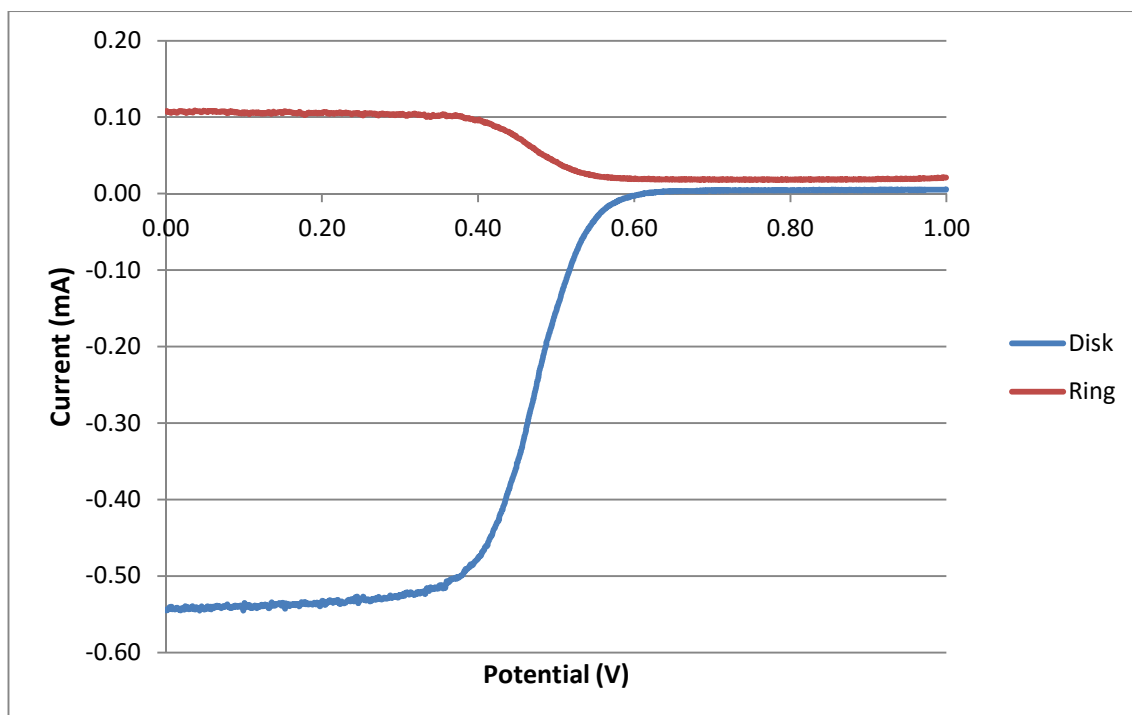
Figure 2.8 - RRDE voltammogram of 10mM K₃[Fe(CN₆)] in 1M KNO₃ using a glassy carbon disk as the working electrode, rotating at 1200rpm.

2.5 - The platinum catalysed oxygen reduction reaction

As the (111) plane of platinum is known to be the most catalytically active (Ishikawa et al., 2007; Markovic, 1995), the vast majority of work considers this plane exclusively. Early studies of the reaction on platinum focussed on the adsorption of O_2 on to the surface and proposed a temperature dependence of O_2 adsorption, with chemisorbed states present below 120 K, and atomically adsorbed $O_{(ads)}$ at temperatures above 150K (Adzic & Wang, 1998; Lynch & Hu, 2000; Puglia et al., 1995; Shi et al., 2006; Sidik & Anderson, 2002; Yang et al., 2010). As the operational temperature of a fuel cell is 310-380 K one would assume a dissociative pathway of reduction, where $O_{2(ads)}$ dissociates prior to proton transfer, to be dominant. However, these studies are performed on a clean Pt surface and so the effect of solvent or surface species such as $OH_{(ads)}$ is not included, this is supported by the work of Groß et al. (2003) who state that O_2 does not dissociate on cold Pt(111) surfaces even at kinetic energies higher than the dissociation barrier. Regarding the adsorption of O_2 to the platinum surface, it is found that O_2 readily displaces adsorbed water at 0 V, but this process becomes increasingly difficult at higher potentials, becoming an activated process at potentials above 0.44 V (Sidik & Anderson,

33

2002). However, this activated adsorption also includes the protonation of O_2, it is not expected that a chemical reaction would have any potential dependency.

Experimental work found that two chemisorbed O_2 species are present, either superoxo-, O_2^-, or peroxo-, O_2^{2-}, like oxygen (Adzic & Wang, 1998; Stipe et al., 1997) characterised by bond frequencies/bond lengths of 850-890 cm^{-1}/1.37-1.39 Å and 690-710 cm^{-1}/1.41-1.43 Å respectively (Adzic & Wang, 1998; Li & Balbuena, 2003; Puglia et al., 1995; Shi et al., 2006; Wang & Balbuena, 2004). The observed bond lengths of the chemisorbed O_2 species indicate that charge donation from the platinum surface is to the anti-bonding orbitals of O_2. This is supported by experimental and computational studies which show donation from the 5d orbitals of platinum to the π^* antibonding orbital of O_2 (Li & Balbuena, 2003; Puglia et al., 1995; Wang & Balbuena, 2004). The adsorption site of O_2^- and O_2^{2-} is also found to differ, with the former occupying a bridge site and the latter an fcc/hcp site (Eichler & Hafner, 1997; Shi et al., 2006; Sidik & Anderson, 2002; Walch et al., 2008; Yang et al., 2010) as shown in Figure 2.9.
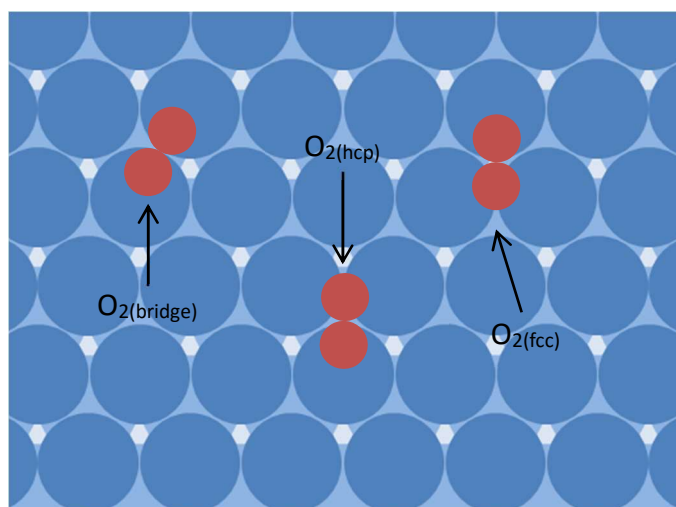
Figure 2.9 - $O_{2(ads)}$ binding sites on the Pt(111) surface.

While $O_{2(ads)}$ on a clean surface prefers to occupy a bridge site, whereby both atoms are involved in binding, as this allows for better overlap of the oxygen anti- bonding orbitals with the platinum surface (Adzic & Wang, 1998; Ford et al., 2010; Li & Balbuena, 2003), the presence of co-adsorbed substrates, such as $O_{(ads)}$ and $OH_{(ads)}$, can alter the mode of O_2 adsorption, resulting in 'end-on' binding. This mode is characterised by a weaker interaction with the surface, with bond strengths differing by up to 50 kJmol^{-1}

(Sidik & Anderson, 2002). The removal of surface blocking species allows for the re-orientation of the end-on bound $O_{2(ads)}$ into a more stable bridge configuration without an associated activation barrier (Sidik & Anderson, 2002). $O_{2(ads)}$ is able to dissociate to $2O_{(ads)}$ from both bridge and fcc/hcp sites (Stipe et al., 1997), while dissociation from the end-on configuration is not thought possible due to the lack of adjacent surface sites. This correlates with the finding that end-on $O_{2(ads)}$ is a precursor for the formation of H_2O_2 and that surface blocking species could be a source of overpotential in the reaction (Anderson, 2002).

$O_{(ads)}$, $OH_{(ads)}$ and $OOH_{(ads)}$ are all reaction intermediates found on the platinum surface with concentrations varying linearly with pH and potential (Antoine et al., 2001). $OOH_{(ads)}$ is found to be short lived and as such the surface blocking species responsible for a drop in activity at higher potentials is $OH_{(ads)}$, which is stable at potentials above 0.6 V, and $O_{(ads)}$, which becomes stable and dominant above 0.8 V, due to their stronger interaction with the surface than molecular O_2 (Eberle & Horstmann, 2014; Ford et al., 2005; Tian & Anderson, 2011; Walch et al., 2008). At higher potentials, the barriers to the reduction of both $O_{(ads)}$ and $OH_{(ads)}$ increase, prolonging the lifespan of such species on the platinum surface (Anderson, 2002; Ford et al., 2010; Tian & Anderson, 2011).

$O_{(ads)}$ can occupy one of four adsorption sites, top, bridge, fcc and hcp with bond strengths quoted as varying between -208.411 and -501.7307 $kJmol^{-1}$ depending on surface coverage and potential of the system, but in all cases decreasing in strength in the order of fcc>hcp>bridge>top (Anderson, 2002; Eichler & Hafner, 1997; Ford et al., 2005; Jacob et al., 2003; Lynch & Hu, 2000; Puglia et al., 1995; Wang & Balbuena, 2004). Adsorption in three-fold hollow sites results in the formation of two covalent bonds to the platinum surface and one donor-acceptor, i.e. lewis acid-lewis base, bond between the $O_{(ads)}$ and three Pt atoms (Jacob et al., 2003). Spectroscopic analysis shows that these bonds consist of overlap of the $O-2p_x/2p_y$ with Pt-6sp and $O-2p_z$ with Pt-5d orbitals (Lynch & Hu, 2000; Puglia et al., 1995). The binding to the hcp site is thought to be similar in nature to that of the fcc site but for the overlap with orbitals originating from second layer platinum atoms (Jacob et al., 2003). Migration of $O_{(ads)}$ across the platinum surface is known to occur via the bridge site with a barrier of between 41.489-50.173 $kJmol^{-1}$ (Ford et al., 2005) though this behaviour is thought to be unlikely at higher potentials

due to the increased coverage of $O_{(ads)}$ (Anderson, 2002; Tian & Anderson, 2011). The stability offered by the fcc site is due to the increased donation from the platinum surface to the $O_{(ads)}$, reflected in increased partial charges of -0.38 e^-, -0.5 e^-, and -0.55 e^- for the top, bridge and fcc sites respectively (Jacob et al., 2003; Li & Balbuena, 2003). The reduction of $O_{(ads)}$ is stated by some to be extremely labile due to low activation barriers (Anderson & Albu, 2000; Capitano et al., 1999) and by others to be difficult, with high barriers due to the migration of $O_{(ads)}$ from fcc-top sites (Michaelides & Hu, 2001). Due to the large number of sources stipulating the prominence of $O_{(ads)}$ on the electrode surface at high potentials, it is felt that the reaction dynamic shifts significantly with increasing potential. If this is the case one would expect to find that $O_{(ads)} + H^+ + e^- \rightleftharpoons OH_{(ads)}$ is labile at low potentials, but becomes endergonic at potentials above 0.8 V.

$OH_{(ads)}$ can occupy a bridge site, but is most stable on top sites due to weak hydrogen bonding between adjacent $OH_{(ads)}$ species (Anderson, 2002; Ford et al., 2005; Walch et al., 2008; Wang & Balbuena, 2004). $OH_{(ads)}$ can originate from either the reduction of $O_{(ads)}$ or from the comproportionation of water, $H_2O_{(ads)} + O_{(ads)} \rightleftharpoons 2OH_{(ads)}$, though the latter reaction only occurs at potentials higher than 0.4-0.6 V and when $O_{(ads)}$ species are available (Anderson, 2002; Berná et al., 2007; Tripković et al., 2010; Walch et al., 2008)[9]. The disproportionation of water is so labile at higher potentials, that this pathway is preferred to the direct protonation of $O_{(ads)}$ (Ford et al., 2010). At these potentials the formation of water from $OH_{(ads)}$ is not thermodynamically favoured, as evidenced by the dominance of the reverse reaction, thus it can be stated that $OH_{(ads)}$ site blocking species arise from the disproportionation of water (Anderson et al., 2005). It is also stated that this disproportionation reaction is favoured at a higher stoichiometric ratio of water to $O_{(ads)}$, with one or two spectator water molecules acting to stabilize the generated $OH_{(ads)}$ groups (Michaelides & Hu, 2001; Nørskov & Rossmeisl, 2004).

---

[9] While some literature sources imply that there are two 'types' of $OH_{(ads)}$ on the surface (Ford et al., 2010; Walch et al., 2008), it is thought that this instead refers to two pathways for $OH_{(ads)}$ generation as opposed to two structurally or electronically distinct species.

There are a number of reactions that occur on the platinum surface, resulting in a considerably more complex reduction mechanism than the overall reaction would imply (Michaelides & Hu, 2001). Three pathways are commonly considered, a dissociative mechanism, an associative mechanism and a peroxide mechanism (Nilekar & Mavrikakis, 2008; Shi et al., 2006; Todorovic & Meyer, 2011; Walch et al., 2008). These pathways have common reduction steps but differ in the O-O scission step, being either the first, second or third step in the overall mechanism, as shown in Figure 2.10.

The reduction of O_2 to H_2O_2 is the least desirable of the three possible pathways shown in Figure 2.10 due to the waste of Gibbs free energy associated with its formation (Anderson & Albu, 1999; Ford et al., 2010). On a clean surface this pathway is not considered to be competitive (Tripković et al., 2010) but at potentials higher than 0.8 V, where $OH_{(ads)}$ and $O_{(ads)}$ surface blocking species are prevalent, any of the three mechanisms can occur (Nilekar & Mavrikakis, 2008).

A wide range of values are stipulated for the activation barrier of the $O_{2(ads)} \rightleftharpoons 2O_{(ads)}$ reaction, these are stated to be potential independent (Tripković et al., 2010) and range from 32.805-85.873 $kJmol^{-1}$ with increasing surface coverage, the steric effect of adjacent $O_{2(ads)}$ hindering dissociation (Capitano et al., 1999; Sidik & Anderson, 2002; Todorovic & Meyer, 2011; Walch et al., 2008; Yang et al., 2010). By contrast the reduction of $O_{2(ads)}$ to $OOH_{(ads)}$ has quoted barriers between 38.595-77.189 $kJmol^{-1}$ (Anderson & Albu, 2000; Sidik & Anderson, 2002; Todorovic & Meyer, 2011; Wang & Balbuena, 2004), but is explicitly stated by many to be both the first and rate-limiting step in the reduction reaction (Anderson & Albu, 2000; Anderson et al., 2005; Antoine et al., 2001; Damjanovic & Brusic, 1967; Ford et al., 2010; Gómez–Marín & Schouten, 2012; Li & Balbuena, 2003; Sidik & Anderson, 2002; Tian & Anderson, 2011; Tripković et al., 2010; Walch et al., 2008; Wang & Balbuena, 2004).
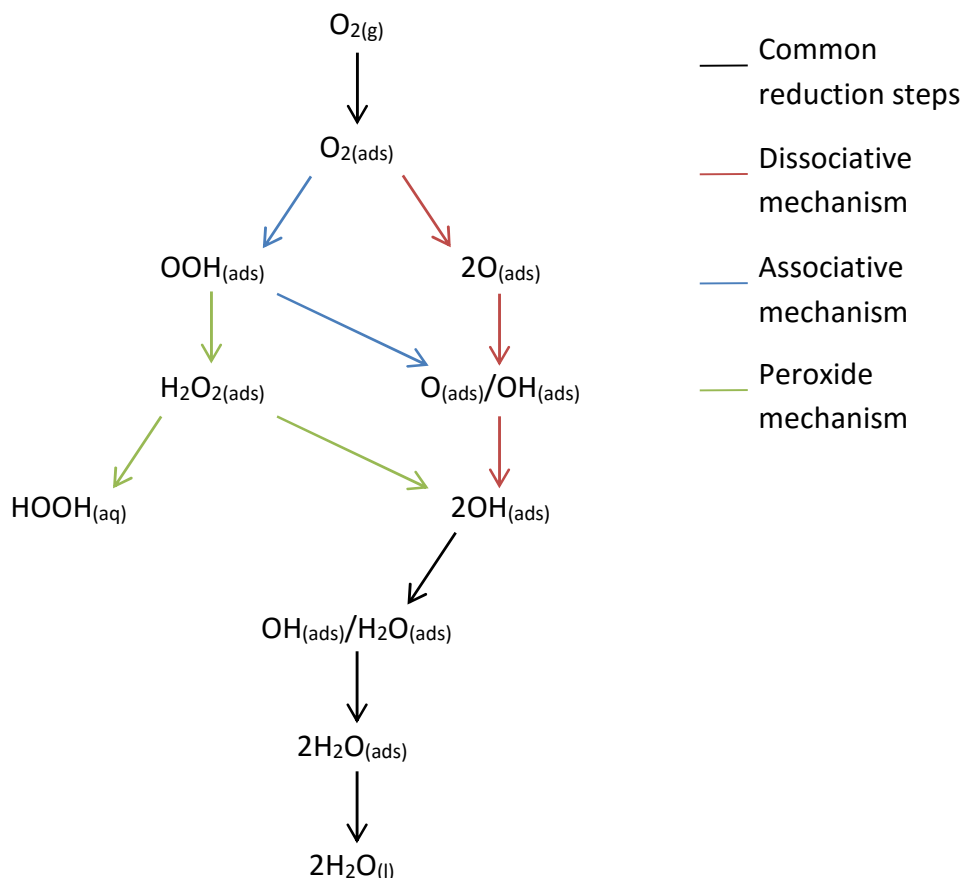
Figure 2.10 - Basic schematic of the three possible oxygen reduction pathways on platinum.

The dissociation of $OOH_{(ads)}$, resulting in $O_{(ads)}$ and $OH_{(ads)}$, is preferred over the protonation to $HOOH_{(ads)}$ as the latter reaction is found to be endergonic (Nilekar & Mavrikakis, 2008; Todorovic & Meyer, 2011) with a barrier as high as 87.803 kJmol^{-1} (Anderson & Albu, 2000; Todorovic & Meyer, 2011). The barrier for $OOH_{(ads)}$ dissociation ranges from 5.789-41.489 kJmol^{-1} and is dependent on both the presence, and type, of co-adsorbed surface species (Sidik & Anderson, 2002; Todorovic & Meyer, 2011; Tripković et al., 2010; Walch et al., 2008; Walch, 2011). The reduced barrier for O-O scission of $OOH_{(ads)}$ compared with $O_{2(ads)}$ is thought to be due to the increased electron occupation of the π/σ anti-bonding orbitals, reflected by significant stretching of the O-O bond of 0.15 Å (Ford et al., 2010; Wang & Balbuena, 2004). The simultaneous protonation/dissociation reaction, resulting in a single water molecule and an $O_{(ads)}$ species is not found to be feasible, being considerably less competitive than both the

dissociation reaction and the asymmetric reduction to $HOOH_{(ads)}$ (Anderson & Albu, 2000; Ford et al., 2010). At higher potentials where surface blocking species hinder the dissociation of $OOH_{(ads)}$, $H_2O_{2(ads)}$ formation is possible but is dependent on $O_{2(ads)}$ binding end-on to the surface through a single O atom (Anderson & Albu, 2000; Walch, 2011).

2.6 - M-N$_x$/C catalysts

While Pt/C currently displays the highest activity towards the ORR, high material cost and scarcity hinder the commercialisation of the technology (Chang et al., 2014; Charreteur et al., 2008; Ikeda et al., 2008; Liang et al., 2014; Liu et al., 2006; Parvez et al., 2012; Si et al., 2013; Szakacs et al., 2014; You et al., 2014; Yuan et al., 2014), thus a large body of work exists that aims to find a viable alternative. As it is well known that the platinum catalysed ORR is 6-7 magnitudes slower than the hydrogen oxidation reaction (Liang et al., 2014; Si et al., 2013), and that a cathodic overpotential in excess of 250 mV exists on this catalyst (Baker et al., 2008; Domínguez et al., 2014; He et al., 2012; Liang et al., 2014; Liu, Li, Ganesan, et al., 2009; Parvez et al., 2012; Xu et al., 2012; Yuan et al., 2014), the vast majority of research within this particular field has focussed on finding materials able to either match, or surpass, the catalytic performance of Pt/C towards the ORR. As PEM fuel cells function at a pH of approximately 1 it is not feasible to use non-noble metal particles, as these would rapidly corrode (Lefèvre et al., 2002), instead research focus has shifted towards metal-organic systems.

2.6.1 - Identity of the active site

In 1964, Jasinski found that cobalt phthalocyanine was active towards the ORR and as such, could potentially be a viable alternative fuel cell cathode catalyst (Jasinski, 1964). For a long time research effectively stalled, with very little progress made towards developing these macrocylic compounds and fine tuning their activity towards oxygen reduction. However, in recent years there has been a resurgence of interest in this branch of electrochemistry, with catalysts now being developed with activities that can rival Pt/C at a fraction of the cost and with negligible environmental effects (Baker et al., 2008; Charreteur et al., 2008; Domínguez et al., 2014; Ikeda et al., 2008; Parvez et al., 2012; Villers et al., 2004; You et al., 2014; Yuan et al., 2014). Macrocylic compounds such as tetraphenylporphyrins and phthalocyanines, as shown in Figure 2.11, are typically

only able to reduce oxygen to hydrogen peroxide which can corrode the catalyst, and thus reduce activity and lifetime (Anderson & Sidik, 2004; Baker et al., 2009; Liu et al., 2006; Marcotte et al., 2004). Tetraphenylporphyrins have been shown to demonstrate higher activity than phthalocyanines, albeit with lower stability in acidic media (Baker et al., 2008). The activity and stability of these macrocycles can be tuned via substitution of peripheral groups (Baker et al., 2008; Baker et al., 2009; Liao et al., 2004), with electron withdrawing substituents increasing the O_2 binding capability of the transition metal centre, while also protecting from oxidative destruction (Liao et al., 2004), and electron donating groups decreasing it (Bikiel et al., 2008; Masa & Schuhmann, 2013).
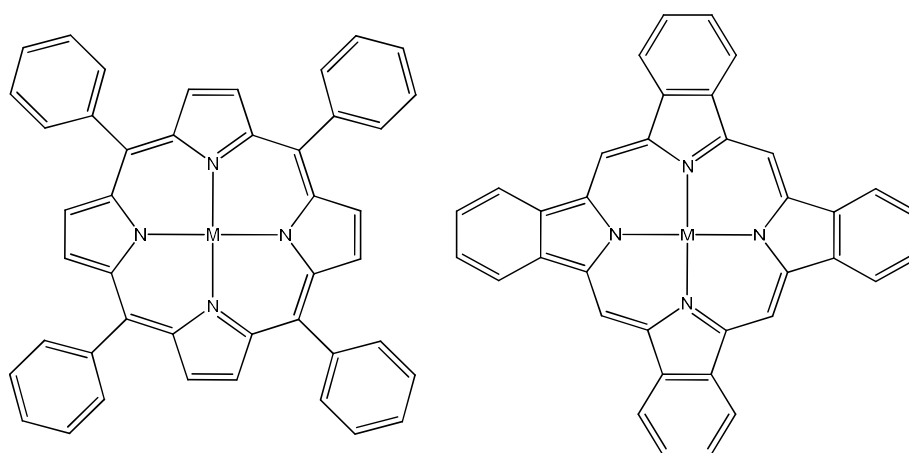
Figure 2.11 – Metal centred tetraphenylporphyrin (left) and phthalocyanine (right).

By pyrolysing such compounds with a carbon support one is able to improve both the stability and activity (Chang et al., 2014; Domínguez et al., 2014; Liu et al., 2006; Schilling et al., 2010; Wei et al., 2000; You et al., 2014), though as yet no catalyst has been synthesised that can match Pt/C in both these regards. However, given the advances that have been made, these pyrolysed compounds have now become the most promising catalyst candidates that may allow for PEM fuel cell commercialisation (Chao et al., 2014; Domínguez et al., 2014; Kattel et al., 2014; Kattel et al., 2013; Li et al., 2012; Liang et al., 2014; Liu et al., 2006; Parvez et al., 2012; Schilling et al., 2010; Wei et al., 2000).

The heat treatment of macrocycles has been shown to result in the partial or complete decomposition of the central macrocycle, thus raising the question of the necessity of starting from such a complex and expensive precursor (Charreteur et al.,

2008; Domínguez et al., 2014; Schilling et al., 2010). Macrocycles undergo a number of structural changes during pyrolysis depending on the pyrolysing temperature; between 200-800 ^oC active sites are structurally related to that of the parent macrocycle, while at temperatures greater than this the macrocycles decomposes into active sites whose structures are uncertain and the source of great discourse (Liu, Li, Ganesan, et al., 2009; Wei et al., 2000). When pyrolysed with a graphitic support above 1000 ^oC these M-N$_x$/C systems have shown activity approaching that of platinum (Lee et al., 2009), thus the identification of the active site generated under these conditions is of paramount importance. Electrochemically active catalysts can be prepared from the pyrolysis of macrocycles containing both nitrogen and a metal atom, or simple nitrogen and metal precursors such as iron or cobalt acetate and ammonia, over a carbon support (Baker et al., 2008; Charreteur et al., 2008; Cheng et al., 2013; Domínguez et al., 2014; Kattel et al., 2014; Li et al., 2012; Liu, Li, Ganesan, et al., 2009; Schilling et al., 2010). Carbon itself is not particularly catalytically active, indeed large overpotentials are required to reduce oxygen over carbon in acidic media (Maldonado & Stevenson, 2005; Marcotte et al., 2004), though doping of a carbon surface with heteroatoms such as nitrogen introduces defective sites onto the surface, which are thought to improve activity (Zhang et al., 2014). That the use of simple precursors generates similar active sites to macrocycles implies that degradation of the active site must occur. Indeed it has been found that porphyrins start to lose their substituted phenyl groups at around 400 ^oC while the central macrocycle (i.e. the M-N$_4$ moiety) remaining stable up to 700 ^oC (Schilling et al., 2010). Wei et al. state that the more commonly studied macrocycles such as phthalocyanines and porphyrins undergo a number of changes when subjected to pyrolysis including decomposition and the formation of new products (Wei et al., 2000). In the presence of a carbon support structure this process is thought to result in surface-bound nitrogen functionalities (such as pyridinic-, pyrrolic- and graphitic-N as shown in Figure 2.12), the generation of metal particles, as well as the possible dissolution of metal ions into the electrolyte or their co-ordination to the afore mentioned nitrogen functionalities (Chen et al., 2013; Pylypenko et al., 2008; Wei et al., 2000; Yuan et al., 2014). The presence of said nitrogen functionalities is dependent on the synthesis conditions. As pyrolysis temperatures increase so too does the relative abundance of

graphitic-N which is thought to be due to the metal-catalysed conversion of pyridinic-N (Bezerra et al., 2008).

2.6.1.1 - Nitrogen functionalities

Chang et al. (2012) pyrolysed carbon supported vitamin B12 at 300-900 $^\circ$C to ascertain the influence of pyrolysis temperature on activity. Interestingly they found that activity peaked when the sample was subjected to a heat-treatment of 700 $^\circ$C and dropped off above this. Using RRDE, electron transfer numbers of 3.02, 3.42, 3.90 and 3.57 e$^-$ when the samples were pyrolysed at 300, 500, 700 and 900 $^\circ$C respectively, values supported by peroxide yields of 49 %, 29 %, 5 % and 22 %. Using X-ray absorption spectroscopy the authors were also able to elucidate the co-ordination number and oxidation state of the central cobalt atom and found that as the temperature increases, the co-ordination number decreases from 6-4 and the oxidation state from +3 to +2/+1 indicating that heat-treatment has a structural influence on the catalyst. The increase in activity is thought to be due to the embedding of a Co-N$_4$/C moiety into the carbon, with this structure only being stable up to 700-900 $^\circ$C, hence the decrease in activity at 900 $^\circ$C is attributed to the thermal degradation of active sites during pyrolysis. However, simple degradation does not account for the XPS results indicating the presence of cobalt with an oxidation state lower than 2+, though this result may be fully explained by the agglomeration of cobalt and the formation of metallic cobalt particles. It has been reported in a number of other journals that this process occurs at higher pyrolysis
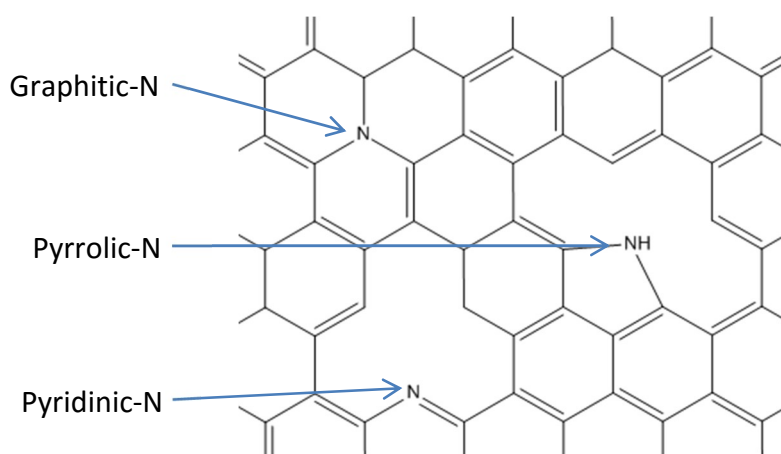
Figure 2.12 – Nitrogen functionalities on carbon.

temperatures or at high metal content in the precursor/carbon mix (Pylypenko et al., 2008; Si et al., 2013; Wei et al., 2000). In a follow up study, Chang et al. (2014) investigated the effect of varying macrocyclic precursors on catalytic activity. By comparing the activities of those samples prepared from the pyrolysis of vitamin B12, which is comprised of a cobalt atom and a corrin ring, Co-TMPP, consisting a cobalt atom and a porphyrin ring, and a cobalt-containing corrole ring. It was found that the type of precursor has a profound effect on the activity of the derived catalyst, with the porphyrin-derived catalyst showing the lowest activity due to the degradation of the central ring and the vitamin B12 derived catalyst having the highest activity. The corrole derived catalyst had middling activity, implying that this ring structure is more stable than a porphyrin at higher temperatures but generates an inferior catalyst, postulated by the authors to be due to the presence of quaternary nitrogen in corrole. These findings suggest that the type of nitrogen precursor can affect the relative abundance of various surface-N functionalities.

By using three different nitrogen sources with varying N/C ratios during pyrolysis with $Co(NO_3)_2 \cdot 6H_2O$ and carbon black in N_2, Chao et al. (2014) attempted to find a link between the N/C ratio of a nitrogen precursor with the relative abundance of various nitrogen functionalities. Those precursors chosen were 10-hydroxybenzo[h]quinoline (10-HBQ), 8-hydroxyquinoline (8-HQ) and bipyridine (BPy) and had N/C ratios of 0.077, 0.111 and 0.2 respectively. XPS analysis showed that while a correlation exists between activity and the content of both graphitic-N and Co-N_x sites, though the authors state that no relationship was found that linked catalytic activity and the N/C ratio of the nitrogen precursor. However, when pyrolysed at 800 °C, the 8-HQ based catalyst was found to have the highest activity, perhaps suggesting that nitrogen content, like metal content and pyrolysis temperature, may have a maximum after which performance decreases. While this postulate is not supported by the finding of others, who state that nitrogen content displays a linear relationship with activity (Charreteur et al., 2008), a more thorough study involving a greater number of nitrogen sources would have allowed for a more detailed description of the role of nitrogen precursors. While the N/C ratios of the three precursors change, the 'type' of nitrogen remains constant throughout the study, that is to say that in all cases only pyridinic-N is used as a precursor

while a carbon surface can be doped with a number of different nitrogen functionalities. Given that Chang et al. (2014) utilised three different macrocycle precursors with different nitrogen functionalities and found not only a shift in activity but also potentially stability, an expanded study that addressed N-functionality in the precursor mix would be of great interest.

Wei et al. (2000) utilised cobalt sulphate and gaseous acetonitrile to ascertain which components are the active sites in the pyrolysed catalyst, be that the nitrogen, the metal or simply defects and a microporous structure generated within the carbon structure. Using a temperature of 1000 °C it was found that carbon pyrolysed in the absence of both nitrogen and metal precursors had exactly the same onset potential as non-pyrolysed carbon, 0.38 V. Pyrolysing carbon in the presence of cobalt sulphate resulted in a 100 mV increase in peak potential to 0.48 V, while pyrolysis with acetonitrile gave the most noticeable improvement, increasing the peak potential by 220 mV to 0.6 V. However, catalysts prepared by pyrolysing carbon with both metal and nitrogen precursors present saw the most significant improvement having an onset potential of approximately 800 mV. These improvements can thus be attributed to the interaction of nitrogen with the surface, metal with the surface or nitrogen with metal. While it would be seem at first glance that the active sites must involve both metal and nitrogen, it is possible that the metal atoms serve only to catalyse the formation of active sites based on nitrogen but are themselves not catalytically active. However, the authors considered this a possibility and so utilised a two-step synthesis procedure whereby carbon was pyrolysed twice, first in the presence of acetonitrile then in the presence of cobalt sulphate. This sample gave the highest reported activity of all those synthesised and would imply that catalytically active sites incorporate both metal and nitrogen. The authors also investigated the effect of the amount of cobalt sulphate used during pyrolysis, and thus the amount incorporated into the catalyst, and found that activity goes through a maximum as cobalt sulphate levels increase but sharply drops off after 0.8 ml of cobalt sulphate solution is added. It is found via XPS analysis that above this level agglomeration occurs giving rise to catalytically inactive metallic cobalt particles which then act as nucleation sites for graphitization and thus become enveloped within the carbon. The findings of Wei et al. (2000) are supported by others, who state that

four factors are required for an active catalyst; carbon, cobalt or iron, nitrogen and a microporous structure (Lefèvre et al., 2009; Zhang et al., 2012) and that at high pyrolysis temperatures macrocycles are destroyed and their nitrogen incorporated into the carbon matrix (Yuan et al., 2014). It is worth noting that despite the strong work presented by Wei et al. (2000) only one pyrolysis temperature is used. This is despite the authors stating that the pyrolysis temperature is highly likely to be a determining factor in catalytic activity though this is stated to be due to the higher stability of samples prepared at higher temperatures.

Lee et al. (2009) investigated the use of $Co(NO_3)_2$ and pyrrole at pyrolysis temperatures between 600-1000 ^{o}C. It was found that given the right synthesis conditions active catalysts can be generated without the need for pyrolysis but that such heat-treatment does improve their activity. Indeed, the best performing catalyst, obtained at 800 ^{o}C, had a peak potential of 810 mV, 90 mV higher than that of the non-pyrolysed catalyst. In conjunction with this improvement in activity a change in the number of electrons transferred is found, from 2.4 e$^-$ with the non-pyrolysed sample to 3.2 e$^-$ in the best performing catalyst. Thus it is safe to say that heat treatment alters the active site such that the ORR mechanism it can catalyse shifts from being predominantly 2 e$^-$ to 4 e$^-$. However it is worth noting that these electron transfer numbers are maximum values taken from a range of potentials. At potentials lower than 0.5 V the reduction pathway on the pyrolysed catalyst is predominantly 4 e$^-$, but this shifts to be exclusively 2 e$^-$ above 0.6 V. Conversely the non-pyrolysed sample is only able to reduce O_2 to H_2O_2 indepent of the electrode potential.

Regardless of the nitrogen source what is known is that both pyridinic and graphitic-N are required on the carbon surface post-pyrolysis to catalyse the ORR (Maldonado & Stevenson, 2004; Parvez et al., 2012). Given that increasing pyrolysis temperatures are found to decrease the abundance of both pyrrolic- and pyridinic-N while increasing the levels of graphitic-N (Domínguez et al., 2014), and that activity peaks at 800 ^{o}C (Chang et al., 2012), one could postulate that graphitic-N is less active than pyridinic-N. That pyridinic-N is considered to be the main site for transition metal binding may perhaps explain this perceived superior activity (Sarapuu et al., 2015), though if this is the case the perceived correlation between activity drop off with decreasing pyridinic-N

concentration may actually be due to the release of metal ions as pyridinic-N either protonates to inactive N-H groups or converts to graphitic-N (Lee et al., 2009). Thus pyridinic-N may either be the ORR active site or simply a component of an M-N$_x$/C active site.

By pyrolysing polyacrylonitrile with a mesoporous silica template, Liu et al. were able to synthesise a highly porous CN$_x$ catalyst that displayed good ORR activity (Liu, Li, Ganesan, et al., 2009). With an onset potential of 0.6 V it is quite apparent that nitrogen functionalities can be introduced into a carbon matrix without the need for a metal ion though the inclusion of 1.2 wt.% Fe, introduced by pyrolysing the CN$_x$ catalyst with iron acetate, increases the onset potential by 200 mV and also results in higher currents. Regarding the active sites for oxygen reduction the authors postulate that both graphitic- and pyridinic-N are electrochemically active though their modes of action differ. It is proposed that graphitic-N adjacent to an edge carbon atom promotes 4 e$^-$ reduction on the carbon but is not an active site. The authors state that they believe pyridinic-N to be the active site for the ORR and that the increased activity found by pyrolysing CN$_x$ with iron acetate is due entirely to the structural and electronic influence placed onto such active sites by carbon-encapsulated iron particles. This conclusion is reached by observing that the more active samples contained higher concentrations of pyridinic-N, that the presence of iron influences neither the content nor type of nitrogen and that increased iron concentrations resulted in higher levels of iron particles leaving the catalyst[10], ascertained by acid-washing the catalyst and noting a decrease in iron levels. If one were to assume that there is a critical size of iron particle above which complete graphitization, and thus incorporation into the catalyst structure, cannot occur then the drop in activity observed at high iron concentrations is fully explained, and the beneficial effect of iron does not require it to be catalytically active towards the ORR;

---

[10] It is perhaps worth noting that the effect of increasing iron concentration was only studied at 1000 °C. As iron agglomeration is known to occur at temperatures higher than 900 °C (Bezerra et al., 2008) it would perhaps have been wise to investigate activity as a function of both temperature and metal loadings simultaneously

the inactivity of iron particles is supported in a number of literature sources (Faubert et al., 1996; Koslowski et al., 2008; Schulenburg, 2003).

The notion that pyridinic-N is the active site is somewhat contested by Parvez et al. (2012), who synthesised N-doped carbon, specifically an N-functionalised graphene, using carbon nitride and pyrolysis temperatures of 800, 900 and 1000 °C. By performing XPS analysis on all three samples both the surface nitrogen content and the relative abundance of different functionalities were reported, as shown in Figure 2.13. It is interesting to note is that the sample with the highest reported activity is that obtained at 900 °C, NG-900. Though from Figure 2.13 it can plainly be seen that the overall nitrogen content decreases significantly from the levels obtained when pyrolysing at 800°C, and that this loss is primarily due to a decrease in pyridinic-N. Thus if catalytic activity is due entirely to pyridinic functionalities present within carbon one would expect to see significantly poorer performance in both NG-900 and NG-1000 than NG-800. No explanation is given within the text as to why this sample shows the highest performance, though it could be due to an increased porosity of the carbon allowing better access to graphitic-N sites, as it has been shown that pyrolysis increases the porosity of the carbon matrix (Lefèvre et al., 2009). Figure 2.12
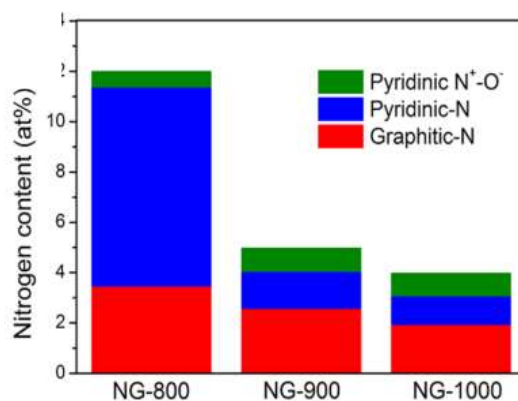
Figure 2.13 - Nitrogen abundance in N-doped graphite, reproduced from (Parvez et al., 2012).

shows that pyridinic-N sites require the removal of at least one carbon atom from pristine graphene, thus the degradation of graphene under these synthesis conditions is clearly possible. From Figure 2.13 it can also be seen that while pyridinic-N concentration decreases significantly above 800 °C, the decrease in graphitic-N is not as

pronounced. It is possible therefore that the higher temperature samples are simply more porous, and that it is in fact graphitic-N which is catalytically active. It could therefore be concluded that both functionalities are ORR active and that in this study the loss of activity due to a decrease in pyridinic-N is overcompensated for by a significant increase in porosity, allowing better access to a significant number of graphitic-N active sites. However, due to the lack of supporting data from this study it is impossible to know for certain if this is the case.

Two unrelated studies used surprisingly similar synthesis techniques to generate nanotubes with varying N-functionality concentrations. Kim et al. (2005) showed that at N-doping levels of 3 wt.%, graphitic and pyridinic functionalities exist at near equal levels. However, at concentrations higher than 5 wt.% the major nitrogen defects are predominantly pyrrolic and pyridinic in nature (Sharifi et al., 2012). Whilst neither of these studies addressed the electrochemical activity of the synthesised nanotubes, doing so would allow for a numerical comparison between these two functionalities and to ascertain if ORR activity is due to graphitic-N, pyridinic-N or both.

Using pyrolysed carbon-supported cobalt polypyrrole, Lee et al. (2009) ascertained the presence of four nitrogen states, pyridinic, pyrrolic, graphitic and N-H, using XPS. It is stated that the XPS peak of pyridinic-N occurs at the near-same energy of Co-N and these peaks could be associated with either functionality, thus the content of pyridinic-N may also be an indicator of the levels of N-coordinated metal ions. While implying that they believe both these functionalities are ORR active, the authors state that pyrrolic- and graphitic-N are responsible for the majority of activity, due to the presence of Co-N functionalities in the less active, non-pyrolysed samples. Of the four functionalities reported within the pyrolysed samples only N-H functionalities are thought to be inactive towards the ORR. Liu et al. also postulate that N-H functionalities are inactive and propose that they form via the protonation of pyridinic-N in acidic conditions (Liu, Li, Ganesan, et al., 2009). That pyridinic-N and Co-N have similar XPS spectra serves to offer more obfuscation to the elucidation of the active site; as opposed to the notion that metal atoms serve only as catalysts for active site formation, or that generated particles exert electronic influences on, but are not a part of, the active site, they could instead constitute the active centre. In a similar study, Zhang et al. (2012) pyrolysed a

variety of carbon supported metal salts, such as iron and cobalt chlorides, nitrates and sulphates, chelated with triethylenetetraamine at 800 °C and used XPS and XRD to analyse the resultant catalysts. As with the work of Lee et al. (2009), the obtained sample contained pyridinic, pyrrolic and graphitic nitrogen functionalities. The authors expand on the work of Lee et al. (2009), by stating that high pyridinic-N levels in iron-based catalysts facilitate O_2 reduction, in cobalt-based systems a similar relationship is found between activity and pyrrolic-N. In addition it was reported that the type of metal precursor has an obvious effect on the catalytic activity with the metal chlorides producing the most active catalysts.

2.6.1.2 - M-N$_x$/C moieties

Domínguez et al. (2014) synthesised a range of Co/Fe-N$_x$/C catalysts by doping carbon with nitrogen, using urea as a precursor, before depositing enough Co- and Fe-centred phthalocyanine to obtain a 20 wt.% metal loading, heat-treating at 800 °C for 1 hour under N_2 and acid-leaching the resultant catalyst with 0.5 M H_2SO_4 for 2 h. It was found that less nitrogen was incorporated into the surface when Fe-phthalocyanine was used as the metal precursor than when using the Co-centred analogue and that decomposition and loss of the N-precursors during pyrolysis results in lower than expected N-surface concentrations of 4.7-4.9 wt.%. With that said the nitrogen that was incorporated was found to be very stable in acidic media and predominantly pyridinic in nature. The ratios of nitrogen to Co/Fe on the surfaces of all the pyrolysed samples were higher than 4, implying that metal-free nitrogen defects must have been present. The acid leaching step was shown to remove the majority of metal atoms not co-ordinated to nitrogen on the surface and those that remain are thought to exist as metallic particles that have been encapsulated by graphite. This treatment was shown to improve the activity of catalysts regardless of the metal used. Again there is little explanation as to why such a performance increase would be observed post acid washing, especially as this finding disputed those of Liu et al. (2009) who state that metallic particles exert a positive influence on nearby active sites. However, this performance increase could be due to the removal of metallic particles that serve to block pores within the carbon matrix, thus performance increases are due to better access of reactants to active sites. The authors also found that an increased

concentration of nitrogen and metal does not necessarily result in higher performance, indeed the best performing catalyst, i.e. the Fe-centred catalyst that was subjected to pyrolysis and acid washing, had the lowest concentrations of both metal and nitrogen, but the highest proportion of graphitic nitrogen when compared with other functionalities, suggesting that this is the active site of such catalysts. However, graphitic nitrogen is stated to be quite stable in acidic conditions and so the significant reduction in performance under CV tests is unexpected. The authors state that they believe such a performance loss to result from the loss of metal from active sites and thus an indication of the role of metal ions in the active site.

Li et al. (2012) attempted to ascertain the role of iron in pyrolysed $M-N_x/C$ catalysts by ascertaining the activity of such catalysts in the absence and presence of small surface blocking species. Starting with the proposal that $Fe-N_2/C$ and $Fe-N_4/C$ moieties are the ORR active sites, the authors postulated that the incorporation of CN^- ligands would likely disrupt $Fe-O_2$ interactions and thus block Fe-based active sites. By doing so the authors found that iron does have a part to play in ORR activity, though the exact nature of the active sites of a catalyst are heavily influenced by the nature of the iron and nitrogen precursors. If using macrocycles, the active layer is said to form on the top of the carbon support as a result of polymerisation. This layer is characterised by low porosity, thus the majority of active sites are inaccessible and a lower overall initial performance results. However, the formed active sites are typically $Fe-N_4/C$ and display good stability in acidic media. Conversely, using small precursors results in a highly porous catalyst layer with active sites found to result from the reaction of iron and nitrogen with amorphous carbon. The resultant active sites are of varying $Fe-N_2/C$ compositions and have much poorer stability, thus it is expected that while a high activity may be initially reported the performance drop-off is expected to be much more pronounced than for macrocycle-derived systems. It is also noted that an increase in peroxide yield is observed when CN^- ions are introduced, this is postulated to be due to the disruption of Fe-OOH bonds, resulting in the preferable desorption of H_2O_2 upon protonation. This could therefore imply a poor tolerance of such catalysts to fuel contaminants which would adversely affect the performance of these catalysts.

Koslowski et al. (2008) utilised [57]Fe Mössbauer spectroscopy to ascertain the nature of catalytic sites generated from the pyrolysis of Fe-TMPP-Cl. It was reported that both Fe-N_4/C and Fe-N_2/C sites were found and that the kinetic current density shows a correlation with the number of Fe-N_4/C accessible to the electrolyte. This finding implies that while Fe-N_2/C may be catalytically active, it is perhaps Fe-N_4/C sites that are responsible for the majority of the observed activity. If this is truly the case it would therefore be useful to find a link between synthesis conditions and the ratio of M-N_4/C and M-N_2/C sites found on the surface.

Fortunately this exact investigation has been performed; across two studies Lefèvre et al. attempted to find a causal link between the nature of nitrogen and metal precursors and the relative abundance of M-N_x/C sites by using time-of-flight single-ion mass spectrometry, ToF-SIMS (Lefèvre et al., 2005; Lefèvre et al., 2002). Both Fe- and Co-based catalysts were synthesised using either Fe/Co-acetate or Fe/Co-TMPP supported on carbon, and pyrolysed at temperatures ranging from 400-1000 $^{\circ}$C in an ammonia-rich environment. The authors were originally concerned with ascertaining the nature of 'low-temperature' and 'high-temperature' active sites observed in earlier studies, determining that the 'low-temperature' site was likely Fe/Co-N_4/C and the 'high-temperature' site likely Fe/Co-N_2/C. The relative abundance of these sites is affected by both the type of precursor and the associated pyrolysis temperature. Using iron acetate and pyrolysing temperatures of 800-900 $^{\circ}$C, Fe-N_2/C site abundance was found to increase up to a maximum of 80 % of active sites. Conversely, when using Fe-TMPP, the highest relative abundance of 50 % is reached for the same site when pyrolysing at 700-800 $^{\circ}$C. The authors state that Fe-N_2/C is more active than Fe-N_4/C and it is quite apparent activity could be fine-tuned via the selection of suitable components and synthesis conditions. However, this observation does not extend to the use of cobalt-containing precursors. Indeed while a ToF-SIMS signal for both Co-N_2/C and Co-N_4/C is detected, the authors were unable to tell if they were from distinctly different sites or fragmentation patterns from the same active site. Thus while one can be certain of the presence of Co-N_4/C in all samples, it is impossible to confirm either the presence or absence of a Co-N_2/C active site, and so a firm conclusion as to the role of precursors

and pyrolysis temperatures for both Co- and Fe- precursors cannot be drawn from this work alone.

Very similar findings are reported by Médard et al. (2006) who pyrolysed iron acetate and Fe-TMPP over a variety of carbons at 900 $^{\circ}$C in an ammonia rich environment. They reported that the nitrogen content of the surface is the most important characteristic of a catalyst, with higher N-content improving both the activity and the selectivity of the catalyst towards direct 4 e^{-} reduction. The authors attribute the activity of the Fe-based catalyst to two active sites, Fe-N_4/C and Fe-N_2/C, stating that latter is the more active or the two catalytic sites, capable of reducing O_2 to $2H_2O$, while the former is capable only of reducing O_2 to H_2O_2. They also re-iterate the finding that the ratio of these two sites is dependent on the type of precursor used, with Fe-N_2/C:Fe-N_4/C ratios of 4:1 and 1:3 reported when using iron acetate and Fe-TMPP as precursors respectively. It is stated that the selection of carbon is not a trivial matter, with some carbons retaining less than 0.1 wt.% of nitrogen after pyrolysis. As the authors state that increased nitrogen content leads to an increased Fe-N_2/C site prevalence, such low nitrogen incorporation would result in a much poorer performance in comparison to those catalysts able to retain higher levels. The work of Li et al. (2011) somewhat supports this finding, stating that the use of precursors such as ethylenediamine, cobalt nitrate and iron sulphate results in a highly active catalyst. These results perhaps indicate that small precursors are able to more efficiently penetrate the pores of a carbon matrix, thus increasing the active site density.

While one would assume that it is necessary to dope a surface with pyridinic-N prior to metal adsorption, given the structural and electrical similarity between this functionality and metal-coordinated nitrogen, Villers et al. (2004) report that doping with any functionality in a two-step pyrolysis method serves to produce active catalysts. It is stated that the polarity induced on the carbon surface by nitrogen doping serves to allow greater dispersion of Fe^{II}, and that in the presence of such a metal ion all functionalities are liable to convert into pyridinic-N thus forming Fe-N_x/C site upon pyrolysis at a suitable temperature, a postulated repeated and supported by the work of Lefèvre et al. (2009). Finally Lefèvre & Dodelet (2003) used RRDE and XPS analysis to show that those catalysts with a higher relative abundance of Fe-N_2/C sites display the

highest electrochemical activity and the lowest peroxide yield; Kattel et al. (2014) support this finding, stating that Fe-N$_2$/C sites are capable of reducing O$_2$ directly to water, while Fe-N$_4$ sites are only capable of catalysing the 2 e$^-$ reduction to peroxide.

2.6.1.3 - Carbon as an integral catalytic component

The influence of carbon on the activity and stability of the active layer has also been the subject of several studies by a number of research groups. Unlike with Pt/C, where the need for carbon is purely structural, in M-N$_x$/C catalysts the carbon has both structural and electrochemical roles. As it is integral to the active site, the type of carbon support has a large influence on the activity and selectivity of a catalyst (Marcotte et al., 2004; Médard et al., 2006). While catalysts derived from macrocycles have been shown to form an electrically conductive polymer after pyrolysis (Lefèvre et al., 2002; Wei et al., 2000), it has been found that such a polymer has poor porosity and thus suffers from poor activity (Li et al., 2012). One interesting approach is the use of electrodeposition, as reported by Schilling et al. (2010), which allows for the selective adsorption of precursors at sites which are 'electrochemically available'. Fe-TMPP-Cl was electrodeposited on carbon nanotubes and three samples were tested; one not subjected to heat-treatment, one heat-treated at 650 ^{o}C and one heat-treated at 850 ^{o}C. It was found that simply electrodepositing porphyrins had no significant effect on the activity, and that the catalyst still displayed poor stability. It was also noted that the non-pyrolysed sample principally followed the 2 e$^-$ reduction pathway to peroxide, which served only to degrade the catalyst layer. However, heat-treatment served to improve both these characteristics, with active sites and preferred pathways changing depending on the pyrolysis temperature. While this study utilised macrocyclic precursors, that optimal activity was attained at 850 ^{o}C, at which temperature on would expect the central macrocycle to have fully degraded, and a significant loss in active sites was reported. The activity of the best catalyst was surprisingly high, having an onset potential of 0.88 V and an electron transfer number of 3.1 e$^-$. Indeed the authors state that the use of electrodeposition and heat-treatment produces superior catalysts to the traditional wet impregnation and heat-treatment methods reported elsewhere. These results imply that while both the desirable 4 e$^-$ and undesirable 2 e$^-$ pathways are followed on the surface, the active sites that catalyse the 4 e$^-$ pathway clearly do so with

an overpotential rivalling that of Pt/C. If this is the case, and this method can be extended to include the use of simple precursors, one may be able to selectively synthesise particular active sites to improve the performance even further. As others have stated that the difficulties in uniformly dispersing precursors on the surface are hindering the development of consistent and reproducible synthesis methods (Maldonado & Stevenson, 2005), the use of electrodeposition could offer an interesting avenue to the synthesis of highly active catalysts.

It is of interest to note the work of Maldonado & Stevenson (2004), who utilised carbon nanofibres to produce an active catalyst via the chemical vapour deposition of metaloporphyrins. Nanofibres are slightly larger and more disordered, though structurally similar, form of carbon nanotubes. That such rigorous standards do not need to be applied during the growth of nanofibres as compared to nanotubes implies that production costs can be reduced.

Graphene has also been shown to exhibit many interesting properties, such as a high surface area, good electrical conductivity and high chemical and thermal stability that many feel it would be particularly well suited towards fuel cell applications (Kattel et al., 2012; Parvez et al., 2012; Tripkovic & Vanin, 2013; You et al., 2014). So impressive is the specific surface areas of graphene that the low active site density that results from heteroatom doping can be somewhat offset (Liang et al., 2014), resulting in a large number of active sites overall and thus significant modifications to the electrical properties (Kattel et al., 2012; Parvez et al., 2012). However, while several graphene and carbon nanotube/nanofibre preparation methods exist, such as heat-treatment with ammonia, the use of ammonia plasma and growth using chemical vapour deposition, they all require vacuum conditions and are thus incredibly difficult and expensive to scale up. It would therefore be beneficial if carbon structures with good electrical conductivity and a high surface area could be synthesised under ambient pressure and, ideally, temperature.

As already stated, the pyrolysis of porphyrins results in an active layer with poor porosity and thus reduced performance (Herrmann et al., 2009; Li et al., 2012). Thus a good active layer should have a high porosity, with the active sites located within the

microporous carbon matrix (Szakacs et al., 2014). An alternative approach to the traditional wet-impregnation/heat-treatment methods described thus far is to produce the active sites and carbon support simultaneously (Liu, Li & Popov, 2009; Maldonado & Stevenson, 2005; Xu et al., 2012).   Charreteur et al. (2008), pyrolysed pristine carbons, which had been loaded with the requisite amount of iron acetate to achieve 0.2 wt.% Fe contents, at 950 $^\circ$C under flowing ammonia. Under such conditions the amorphous carbon is gasified, producing a highly porous carbon structure; thus the greater the amorphous content, the higher the porosity. Confirmation of the presence of active sites within these pores is given by the observation that activity of the generated catalyst bears a linear correlation with nitrogen content, and that nitrogen content was higher in those carbons with a higher amorphous phase content.

Herrmann et al. (2009), utilised a different approach to the generation of a microporous network; by pyrolysing Co-TMPP in the presence of a transition metal oxelate such as FeC_2O_4, a highly porous catalyst was produced. It was found that upon high temperature decomposition of the oxelate, a nano-scaled template was produced, upon which the pyrolysis products of the porphyrin were able to polymerise. The oxelate template was then removed via hydrochloric acid treatment resulting in a highly porous catalyst that does not require the incorporation of a carbon source, as the entire active layer results from the carbonisation of the porphyrin. It is worth noting that the authors state that the nature of both the porphyrin precursor and the oxelate have a significant effect on the electrochemical activity and porosity of the derived catalyst. The inclusion of heteroatoms such as sulphur in the precursor is likely to have a significant influence on both the electroactivity and porosity of the derived catalyst, while the degree of graphitization is strongly influenced by the oxelate used; the best performing catalysts, which utilise Co-TMPP and either FeC_2O_4 or SnC_2O_4, display current densities comparable to those of Pt/C catalysts.

Sarapuu et al. (2015), took a similar tact by synthesising nitrogen-doped carbon aerogels. Aerogels are particularly well suited towards fuel cell applications due to their low mass density, continuous and tuneable porosity, high surface area, good conductivity and chemical stability. Aerogels are typically synthesised using templates which are removed after the carbonisation of organic precursors, similar to the

oxelate/porphyrin synthesis method, and can be sustainably produced by using biomass-derivatives as aerogel precursors. The advantage of this method is that the pore size of the resulting aerogel can be tuned and controlled via precursor selection, thus allowing greater flexibility and reproducibility. That this method does not require vacuum conditions only adds to its appeal as a synthesis technique. While this particular study was performed in alkaline media, the observation that electron transfer numbers have a small range across a full potential sweep and that peroxide yields are incredibly low highlights just how effective this synthesis method could be.

2.6.2 - Stability issues

While there has been a significant improvement in the activities reported from M-N_x/C catalysts since the work of Jasinski, there has been precious little advancement in increasing their stability within acidic media. As such, many synthesised catalysts show a rapid decrease in performance over the first two hours of operation (Banham et al., 2015; Lalande et al., 1997), often followed by a steady decline in activity to zero. The low stability of non-precious metal catalysts is a significant roadblock that must be overcome for fuel cells to achieve full commercialisation (Baker et al., 2009; Banham et al., 2015). The first step in mitigation is to identify the mode of degradation, though a consultation of the literature highlights the relatively small amount of research as to the nature of active site degradation. That a rapid performance decrease followed by a more gradual decline is observed perhaps indicates that more than one de-activating mechanism exists. The two most commonly cited degradation pathways are the attack of the active site by hydrogen peroxide generated by incomplete reduction of O_2, and the protonation and anion adsorption of nitrogen functionalities by the acid electrolyte.

2.6.2.1 - Attack by H_2O_2

Lefèvre & Dodelet (2003) observed that on Fe-based catalysts prepared via the pyrolysis of both macrocyclic and simple precursors, the voltage of maximum current decreased after exposure to hydrogen peroxide, though this same performance loss was not observed when said catalysts were subjected to acid treatment. Such was the sensitivity of the generated catalysts that treatment with a weak peroxide solution, 5 vol.% H_2O_2, was found to degrade the catalysts performance. By measuring the iron

content of the catalyst before and after peroxide treatment, the authors were able to correlate the loss of activity to the loss of iron from the catalyst. It was also observed that the ratio of Fe-N_2/C to Fe-N_4/C bore no correlation to the loss in activity, implying that neither of these two sites were comparably more stable. The authors also conclude that a higher stability can be achieved by increasing the iron loading of a catalyst, though this seems somewhat counterintuitive, given that one would expect such samples to show a much more significant decrease in activity. However, this conclusion is based on such samples being prepared at 900 $^{\circ}$C, at which temperature metal particles are known to form. As others have stated that metal particles encapsulated by graphite exert a positive influence on nearby nitrogen functionalities (Liu, Li, Ganesan, et al., 2009), it could be postulated that these particular catalysts are more resistant due to a lower abundance of Fe-N_x/C active sites, and a higher abundance of stable nitrogen functionalities such as graphitic-N (Lee et al., 2009; Maldonado & Stevenson, 2004; Parvez et al., 2012).

Schulenburg (2003) investigated the effect of both acid-washing and peroxide treatment on the performance of Fe-TMPP pyrolysed at 900°C using electrochemical techniques and ^{57}Fe Mössbauer spectroscopy. By subjecting the generated catalyst to a 100 h potentiostatic hold while purging with O_2, it was found that the activity displayed the common degradation behaviour observed by others; namely a rapid decrease over 2 h followed by a steady decline to inactivity. The as-synthesised catalyst was stirred in either 0.5 M H_2SO_4 or 30 vol.% H_2O_2 for 100 h, and the samples subjected to a 100 h potentiostatic hold. It was observed that the acid treated sample displayed comparable performance to the untreated sample, though a significant performance loss was found for the sample subjected to peroxide treatment. Four distinct Fe- species were observed across the three samples: metallic iron which disappeared after acid treatment, Fe_2O_3 which remained after acid treatment but was thought to be inactive, and two active sites, one four-coordinated iron atom and one six-coordinated iron atom. Peroxide treatment was shown to completely remove the four-coordinated-iron active site and some of the six-coordinated-iron active site, suggesting that one, or both, of these active sites are responsible for ORR activity.

Gubler proposed that the instability of Fe-based catalysts is due to the low redox potential of the metal, and its ability to act as a Fenton's reagent, whereby Fe^{2+} serves to promote the decomposition of H_2O_2 into two ·OH free radicals, which attack the membrane and active site (Gubler et al., 2011; Gubler & Koppenol, 2012). The ability of a metal to act as a Fenton's reagent is dependent on the redox potential of the metal centre being lower than the single electron reduction potential of H_2O_2. As cobalt-based catalysts have been shown to have higher stability than Fe-based analogues and the Co^{II}/Co^{III} redox potential is much higher than the Fe^{II}/Fe^{III} redox potential , the notion that peroxide has an adverse effect on catalytically active sites seems logical (Gubler & Koppenol, 2012).

2.6.2.2- Protonation of nitrogen functionalities and anion adsorption

Using XPS and pyrolysis temperatures of 800 and 1100 °C, Liu et al. (2009) compared the relative abundance of nitrogen functionalities on a heat-treated Co-Fe-N chelate. It was found that the lower temperature sample showed a greater initial activity than that prepared at high temperature, though the high temperature sample was considerably more stable in acidic media. A comparison of the XPS results of these two catalysts showed a significant change in the relative abundance of nitrogen functionalities present. In the lower temperature sample pyridinic-N, pyridinic-N-O and graphitic-N are all present with contributions of 30 %, 12 % and 57 % respectively, while at 1100 °C these contributions shift to 0 %, 33 % and 66 %. These results clearly indicate that pyridinic-N is catalytically active and unstable in acid media; the loss of performance experienced by this sample indicative of the degradation of the site. It is stated that the lone pair of electrons on pyridinic-N is protonated, rendering the nitrogen inactive which is also reported by Lee et al. (2009). Herranz et al. (2011) postulate that this protonation of pyridinic-N does occur, and is a source of instability of a catalyst, but that such functionalities are not themselves a component of the active site. It is proposed that the protonation of pyridinic-N adjacent to the active site results in anion adsorption which serves to block the active site of the catalyst, as shown in Figure 2.14. Such findings are supported by the observed increase in activity after either re-heating the catalyst or by washing with NaOH.

2.6.3 - Computational investigations

Due to the relative youth of pyrolysed M-N_x/C catalysts, and the historic difficulty in ascertaining likely structures of the active site, there is not as great a repository of information regarding computational investigations of the ORR on such surfaces. Due to the heteroatomic nature of the active sites, the ORR pathway is considerably more complex on such catalysts and even small changes in the metal ion and the surrounding structure can have profound impacts on the preferred reduction mechanism (Li et al., 2012; Tripkovic & Vanin, 2013). While it has already been established that the generation of peroxide on platinum is undesirable, the formation of H_2O_2 by non-precious metal catalysts is even less desirable, due to the adverse

As prepared   High   Low

OH⁻ or heat (T>300°C)
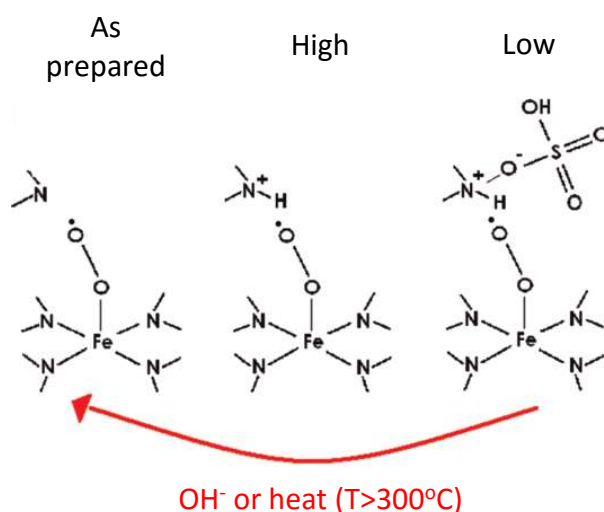
Figure 2.14 - Proposed mode of anion adsorption resulting in activity loss, reproduced from Herranz et al., 2011.

effects on the membrane and active site (Baker et al., 2008), as detailed in Section 2.6.2.1.

Across the literature a number of basal and edge active sites have been modelled both with, and without, axial groups present. In the absence of an axial group, side-on adsorption of O_2 is favoured and four-electron reduction to water is promoted via increased donation from the metal, to the $O_2\pi*$ orbitals (Kattel & Wang, 2013a; Szakacs et al., 2014). However, the incorporation of an axial ligand reduces the ability of the

central metal ion to donate significant electron density to allow for side-on interaction with O_2, as such when an axial group is incorporated into the active site, end-on adsorption is preferred (Szakacs et al., 2014). Both side-on and end-on adsorption involve the interaction of the π and π^* of O_2 with the $3d_{z^2}$ and either the $3d_{xz}$ or $3d_{yz}$ orbitals (Szakacs et al., 2014), though the strength of binding can be altered with variations in the metal centre and the number of metal-coordinated nitrogen atoms (Kattel & Wang, 2013a). The nature of the axial group modelled thus has profound impacts on the results obtained and presents an interesting avenue towards modelling the effect of the carbon support. For example highly ordered graphene or multiwalled nanotubes could be modelled using a second graphene layer (Ikeda et al., 2008), nitrogen doped surfaces by the incorporation of a pyridine group (Szakacs et al., 2014) or single-walled nanotubes by the omission of an axial group all together (Chen et al., 2013; Kattel et al., 2013; Kattel et al., 2014; Kattel & Wang, 2014)**.**

Regardless of the adsorption mode it is found that O_2 binds to the surface more strongly than H_2O, implying that the replacement of water with oxygen is energetically favourable, and that surface blocking by adsorbed water is not observed (Szakacs et al., 2014). However, at increasing potentials it is also found that certain intermediates become stable, resulting in Gibbs free energy 'sinks', suggesting that intermediates are capable of blocking the electrode surface in much the same way as $OH_{(ads)}$ can block the platinum surface (Kattel et al., 2013; Szakacs et al., 2014).

The majority of literature on this subject comes from the group of Kattel et al. who have modelled a variety of active sites, though never with an axial ligand (Kattel et al., 2013; Kattel et al., 2014; Kattel & Wang, 2013a; Kattel & Wang, 2014). Across these four recent studies Co- and Fe- centred N_4, N_2 and N_{2+2} sites have been modelled and several conclusions drawn regarding their activity, namely:

- O_2 binds end-on to basal N_4 sites but side-on to the N_2 counterparts
- Intermediates bind more strongly to $Fe-N_x/C$ active sites than $Co-N_x/C$
- Reduction of O_2 to OOH occurs on all catalysts
- OOH binds more strongly than O_2 to all metal centres

- Basal Fe-N_x/C active sites promote the 4e$^-$ pathway by the formation, and spontaneous dissociation, of peroxide

It is also repeatedly stated that while edge-sites are catalytically active, they are not 'expected' to be as stable as their basal counterparts and hence are not investigated. However, given experimental observations that active sites are found within the microporous network formed during pyrolysis it seems likely that edge-sites play a significant role in the reduction of O_2. Their omission from the studies of Kattel et al. is due to the less negative 'formation' energies calculated using:

$$E_f = E_{F/N/C} + yE_C - (E_{graphene} + xE_N + zE_H + E_{Fe})$$

Equation 2.13 - Formation energy of M-N_x/C active sites as calculated by (Kattel et al., 2013; Kattel et al., 2014; Kattel & Wang, 2013a; Kattel & Wang, 2014)**.**

where $E_{graphene}$ is the energy of optimised graphene, E_{Fe} is energy of Fe ion, E_C is the total energy of graphene per carbon atom, E_N is the energy of an isolated N atom, E_H is the energy of an isolated H atom (Kattel et al., 2014; Kattel & Wang, 2013a; Szakacs et al., 2014). However, at no point do the authors state that the data used to calculate the formation energies was obtained from simulations at a higher temperature. As it is known that active site formation is temperature dependent, and that such temperatures are not inconsiderable, using this equation in conjunction with room temperature values is unlikely to provide accurate data. At room temperature it would perhaps be more reasonable to assess the stability of the active site, specifically the ease with which the metal ion can be removed - a known degradation pathway.

Unfortunately, as Equation 2.13 utilises terms for the removal of carbon from a pristine graphite sheet, the doping of nitrogen, and the addition of a metal ion, it is incapable of describing stability. That the 'formation energy' and 'stability' of active sites are obtained from the same equation and thus treated synonymously implies that any results obtained pertaining to the stability of active sites must be treated with caution and scepticism.

2.7 - Summary

That platinum is still the best performing catalyst for the ORR currently prevents the widespread commercialisation of PEM fuel cells, not least due to the material scarcity, cost and large overpotential that exists at the cathode. Recent work has focussed on replacing platinum with low cost non-precious metal catalysts, specifically those made via the pyrolysis of metal, nitrogen and carbon. These catalysts have the benefit of being both easy to produce and low environmental impact though their activity and stability require significant improvement before they are able to usurp Pt/C as the default catalyst within a fuel cell. That both the nature of the active site and the relationship between its structure, activity and electrochemical stability are still very much unknown presents an interesting avenue for research. Little work has focussed on the computational investigation of the plausible active sites, but it is felt that such research can provide a signpost towards the development of highly active and stable carbon based catalysts.

2.8 - Research aims

Uncertainty regarding the nature of the active sites and their stability under the operating conditions of the ORR provides the focus of this work. Due to the small volumes of computational studies performed on these systems, and the possible sources of error resulting from assumptions made within said work, it is felt that any computational investigations should be supported as much as possible by experimental comparison. However, due to the nature of the active sites of interest, and the conditions required for their synthesis, it is impossible to experimentally isolate only those active sites of interest. That these active sites are electronically similar to, and derived from, porphyrins which can be isolated and purified, provides an opportunity to develop and calibrate a computational method.

As such, an initial computational and experimental study of Pt/C and a variety of porphyrins is performed. This study comprises computational assessments of the reversible potentials of each elementary reaction on the active site surface, the preferred reduction pathway and, where applicable, redox potentials. These calculated

values are then compared to cyclic voltammograms and rotating disk electrode characterisations of each investigated catalyst, and the efficacy of the method assessed.

With a methodology in place, 16 M-N$_x$/C active sites are proposed, and their redox potentials, preferred reduction pathways and the one-electron reduction potentials for a range of elementary reactions are calculated. These active sites are not necessarily expected to be highly active towards the ORR, but represent a suitable sample size to allow for the quantification of the effects of each active site component towards the reduction reaction. The structure of this research is depicted in Figure 2.15.
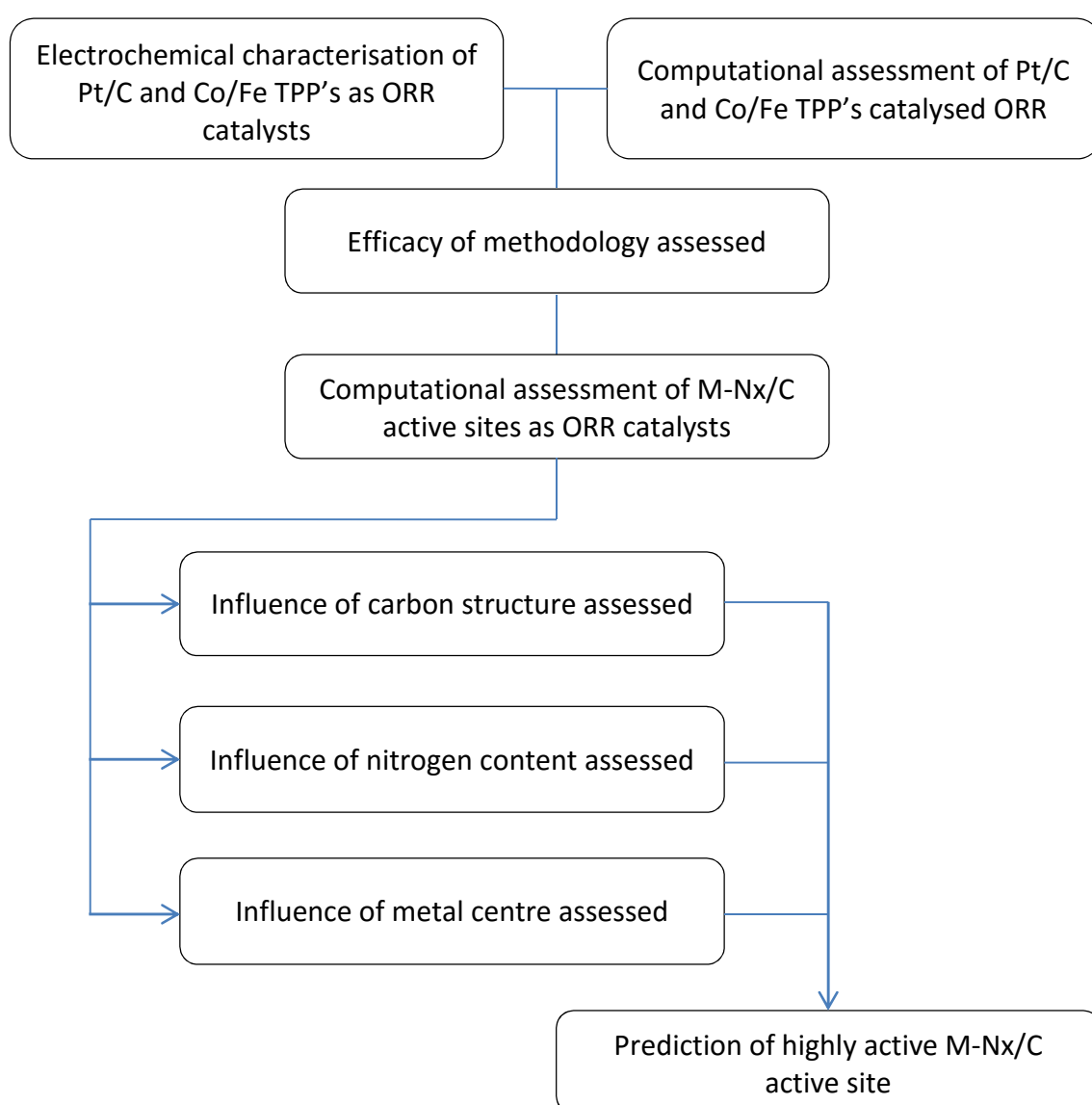
Figure 2.15- Flow chart of research structure

Chapter 3 – Platinum and Co/Fe-tetraphenylporphyrins as ORR catalysts

3.1 - Electrochemical characterisation

All experiments were performed using state-of-the-art electrochemical equipment (Scientific & Medical Products Ltd., Stockport, UK), analytical grade solvents (Sigma Aldrich, St. Louis, MO, USA) porphyrins of purities above 97 % (Porphyrin Systems GbR, Appen, DEU) and 20 wt% platinum on black (Alfa Aesar, Haverhill, MA, USA). The electrochemical setup was comprised of a Gamry RDE710 Rotating Electrode, coupled to a rotating disk electrode tip. A 5 mm diameter glassy carbon disk loaded with catalyst was inserted into the electrode tip and used as the working electrode. Measurements were performed using a Gamry Series 600 Potentiostat coupled to the working electrode, a standard hydrogen electrode and a platinum wire counter electrode.

3.1.1 - Catalyst ink preparation

As porphyrins are known to poorly adsorb onto the glassy carbon electrode surface (Baker et al., 2008; He & Mugadza, 2012), and to allow for direct comparison between the activity of platinum and porphyrins, 4 mg of each porphyrin was mixed with 16 mg of Ketjen black to obtain 20 wt.% mixtures. Catalyst inks were prepared in a similar manner as Flyagina (2014), namely by treating 2.5 mg of a 20 wt.% catalyst on carbon mix, 125 µl of 5 % Nafion solution and 2.5 ml ethanol for 30 minutes in an ultrasonic bath. The glassy carbon disk was sequentially polished with 1 µl, 0.3 µl and 0.05 µl alumina slurry, rinsed with ethanol after each polish, before being allowed to dry in air for 15 minutes. A 20 µl aliquot of ink was deposited on the polished disk and allowed to dry in air for 30 minutes. The disk was then inserted into the RDE tip and coupled to the rotating electrode.

3.1.2 – Cyclic voltammetry

Figure 3.1 shows the CV of 20 wt.% Pt/C performed in O_2-saturated electrolyte, with the oxide formation, oxide reduction, hydrogen adsorption and hydrogen desorption regions marked. Of these four regions, oxide formation and reduction are of great
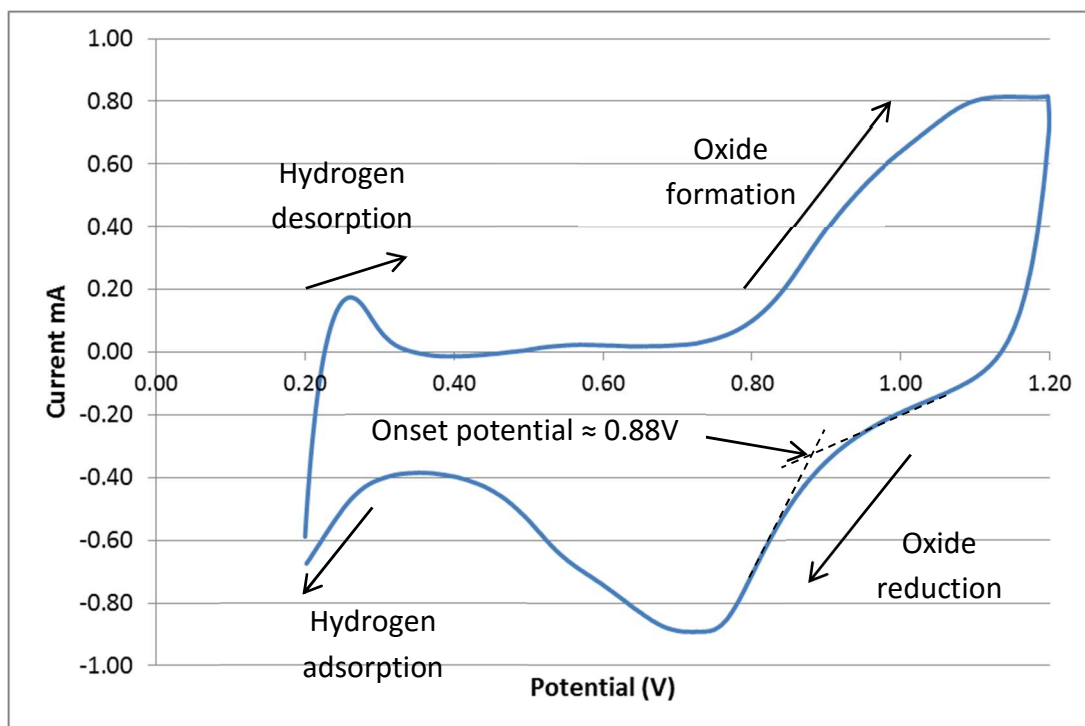
Figure 3.1 - Annotated CV of 20 wt.% Pt on carbon performed in O_2-saturated 0.5 M H_2SO_4.

interest when considering the oxygen reduction reaction. The onset potential of oxide reduction, approximately 0.88 V, coupled with the peak current of approximately 0.9 mA, shows that 20 wt.% Pt/C is adept at catalysing the oxygen reduction.

By comparing Figure 3.1 with Figure 3.2, which shows the CV of 20 wt% Co-TPP/C performed under identical conditions and annotated with regions of interest, one observes several differences; namely the considerably lower onset potential for oxide reduction, and thus lower potential of peak current, and the considerably smaller associated peak current displayed by Co-TPP. These features are observed for all porphyrins, with the potentials of peak currents for the porphyrins in the range of 0.42 - 0.55 V, and peak currents reaching a maximum of approximately 0.48 mA, around half that of platinum. Figure 3.2 also shows the presence of two reduction peaks, highlighted by red and blue boxes, which could result from a number of surface bound species. Co-TPP and Fe-TMPP have similar redox peaks at approximately 0.825 V , as shown in Figure 3.3, and it is possible that this peak is present, albeit with a considerably lower intensity, when using Fe-TCPP and Co-TMPP as the catalyst. The sharpness of these peaks, and the return to near-identical current, implies that they do not correspond to oxygen
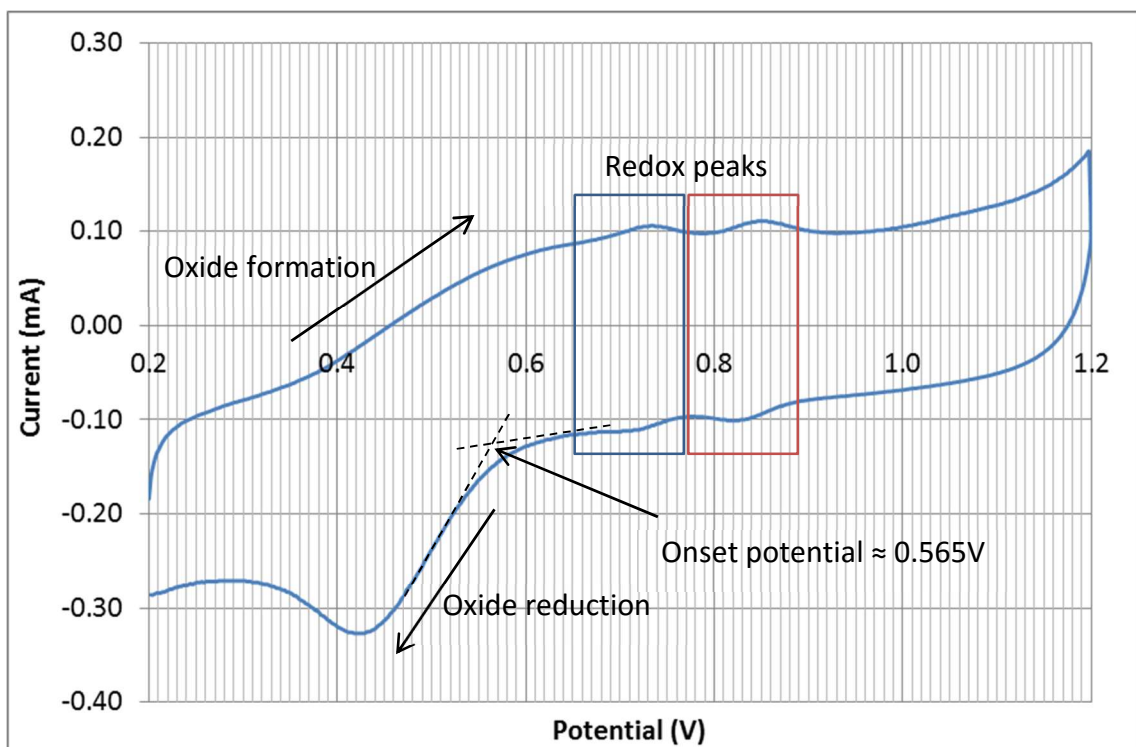
Figure 3.2 - Annotated CV of 20 wt.% Co-TPP on carbon performed in O$_2$-saturated 0.5 M H$_2$SO$_4$.
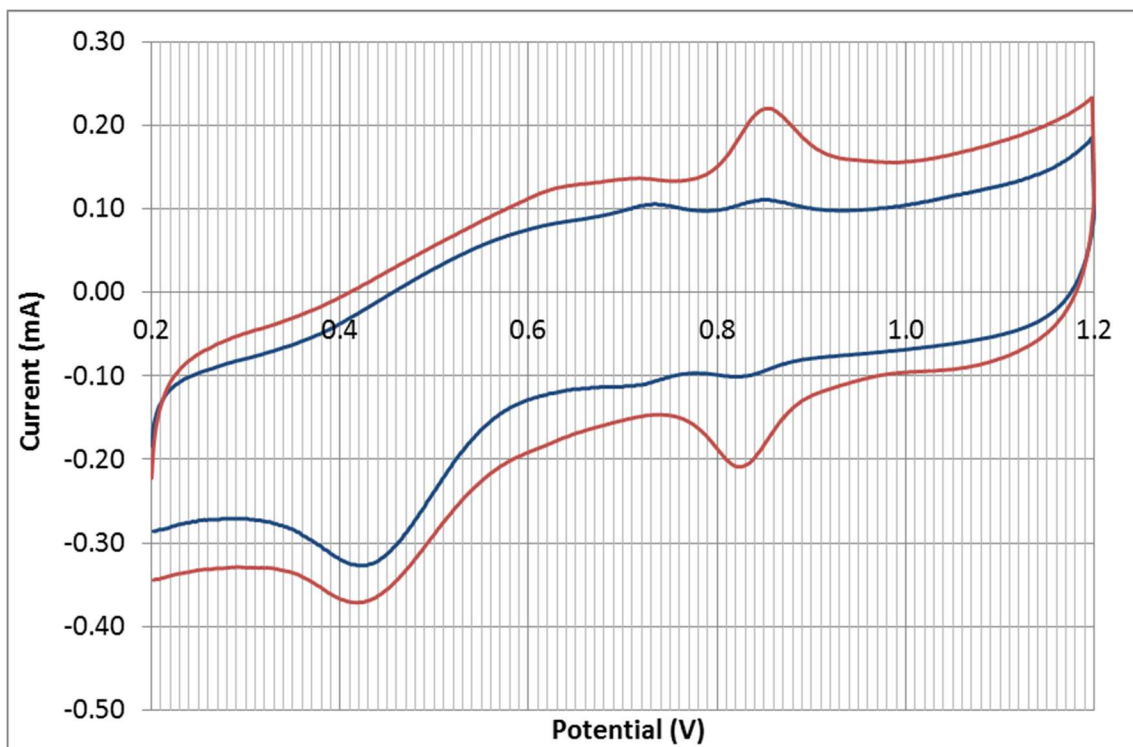
Figure 3.3 - Comparison of the CV's of 20 wt.% Co-TPP, blue, and Fe-TMPP, red, on carbon showing the presence of a redox peak at approximately 0.825 V.

reduction. Instead it is proposed that they correspond to the redox reaction of the N_4-ring system; the increased intensity is thus attributed to the loss of either Co or Fe from the centre of the ring, possibly as a result of generated peroxide or via the acid leaching of the central metal. This has been reported previously in the literature, albeit at a slightly lower potential of 0.78 V (Liu et al., 2006). The corresponding anodic/cathodic peaks at approximately 0.72 V present in the Co-TPP air-saturated trace are unique to this porphyrin. The exact source of such peaks is not known but cannot be attributed to metal ions in the solution as the redox potential of the $Co^{II/III}$ pair is 1.92 V (Banham et al., 2015). Two possible explanations therefore exist; either additional functionalities exposed within the carbon support are responsible for the current response, though this appears to be unlikely due to the lack of a similar peak in any other trace, or there exists a secondary degradation pathway, again possibly due to the generated peroxide, that results in destruction of macrocycle structure, as shown in Figure 3.4, allowing for a higher redox potential but a reduction, or possible loss, of electrocatalytic activity.
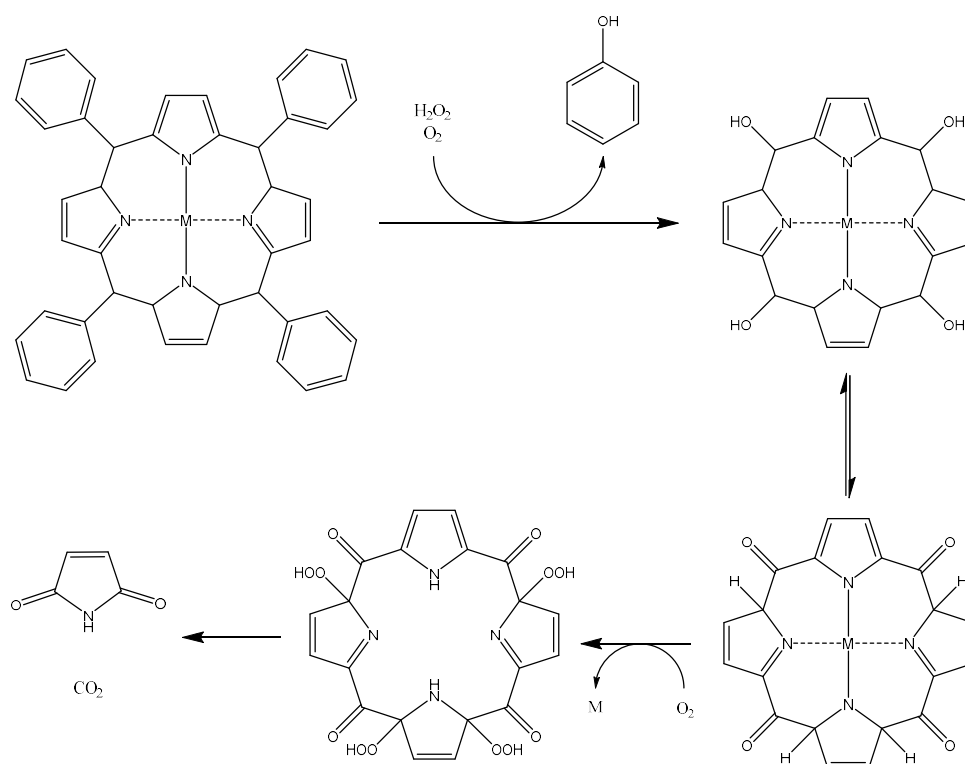
Figure 3.4 - Proposed degradation pathway of Co/Fe-centred tetraphenyl porphyrin in the presence of peroxide and oxygen.

In all traces there is a significant increase in current response below approximately 0.6 V, which is thought to correspond to two actions; the reduction of the metal centre from a +3 to +2 state and the reduction of oxygen. As it is stated that only the +2 states of both Co and Fe are capable of reducing oxygen (Anderson & Sidik, 2004; Elbaz & Garzon, 2013), it is logical that the current corresponding to both reactions occurs at near identical potentials. It is plausible that the oxygen reduction reaction actually has a formal reduction potential much higher than 0.6 V, but is limited by the redox potential of the central metal. Were this the case then one would expect to see a large current increase around the redox potential, where all electrically connected metal centres enter the +2 state and those that are able reduce oxygen, followed by a reduction in the current as the number of sites able to reduce from +3 to +2 decrease and only oxygen reduction occurs, and a subsequent increase as the oxygen reduction reaction becomes more labile and other side reactions become viable. This overall trend is observed for all but Co-TCPP and Co-TMPP, which exhibit a plateau possibly resulting from a second, less pronounced peak, at a lower potential as highlighted in Figure 3.5.
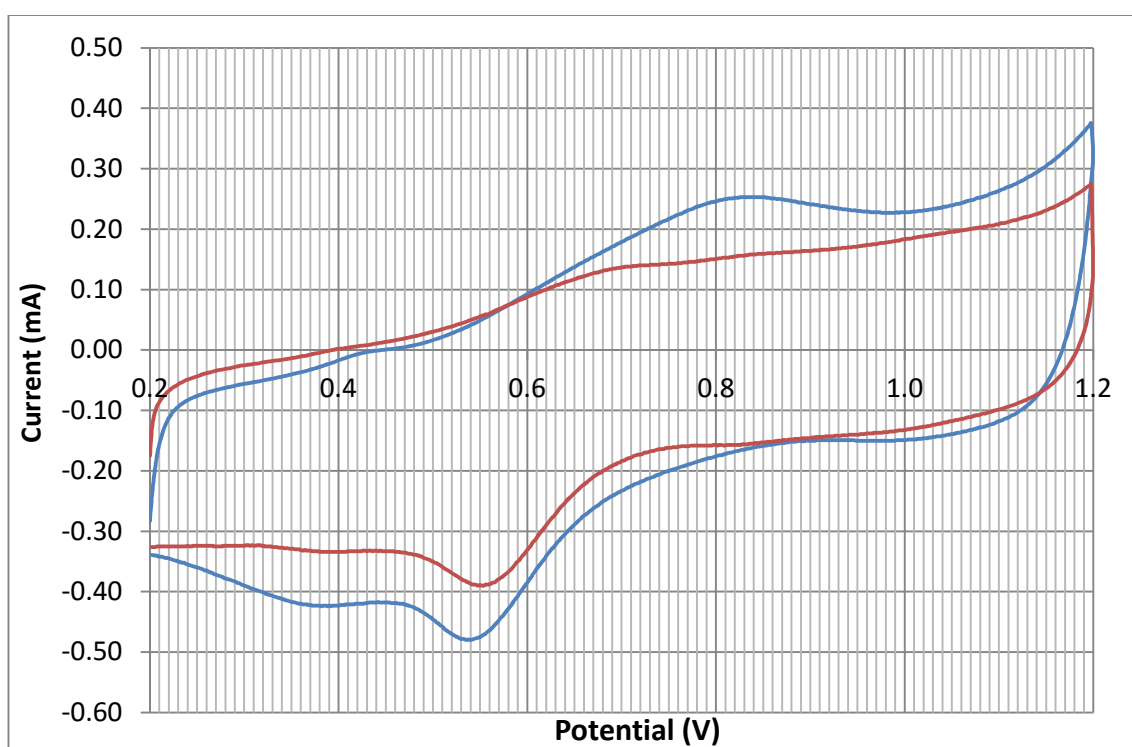
Figure 3.5 - Comparison of the CV's of 20wt.% Co-TCPP, blue, and Co-TMPP, red, on carbon showing the presence of a plateau current at approximately 0.4V.

This current response is not likely to result from the redox of an alternative active site generated via either the destruction or degradation of the active site, as no analogous peak exists in the forward sweep. Therefore it is proposed that this corresponds to the oxygen reduction occurring at a lower potential than the redox potential of the porphyrin.

3.1.3 - Rotating disk electrode

Figure 3.6 shows the disk current as a function of potential and electrode rotation rate when linear sweep voltammograms of 20 wt.% Pt/C were performed in air-saturated 0.5 M H_2SO_4. As can be seen, there is a marked increase in current with an increase in rotation rate at potentials below 0.8 V, confirming the conclusion drawn from Figure 3.1 that oxygen reduction only occurs below this potential. The reduction current plateaus at approximately 0.5 V which is maintained until approximately 0.3 V. A Koutecky-Levich plot is therefore performed, as described in Section 2.4.2, using the currents obtained at 0.4 V, and is shown in Figure 3.7 alongside plots for the idealised two- and four-electron transfer reactions. The non-zero intercept for Pt/C is indicative of kinetic losses, as described by Equation 2.10, while the gradient gives an electron transfer number of 3.97. This shows the reaction is very close to an ideal n=4 reaction but that side reactions have a very small part to play in the overall reaction. The change in current response observed at approximately 0.5 V in Figure 3.6 implies that there is a change in the main reduction mechanism, however as the current does not plateau above 0.5 V, i.e. the current response is not parallel between different rotation rates above 0.5 V, a Koutecky-Levich analysis would not give accurate electron transfer numbers. These data thus show that platinum is able to catalyse the four electron pathway, although side reactions begin to influence the overall mechanism above 0.5 V, up to potentials of approximately 0.88 V, although the performance drops off rapidly above 0.7 V.

Figure 3.8 shows the RDE currents as a function of both potential and rotation rate when using 20 wt.% Fe-TMPP on carbon as the catalyst, while the Koutecky-Levich plots of each porphyrin are displayed in Figure 3.9 using currents obtained at 0.1 V. In
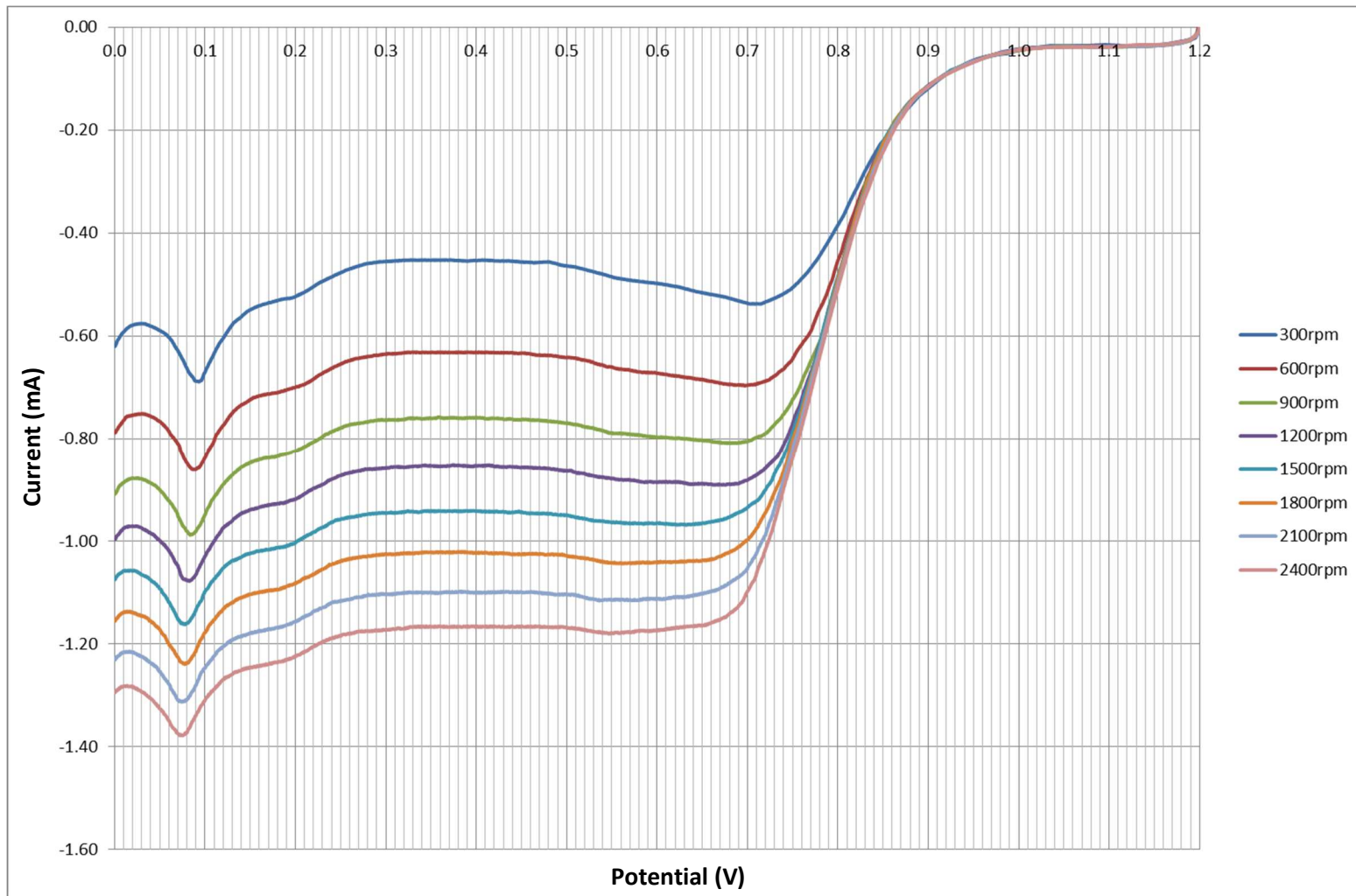
Figure 3.6 - RDE currents obtained from 20 wt.% Pt on carbon performed in O₂-saturated 0.5 M H₂SO₄.
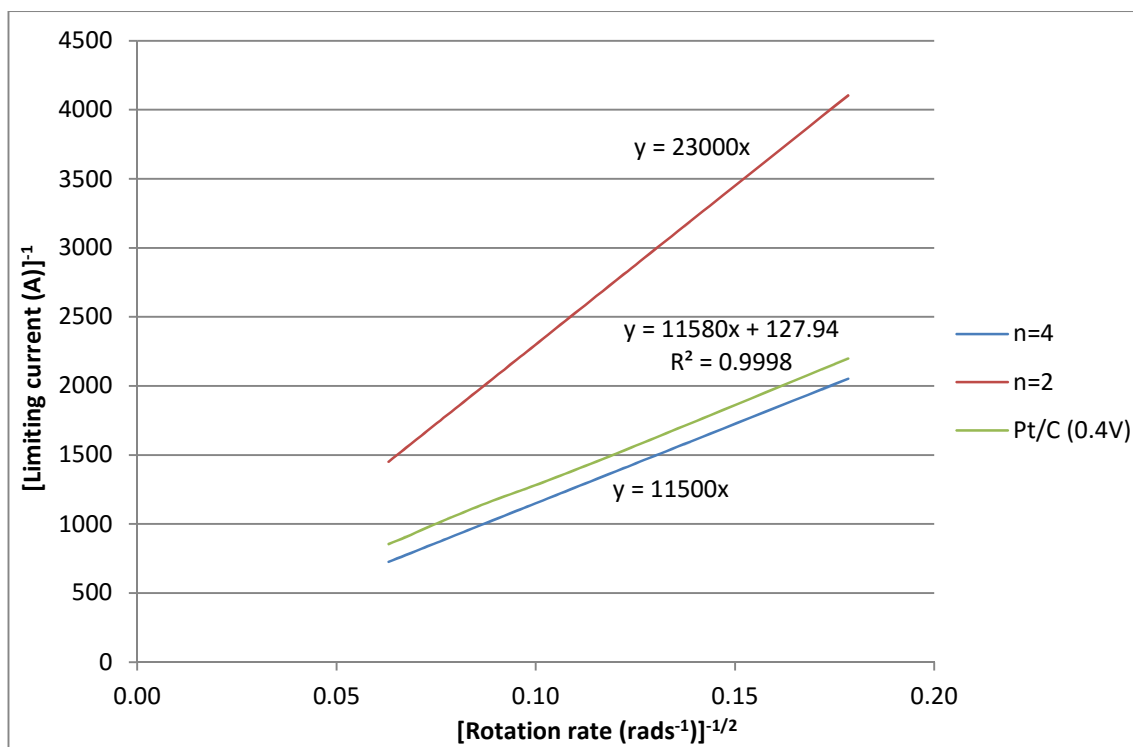
Figure 3.7 - Koutecky-Levich plot of 20 wt.% Pt/C, for comparison the theoretical plots of ideal n=4 and n=2 reactions are also shown.

contrast to Figure 3.6, the plateau current in Figure 3.8 is located at a significantly lower potential, due to the markedly lower onset potential. Also, there appears to be no deviation from this plateau, thus suggesting that side reactions do not occur between 0.05-0.6 V. It is also interesting to note that the peak observed at approximately 0.825 V in Figure 3.5 is still present, but the current response does not vary with rotation rate, which indicates that this is due to a redox reaction on the electrode surface. These results are representative of the trends observed for all porphyrins; thus one can infer that porphyrins follow a single, simple reduction pathway and that species present on the surface with redox potentials higher than 0.6V do not catalyse the ORR. The electron transfer numbers obtained from the Koutecky-Levich plots in Figure 3.9 range in value from 1.89-1.93; showing that each porphyrin primarily follows a 2 e$^-$ pathway, albeit inefficiently. The deviation from an ideal 2 e$^-$ pathway is likely due to the incomplete reduction of oxygen a loss resulting from degradation pathways which consume O_2, as shown in Figure 3.4.
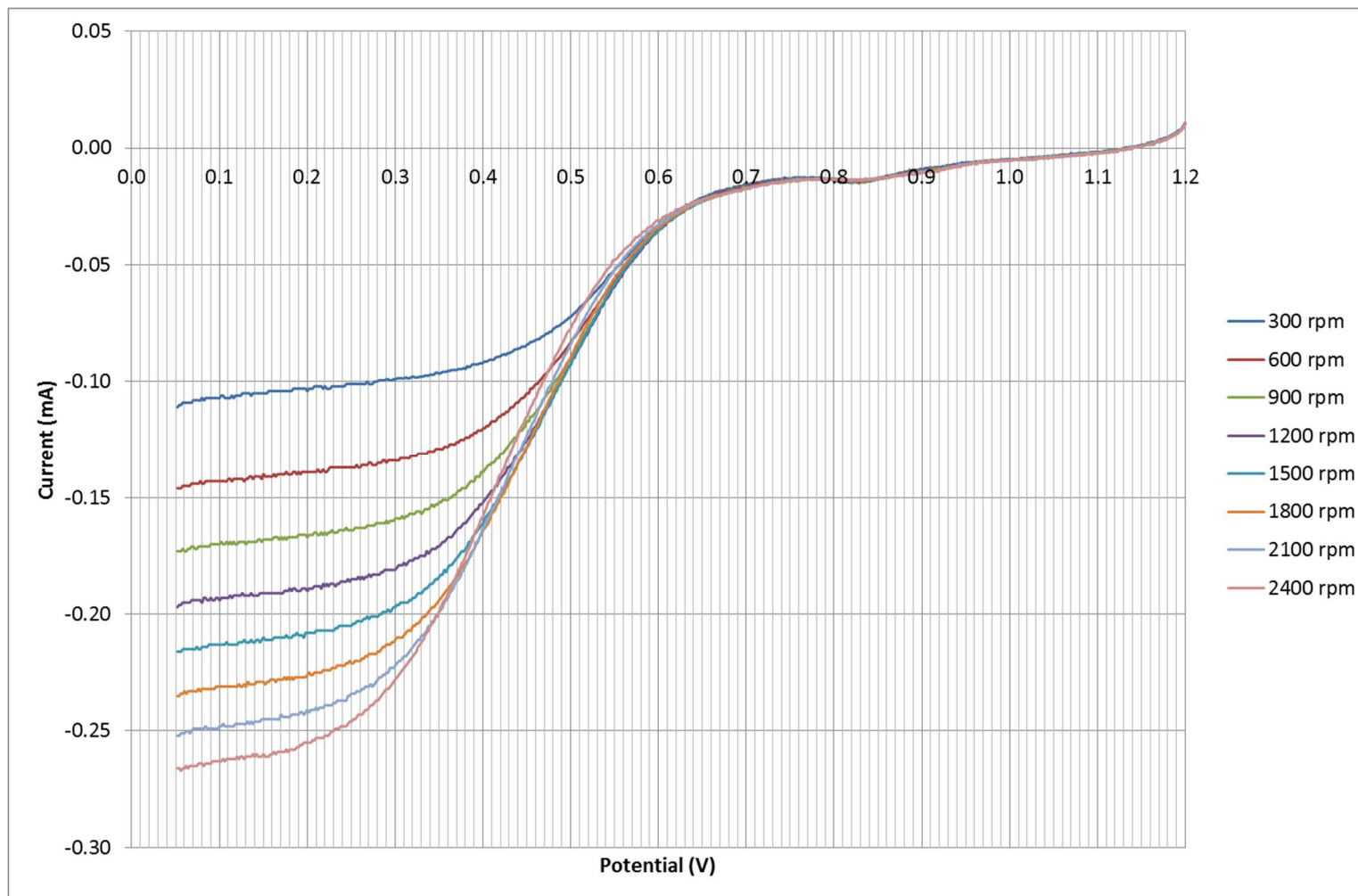
Figure 3.8 - RDE currents obtained from 20wt.% Fe-TMPP on carbon performed in O$_2$-saturated 0.5M H$_2$SO$_4$.
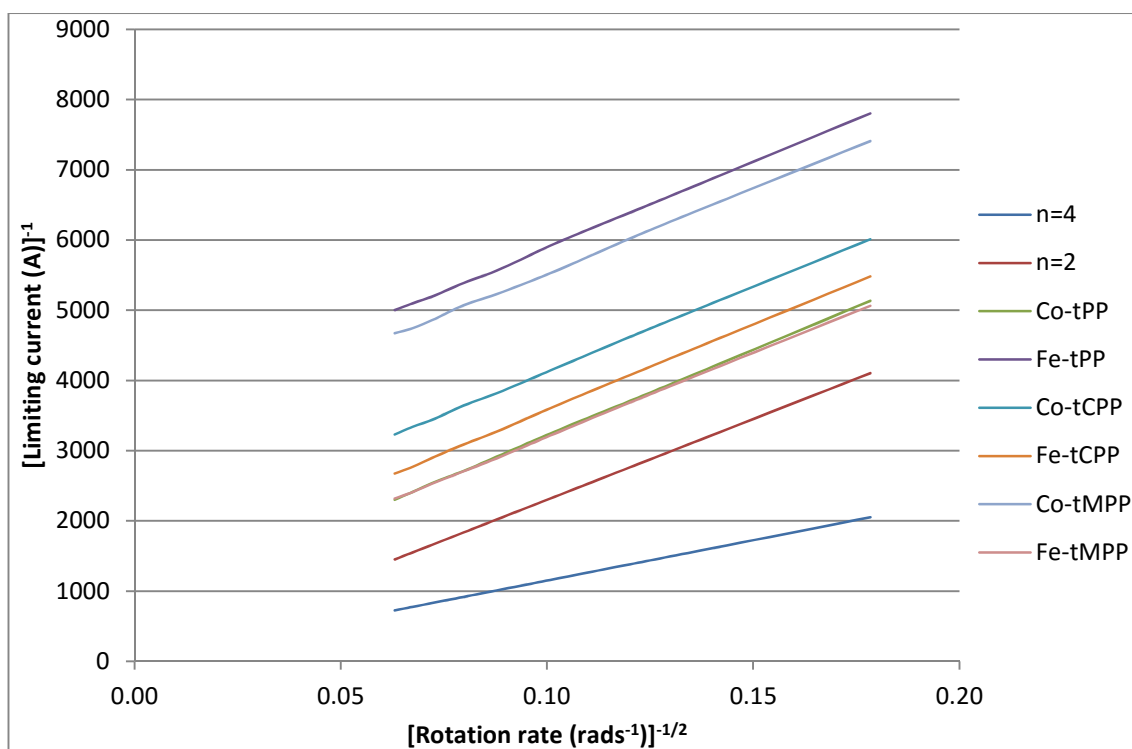
Figure 3.9 - Koutecky-Levich plot of 20 wt.% porphyrins-on-carbon inks.

3.2 - Computational characterisation

Before discussing the suitability of a catalyst for the ORR it is important to identify how an ideal catalyst would behave. The overall reduction of $O_{2(g)}$ to $2H_2O_{(aq)}$ has a reversible potential of 1.229 V and involves four electron transfer reactions. The reversible potential is the potential at which both the forward and reverse reactions, i.e. the reduction of $O_{2(g)}$ to $2H_2O_{(aq)}$ and the oxidation of $2H_2O_{(aq)}$ to $O_{2(g)}$, are feasible; at this potential the Gibbs free energy change of both reactions is 0 kJmol^{-1}. The reduction reaction is only thermodynamically feasible at potentials lower than the reversible potential; higher than this and the Gibbs free energy change becomes positive and the reaction is unlikely to occur. Why then is this reaction non-spontaneous at potentials lower than 1.229 V without a catalyst present? While the overall reduction reaction has a reversible potential of 1.229 V, this is simply the average of the four one-electron transfer reactions shown in Figure 3.10, each with their own reversible potentials. Thus for the overall reaction to proceed at 1.229 V, each one-electron transfer reaction must have a reversible potential of 1.229 V. The reversible potentials of some of the reactions

in Figure 3.10 are well established within the literature while the others can be calculated with relative ease from known values:

$$O_{2(g)} + H^+ + e^- \rightleftharpoons OOH_{(aq)} \ (U_{rev} = -0.125 \ V) \tag{3.1}$$

$$OOH_{(aq)} + H^+ + e^- \rightleftharpoons H_2O_{2 \ (aq)} \ (U_{rev} = 1.515 \ V) \tag{3.2}$$

$$H_2O_{2 \ (aq)} + H^+ + e^- \rightleftharpoons OH_{(aq)} + H_2O_{(l)} \ (U_{rev} = 0.806 \ V) \tag{3.3}$$

$$OH_{(aq)} + H^+ + e^- \rightleftharpoons H_2O_{(l)} \ (U_{rev} = 2.720 \ V) \tag{3.4}$$
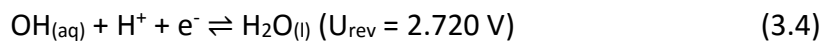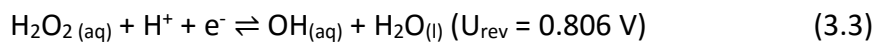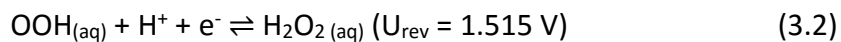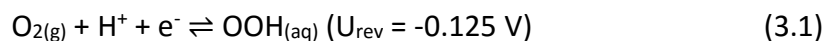
The very low reversible potential of the one electron reduction of $O_{2(g)}$ infers that the non-catalysed reaction simply cannot proceed, hence why acidic solutions can be saturated with O_2 under standard conditions. Any electro-active species must therefore be able to shift these potentials to more useful values and so we are able to identify the key feature of the perfect catalyst; the ability to shift the reversible potentials of the one-electron transfer reactions to 1.229 V.
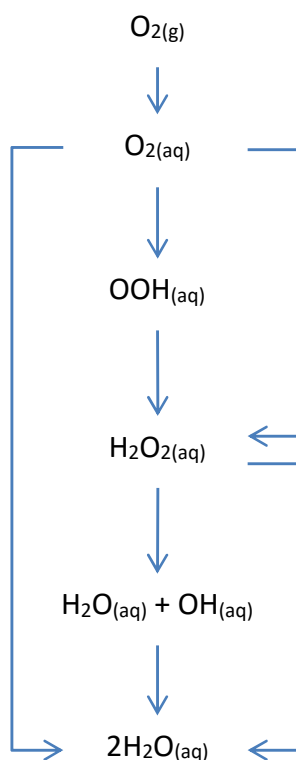
Figure 3.10 - Reaction schematic for the non-catalysed ORR

3.2.1 - The perfect catalyst

Anderson et al. showed that one can predict the binding strength of substrates on a perfect catalyst (Anderson, 2010), i.e. one that allows complete reduction of oxygen with no overpotential. It is felt that a description of such a catalyst would serve as a 'gold standard' benchmark and allow for the direct comparison of various catalysts and potentially offer insight as to how to fine-tune catalyst behaviour.

As established in Section 2.2.1 the redox potential of a reaction on a catalyst surface is related to the non-catalysed redox potential in solution and the Gibbs free energy change of adsorption of the associated substrates, as described by Equation 2.5. Using this equation it is possible to determine the ideal binding strength of each substrate relative to the binding strength of $O_{2(ads)}$. If the Gibbs free energy change of adsorption for $O_{2(ads)}$ were -1 $kJmol^{-1}$ it could be said that for there to be no adsorption related losses $H_2O_{(ads)}$ must have a $\Delta G_{(ads)}$=-0.5 $kJmol^{-1}$, as one O_2 molecule replaces two H_2O molecules on the surface. Similarly, knowing that the non-catalysed redox potential for the one electron reduction of O_2 to OOH is -0.125 V, Equation 2.6 can be used to find that the ideal binding strength of $OOH_{(ads)}$ is -2.354 $kJmol^{-1}$. Using these values, and the reversible potentials of the other, non-catalysed elementary steps, one can calculate the ideal adsorption energies of the other surface bound species, as shown in Table 3.1.

Table 3.1 – Ideal adsorption energies ($kJmol^{-1}$) of ORR intermediates on a catalyst surface normalised to -1 $kJmol^{-1}$ for O_2.

	E^0	$\Delta_{ads}G_{(Red)}$	$\Delta_{ads}G_{(Red)}$
$O_{2(ads)} + H^+ + e^- \rightleftharpoons OOH_{(ads)}$	-0.125 V	1.000	2.345
$OOH_{(ads)} + H^+ + e^- \rightleftharpoons H_2O_{2\ (ads)}$	2.12 V	2.354	2.068
$O_{(ads)} + H^+ + e^- \rightleftharpoons OH_{(ads)}$	2.12 V	2.882	1.991
$OH_{(ads)} + H^+ + e^- \rightleftharpoons H_2O_{(ads)}$	2.72 V	1.991	0.500

3.2.2 - Platinum catalysed ORR

As detailed in Section 2.5 the platinum catalysed oxygen reduction reaction is much more complex than one would first assume. Within the relevant literature there exists a wide range of methodologies therefore direct comparison of such results is impossible;

for example even ascertaining the adsorption energy of O_2 on platinum is difficult due to the wide range of values quoted. However, general conclusions can be used as signposts towards developing a solid methodology for the thorough investigation of the reaction. In doing so, one develops a benchmark against which alternative catalysts can be compared and competitive catalysts developed. From the literature review a number of reactions were found to be feasible at a range of potentials, these reactions form a variety of pathways within the overall reaction mechanism presented within Figure 3.11. While $OH_{(ads)}$ disproportionation is also mentioned in the literature as being a potential pathway to reduction, there are only two possible reactions that would generate $O_{(ads)}$ from $OH_{(ads)}$, while both were investigated it was found that only one was feasible and neither were ever competitive on the platinum surface. As such $OH_{(ads)}$ disproportionation is not explored any further.

A consultation of relevant literature sources show that a wide range of methodologies have been used to describe similar systems, with techniques ranging in complexity depending on the focus of the model. While the sizes of the systems used in other works range from a single platinum atom to a semi-infinite surface, it has been shown that to generate results which correlate well with experiment, a platinum cluster must be of adequate diameter to exclude edge effects and consist of either one or three layers (Jacob et al., 2003). It is also noted within the literature that the spin state of the metal cluster must be taken into consideration to allow for the electronic structure to be properly modelled and, by extension, adsorption energies of reduction intermediates (Kua & Goddard, 1998; Walch, 2011). In addition to considering the size of the platinum cluster one must use a methodology and basis set combination capable of describing the interactions between oxygen, hydrogen and platinum at a high level. The more in-depth and accurate DFT models use LANL2DZ to describe the platinum surface and a split-valence basis set for the description of oxygen and hydrogen. As discussed in Section 2.3.3 there is a trade-off between the accuracy and speed of a calculation, with basis sets carefully selected to allow for the description of effects that are deemed to be of interest for the systems under investigation. As the purpose of this study is to not only ascertain the electro-catalytic activity of platinum
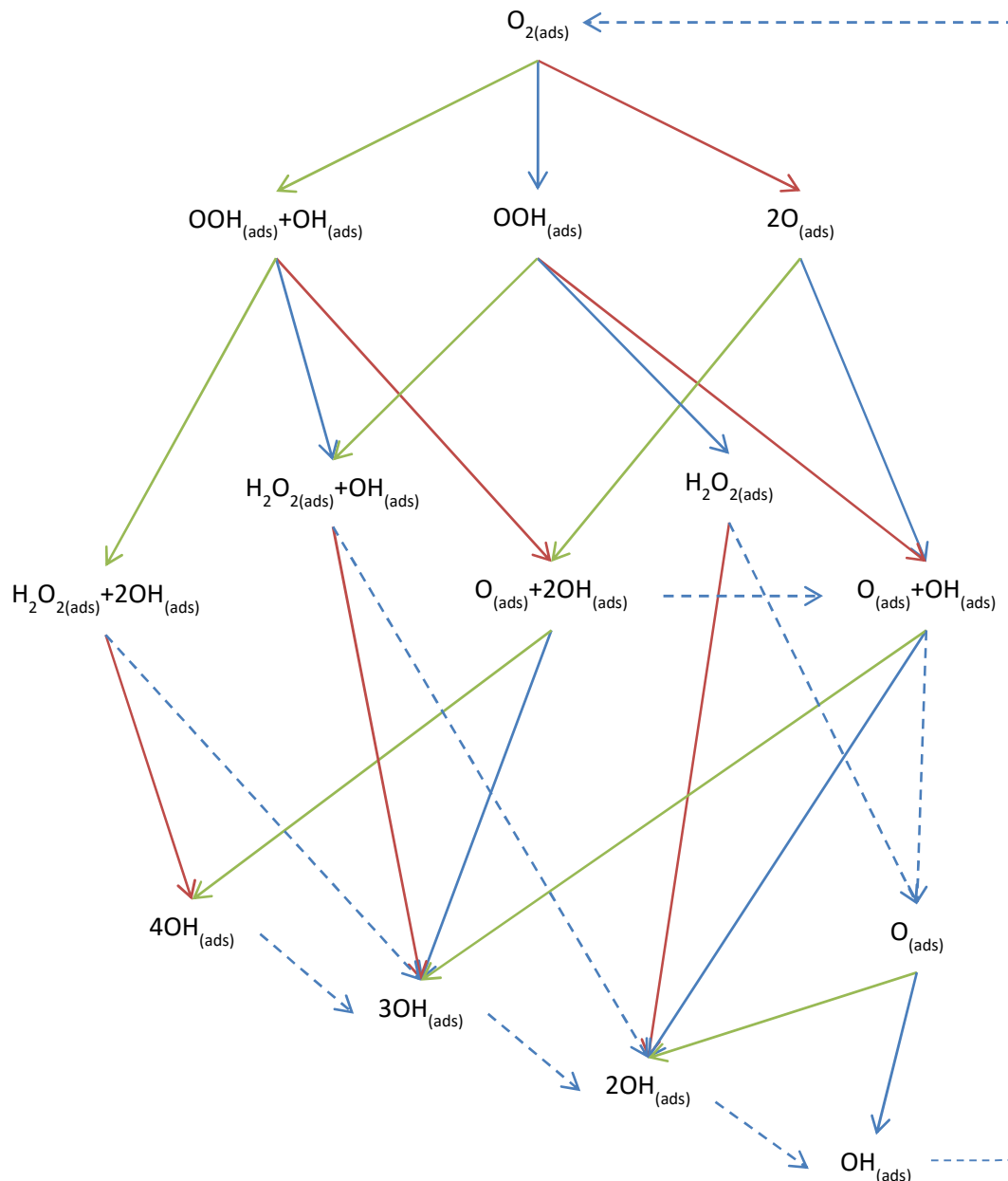
Figure 3.11 - Detailed reaction mechanism of the platinum catalysed ORR, blue arrows are electron transfer steps, red arrows are chemical steps, green arrows are $H_2O_{(ads)}$ disproportionation steps and blue dashed arrows are the removal of water

but also the nature of bonding of substrates to the surface in order to form a comprehensive benchmark it is thought that accuracy should be sought over speed, as such 6-311++g(d,p) is utilised for the description of O and H. This triple-zeta polarised split-valence basis set includes both diffuse and polarization functions for both oxygen and hydrogen and thus proves capable for the description of intermediates in the reduction chain. Implicit solvation was also included in all calculations using the CPCM

model which allows for a good description of solvents with a high permittivity, such as water. NBO6 (E. D. Glendening, J, K. Badenhoop, A. E. Reed, J. E. Carpenter, J. A. Bohmann, C. M. Morales, C. R. Landis, 2013) was utilised for population and natural bond orbital analysis calculations of the structures optimised with Gaussian09 (M. J. Frisch, G. W. Trucks, H. B. Schlegel & M. A. Robb, J. R. Cheeseman, G. Scalmani, V. Barone, B. Mennucci, G. A. Petersson, H. Nakatsuji, M. Caricato, X. Li, H. P. Hratchian, A. F. Izmaylov, J. Bloino, G. Zheng, J. L. Sonnenberg, M. Hada, M. Ehara, K. Toyota, R. Fukuda, J. Hasegawa, M. Ishida, T, 2013).

A single layer Pt_{19} cluster was used as a model for the platinum surface, the interatomic distance between each neighbouring platinum atom was kept fixed at 2.775 Å and the overall geometry arranged to represent the Pt(111) surface. While larger clusters were initially desired, the associated computation times were simply too long and preliminary investigations did not show a significant difference in adsorption energies. In an effort to compromise between accuracy and speed the inclusion of partial layers was also tested though such models were sometimes unable to optimise to known configurations, such as bridge $O_{2(ads)}$ and fcc/hcp $O_{(ads)}$.

The lowest energy spin state of the Pt_{19} cluster was found by performing single point energy calculations at increasing spin values up to 3 values larger than the minimum, this ensured that true minima were found and not erroneous points on the potential energy surface. While not allowing for the distinction between fcc and hcp sites, the Pt_{19} cluster allows for the high symmetry adsorption sites of platinum, i.e. the top, bridge and hollow adsorption sites, to be otherwise modelled. The lack of specificity regarding exactly which 'type' of hollow site is being modelled is not thought to be limiting, as adsorption energies to these sites are known to be near-degenerate (Ford et al., 2005; Jacob et al., 2003).

3.2.2.1 - Adsorption and reactivity of O_2

$O_{2(ads)}$ is known to occupy one of two adsorption sites on a clean platinum surface, either in a hollow or at the bridge site with adsorption energies of -21.517 kJmol^{-1} and -37.340 kJmol^{-1} respectively. Regardless of adsorption site, $O_{2(ads)}$ exists on the platinum surface as a superoxo-like species, with a net charge only varying slightly from -0.936 e$^-$

to -0.921 e⁻ for bridge and hollow respectively. Table 3.2 shows the breakdown of α and β electron donation at each adsorption site.

From Table 3.2 it can be observed that while the net charge transfer from the surface to the oxygen is only approximately 1 e⁻ in both cases, the extent of α and β charge donation differs between the two adsorption sites. At the bridge site both atoms donate partial α charge to form two covalent bonds to the surface, one from each oxygen atom to the adjacent platinum atoms, this interaction being primarily between oxygen 2p orbitals and Pt $5d_{z2}$ orbitals. At the hollow site only one oxygen atom interacts with the platinum surface in this way, thus the α charge donated to the surface from $O_{2(ads)}$ is substantially lower at this adsorption site. β interaction predominantly takes the form of back-bonding between the Pt $5d_{xz}$/$5d_{yz}$ orbitals and the π^* orbitals of $O_{2(ads)}$. Again, the higher surface co-ordination inherent of the bridge site allows for more substantial charge transfer from the surface to the adsorbate, and both oxygen atoms accept very similar partial charges. Thus despite the very similar net charge transfer at both sites, the increased interaction at the bridge site leads to a more exergonic adsorption.

At 0 V, $O_{2(ads)}$ can participate in one of three reactions; dissociation to two $O_{(ads)}$ atoms, ΔG = -105.760 kJmol⁻¹, direct protonation to $OOH_{(ads)}$ with ΔG = -81.404 kJmol⁻¹, or indirect protonation, i.e. protonation resulting from the disproportionation of co-adsorbed water, to $OOH_{(ads)}$ and $OH_{(ads)}$ with a Gibbs free energy change of -21.708 kJmol⁻¹. At the bridge site, O_2 has an O-O bond strength of 127.073 kJmol⁻¹ and a Pt-O

Table 3.2 – Total, α and β valence occupations and partial charges (e⁻) of O_2 when bound to bridge and hollow adsorption sites on Pt_{19}.

		Valence			Charge		
		Total	α	ß	Total	α	ß
Bridge	**O1**	0.480	-0.269	0.749	-0.471	0.275	-0.746
	O2	0.474	-0.265	0.740	-0.465	0.272	-0.736
	Total	0.954	-0.534	1.489	-0.936	0.547	-1.482
Hollow	**O1**	0.495	-0.052	0.547	-0.495	0.051	-0.546
	O2	0.431	-0.262	0.692	-0.426	0.265	-0.691
	Total	0.926	-0.314	1.239	-0.921	0.316	-1.237

bond strength of 37.340 $kJmol^{-1}$. One would not expect the spontaneous dissociation of O_2 to be favoured over the protonation reaction, as the latter involves the cleavage of a substantially weaker bond. With that said the protonation reaction is potential dependent; as the potential of the cell increases the activation barrier also increases and the overall reaction becomes less spontaneous. Conversely, one would not expect H_2O disproportionation to contribute at all towards the dominant pathway; the O-H bonds of H_2O are stronger than the O-O bond of $O_{2(ads)}$ and, as this reaction requires an additional surface site, it does not offer a viable alternative protonation pathway if the surface were to become saturated with surface blocking species. Thus the direct protonation reaction is likely to be dominant at lower potentials but is likely to become less preferred as the working potential of the cell increases towards to the reversible potential of the protonation reaction, 0.844 V.

3.2.2.2 - Favoured pathway

Table 3.3 shows the Gibbs free energy change of each elementary reaction shown in Figure 3.11. At potentials below 0.844 V on a clean surface the associative pathway, i.e. the pathway where O_2 reduces to $OOH_{(ads)}$, dominates. NBO analysis of the Pt-O bonds formed between the surface and $O_{2(ads)}$ at the bridge site show that these bonds have rather significant ionic character, with the centre of charge for the α and β bonding orbitals of both Pt-O bonds being 65-72 % shifted towards the oxygen atoms. That these Pt-O bonds have ionic character is further supported by the observation that the addition of an electron to the Pt-$O_{2(bridge)}$ system does not result in yet more charge donation from the surface to the substrate. Instead it is found that the vast majority of the additional electronic charge moves to compensate for the $δ^+$ charge of the Pt cluster resulting from the initial adsorption reaction. This further supports the selectivity of the platinum surface for the associative pathway as for dissociation to occur one would expect additional electron charge to occupy the O-O anti-bonding orbital which would have the effect of further elongating the O-O bond, making the dissociation reaction much more labile. It is therefore postulated that during the protonation reaction a 2p lone pair from a molecularly adsorbed oxygen atom interacts with the empty 1s orbital of the approaching proton. This migration of charge

Table 3.3 - Gibbs free energy change, equilibrium constant and reversible potential of each elementary reaction shown in Figure 3.11.

	$\Delta G_{(r)}$	K_{eq}	U_{rev}
$O_{2(g)} + 2H_2O_{(ads)} \rightleftharpoons O_{2(ads)} + 2H_2O_{(l)}$	-14.828	3.97×10^2	
$H_2O_{2\,(ads)} + O_{2(g)} \rightleftharpoons O_{2(ads)} + H_2O_{2\,(aq)}$	51.905	7.97×10^{-10}	
$O_{2(ads)} + H^+ + e^- \rightleftharpoons OOH_{(ads)}$	-81.404	1.86×10^{14}	0.844
$OOH_{(ads)} + H^+ + e^- \rightleftharpoons H_2O_{2\,(ads)}$	-104.618	2.18×10^{18}	1.084
$OOH_{(ads)} + H^+ + e^- \rightleftharpoons O_{(ads)} + H_2O_{(ads)}$	-201.226	1.87×10^{35}	2.086
$H_2O_{2(ads)} + H^+ + e^- \rightleftharpoons OH_{(ads)} + H_2O_{(ads)}$	-214.332	3.72×10^{37}	2.221
$O_{(ads)} + H^+ + e^- \rightleftharpoons OH_{(ads)}$	-117.724	4.32×10^{20}	1.220
$OH_{(ads)} + H^+ + e^- \rightleftharpoons H_2O_{(ads)}$	-59.146	2.33×10^{10}	0.613
$O_{2(ads)} \rightleftharpoons 2O_{(ads)}$	-105.760	3.46×10^{18}	
$OOH_{(ads)} \rightleftharpoons O_{(ads)} + OH_{(ads)}$	-142.079	8.04×10^{24}	
$H_2O_{2\,(ads)} \rightleftharpoons 2OH_{(ads)}$	-155.186	1.59×10^{27}	
$O_{2(ads)} + H_2O_{(ads)} \rightleftharpoons OOH_{(ads)} + OH_{(ads)}$	-21.708	6.39×10^3	
$OOH_{(ads)} + H_2O_{(ads)} \rightleftharpoons H_2O_{2\,(ads)} + OH_{(ads)}$	-45.471	9.35×10^7	
$O_{(ads)} + H_2O_{(ads)} \rightleftharpoons 2OH_{(ads)}$	-58.578	1.85×10^{10}	
$O_{2(ads)} + OH_{(ads)} \rightleftharpoons OOH_{(ads)} + O_{(ads)}$	36.879	3.43×10^{-7}	
$OOH_{(ads)} + OH_{(ads)} \rightleftharpoons H_2O_{2\,(ads)} + O_{(ads)}$	13.106	5.04×10^{-3}	

away from the oxygen nucleus has the effect of shifting the centre of charge of the Pt-O bonding NBO further towards the oxygen nucleus to compensate, resulting in the heterolytic cleavage of the Pt-O bond. The incumbent electron thus moves to offset the δ^+ charge now present on the platinum atom. This is shown graphically in Figure 3.12.

$OOH_{(ads)}$ can react in one of four ways, it can either dissociate to $O_{(ads)}$ and $OH_{(ads)}$, ΔG = -142.079 kJmol^{-1}, directly protonate to $H_2O_{2(ads)}$, ΔG = -104.618 kJmol^{-1}, simultaneously protonate and dissociate to $O_{(ads)}$ and $H_2O_{(ads)}$, ΔG = -201.226 kJmol^{-1}, or indirectly protonate via the disproportionation of water to form $H_2O_{2(ads)}$ and $OH_{(ads)}$, ΔG = -45.471 kJmol^{-1}. All three of these reactions are thermodynamically feasible with large K_{eq} values indicating that they all heavily favour product formation. The selection of a preferred pathway here is not as clear cut as with the protonation of $O_{2(ads)}$, as $OOH_{(ads)}$ has a single Pt-O bond of significantly greater strength than either Pt-O bond in the $O_{2(ads)}$ system. NBO analysis shows that this increased bond strength is due to both a shifting
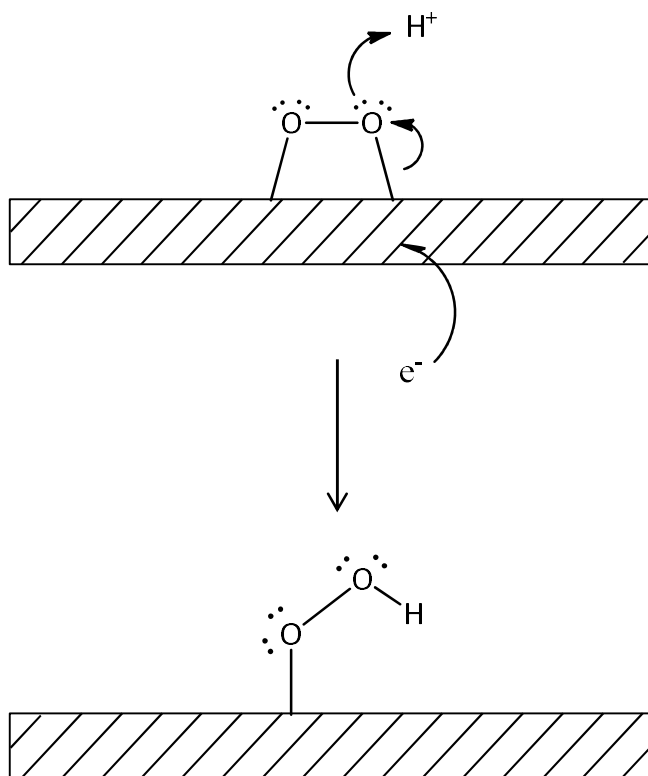
Figure 3.12 – Charge migration during the protonation of $O_{2(ads)}$ on the platinum surface

of the centre of the bond towards the platinum atom, though the centre of the bond is still biased towards the oxygen atom, and a decrease in the anti-bonding orbital occupation of this Pt-O bond. However, this decrease in anti-bonding occupation is due to an increased donation of charge towards the O-O bond, possibly as a result of charge donation from the terminal oxygen to the bonded proton. The net result of this electronic re-organisation is actually an increase in bond strength of both the Pt-O and O-O bonds in $OOH_{(ads)}$ compared to $O_{2(ads)}$; the O-O bond strength increases slightly from 127.073 kJmol^{-1} to 135.660 kJmol^{-1} while there is a significant increase from 34.736 kJmol^{-1} to 161.712 kJmol^{-1} for the Pt-O bond. Thus at 0 V on a clean surface one would expect either of the reactions involving the dissociation of the O-O bond to be favoured. Of these two reactions the protonation/dissociation of $OOH_{(ads)}$ to $[O_{(ads)} + H_2O_{(ads)}]$ is the most exergonic, suggesting that at equilibrium, when the ORR is under thermodynamic control, this reaction would appear favoured. However, this observation belies the feasibility of such a reaction. If one maps the electrostatic potential of the system as a function of the electron density, i.e. if one generates a surface at a fixed distance from the nuclei, this distance being a function of electron density, and then maps onto this

82

the electronic potential energy at each point on the surface, one can see that an approaching proton will be more attracted to the central oxygen atom, not the terminal –OH group as shown in Figure 3.13. This implies that a protonation reaction is considerably more likely to result in the formation of peroxide than $O_{(ads)}$ and $H_2O_{(ads)}$. As this would require the cleavage of the stronger Pt-O bond one can conclude that the dissociation of $OOH_{(ads)}$ to $O_{(ads)}$ and $OH_{(ads)}$ is favoured.
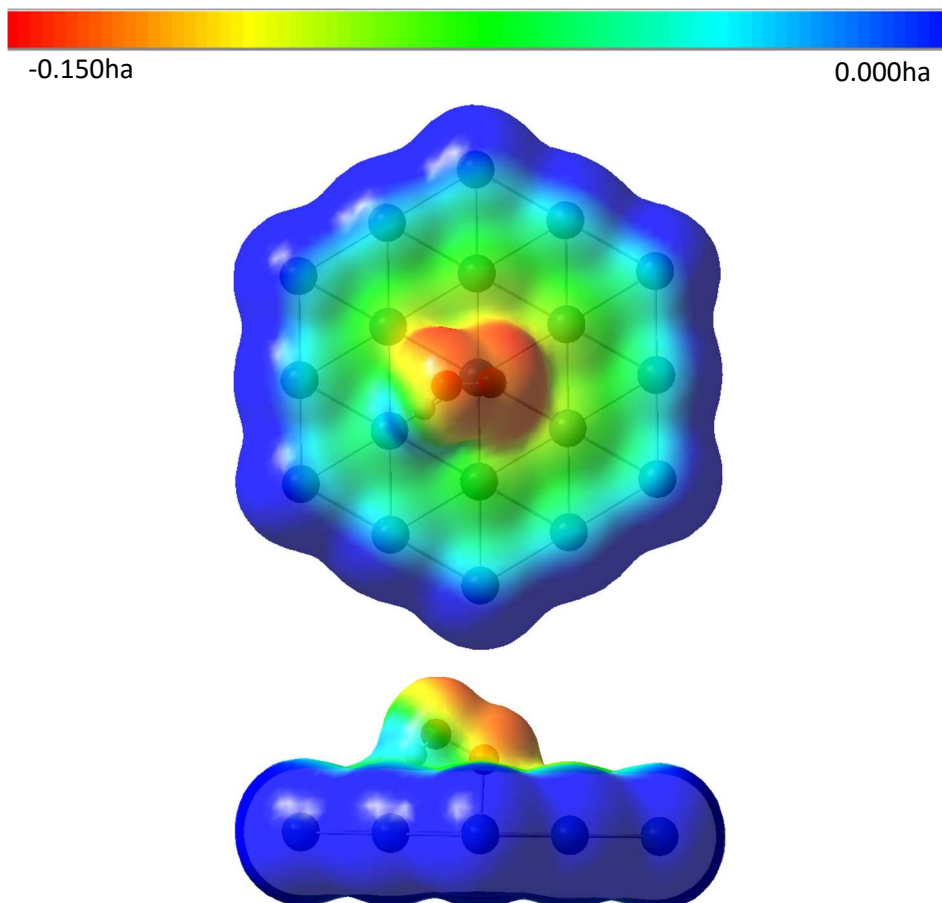
Figure 3.13 – The electrostatic potential of OOH$_{(ads)}$ on Pt$_{19}$ mapped as a function of its electron density, red indicates areas susceptible to electrophilic attack while blue indicates areas equally susceptible to either nucelophilic or electrophilic attack.

Post-dissociation it is expected that $O_{(ads)}$ migrates from the top adsorption site to the fcc site, this transition being exothermic by -29.595 kJmol^{-1}. The increased stability of the fcc site is due to the increased co-ordination of the oxygen atom to the surface. At the top site an oxygen atom interacts with a single platinum atom via a single covalent bond with slight ionic character, polarized towards the oxygen. The bonding at the

hollow site is very similar to that of gas phase O_2, with oxygen forming one and two 'one-half' bonds with the surface, evidenced by a single α bond and three β bonds to three platinum atoms, all of which are more polarized towards the oxygen than at the top site with the centre of each bond shifted 63-73 % towards the fcc oxygen. This increased co-ordination and polarization of the Pt-O bonds means that while the oxygen has a more negative partial charge at the fcc site, it is less reactive than at the top site. At the bridge site the oxygen still formally co-ordinates to the surface via two predominantly covalent bonds. Indeed so similar is the bonding at the bridge site to that at the hollow that one could say the only difference is the van der Waals type interaction with the surface between an oxygen lone pair and an acceptor orbital on the platinum surface. This notion is further supported by the partial charge of the oxygen at these two sites, which is not significantly altered on migration from the hollow to the bridge sites. However, while a classic approach to bonding would imply that two covalent bonds are formed, NBO analysis shows that there is a single α bond and two β bonds, implying that bridge oxygen would readily accept an electron and react with a proton. Thus it can be said that atomic oxygen on the Pt(111) surface occupies a hollow site and migrates to bridge sites to reduce. While oxygen can exist on the top site it is thought that such a species is short-lived, arising only as the result of a dissociation reaction involving either $O_{2(ads)}$ or $OOH_{(ads)}$, and quickly migrating to a more stable hollow site. The protonation of atomic oxygen is the most efficient reaction in the ORR, having a reversible potential of 1.220 V, near identical to that of the overall reduction reaction, 1.229 V; the resulting over-potential of this reaction is therefore very low, barely reducing the effective potential of the cell.

While the reduction of $OH_{(ads)}$ to $H_2O_{(ads)}$ is the simplest of all the intermediate reactions studied, it is also the source or the most significant loss in the ORR. As there are no possible side reactions, once the direct protonation reaction becomes unfeasible above the reversible potential of the reaction, 0.613 V, the accumulation of $OH_{(ads)}$ on the surface starts to become problematic. Above this potential $OH_{(ads)}$ start to block surface sites reducing the ease with which earlier reduction intermediates react and cutting off particular pathways. It is also important to note that above this potential, water will begin to disproportionate, most likely in the presence of $O_{(ads)}$ species,

resulting in a 'bloom' of $OH_{(ads)}$ which serves to block surface sites. As this surface blocking increases, the prevalence of adjacent surface sites reduces thus forcing O_2 to adsorb 'end-on', reducing the ease with which $OOH_{(ads)}$ can dissociate and thus facilitating the reduction of $OOH_{(ads)}$ to HOOH; over time the performance of the cell would therefore reduce significantly.

Knowing the preferred pathway allows one to calculate the E_{eff} value using Equation 2.4. The losses associated with O_2 adsorption and O-OH dissociation serve to reduce the total Gibbs free energy by -156.908 $kJmol^{-1}$, which corresponds to a total loss in performance of 0.407 V, and a maximum potential of 0.822 V. The overall preferred reduction mechanism at varying potentials is summarized graphically in Figure 3.14.
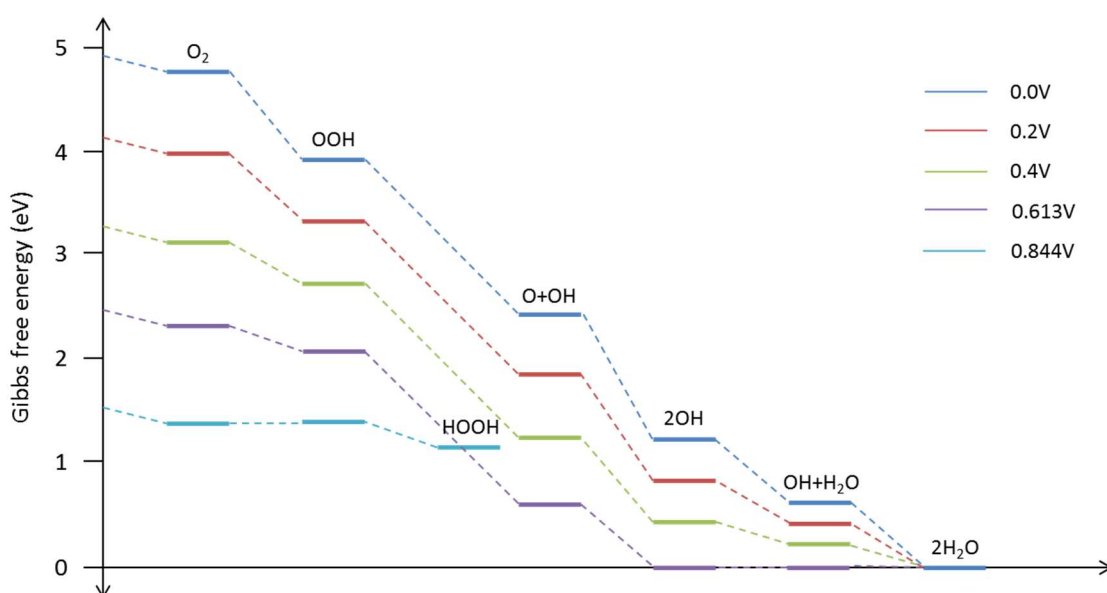
Figure 3.14 - Reaction schematic for the ORR on platinum as a function of imposed potential

3.2.3 - Porphyrin catalysed ORR

The reduction of O_2 on a macrocyle is considerably more complex than on a heterogenous surface, with multiple binding sites and thus a considerably more complex reduction mechanism. There exists little work regarding the computational investigation of the catalytic ability of non-pyrolysed macrocycles such as porphyrins. It is known that the combination of B3LYP and 6-31G-derived basis sets produce geometries, energies and frequencies that correlate well to experimental data (Jensen & Ryde, 2004; Seidel et al., 2011; Zhang et al., 2005) with a high quality, ideally triple-zeta, basis set needed

to describe the central ring structure (Liao et al., 2004). Several studies have concluded that O_2 binding to Co- and Fe- based macrocycles is due to interaction between O_2 π and Pt $3d_{z2}$ orbitals (Bikiel et al., 2008; Kieber-Emmons et al., 2011; Masa & Schuhmann, 2013), that metals in a +2 state display higher activity than more oxidised states (Bikiel et al., 2008) and that porphyrins containing Ni, Cu and Zn display poor activity towards the ORR (Masa & Schuhmann, 2013). It has been shown that substitution effects on a porphyrin can significantly alter the interaction of O_2 with the central metal (Masa & Schuhmann, 2013; Tai et al., 2013; Zhang et al., 2005), with electron withdrawing substituents increasing the O_2 binding capability of a porphyrin and electron donating groups decreasing it (Bikiel et al., 2008; Masa & Schuhmann, 2013). This variation in binding capabilities has been stated to be due to a number of effects, with some reporting correlation between activity and metal E_{HOMO}, E_{LUMO} and E_g (Tai et al., 2013) and/or electrophilicity of the central metal (Masa & Schuhmann, 2013), while others report that the nature of the central metal varies little as the macrocycle acts as an electron 'buffer' (Liao et al., 2004). However, due to the very small amount of follow-up work on these findings there is little relevant data to support any one of these three hypotheses. In this work B3LYP is used, with 6-311G describing the axial ligand and substituted phenyl groups and 6-311++G(d,p) for the central ring structure and adsorbed intermediates. The proposed reduction reactions are shown as part of an overall reaction schematic in Figure 3.15.

For dissociation and disproportionation reactions a secondary adsorption site is required. The favoured secondary site was found by optimising the structure of the porphyrin with two adsorbed oxygen atoms; one on the central metal and one over the carbon/nitrogen atoms as shown in Figure 3.16. For all porphyrins it was found that the favoured secondary site bridges the two carbon atoms opposite the nitrogen atom of an amine ring. However, further investigations showed that on all porphyrins dissociation/disproportionation reactions were unlikely to occur, with the dissociated products of each plausible reaction considerably higher in energy than the reactants, thus these pathways are not considered in great detail in the following sections.
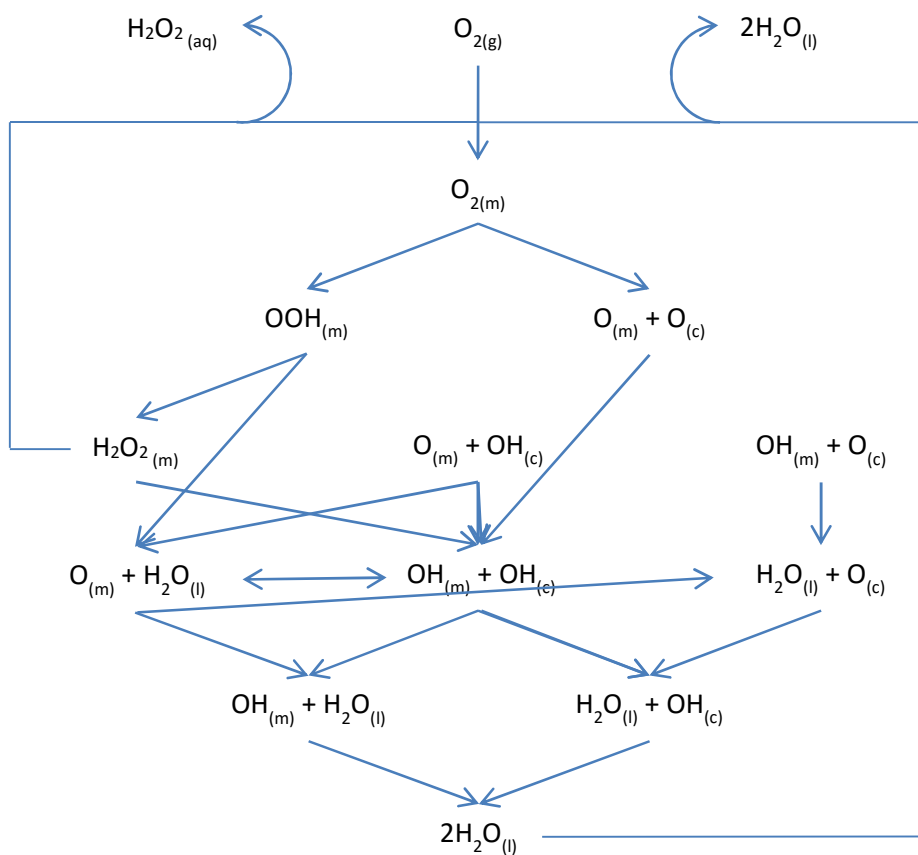
Figure 3.15- Proposed mechanisms for porphyrin catalysed oxygen reduction.
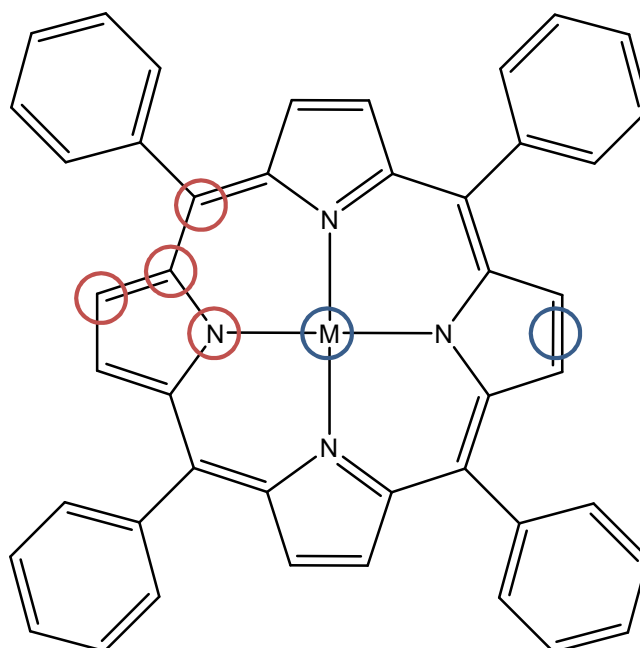
Figure 3.16 - Proposed secondary adsorption sites on tetraphenyl porphyrin highlighted by red circles. The two favoured sites are highlighted by blue circles.

3.2.3.1- Adsorption of O₂

O₂ is found to bind favourably to the central metal of all six porphyrins when in the +2 oxidation state but little to no interaction when in a higher oxidation state. As such the following results concentrate only on the Co^{II}- and Fe^{II}-centred porphyrins. Two modes of adsorption were initially considered and modelled, side-on with each oxygen atom forming a bond with the metal atom, and end-on where only one oxygen atom binds to the central metal. In all cases it was found that O₂ favoured end-on adsorption, with the O₂ bent on the surface and an approximate half electron charge on the terminal oxygen as shown in Figure 3.17. NBO analysis of the oxy-porphyrin complex shows that the majority of charge is donated from the macrocycle to the oxygen, with the metal-oxygen interaction being primarily ionic and involving donation from oxygen lone pairs to the metal $3d_{z^2}$ orbital, and back donation from the metal $3d_{yz}$ to the $2\pi^*$ orbital of the bound O₂. These results imply that the metal centre of the porphyrin acts as an electron 'conduit' allowing initial charge donation from the macrocycle, with a small 'direct' interaction between the metal and the substrate. This is further supported by the change in partial charges, as shown in Table 3.4.
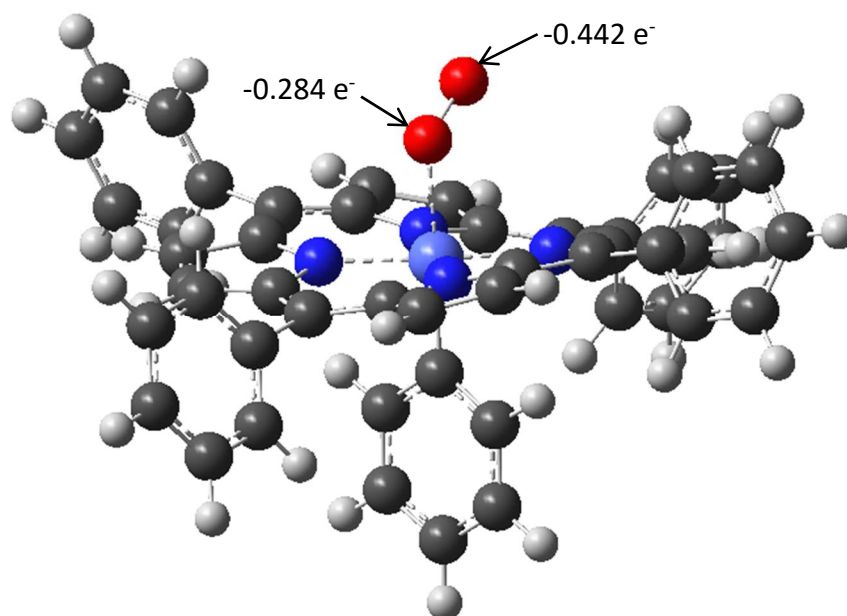
Figure 3.17 - O₂ adsorbed on Co-TPP annotated with the partial charges on each oxygen atom.

Table 3.4 - Change in partial charges (e⁻) of porphyrins upon adsorption of O_2.

	TPP		TCPP		TMPP	
	Co	**Fe**	**Co**	**Fe**	**Co**	**Fe**
meso	0.082	0.044	0.120	0.039	0.078	0.043
axial	-0.117	0.067	-0.125	0.069	-0.114	0.066
macro	0.782	0.458	0.749	0.468	0.790	0.453
metal	0.054	0.246	0.044	0.228	0.045	0.250
substrate	-0.801	-0.816	-0.788	-0.803	-0.798	-0.811

Table 3.4 also shows that the extent of donation from the macrocycle/metal differs between the Fe-centred and Co-centred analogues. Charge donation from Co-centred porphyrins primarily comes from the macrocycle, with the metal centre partial charge barely changing upon binding O_2. Conversely, Fe is much more involved in charge donation, with approximately a third of the total charge donated to the $O_{2(ads)}$ coming from the metal. This difference is found to be due to the lower energy levels of Co $3d_{yz}$ orbitals compared to the Fe $3d_{yz}$ orbitals. When binding oxygen, charge is donated to orbitals on the oxygen that lie higher in energy than the Co $3d_{yz}$ orbitals but lower than the Fe $3d_{yz}$, thus back bonding is favoured for Fe-centred porphyrins, but not for the Co-centred. However, the higher energy of the $3d_{z^2}$ orbital in Fe-centred porphyrins means that donation from the O_2 lone pairs to the porphyrin is not as labile as for Co-centred compounds, thus Fe-centred porphyrins donate more charge to O_2 than their Co-centred analogues but do not have as strong an interaction as shown in Table 3.5.

Table 3.5 - Relationship between the charge donation (e⁻) from the porphyrin to $O_{2(ads)}$ and the Gibbs free energy change of adsorption (kJmol⁻¹).

	TPP		TCPP		TMPP	
	Co	**Fe**	**Co**	**Fe**	**Co**	**Fe**
Charge donation	-0.801	-0.816	-0.788	-0.803	-0.798	-0.811
ΔG_{ads}	-47.7609	-30.3933	-41.6822	-20.7446	-48.2433	-31.4547

In each case, the protonation reactions are more favoured on the Fe-centred porphyrins than the Co-centred analogues as shown by the data contained within Table 3.6. As the adsorption strength of $OOH_{(ads)}$ does not differ between Co- and Fe-centred complexes, the reversible potential for the one electron reduction reaction can be considered to be a function of the Gibbs free energy change of adsorption of O_2; the more exergonic the adsorption, the lower the reversible potential of this first electrochemical reaction.

Table 3.6 – Reversible potentials (V) for the porphyrin catalysed one-electron reduction of O_2.

	Co	Fe
TPP	0.387	0.561
TCPP	0.414	0.646
TMPP	0.420	0.572

3.2.3.2 - Preferred pathways

As dissociation reactions are not considered viable, OOH must be reduced to either H_2O_2 or $O+H_2O$ on each of the porphyrins. At first glance one may consider these pathways competitive with reasonably similar reduction potentials, as shown in Table 3.7, however this is not thought to be the case. Bond strengths were calculated and ESP-on-density maps were produced for $OOH_{(ads)}$ on each porphyrin. The ESP-on-density map of $OOH_{(ads)}$ on Co-TPP is shown in Figure 3.18 and is indicative of $OOH_{(ads)}$ on all porphyrins. From the bond strengths and ESP-on-density maps it is found that the O-OH bond is much stronger than the metal-OOH bond in all cases, and that the likely site of nucleophilic attack is on the metal bound oxygen.

Table 3.7 - Redox potentials (V) of the porphyrin catalysed OOH protonation reactions.

	TPP		TCPP		TMPP	
	Fe	Co	Fe	Co	Fe	Co
$OOH_{(m)} + H^+ + e^- \rightleftharpoons H_2O_{2\,(m)}$	0.463	0.484	0.561	0.606	0.462	0.449
$OOH + H^+ + e^- \rightleftharpoons O + H_2O$	0.618	0.434	0.609	0.476	0.634	0.366

The reduction of the peroxide on any porphyrin is unlikely to be plausible despite the apparently high reversible potential of the reaction, for a number of reasons. Firstly, when the redox potential of the Co/Fe catalyst is lower than that of the one electron reduction of peroxide, 0.806 V, it is expected that the formation of two OH radicals occurs (Banham et al., 2015). In such a scenario it is not expected that such radicals would bind to the metal centre and the porphyrin ring, instead a degradation pathway is expected to dominate whereby meso-phenyl groups are lost, forming phenols, and replaced with hydroxyl groups, as shown in Figure 3.4. However such a degradation pathway is not modelled within this work and so it is impossible to conclusively state if this reaction would occur without expanding the scope of the
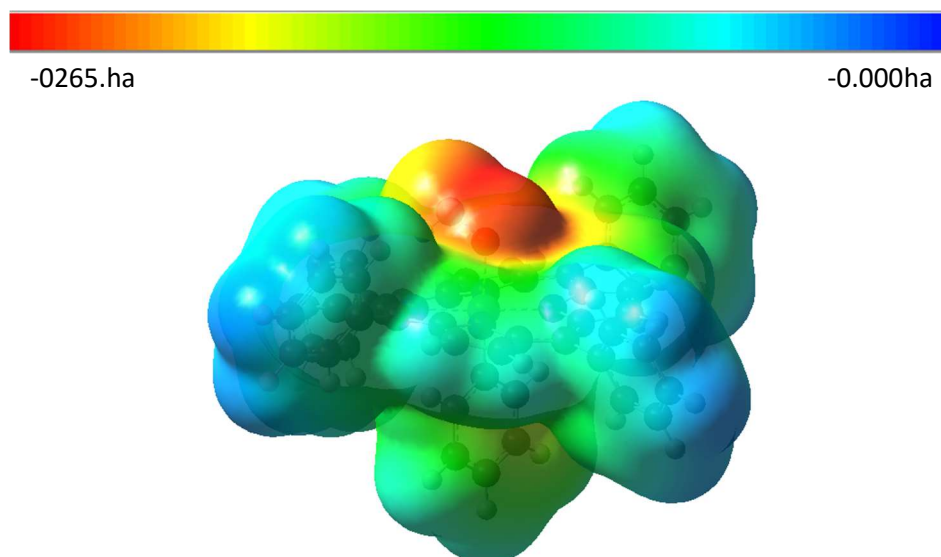
Figure 3.18 - ESP-on-density map of OOH adsorbed on Co-TPP

research. Secondly, in all cases there appears to be little interaction between the central metal and the formed peroxide. In all cases the oxygen atoms of peroxide are well separated from the metal centre and the surrounding porphyrin ring, with the only interaction worth note being a proposed van der Waals interaction between a peroxide hydrogen atom and a nitrogen atom on the porphyrin ring, as shown in Figure 3.19. That the peroxide does not interact with the metal centre, in conjunction with the lower redox potential of the porphyrin than the one-electron reduction potential of peroxide and the labile replacement of peroxide with O_2, leads to the conclusion that upon formation peroxide either dissociates from the surface or contributes to the degradation of the catalyst.

3.3 - Comparison of computational and experimental results

Computational redox potentials were calculated and normalised to the standard hydrogen electrode using Equation 3.1:

$$E^0 = \frac{(G_{red} - G_{ox})}{nF} - 4.42eV$$

Equation 3.1 - Calculation of computational redox potentials

where E^0 is the redox potential, G_{red} and G_{ox} are the Gibbs free energies of the reduced and oxidised forms of the porphyrins respectively, n is the number of electrons
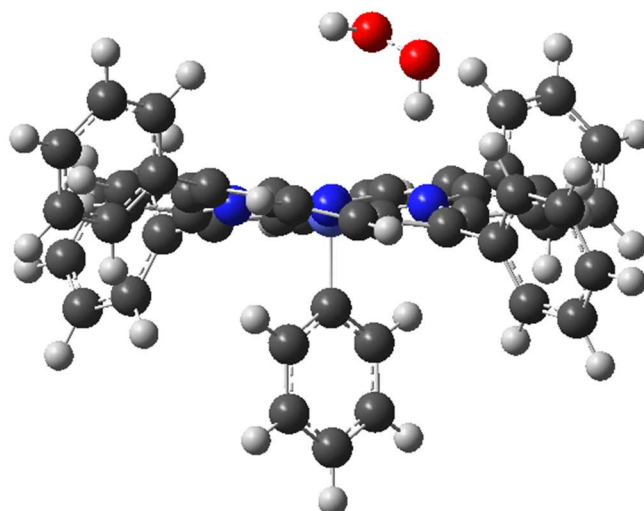
Figure 3.19 - Interaction between hydrogen peroxide and Co-TPP

transferred during the reactions, F is the Faraday constant, 96485.332 Cmol^{-1}, and 4.42 eV is the energy of the electron transferred in the standard hydrogen electrode. The calculated potentials are shown alongside the redox potentials determined experimentally and the difference between the two in Table 3.8. It can be seen that the redox potentials are drastically underestimated by the computational model. The reason for this underestimation is proposed to be due to the use of an axial benzene ligand as a model for the carbon support. The high electronegativity of the benzene results in a reasonably high partial charge on the axial ligand in the +2 state and little change to the partial charge on the central metal. A more extensive graphene-like ligand would likely benefit from the inherent electron resonance, allowing for a more significant change in the partial charge of the central metal. However, while attempts were made to model such a ligand were made, it was found that the system was too large to optimise within a reasonable timeframe[11] using the method and basis set combination necessary to properly describe it. However, modelling redox potentials in the absence of an axial ligand produced redox potentials of a more reasonable value, i.e. between 0.2-1 V, but the differences between the calculated values and those found

---

[11] i.e. <1000 processor hours per calculation

experimentally were found to be inconsistent, with no clear trend as to their under or overestimation. As the underestimation of the redox potentials is near

Table 3.8 - Predicted reversible potentials, experimentally obtained redox potentials and the associated correction factor for each porphyrin

	Redox Onset		
	Predicted	Actual	Correction
Co-TPP	-1.348	0.425	1.773
Fe-TPP	-1.252	0.49	1.742
Co-TCPP	-1.199	0.54	1.739
Fe-TCPP	-1.263	0.495	1.758
Co-TMPP	-1.206	0.55	1.756
Fe-TMPP	-1.365	0.42	1.785
		Avg.	1.759
		St.Dev	0.016

constant between each result when using an axial benzene ligand, it is felt that its use as a representation of the carbon support is suitable, provided a correction factor is applied.

Regarding preferred pathways the use of ESP-on-density maps and bond-strength calculations are clearly able to predict the preferred pathway on both platinum and porphyrins at 0 V and the potential effects noted from Figure 3.6 (namely the shift towards side reactions) are explained by calculating the reversible potentials of the elementary reactions. In the case of platinum it is observed that the reduction of $OH_{(ads)}$ species, which becomes unfeasible above 0.613 V, leads to a shift in the reduction mechanism towards peroxide formation and the inclusion of side reactions within the preferred pathway. However, as platinum is able to catalyse the ORR up to 0.87 V, the overall activity of the catalyst is therefore postulated to be governed either by the one-electron reduction potential of O_2, calculated to be 0.844 V, or the E_{eff} potential, which is predicted to be 0.822 V. While neither of these values are exactly the same as that observed in experiment, it is felt that both lie within a reasonable margin of error to assign the activity to either.

Figure 3.20 and 3.21 show the air-saturated CV's of the Fe-centred and Co-centred porphyrins respectively, these figures are annotated with the calculated one- electron

reduction potentials from Tables 3.6 and 3.7. As it has already been established that the redox potentials can be predicted with good accuracy provided an adequate
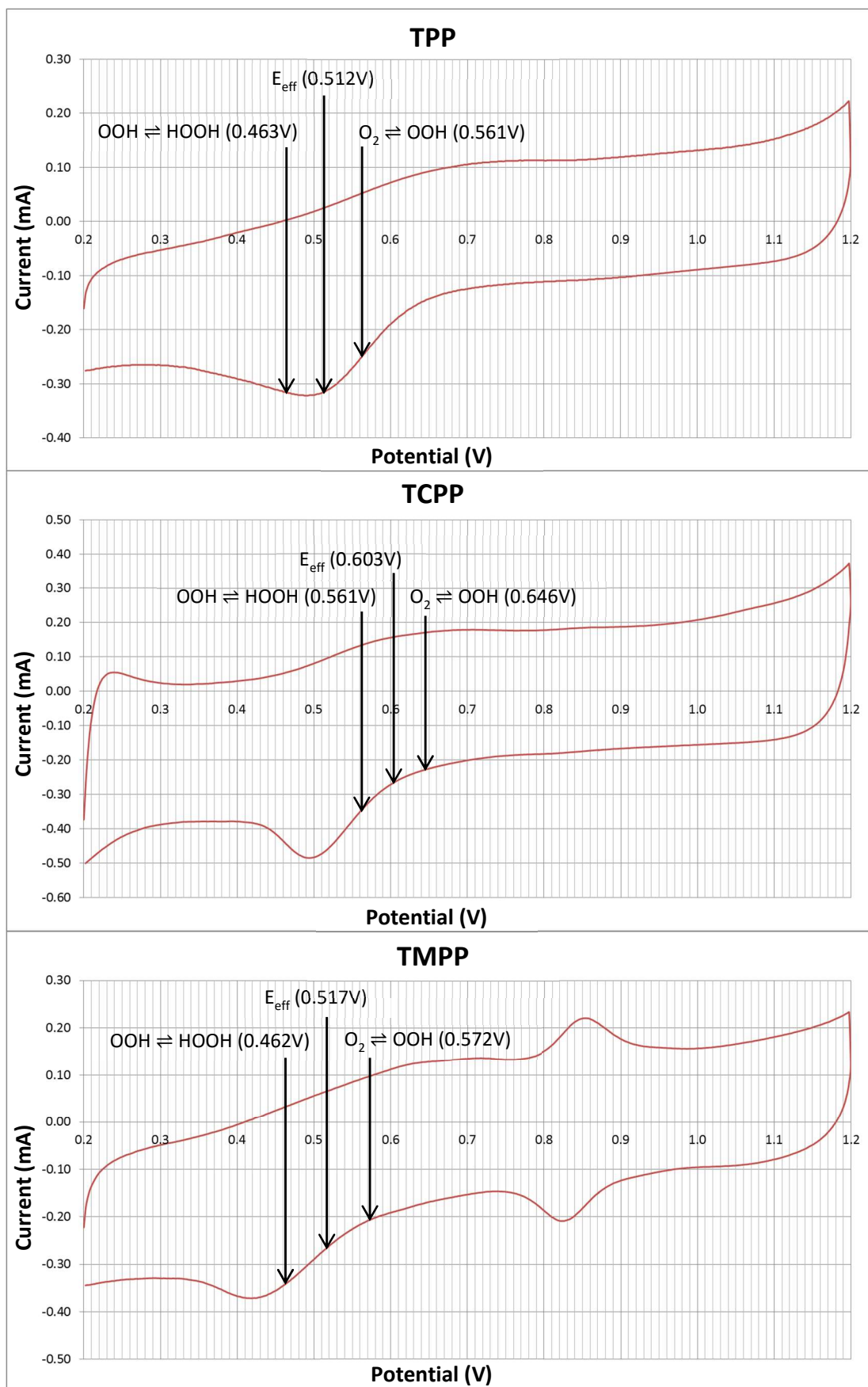
Figure 3.20 - Annotated CV's of Fe-centred porphyrins.
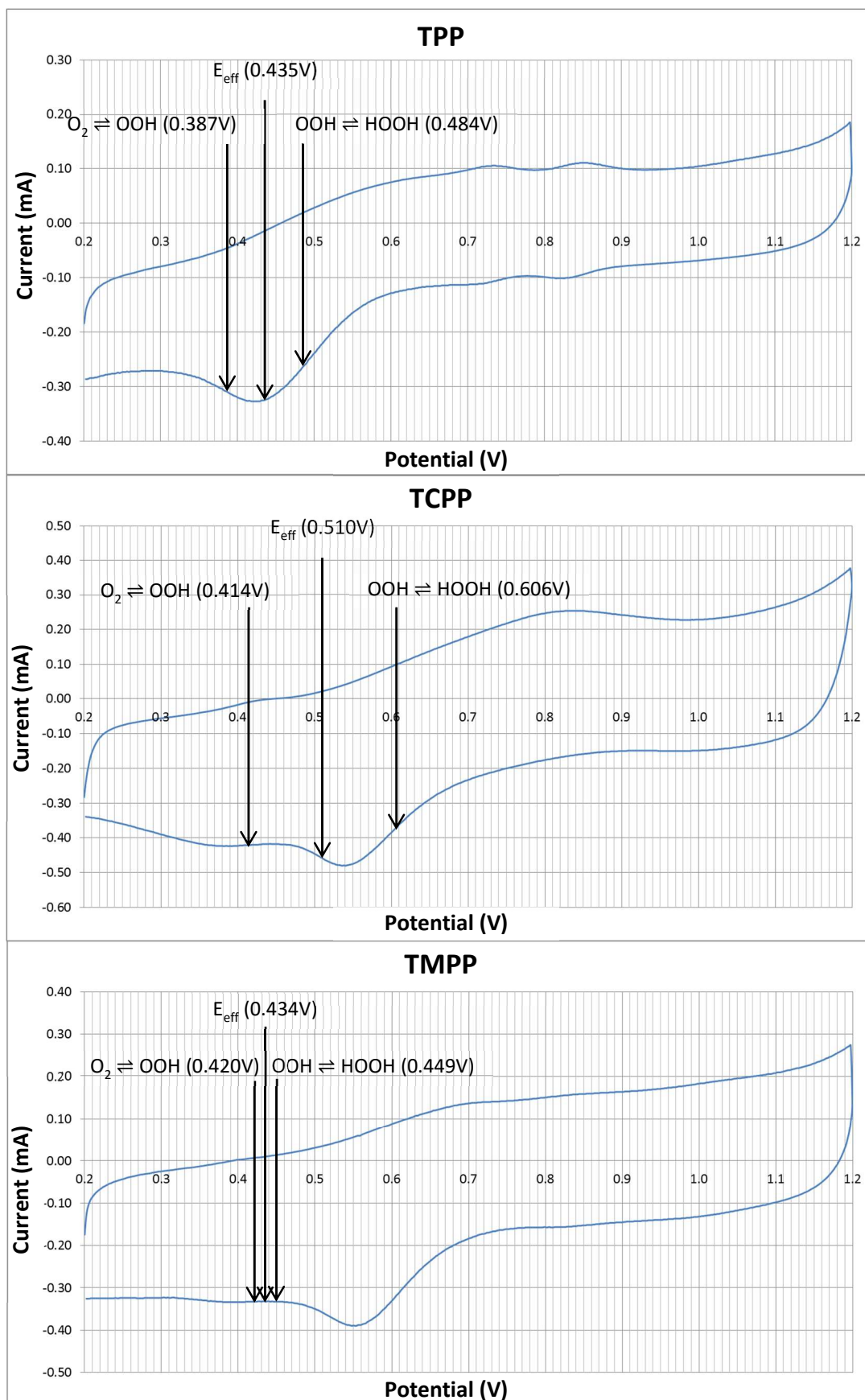
Figure 3.21 - Annotated CV's of Co-centred porphyrins.

correction factor is applied, these values have not been included. Regarding the Fe-centred porphyrins, almost all the one-electron reduction reactions have reversible potentials higher than E_p^a, which is attributed to porphyrin redox. The only exception to this, the one electron reduction of OOH$_{(ads)}$ on Fe-TPP, is less than 0.03 V lower than this. The proximity of the reduction potentials of Fe-TPP to E_p^a would be expected to produce a single broad peak which is a function of the three electron transfer reactions taking place. Indeed the main redox peak is noticeably narrower for Fe-TCPP, where the one-electron reduction potentials are, at the lowest more than 0.6 V higher than E_p^a. The proximity of the one-electron reduction potential of OOH$_{(ads)}$ to E_p^a of Fe-TMPP produces a less defined peak than that observed for Fe-TCPP, though it is still more defined than that of Fe-TPP.

Conversely, the one electron reduction potential of O$_2$ is lower than E_p^a for all the Co-centred porphyrins. On both Co-TCPP and Co-TMPP this potential is significantly lower than E_p^a, as evidenced by a plateau near to the predicted one-electron reduction potentials, which is postulated to result from the slight crossover of the redox and one electron reduction peaks. This is not observed in the CV of Co-TPP due to the proximity and convolution of the redox and one-electron reduction peaks. However, there seems to be little relationship between the E_{eff} values predicted for any of the porphyrins and experimentally observable behaviour. While the E_{eff} values correlate well with the potential of maximum current for Fe-TPP, Co-TPP and Co-TCPP, these values appear to correspond to the ORR onset potential for Fe-TCPP, Fe-TMPP and Co-TMPP. The lack of congruity across all porphyrins regarding the physical meaning of this E_{eff} value coupled with the ability to explain observed trends using other calculated values, such as the redox potential of the porphyrin and the one-electron reduction potentials of O$_2$, lead one to conclude that E_{eff} has little relevance to the catalytic activity.

3.4 - Conclusions

From Section 3.3 it can be seen that B3LYP/6-31G/6-311++G(d,p) is capable of describing the electrochemical activity of Co- and Fe-centred porphyrins. The use of an axial benzene ligand as a model for the carbon support is able to predict redox potentials with good accuracy, provided a correction factor is applied. No such correction factor is

required when calculating one-electron reversible potentials as the influence of the benzene ligand remains near constant, provided the porphyrin remains in the same oxidation state. While others state that the effective reduction potential is a function of the total Gibbs free energy transferred in electrochemical reactions, see Equation 2.4 (Anderson, 2012), this is not found to be the case. Instead it is postulated that the activity of a porphyrin is a function of both the redox potential and the one-electron reversible potentials; the lowest of these determines the maximum potential at which the reaction can proceed. These values are seemingly interconnected; while the redox potential of a porphyrin can be increased by modulating the substituent groups and/or the central metal, doing so decreases the one-electron reduction potential of O_2. This catch-22 situation presents problems for designing future catalysts as it results from the difference in energy between the O_2 2p orbitals and the 3d orbitals of the metal. Decreasing the energies of the 3d orbitals of the metal ions by modulating the substituent groups results in an increased redox potential but increases the energy difference between these and the O_2 2p orbitals, allowing for more significant donation from the oxygen to the metal and thus a more exergonic adsorption of O_2; this in turn results in a lower one-electron reduction potential for the first electrochemical reaction. This conclusion supports the notion that the E_{HOMO}, E_{LUMO} and E_g affect the activity of a porphyrin as postulated by Tai et al. (2013).

These results agree with the few findings obtained from literature, namely that substituent effects do have an effect on the activity of a porphyrin (Masa & Schuhmann, 2013; Tai et al., 2013; Zhang et al., 2005) and that the +2 state of the central metal displays higher activity than more oxidised states (Bikiel et al., 2008). However, while several report that O_2 binding is a result of interaction between O_2 π and Pt $3d_{z^2}$ orbitals (Bikiel et al., 2008; Kieber-Emmons et al., 2011; Masa & Schuhmann, 2013), it is found that the interaction of $3d_{yz}$ and O_2 π^* orbitals also has a significant influence and backbonding interactions between the central metal and O_2 serve to aid reduction.

None of the porphyrins exhibit activity close to that of platinum (see Section 3.2.2) which is capable of reducing O_2 to $2H_2O$ up to approximately 0.6 V without the formation of surface blocking species and up to approximately 0.85 V as side reactions become viable. While platinum is capable of promoting O-O bond dissociation, no porphyrin is

due to the inability of the surrounding structure to favourably adsorb reduction intermediates. However, the more homogenous structure proposed to surround pyrolysed M-N$_x$C sites, as discussed in Section 2.6, may allow for the more favourable 4 e$^-$ pathway to be followed. This postulate is explored in the following chapters.

Chapter 4- Fe- and Co-centred N$_x$/C active site characterisation

4.1 - Introduction

Section 2.6.1 detailed relevant research into M-N$_x$/C active sites, currently one of the most promising candidates to replace platinum as the cathode catalyst within PEM fuel cells (Chao et al., 2014; Domínguez et al., 2014; Kattel et al., 2014; Kattel et al., 2013; Li et al., 2012; Liang et al., 2014; Liu et al., 2006; Parvez et al., 2012; Schilling et al., 2010; Wei et al., 2000). These active sites were originally developed via the heat-treatment of porphyrins and phthalocyanines (Chang et al., 2014; Domínguez et al., 2014; Liu et al., 2006; Schilling et al., 2010; Wei et al., 2000; You et al., 2014), but recent work has shown that catalyst of similar activity can be synthesised using simple iron- and nitrogen-containing precursors with carbon (Baker et al., 2008; Charreteur et al., 2008; Cheng et al., 2013; Domínguez et al., 2014; Kattel et al., 2014; Li et al., 2012; Liu, Li, Ganesan, et al., 2009; Schilling et al., 2010). The nature of the active sites produced by pyrolysing such precursors between 700-900 ^{o}C with a carbon support is a matter of contention within the literature, with some stating that nitrogen functionalities are responsible for ORR activity (Lee et al., 2009; Liu, Li, Ganesan, et al., 2009; Maldonado & Stevenson, 2004; Parvez et al., 2012) while others favour M-N$_x$/C active sites, similar to those of the central moiety of porphyrins and phthalocyanines (Liu, Li, Ganesan, et al., 2009; Wei et al., 2000). From the critical review presented within Section 2.6 it is deemed highly likely that the latter of these two are the most adept at catalysing the reduction of oxygen to water. Previous computational work has focussed on active sites hosted within micropores of graphene and used models representative of single layer graphene (Kattel et al., 2013; Kattel et al., 2014; Kattel & Wang, 2013b; Kattel & Wang, 2014; Szakacs et al., 2014). However, experimental work has shown that the pyrolysis of simple precursors with amorphous carbon produces catalysts with comparable activity to that of Pt/C (Charreteur et al., 2008).

Of the work concerning M-N$_x$/C active sites it is difficult to elucidate the stoichiometry of the most active species. Regarding the nature of active sites it has been

reported that the use of cobalt- and iron-containing precursors produces catalysts of varying activity and stability (Domínguez et al., 2014; Kattel et al., 2014; Koslowski et al., 2008; Lefèvre et al., 2005; Lefèvre et al., 2002; Lefèvre et al., 2009; Lefèvre & Dodelet, 2003; Li et al., 2012; Li et al., 2011; Liu, Li, Ganesan, et al., 2009; Médard et al., 2006; Villers et al., 2004). It is also found that the activity is related to the amount of nitrogen within the central moiety of the site, with both $M-N_2$ and $M-N_4$ stoichiometry's reported to be active towards the ORR (Koslowski et al., 2008; Lefèvre et al., 2005; Lefèvre et al., 2002). Of these it is proposed that $M-N_2$ active sites are more active while $M-N_4$ active sites are more stable (Lefèvre et al., 2005; Lefèvre et al., 2002; Médard et al., 2006). However, no synthesis method is currently able to produce such active sites with specific stereochemistry and so elucidating the nature of the most active site is experimentally impossible. This chapter attempts to ascertain the nature of the most active sites, by computationally modelling both the redox potentials of $M-N_x/C$ active sites and their activity towards the ORR, and to ascertain the role carbon plays as an integral component of the catalyst. It is proposed that by doing so highly active sites can be found, and that these results can inform future work into the synthesis of catalysts that can compete with platinum in terms of their activity towards the ORR, and their stability in acidic media.

4.2 - Methodology

Using the literature reviewed in Section 2.6.1.2, a number of active sites are proposed, each has a Co or Fe atom bound to either 2 or 4 nitrogen atoms which are themselves embedded within a carbon structure. As it has been shown that active sites developed during pyrolysis of amorphous host active sites (Charreteur et al., 2008; Lefèvre et al., 2009), and that graphene has unique properties that could enhance an active sites activity towards the ORR (Kattel et al., 2012; Parvez et al., 2012; Tripkovic & Vanin, 2013; You et al., 2014), two proposed carbon structures have been modelled; one being graphene-like, and the other a disrupted graphene-like structure that is proposed to represent amorphous carbon. Using these two carbon structures, 8 proposed Fe- and Co-centred active sites were modelled. Given the elemental and structural similarities between these active sites and porphyrins, the same method and basis set combination was used; with 6-311G++(d,p) describing the central metal/nitrogen moiety and the

adsorbed substrates, while 6-311G was used to describe the axial benzene ligand and the more extended equatorial carbon structure.

As with the porphyrins described in Section 3.2.3, the heterogenous nature of the catalytic surface necessitates the need for a secondary adsorption site for dissociation pathways, the proposed secondary sites are shown in Figure 4.2. For each N_2/C site it was found that when a second oxygen atom is bound to a metal-coordinated carbon the central ring structure is disrupted by the formation of a phenol-like functionality. Figure 4.3 shows this phenol-like functionality on Co-N_{2h}/C_g which is representative of the trend observed on all N_2/C active sites, for ease of visualisation the axial benzene has been removed from the image. It is proposed that this leads to degradation of the active site by weakening the interaction of the metal with the surface, promoting metal leaching to the electrolyte. That N_2/C sites are said to be less stable than N_4/C sites further supports this postulate. As the purpose of this work is to explore the activity of an active site over its stability, this configuration was not included in optimisation calculations, though this proposed lack of stability should be considered alongside derived activity calculations and could form part of an extended investigation into the stability of those sites found to be electrochemically active.

With the identity of the favoured secondary sites known, the reduction pathways were modelled as they were with porphyrins and following the overall mechanism detailed in Figure 3.15. Redox potentials were calculated by optimising the structures for high and low spin +2/+3 configurations of the active site, and corrected using the correction factor derived in Section 3.3, 1.890 V.

4.3 - Redox potentials

Redox potentials for each active site are shown in Table 4.1, from this table several overall trends can be observed. Firstly, with the exception of the Co-N_4/C pair, all graphene active sites have a higher reversible potential than their amorphous counterparts, indeed so pronounced is the effect of the graphene structure that for the Co-N_2/C active sites the redox potentials exceed the maximum reversible potential of the ORR. Secondly, the Co-N_x/C_g active sites, in general, have a higher redox potential than their Fe-centred analogues, though conversely the Co-N_x/C_a have

Basal graphene (C$_g$)   Amorphous carbon (C$_a$)

Carbon support

N$_4$ N$_{2h}$ N$_{2p}$ N$_{2t}$

Central moiety
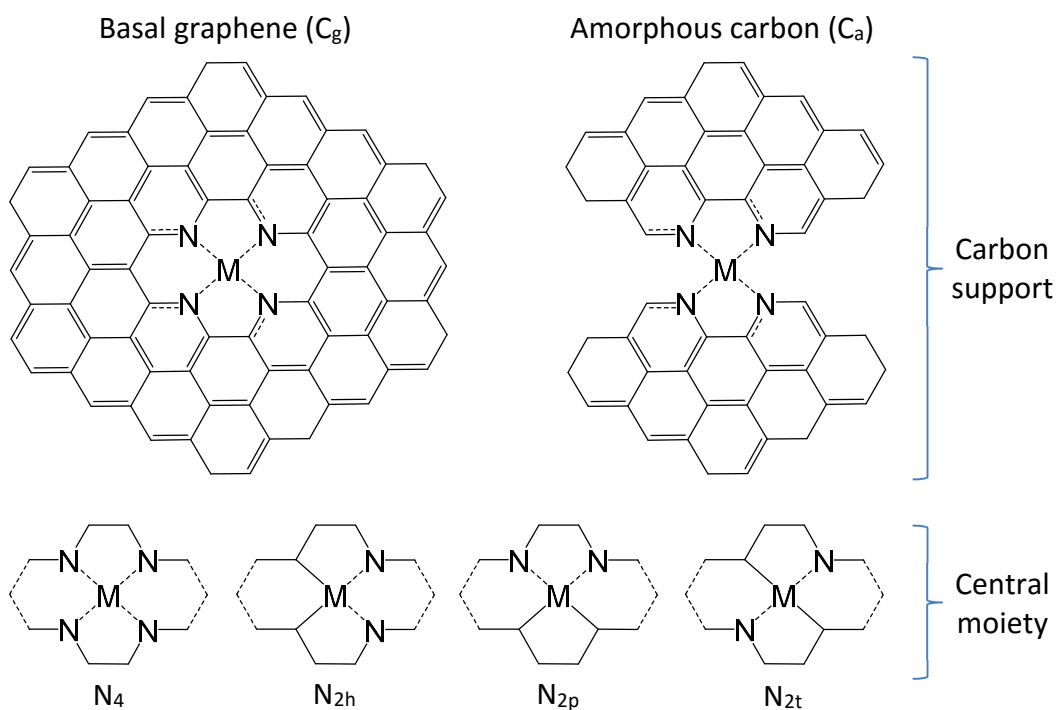
Figure 4.1 - Structure of proposed M-N$_x$/C active sites components.

Co or Fe   N or C
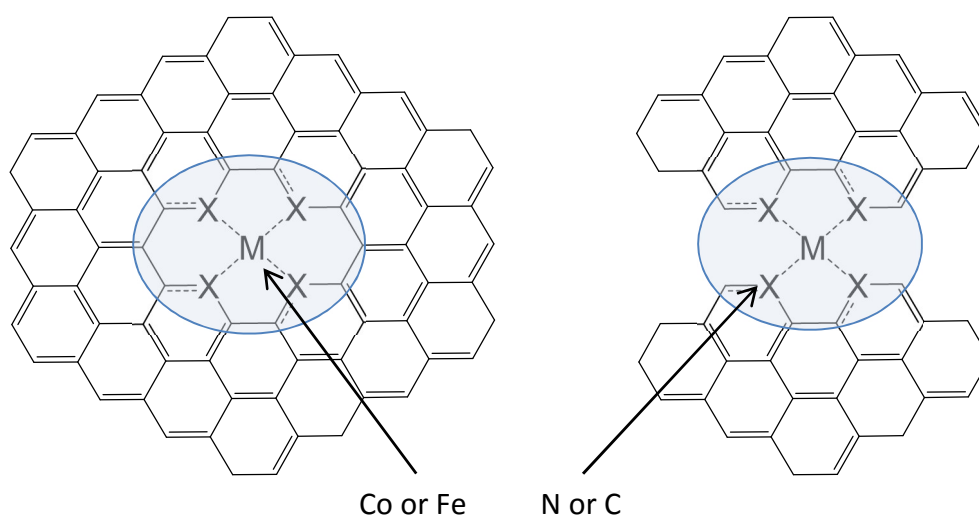
Figure 4.2 - Proposed secondary active site locations highlighted by a blue outline. The favoured secondary active site was found by optimising the structure with an oxygen on the central metal and at each atom within the blue highlight.
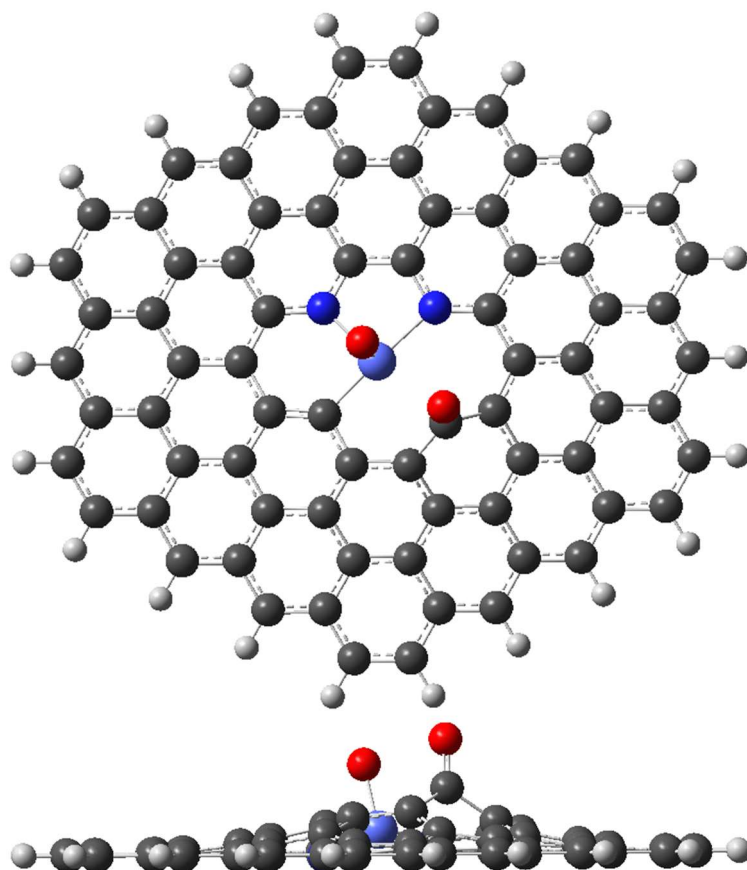
Figure 4.3 - Formation of phenol-like functionality upon adsorption of oxygen atom to a carbon atom adjacent to the central metal of Co-N_{2p}/C_g.

Table 4.1 - Predicted redox potentials (V) for each Co- and Fe-N_x/C active site.

	Fe-centred		Co-centred	
	C_g	C_a	C_g	C_a
N_4	0.592	0.406	0.689	0.732
N_{2h}	0.890	0.508	1.100	0.340
N_{2t}	0.896	0.780	1.125	0.308
N_{2p}	1.323	0.853	1.135	0.696

significantly lower redox potentials than the Fe-N_x/C_a active sites. Finally, with the exception of Co-N_4/C_a, the N_4/C active sites have markedly lower redox potentials than N_2/C active sites. These results clearly imply that both the metal centre and the N_x/C support influence the redox potential of the active site.

That the graphene active sites display higher redox potentials than their amorphous counterparts is perhaps not a surprise. Graphene displays an impressive ability to both

accept and donate electronic charge (Voggu et al., 2008) and the decreased electron resonance of the amorphous carbon support means that an additional electron is not as readily stabilised as it would be by a more connected, and thus more resonant, graphene ligand.

When one maps how the charge density increases across each C_g active site upon the addition of an electron, i.e. upon reduction of the active site from a formal +3 state to a formal +2 state, one notes that in all cases the majority of the additional electronic charge is located on the equatorial N_x/C ligand. One would thus expect a higher redox potential to result from a more significant charge donation to this equatorial ligand however, no correlation between these values exists as can be seen from the data presented in Table 4.2. This lack of correlation implies that the redox potential is not simply governed by the amount of partial charge transferred to the carbon structure but also the electronic configuration of the carbon surface, i.e. the occupation and energy of the multiple valence orbitals for each carbon and nitrogen within the equatorial ligand.

Table 4.2 - Change in partial charges of active site components and the calculated redox potentials

	Iron				Cobalt			
	Eq	Axial	Metal	Redox (V)	Eq	Axial	Metal	Redox (V)
N_4-C_g	-0.941	-0.048	-0.010	**0.592**	-0.979	-0.019	-0.002	**0.986**
N_{2p}-C_g	-0.963	-0.041	0.004	**1.323**	-0.950	-0.051	0.000	**1.135**
N_{2h}-C_g	-0.975	-0.025	0.000	**0.890**	-0.933	-0.097	0.030	**1.100**
N_{2t}-C_g	-0.809	-0.010	-0.181	**0.896**	-0.914	-0.075	-0.010	**1.125**

Given the incredibly intricate nature of this extended electronic structure, attempting to find correlations between subtle changes within it and the redox potential are near impossible. Table 4.2 also shows that, at least when embedded in graphene planes, those active sites with only two nitrogen atoms display higher redox potentials than N_4/C active sites, implying that the nitrogen atom may act as an 'inhibitor' to higher redox potentials.

NBO analysis shows that Fe-N and Co-N interaction is predominantly ionic, featuring an sp^3 hybridised lone pair lightly interacting with the Co 3d$_{xy}$ orbital. Strictly speaking

this interaction does not constitute a formal covalent bond, but NLMO analysis, which allows for the inclusion of localised electronic interactions onto the orbitals, shows that these sp^3 'lone pairs' include 5-15 % $3d_{xy}$ character. Thus while one cannot formally assign this as a covalent bond, it is clear that the metal centre of the active sites is able to electronically connect to the equatorial ligand via these nitrogen atoms, and that electron charge can be donated/accepted by the metal centre via this interaction.

Conversely, the Fe-C and Co-C interaction is much more covalent in nature, though again this involves the crossover of sp^3 hybridized lone pairs with the $3d_{xy}$ orbital of the central metal. This crossover is much more significant in metal-carbon bonds than metal-nitrogen bonds due to the increased electronegativity of nitrogen compared with carbon; that nitrogen is less willing to donate charge means that its interaction with the δ^+ metal is less extensive than carbons.

At this point it is worth noting some of the limitations of NBO analysis, and how caution should be used when interpreting results. While Table 4.2 shows that, in general, little change in the partial charge of the metal is observed upon redox, this may not actually be the case. Using Fe-N_{2p}/C_g and Co-N_{2p}/C_g as an example, one would expect that given the similarities in the change in partial charge of the equatorial carbon support, axial ligand and metal centre, these two active sites would have very similar redox potentials. However, the Co-centred analogue of this active site is seen to have a redox potential almost 0.2 V lower than the Fe-centred active site, an observation that is difficult to explain without considering the influence of the metal centre.

NBO analysis attempts to confine electrons to simple bonding and non-bonding orbitals to allow for a simpler analysis of how bonds are formed and from where they originate, but in reality two electrons occupying a single bond do not stay within this well described orbital. Indeed orbital crossover allows for these electrons to occupy a much more complex molecular orbital consisting of many overlapping bonding and non-bonding orbitals. Thus while partial charges indicate that the majority of an electrons charge is soaked up by the equatorial carbon support upon redox, the molecular orbital that stems from the addition of this electron interacts with the atomic orbitals of the central metal and the extent of this crossover differs between N_2/C structural isomers.

Simply put, an electrons influence is felt across the entire molecule and one should not treat partial charges as being an exact description of an electrons location, merely an indication of where this charge would originate. It is little surprise therefore, that an additional electron on any of the active sites would be attributed to the surrounding carbon structure as this is the conductive support that electrically connects the active sites to the anode. The limitations of NBO analysis are covered in more detail in Section 5.3.1.

To truly ascertain how the isomerism of N_2/C active sites, and the nature of the central metal, affects the redox potential, one must thus look at how charge density changes across all molecular orbitals, not just a single NBO. This presents some difficulty as hundreds of distinct molecular orbitals exists for each active site which differ in energy, formal electron occupation and atomic and NBO makeup; attempting to present each and find trends between each is an exercise in futility. Instead one should attempt to see how electron density changes across the entire molecule, considering all molecular orbitals simultaneously. This is much simpler as Gaussian allows for the mapping of charge density for an entire molecule as default. On its own the charge density typically presents itself as a 'blob' that encompasses the entire system. However, by mapping this charge density for both the +3 and +2 states of the active site, and subtracting one from the other, one is able to ascertain how the electron density changes at every point within the system upon the addition of a single electron to the +3 state of the active site. Furthermore, by mapping the electrostatic potential, ESP, of the system onto this change in charge density, one is able to find where this change is most significant. Figure 4.4 shows this process for the $Co-N_{2p}/C_g$ active site, while Figure 4.5 shows the ESP mapped as a function of the change in charge density for the basal plane active sites.

As can be seen from Figure 4.5 the lower redox potentials exhibited by both the N_4/C_g active sites are clearly due to the lack of significant overlap between the N- centric orbitals and the metal centre. Conversely the higher redox potentials of the

Co^{III}-N$_{2p}$/C$_g$ charge density

Co^{II}-N$_{2p}$/C$_g$ charge density
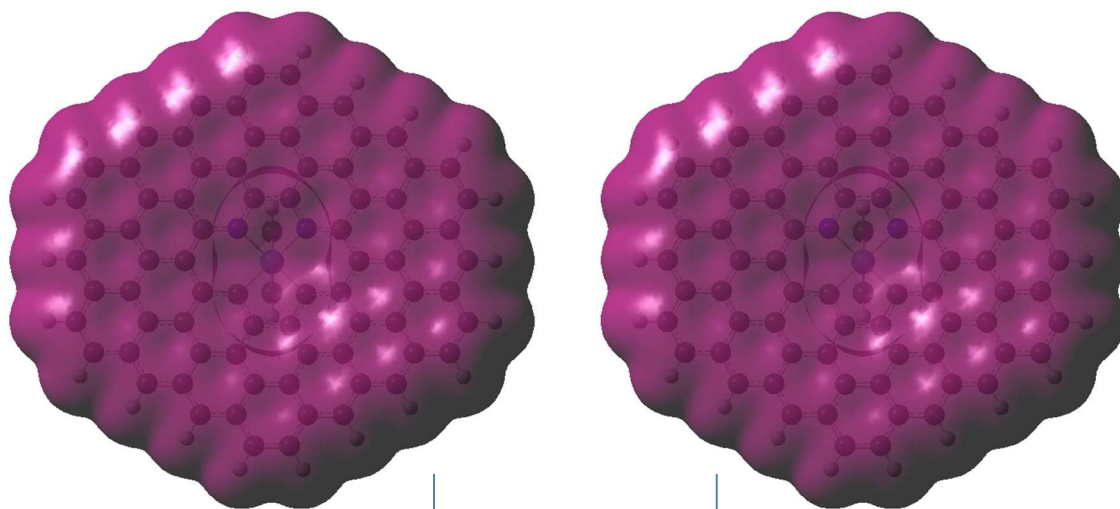
The difference between the two charge densities is then calculated. Turquoise areas indicate areas of decreasing charge density while purple areas indicate areas of increasing charge density.
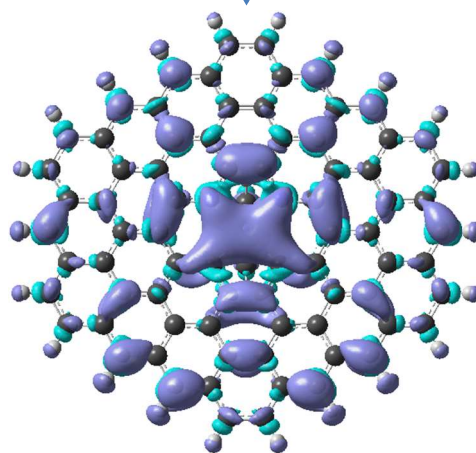
Onto this the electrostatic potential is mapped. Dark blue areas indicate areas of lower electron density, red areas indicate areas of higher electron density. One can thus observe that the areas of increased electron occupation are the areas where N and C orbitals overlap with the metal centre.
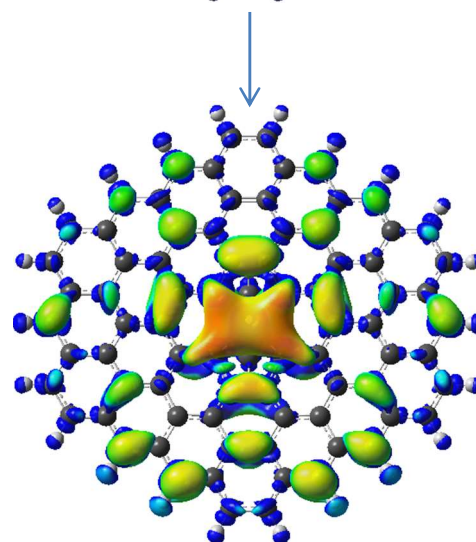
Figure 4.4 - How electrostatic potential is mapped as a function of the change in charge density during a redox reaction.

Fe-N₄ E⁰ = 0.592 V

Co-N₄ E⁰ = 0.689 V

Fe-N₂ₚ E⁰ = 1.323 V

Co-N₂ₚ E⁰ = 1.135 V

Fe-N₂ₕ E⁰ = 0.890 V

Co-N₂ₕ E⁰ = 1.100 V

Fe-N₂ₜ E⁰ = 0.896 V

Co-N₂ₜ E⁰ = 1.125 V
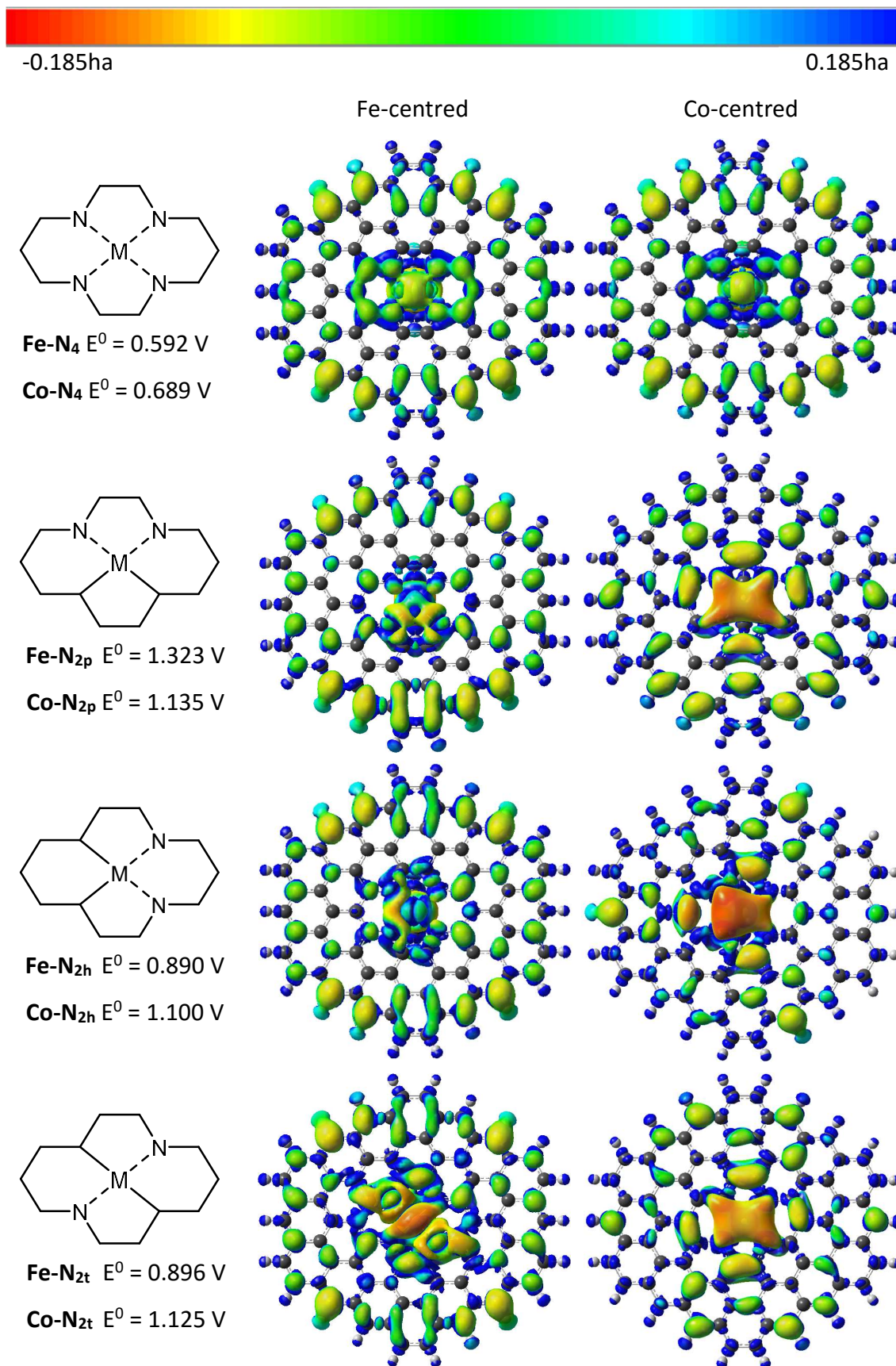
Figure 4.5 - ESP mapped as a function of the change in charge density during +2/+3 redox for each graphene-embedded active site under investigation.

N_2/C_g active sites are due to the overlap of carbon-centric orbitals, for both Fe- and Co-centred active sites, and N-centric orbitals, for Co-centred active sites, with those of the central metal. This overlap appears smoother for the Co-N_2/C_g active sites than the Fe-N_2/C_g analogues due to the lack of spin transition between the +3 and +2 states.

Formally spin transitions are forbidden; as stated in Section 2.3.1 an electron has four quantum numbers that describe it and changing any of these requires an input of free energy, thus the spontaneous inversion of an electrons spin (i.e. from α to ß) is not feasible. However, when comparing the optimised geometries of the +3 and +2 states of each active sites it is noted that the out-of-plane distortion of the Co and Fe centres differ. It is postulated that this structural change could elicit a shift in theorbital configuration of the central metal. For the Co-centred active sites this shift in orbital configuration does not affect the lowest spin state, with both +2 and +3 states being low-spin, but for the Fe-centred active sites it is found that the +3 state favourably adopts a low-spin configuration while the +2 state is high-spin. This shift in spin state means that there is a more significant re-organisation of α and ß electrons for the Fe-centred active sites than the Co-centred sites, which is reflected by the more convoluted ESP on charge density maps around the metal centre for the Fe-centred active sites in Figure 4.5.

As with the graphene-centric active sites the redox potentials of the M-N_x/C_a active sites are linked to the crossover of carbon- and nitrogen-centric orbitals with the metal centre. Figure 4.6 shows the electrostatic potential mapped as a function of the change in charge density for these amorphous carbon active sites. As with those active sites presented in Figure 4.5 it is quite apparent that the crossover of orbitals originating from carbon and nitrogen atoms with those of the central metal is necessary to achieve high redox potentials. This crossover is observed for all but Co-N_{2h}/C_a and Co-N_{2t}/C_a, which are found to have the lowest redox potentials of all the active sites modelled. The inability of these two active sites to reach higher potentials is postulated to be due, at least in part, to the increased area of the central moiety. If one were to remove the central metal from each of the active sites and calculate the area of the 'hole' left behind, one notes that the metals within the amorphous active

Fe-N₄ $E_0 = 0.406$ V

Co-N₄ $E_0 = 0.732$ V

Fe-N₂ₚ $E_0 = 0.896$ V

Co-N₂ₚ $E_0 = 0.696$ V

Fe-N₂ₕ $E_0 = 0.508$ V

Co-N₂ₕ $E_0 = 0.340$ V

Fe-N₂ₜ $E_0 = 0.780$ V

Co-N₂ₜ $E_0 = 0.308$ V
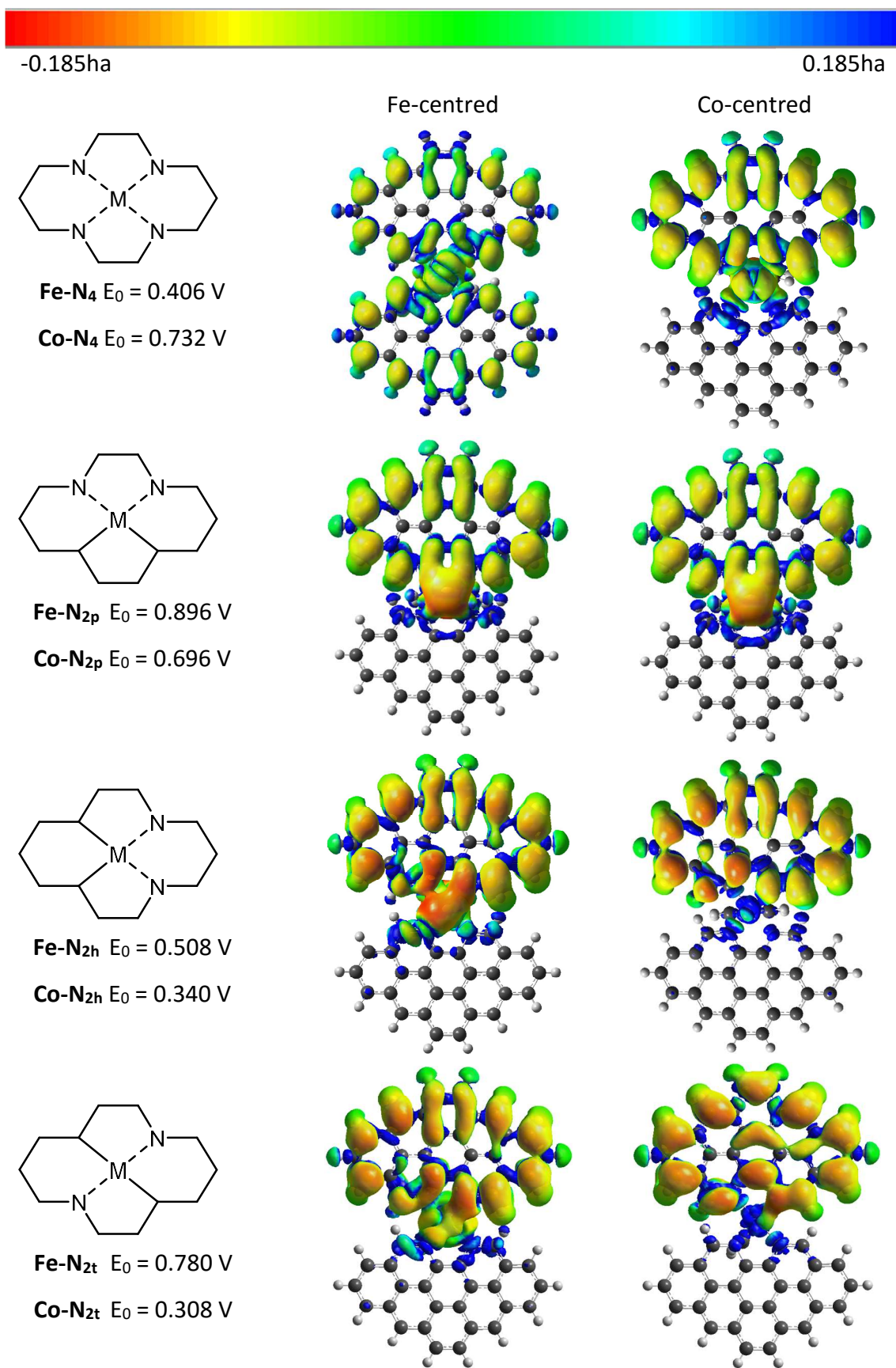
Figure 4.6 - ESP mapped as a function of the change in charge density for each edge plane active site under investigation.

sites are contained within notably larger areas than in the graphene analogues. Of these holes, those for the N_{2h}/C_a and N_{2t}/C_a active sites are markedly larger than those of N_{2p}/C_a and N_4/C_a. As it is known that the ionic radius of cobalt is smaller than that of iron, it could be postulated that, within the Co-N_{2h}/C_a and Co-N_{2t}/C_a active sites, the additional electronic charge introduced to the system during the redox reaction is simply not able to overlap with the central metal, resulting in a low redox potential, this hypothesis is explored in greater detail in Section 5.1.1.

It is also interesting to note the differences in how the N_x/C_g and N_x/C_a active sites are able to stabilise the additional electronic charge transferred during the redox reaction. By comparing the results shown in Figures 4.5 and 4.6, one notes that with the exception of Fe-N_4/C_a, all the amorphous active sites stabilise the additional electronic charge on one equatorial fragment alone. Conversely the increased interaction between the central metal and the carbon structure of the graphene-like active sites means that charge is more evenly distributed around the equatorial ligand, and that the charge density on the carbon support is considerably lower than in the amorphous active sites. It is hypothesised that this increased charge density could have repercussions on the efficacy with which these amorphous active sites are able to catalyse the ORR.

4.4 - Preferred pathways

4.4.1 - Displacement of water and peroxide by O₂

Regardless of the ORR mechanism, it is essential that the displacement of the reduction products by O_2 is promoted to allow turnover of the active site. Table 4.3 gives the Gibbs free energy change for the displacement of both peroxide and water by O_2 on each of the active sites investigated. From this it can be seen that these displacement reactions are exergonic on all active sites, though these displacement reactions are more exergonic on amorphous active sites than their grapheme counterparts.

The optimised geometries of both $2H_2O_{(ads)}$ and H_2O_2 $_{(ads)}$ on each of the catalysts also show that neither of these two products have any significant interaction with the

Table 4.3 – Gibbs free energy change (kJmol^{-1}) for the displacement of peroxide and water by O$_2$ on the 16 M-N$_x$/C active sites investigated.

	H$_2$O$_2$ displacement		2H$_2$O displacement	
	C$_g$	C$_a$	C$_g$	C$_a$
Fe-N$_4$	-35.043	-125.263	-32.291	-68.342
Co-N$_4$	-20.379	-114.023	-25.848	-109.927
Fe-N$_{2h}$	-37.272	-127.234	-37.387	-111.032
Co-N$_{2h}$	-53.185	-139.041	-47.863	-132.774
Fe-N$_{2t}$	-44.037	-111.332	-61.796	-109.37
Co-N$_{2t}$	-64.729	-134.342	-78.579	-131.53
Fe-N$_{2p}$	-48.482	-91.273	-65.081	-96.248
Co-N$_{2p}$	-60.757	-78.438	-44.283	-111.34

surface beyond weak van der Waals interactions between hydrogen atoms of the products, and the nitrogen atoms surrounding the metal centre. This infers that, should the formation of peroxide be favoured by any of the catalysts, it will be displaced from the surface by O$_2$ and not undergo any further reduction.

4.4.2 - N$_4$/C active sites

The Gibbs free energy change for each of the elementary reduction reactions on all four N$_4$/C active sites are shown in Table 4.4, alongside the reversible potentials for each elementary reaction.

4.4.2.1- First electron transfer reactions

From the optimised geometries, and the data presented in Table 4.4, it can be determined that the reduction of O$_{2(ads)}$ to OOH$_{(ads)}$ dominates up to the reversible potential of this reaction for all catalysts, due to the end-on adsorption of O$_2$. As this mode of adsorption results in a δ$^-$ charge on a terminal oxygen atom, and given the acidic nature of a PEM fuel cell, it is thought unlikely that any other reaction would be competitive while the protonation reaction is entropically favoured. The graphene-like active sites, Fe-N$_4$/C$_g$ and Co-N$_4$/C$_g$, are able to reduce O$_2$ at higher potentials than their amorphous counterparts, with reversible potentials of 0.661 V and 0.772 V respectively, compared to reversible potentials of 0.410 V for Fe-N$_4$/C$_a$ and 0.473 V for Co-N$_4$/C$_a$.

Table 4.4 - Gibbs free energy changes for each N_4/C catalysed reduction reaction and the reversible potentials of those electron transfer reactions.

	Fe-N$_4$/C$_g$		Fe-N$_4$/C$_a$		Co-N$_4$/C$_g$		Co-N$_4$/C$_a$	
	ΔG (kJmol^{-1})	E^0 (eV)	ΔG (kJmol^{-1})	E^0 (eV)	ΔG (kJmol^{-1})	E^0 (eV)	ΔG (kJmol^{-1})	E^0 (eV)
$O_2 \rightleftharpoons 2O$	-16.131		-61.993		90.144		-8.879	
$O_2 + H^+ + e^- \rightleftharpoons OOH$	-63.800	0.661	-39.600	0.410	-74.449	0.772	-45.621	0.473
$2O + H^+ + e^- \rightleftharpoons OH_{(m)} + O_{(c)}$	-72.611	0.753	-60.392	0.626	-207.756	2.153	-119.631	1.240
$2O + H^+ + e^- \rightleftharpoons O_{(m)} + OH_{(c)}$	-28.279	0.293	-49.604	0.514	-15.832	0.164	-54.091	0.561
$OOH_{(m)} \rightleftharpoons O_{(m)} + OH_{(c)}$	19.389		-71.996		148.761		-17.349	
$O_{(m)} + OH_{(c)} \rightleftharpoons OH_{(m)} + O_{(c)}$	-44.332		-10.788		-191.924		-65.540	
$OOH_{(m)} + H^+ + e^- \rightleftharpoons H_2O_{2\ (m)}$	-35.289	0.366	30.731	-0.319	-39.304	0.407	25.512	-0.264
$O_{(m)} + OH_{(c)} + H^+ + e^- \rightleftharpoons 2OH_{(m+c)}$	-77.106	0.799	-27.316	0.283	-253.859	2.631	-125.118	1.297
$O_{(m)} + OH_{(c)} + H^+ + e^- \rightleftharpoons O_{(m)} + H_2O_{(c)}$	-184.727	1.915	-119.392	1.237	-276.623	2.867	-109.544	1.135
$OH_{(m)} + O_{(c)} + H^+ + e^- \rightleftharpoons 2OH_{(m+c)}$	-32.774	0.340	-16.528	0.171	-61.936	0.642	-59.578	0.617
$OH_{(m)} + O_{(c)} + H^+ + e^- \rightleftharpoons H_2O_{(m)} + O_{(c)}$	-137.623	1.426	-141.401	1.466	-121.456	1.259	-132.013	1.368
$H_2O_{(m)} + O_{(c)} \rightleftharpoons O_{(m)} + H_2O_{(c)}$	-2.773		32.798		36.757		88.009	
$H_2O_{(m)} + O_{(c)} + H^+ + e^- \rightleftharpoons H_2O_{(m)} + OH_{(c)}$	-274.940	2.850	-56.296	0.583	-297.338	3.082	18.510	-0.192
$O_{(m)} + H_2O_{(c)} + H^+ + e^- \rightleftharpoons OH_{(m)} + H_2O_{(c)}$	-156.645	1.624	-143.680	1.489	-202.820	2.102	-204.020	2.115
$2OH + H^+ + e^- \rightleftharpoons OH_{(m)} + H_2O_{(c)}$	-264.267	2.739	-235.757	2.443	-225.583	2.338	-188.445	1.953
$2OH + H^+ + e^- \rightleftharpoons H_2O_{(m)} + OH_{(c)}$	-379.789	3.936	-181.170	1.878	-356.858	3.699	-53.925	0.559
$H_2O_{(m)} + OH_{(c)} \rightleftharpoons OH_{(m)} + H_2O_{(c)}$	115.522		-54.587		131.275		-134.520	
$H_2O_{(m)} + OH_{(c)} + H^+ + e^- \rightleftharpoons 2H_2O$	59.244	-0.614	-85.927	0.891	87.902	-0.911	-122.411	1.269
$OH_{(m)} + H_2O_{(c)} + H^+ + e^- \rightleftharpoons 2H_2O$	-56.278	0.583	-31.341	0.325	-43.373	0.450	12.109	-0.125

While the protonation reaction is thought to dominate up to the reversible potential, it is feasible that the dissociation reaction is viable at potentials above this for all but Co-N_4/C_g. Should this dissociation reaction become viable, either of the two oxygen atoms may reduce as the ESP-on-density maps shown in Figure 4.7 indicate that both oxygen atoms have comparable reactivity. However it is thought that the more exergonic of the two competing reactions would be favoured, given the inferred entropic loss associated, which in all cases results in the formation of a metal co-ordinated OH. For the Fe-N_4/C active sites this means that it is entirely plausible for the first electron reduction reaction to proceed up to 0.753 V and 0.626 V dependent pathways, with the direct protonation of $O_{2(ads)}$ dominant at lower potentials, and a dissociation reaction followed by a protonation reaction becoming more viable with increasing potential.

This potential dependency is also thought to occur for the reduction of $O_{2(ads)}$ on Co-N_4/C_a, though the maximum potential that could be achieved is much higher, as this active site is able to catalyse the reduction of $2O_{(ads)}$ up to 1.24 V. Conversely, Co-N_4/C_g is not able to catalyse the dissociation of O_2 and so only one pathway is viable for the first electron transfer on this site; the direct protonation resulting in $OOH_{(ads)}$. While this is unable to match Co-N_4/C_a with regards to maximum potential, it is still slightly higher than either of the Fe-centred active sites, and not considerably lower than that of Pt/C, which catalyses the reduction of $O_{2(ads)}$ up to 0.844 V, as reported in Section 3.2.2.1. Thus each active site is able to at least catalyse the first electron transfer reaction, though the pathway via which each does so is found to be potential dependant.

4.4.2.2- Second electron transfer reactions

Neither of the two N_4/C_g active sites are able to promote the dissociation of $OOH_{(ads)}$, thus the reduction to peroxide is favoured. For Co-N_4/C_g, this therefore means that it is only capable of reducing $O_{2(ads)}$ directly to peroxide, as no dissociation pathway is favoured and the replacement of peroxide by O_2 is favoured as evidenced by the data given in Table 4.4. While it is thermodynamically feasible that peroxide is reduced further via a 2+2 e$^-$ pathway, this is not thought to be viable, as the peroxide

Fe-N$_4$/C$_g$

Fe-N$_4$/C$_a$ Co-N$_4$/C$_a$
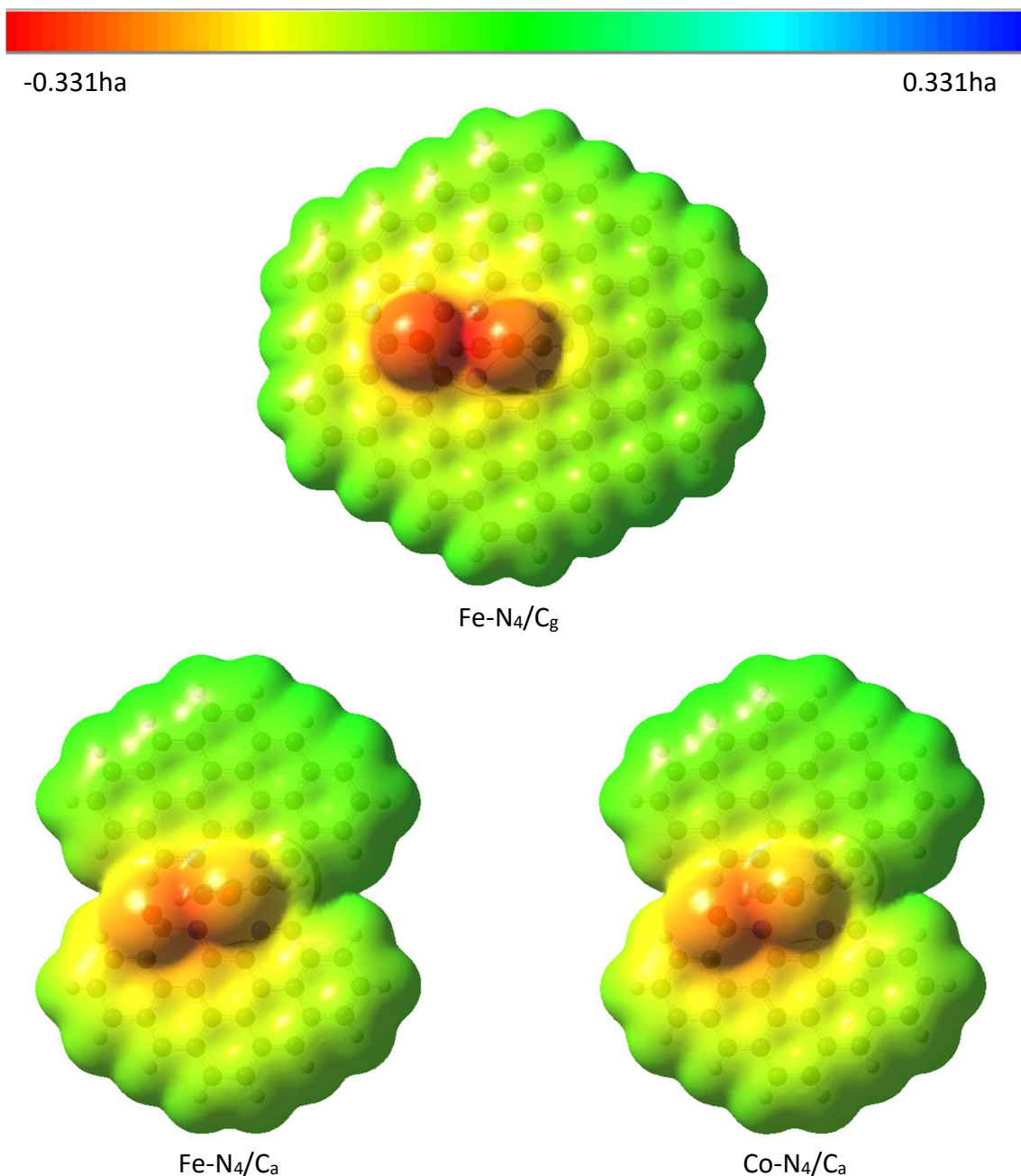
Figure 4.7 - ESP-on-density maps of 2O$_{(ads)}$ on those N$_4$/C active sites capable of dissociating O$_{2(ads)}$.

exhibits no interaction with the surface, save for weak van der Waals interaction. Thus this final one-electron reduction reaction becomes potential limiting, meaning that this Co-N$_4$/C$_g$ is only capable of achieving reduction potentials of 0.407 V, following the undesirable peroxide pathway. It is therefore not felt that this active site is a viable candidate for use within PEM fuel cells. This is also thought to be the case for Fe-N$_4$/C$_g$; the formation of OOH$_{(ads)}$ is promoted up to potentials of 0.661 V while its reduction is

only favoured up to 0.366 V. Thus above 0.366 V, OOH$_{(ads)}$ forms and cannot be subsequently reduced resulting in active site blocking, despite the ability of Fe-N$_4$/C$_g$ to promote the dissociation of O$_{2(ads)}$.

From Table 4.4 it can also be seen that both amorphous active sites promote the dissociation of OOH$_{(ads)}$, resulting in a metal co-ordinated O$_{(ads)}$ and an OH$_{(ads)}$ located on the carbon support, over the formation of peroxide which is endergonic for both N$_4$/C$_a$ active sites. These sites are able to promote the selective dissociation of OOH$_{(ads)}$ due to the high back-bonding interactions causing significant elongation of the O-OH bond while strengthening the metal-oxygen bond. This is further supported by bond strength calculations indicating the lower energy of the O-OH bonds compared to the metal-oxygen bonds.

In both instances it is found that the hydrogen atom of the carbon-bound OH$_{(ads)}$ is directed away from the metal-coordinated O$_{(ads)}$, implying that while the transfer of this hydrogen is thermodynamically feasible, there would be an associated activation barrier due to steric hindrance resulting from the rotation of the OH$_{(ads)}$ group to allow such a transfer. Coupled with this, ESP on density maps show that the partial charge on the metal-coordinated O$_{(ads)}$ is of significantly higher energy than that of the OH$_{(ads)}$ located on the carbon support, as shown in Figure 4.8, implying that the protonation of this metal-bound oxygen would be heavily favoured up to the limiting potential of this reaction.

For Fe-N$_4$/C$_a$ the protonation of [O$_{(m)}$ + OH$_{(c)}$] to 2OH$_{(ads)}$ has a very low reversible potential of 0.283 V due to the extremely strong Fe-O double bond. The alternative reaction, resulting in the protonation of the carbon-bound OH is more thermodynamically favoured with a reversible potential of 1.237 V, though given the comparatively lower energy of the charge density on this OH$_{(ads)}$ group it is expected that this reaction would have a more significant activation energy, resulting in a much slower reaction and thus a significant kinetic loss (which would correlate to lower current). Were this reversible potential higher than the one-electron reduction potential of O$_2$ (which forces the reduction reaction to follow this particular pathway), this would not be a significant issue as the formation of [O$_{(m)}$ + OH$_{(c)}$] would cease
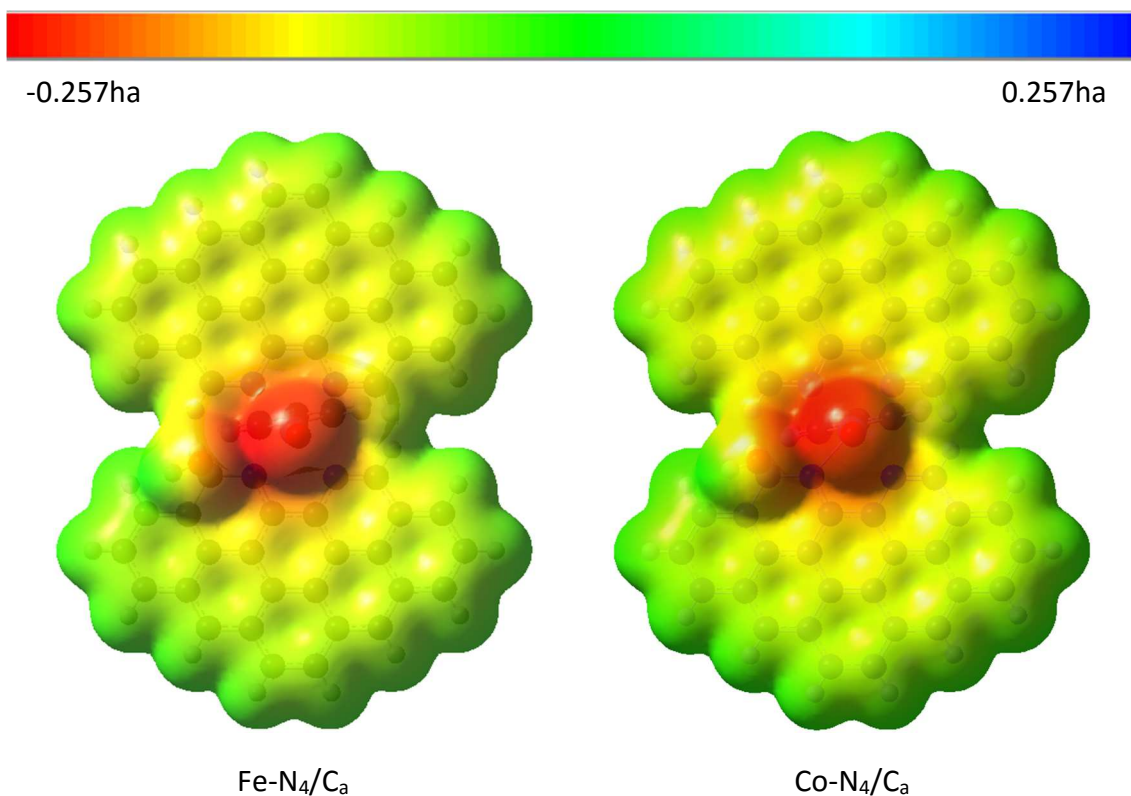
Figure 4.8 - ESP on density maps of [$O_{(m)}$ + $OH_{(c)}$] on Co- and Fe-N_4/C_a active sites.

before the reduction of the metal-bound O became thermodynamically unfeasible. As this is not the case it is proposed that the formation of metal-bound $O_{(ads)}$ could block the active site, resulting in a cessation of catalytic activity. As previously stated, the transfer of a proton from the carbon-bound OH to the metal bound O is thought to have a significant activation barrier, though given the low ESP on the $OH_{(c)}$, it is plausible that this barrier is lower than that of the protonation reaction. Thus if Fe-N_4/C_a is capable of reducing to $2H_2O$, it must do so at lower potentials via the dissociation of $OOH_{(ads)}$, followed by the proton transfer from $OH_{(c)}$ to $O_{(m)}$, resulting in [$OH_{(m)}$ + $O_{(c)}$] which subsequently reduces to either $2OH_{(ads)}$ at potentials below 0.171 V, or [$H_2O_{(m)}$ + $O_{(c)}$] up to potentials of 0.410 V, the reversible potential for the formation of $OOH_{(ads)}$.

At higher imposed potentials, where both N_4/C_a active sites promote the dissociation of O_2 and the subsequent protonation resulting in [$OH_{(m)}$ + $O_{(c)}$], the further reduction to [$H_2O_{(m)}$ + $O_{(c)}$] is favoured. For Fe-N_4/C_a this is somewhat obvious, the formation of [$OH_{(m)}$ + $O_{(c)}$] only dominates at potentials above 0.410 V, much higher than the reversible potential of the [$OH_{(m)}$ + $O_{(c)}$ + H^+ + e^-] $\rightleftharpoons$ $2OH_{(ads)}$ reaction, U_{rev} = 0.171 V.

Thus only the reduction of the $OH_{(m)}$ group is thermodynamically feasible, which results in the formation of $[H_2O_{(m)} + O_{(c)}]$.

For Co-N$_4$/C$_a$ it is possible that the formation of $2OH_{(ads)}$ is viable, though at the potential where this pathway becomes viable, 0.473 V, this reaction has a Gibbs free energy change of -13.894 kJmol^{-1}; conversely the reduction to $[H_2O_{(m)} + O_{(c)}]$ is significantly more exergonic, ΔG = -86.356 kJmol^{-1}, and thus it is postulated that both pathways are viable in this small potential range, with the latter becoming favoured as the potential increases to 0.617 V and dominant beyond this up to a maximum potential of 1.240 V, the reversible potential for the reduction of 2O to $[OH_{(m)} + O_{(c)}]$.

4.4.2.3 - Third and fourth electron transfer reactions

As neither of the N$_4$/C$_g$ active sites are deemed to be capable of reducing O$_2$ any further than peroxide, their ability to catalyse the third and fourth electron transfer reactions are not included within this section. From Table 4.4 it can be seen that neither of the two edge-plane active sites favour the disproportionation of $[H_2O_{(m)} + O_{(c)}]$ resulting in one metal- and one carbon-bound OH group.

For Co-N$_4$/C$_a$ the migration of the carbon-bound oxygen of the $[H_2O_{(m)} + O_{(c)}]$ system to the central metal is endergonic, as is the reduction of the $[H_2O_{(m)} + O_{(c)}]$ to $[H_2O_{(m)} + OH_{(c)}]$ and as such further reduction is unlikely at potentials where the formation of $[H_2O_{(m)} + O_{(c)}]$ is dominant, i.e. above 0.617 V. However at potentials below this, the protonation of $[O_{(m)} + OH_{(c)}]$, which results from the formation and dissociation of $OOH_{(ads)}$, to $2OH_{(m+c)}$ is proposed to be favoured (due to the higher ESP on the metal bound oxygen compared to $OH_{(c)}$). This can subsequently be reduced to either $]H_2O_{(m)} + OH_{(c)}]$ up to potentials of 0.559 V and either further reduced to 2H$_2$O within this range, or reduced to $[OH_{(m)} + H_2O_{(c)}]$ up to the limiting potential of 0.617 V, though the subsequent reduction to 2H$_2$O is not feasible and results in blocking of the metal centre by $OH_{(ads)}$.

For Fe-N$_4$/C$_a$ both the migration and the protonation of $[H_2O_{(m)} + O_{(c)}]$ are viable, with Gibbs free energy changes of -32.801 kJmol^{-1} and -56.252 kJmol^{-1} respectively. It is proposed that, in an acidic environment, the protonation reaction would be favoured

up to 0.583 V, after which migration could be feasible. It is uncertain if this migration would occur under fuel cell operating conditions, given the ability of O_2 to displace water from the active site and the availability of the metal centre to bind it. It is instead proposed that the protonation reaction is potential limiting, and that above 0.583 V $OH_{(ads)}$ begins to saturate the carbon support surrounding the metal centre. However, up to 0.583 V the further reduction to $2H_2O$ is favoured and thought to dominate, having a Gibbs free energy change of -85.970 kJmol^{-1}. At potentials where the formation of $[H_2O_{(m)} + O_{(c)}]$ is not favoured, i.e. below 0.283 V, the second electron reduction reaction favours the formation of $2OH_{(m+c)}$. The low potential of this pathway means that any of the third and fourth electron transfer reactions are viable, and complete reduction to $2H_2O$ is favoured.

Though both N_4/C_a active sites are capable of reducing $2OH_{(m+c)}$ via either of the two plausible pathways ESP-on-density maps of the two $2OH_{(m+c)}$ systems implies that the reduction of the metal bound OH group is favoured, as shown in Figure 4.9, thus allowing both active sites to fully catalyse the 4 e$^-$ pathway. However, this complete reduction is only feasible below 0.583 V and 0.559 V, for Fe-N_4/C_a and Co-N_4/C_a respectively.

-0.263ha   0.263ha

Fe-N_4/C_a Co-N_4/C_a
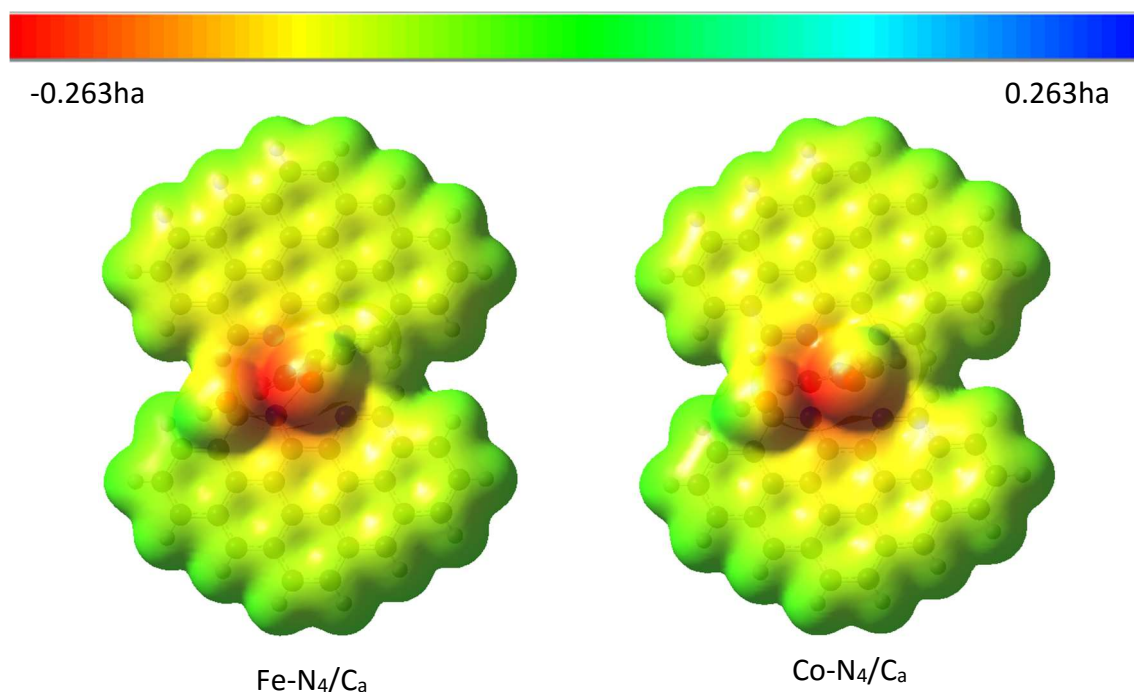
Figure 4.9 - ESP-on-density maps of $2OH_{(m+c)}$ on both N_4/Ca active sites.

4.4.3 - N$_{2h}$/C active sites

The Gibbs free energy change for each of the elementary reduction reactions on all four N$_{2h}$/C active sites are shown in Table 4.5, alongside the reversible potentials for each elementary reaction.

4.4.3.1 - First electron transfer reactions

The reduction of O$_{2(ads)}$ is viable on all active sites with the exception of Fe-N$_{2h}$/C$_a$, on which neither the dissociation nor protonation reaction are thermodynamically viable. That O$_2$ can favourably adsorb to the surface over water and peroxide implies that, unless alternative side reactions are viable, this particular active site will simply adsorb O$_2$ and display no catalytic activity towards its reduction. Fe-N$_{2h}$/C$_g$ and both Co-N$_{2h}$/C active sites are all able to reduce O$_{2(ads)}$ to OOH$_{(ads)}$ albeit at potentials considerably lower than the same reaction on Pt/C. For Co-N$_{2h}$/C$_a$ this reaction becomes potential limiting as it is not capable of catalysing the dissociation of O$_{2(ads)}$ and so at potentials over 0.390 V, O$_{2(ads)}$ would be expected to block the active site and no catalytic activity would be observed. Conversely both graphene active sites are able to favourably dissociate O$_{2(ads)}$, and so at potentials above 0.235 V and 0.435 V, for Fe-N$_{2h}$/C$_g$ and Co-N$_{2h}$/C$_g$ respectively, the first electron transfer reaction is predicted to be the protonation of 2O$_{(ads)}$. For Fe-N$_{2h}$/C$_g$, only one protonation reaction is viable for 2O$_{(ads)}$, which results in [O$_{(m)}$ + OH$_{(c)}$], and this is feasible up to potentials beyond the maximum operating potential of the cell. For Co-N$_{2h}$/C$_g$, both protonation reactions are thermodynamically feasible at 0 V, though at the potential where the dissociation of O$_2$ is likely to become dominant, i.e. above 0.435 V, the reduction of the metal bound oxygen atom is considerable more exergonic and so the formation of [OH$_{(m)}$ + O$_{(c)}$] is postulated to be the dominant first electron reduction reaction.

4.4.3.2 - Second electron transfer reactions

From Table 4.5 it can be concluded that the reduction of OOH$_{(ads)}$ to peroxide is not thermodynamically favoured at any potential for Co-N$_{2h}$/C$_a$, being endergonic by 42.551 kJmol^{-1} at 0 V. Instead it is found that the dissociation of OOH$_{(ads)}$ to [O$_{(m)}$ + OH$_{(c)}$] is promoted, with this reaction having a Gibbs free energy change of -164.413

Table 4.5 - Gibbs free energy changes for each N_{2h}/C catalysed reduction reaction and the reversible potentials of those electron transfer reactions.

	Fe-N_{2h}/C_g		Fe-N_{2h}/C_a		Co-N_{2h}/C_g		Co-N_{2h}/C_a	
	ΔG (kJmol^{-1})	E^0 (eV)	ΔG (kJmol^{-1})	E^0 (eV)	ΔG (kJmol^{-1})	E^0 (eV)	ΔG (kJmol^{-1})	E^0 (eV)
$O_2 \rightleftharpoons 2O$	-181.755		55.773		-112.227		97.143	
$O_2 + H^+ + e^- \rightleftharpoons OOH$	-22.655	0.235	13.167	-0.136	-42.011	0.435	-37.623	0.390
$2O + H^+ + e^- \rightleftharpoons OH_{(m)} + O_{(c)}$	30.314	-0.314	-179.193	1.857	-194.547	2.016	-135.292	1.402
$2O + H^+ + e^- \rightleftharpoons O_{(m)} + OH_{(c)}$	-129.626	1.343	-170.579	1.768	-48.278	0.500	-299.155	3.101
$OOH_{(m)} \rightleftharpoons O_{(m)} + OH_{(c)}$	-288.726		-127.972		-118.494		-164.388	
$O_{(m)} + OH_{(c)} \rightleftharpoons OH_{(m)} + O_{(c)}$	159.940		-8.614		-146.269		163.863	
$OOH_{(m)} + H^+ + e^- \rightleftharpoons H_2O_{2\,(m)}$	-74.204	0.769	-20.064	0.208	-38.936	0.404	42.533	-0.441
$O_{(m)} + OH_{(c)} + H^+ + e^- \rightleftharpoons 2OH_{(m+c)}$	-56.482	0.585	-50.260	0.521	-251.877	2.611	-14.855	0.154
$O_{(m)} + OH_{(c)} + H^+ + e^- \rightleftharpoons O_{(m)} + H_2O_{(c)}$	133.648	-1.385	-57.128	0.592	-22.692	0.235	15.837	-0.164
$OH_{(m)} + O_{(c)} + H^+ + e^- \rightleftharpoons 2OH_{(m+c)}$	-216.423	2.243	-41.646	0.432	-105.608	1.095	-178.718	1.852
$OH_{(m)} + O_{(c)} + H^+ + e^- \rightleftharpoons H_2O_{(m)} + O_{(c)}$	-273.482	2.834	-92.698	0.961	-104.196	1.080	-163.280	1.692
$H_2O_{(m)} + O_{(c)} \rightleftharpoons O_{(m)} + H_2O_{(c)}$	247.191		44.185		227.773		15.254	
$H_2O_{(m)} + O_{(c)} + H^+ + e^- \rightleftharpoons H_2O_{(m)} + OH_{(c)}$	-48.353	0.501	-100.528	1.042	-36.259	0.376	-53.387	0.553
$O_{(m)} + H_2O_{(c)} + H^+ + e^- \rightleftharpoons OH_{(m)} + H_2O_{(c)}$	-174.693	1.811	-45.804	0.475	-192.024	1.990	-186.279	1.931
$2OH + H^+ + e^- \rightleftharpoons OH_{(m)} + H_2O_{(c)}$	15.438	-0.160	-52.673	0.546	37.161	-0.385	-155.587	1.613
$2OH + H^+ + e^- \rightleftharpoons H_2O_{(m)} + OH_{(c)}$	-105.413	1.093	-151.581	1.571	-34.847	0.361	-37.949	0.393
$H_2O_{(m)} + OH_{(c)} \rightleftharpoons OH_{(m)} + H_2O_{(c)}$	120.851		98.908		72.008		-117.638	
$H_2O_{(m)} + OH_{(c)} + H^+ + e^- \rightleftharpoons 2H_2O$	36.313	-0.376	-46.673	0.484	20.740	-0.215	-86.762	0.899
$OH_{(m)} + H_2O_{(c)} + H^+ + e^- \rightleftharpoons 2H_2O$	-84.538	0.876	-145.581	1.509	-51.268	0.531	30.876	-0.320

kJmol^{-1}. Subsequent proton transfer between the carbon-bound OH and the metal-bound oxygen is not promoted; indeed the only thermodynamically viable reaction is the protonation resulting in 2OH$_{(ads)}$, though with a reversible potential of 0.154 V, this reaction likely limits the maximum potential of O$_2$ reduction on this particular active site.

As the first electron transfer reaction is not potential limiting on either of the basal plane active sites, a number of reaction pathways are viable. For Fe-N$_{2h}$/C$_g$, at potentials below 0.235 V, OOH$_{(ads)}$ production is favoured. Within this potential range, OOH$_{(ads)}$ is able to either reduce to peroxide, or dissociate to [O$_{(m)}$ + OH$_{(c)}$] as both reactions remain exergonic. Bond strength calculations show that the Fe-OOH$_{(ads)}$ bond has an energy of 133.640 kJmol^{-1} while the O-OH bond is slightly stronger, having an energy of 144.316 kJmol^{-1}, though this difference is not substantial enough to conclusively state which reaction pathway would be favoured. The ESP-on-density map of OOH$_{(ads)}$ on Fe-N$_{2h}$/C$_g$, as shown in Figure 4.10, shows that protonation is highly likely, due to the high electron density around the metal bound oxygen, thus below 0.235 V it can be concluded that this active site generates peroxide, which is replaced on the active site by O$_2$. Above 0.235 V the dissociation of OOH$_{(ads)}$ is favoured

-0.244ha   0.244ha
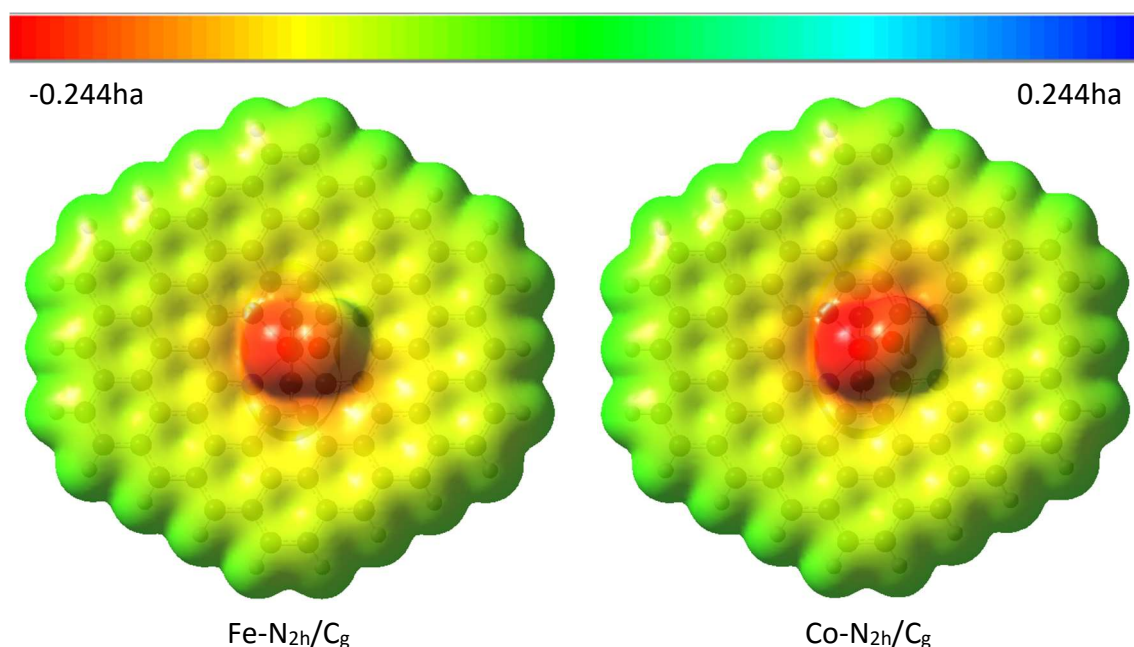
Fe-N$_{2h}$/C$_g$ Co-N$_{2h}$/C$_g$

Figure 4.10 - ESP-on-density maps of OOH$_{(ads)}$ adsorbed on both N$_{2h}$/C$_g$ active sites.

resulting in the formation of [$O_{(m)}$ + $OH_{(c)}$], which can subsequently reduce to $2OH_{(ads)}$ up to potentials of 0.585 V.

As with Fe-N$_{2h}$/C$_g$, Co-N$_{2h}$/C$_g$ is able to catalyse the first electron transfer reaction beyond the maximum operating potential of a PEM fuel cell. Up to potentials of 0.435 V, this active site promotes the formation of $OOH_{(ads)}$, which can itself be reduced to peroxide up to potentials of 0.404 V. As the catalyst is also capable of promoting the dissociation of $OOH_{(ads)}$, [$O_{(m)}$ + $OH_{(c)}$] formation is favoured between these two reversible potentials, i.e. between 0.404 V and 0.435 V. This is subsequently reduced to $2OH_{(ads)}$ as the alternative protonation reaction, the formation of [$O_{(m)}$ + $H_2O_{(c)}$], has a reversible potential below the range at which $OOH_{(ads)}$ would be expected to dissociate. Above 0.435 V, Co-N$_{2h}$/C$_g$ favours the formation of [$OH_{(m)}$ + $O_{(c)}$] as the first electron transfer reaction, which can be reduced to either $2OH_{(ads)}$ of [$H_2O_{(m)}$ + $O_{(c)}$] up to near identical potentials. From the ESP-on-density map shown in Figure 4.11 one can state that these two reactions are likely to be competitive, as no discernible difference between the charge density can be seen between the carbon bound oxygen and the metal bound OH.

-0.244ha   -0.244ha
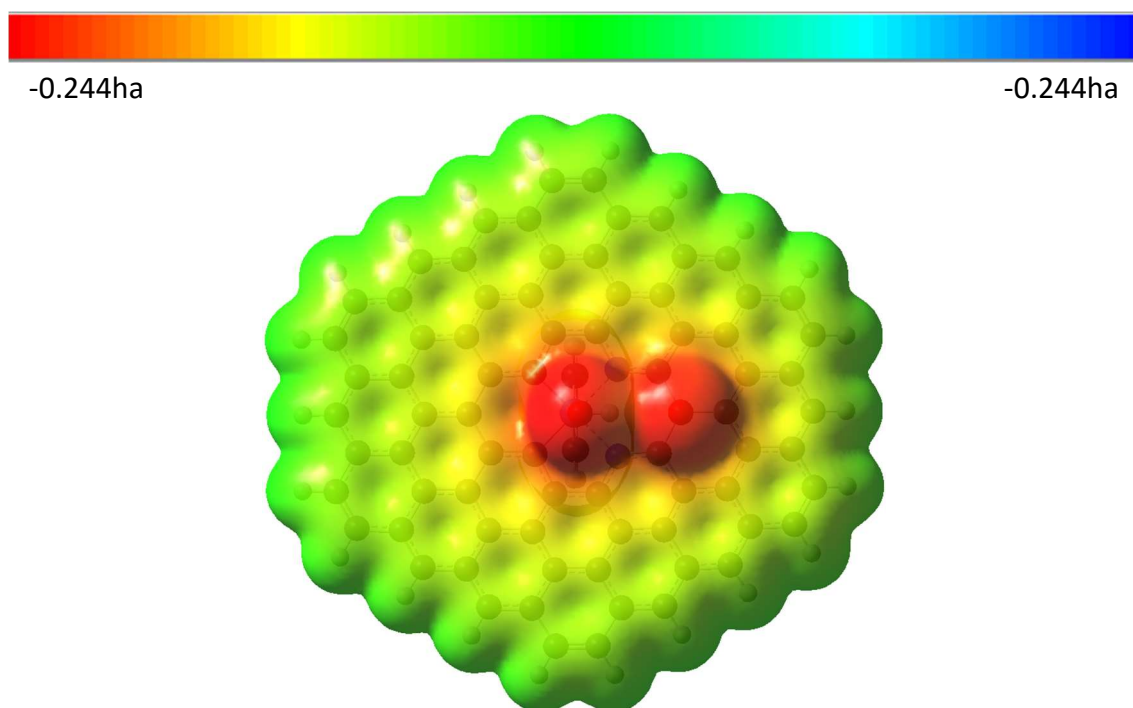
Figure 4.11 - ESP-on-density map of [$OH_{(m)}$ + $O_{(c)}$] on Co-N$_{2h}$/C$_g$.

From these results it can be stated that while both N_{2h}/C_g active sites promote the formation of peroxide, this is only feasible at low potentials; below 0.235 V for Fe- N_{2h}/C_g and below 0.435 V for Co-N_{2h}/C_g. At higher potentials, where the formation of peroxide is not favoured, Fe-N_{2h}/C_g catalyses the formation of $2OH_{(m+c)}$ up to a limiting potential of 0.585 V, while   Co-N_{2h}/C_g. is able to promote the formation of either $2OH_{(m+c)}$ or $[H_2O_{(m)} + O_{(c)}]$, up to potentials of 1.095 V and 1.080 V respectively. While Co-N_{2h}/C_a does not favour the generation of peroxide, it is only capable of reducing O_2 to $2OH_{(m+c)}$ up to a maximum of 0.154 V via the formation and dissociation of $OOH_{(ads)}$.

4.4.3.3 - Third and fourth electron transfer reactions

The reduction of $2OH_{(m+c)}$, as catalysed by Co-N_{2h}/C_g, is selective towards the generation of $[H_2O_{(m)} + OH_{(c)}]$, though only up to 0.361 V. Above this potential neither the reduction of the carbon bound OH, nor the reduction of the metal bound OH, are thermodynamically favoured. Similarly, while the reduction of $[H_2O_{(m)} + O_{(c)}]$ is favourable up to potentials of 0.376 V, this reaction again leads to the formation of $[H_2O_{(m)} + OH_{(c)}]$. Thus even though the third electron transfer reaction is found to be viable, the reversible potential for the removal of the final, carbon-bound, OH is negative and so it's removal from the surface is not favoured within the operating potential of a PEM fuel cell. However, as the metal centre, which is the site for O_2 adsorption, is not blocked up to 0.361-0.376 V, it is plausible that further reduction of O_2 could still be viable, though it is posited that continuous reduction up to 0.376 V would result in an OH saturated carbon support. In much the same way as $OH_{(ads)}$ blocks the platinum surface, as reported in Section 3.2.2.2, it is likely that the reduced availability of a secondary active site would cause a shift in the reduction reaction, possibly favouring peroxide formation.

Fe-N_{2h}/C_g promotes the formation of $2OH_{(m+c)}$ as the product of the second electron transfer reaction up to 0.585 V. The reduction of this intermediate to $[H_2O_{(m)} + OH_{(c)}]$ is thermodynamically favoured in this potential range, though as with Co-N_{2h}/C_g, the subsequent removal of carbon-bound OH is not favoured within the operating potential range of a PEM fuel cell.

Co-N_{2h}/C_a is capable of reducing $2OH_{(m+c)}$ in the potential range that the formation of $2OH_{(m+c)}$ can be formed, 0-0.154 V. The large difference in the Gibbs free energy of these two reactions implies that the reduction to $[OH_{(m)} + H_2O_{(c)}]$ is likely favoured, though this cannot be further reduced due to the endergonic nature of the final electron transfer reaction. As this reduction product blocks the metal at the centre of the active site, it is felt that this final reduction reaction serves to prevent this particular moiety from contributing towards the reduction of O_2.

4.4.4 - N_{2t}/C active sites

The changes in Gibbs free energy for the elementary reduction reactions, as catalysed by all four N_{2t}/C active sites, are shown in Table 4.6.

4.4.4.1 - First electron transfer reactions

The one electron reduction potentials of O_2 are found to be very low for all N_{2t}/C active sites, with the Fe-centred N_{2t}/C active sites capable only of catalysing this reaction up to 0.183 V and 0.170 V for the graphene and amorphous carbon analogues respectively. As with the other N_2/C active sites this is found to be due to the poor electron transfer to the adsorbed OOH during this electron transfer reaction, with the majority of incumbent charge stabilised by the carbon support. None of the four active sites are capable of catalysing the dissociation of $O_{2(ads)}$ leading to the conclusion that the first electron transfer reaction, resulting in the formation of $OOH_{(ads)}$, is potential limiting. This means that the maximum potential at which complete 4 e^- reduction of O_2 is possible is 0.183 V, 0.170 V, 0.308 V and 0.407 V for Fe-N_{2t}/C_g, Fe-N_{2t}/C_a, Co-N_{2t}/C_g and Co-N_{2t}/C_a respectively.

4.4.4.2 - Second electron transfer reactions

As can be seen from Table 4.6, the reduction of $OOH_{(ads)}$ to $HOOH_{(ads)}$ is thermodynamically viable beyond the point at which O_2 can be reduced on both the N_{2t}/C_g active sites. While both of these graphene active sites are able to catalyse the dissociation of $OOH_{(ads)}$, the viability of this pathway is not clear. Certainly for Fe-N_{2t}/C_g the substantially more exergonic nature of the protonation reaction when compared to the dissociation, even at the limiting potential for the reduction of $O_{2(ads)}$ (0.183 V), would imply that this pathway dominates. However, while the protonation reaction

Table 4.6 - Gibbs free energy changes for each N_{2t}/C catalysed reduction reaction and the reversible potentials of those electron transfer reactions.

	Fe-N$_{2t}$/C$_g$		Fe-N$_{2t}$/C$_a$		Co-N$_{2t}$/C$_g$		Co-N$_{2t}$/C$_a$	
	ΔG (kJmol^{-1})	E^0 (eV)	ΔG (kJmol^{-1})	E^0 (eV)	ΔG (kJmol^{-1})	E^0 (eV)	ΔG (kJmol^{-1})	E^0 (eV)
O$_2$ ⇌ 2O	196.543		46.135		206.874		134.846	
O$_2$ + H$^+$ + e$^-$ ⇌ OOH	-17.696	0.183	-16.428	0.170	-29.689	0.308	-39.272	0.407
2O + H$^+$ + e$^-$ ⇌ OH$_{(m)}$ + O$_{(c)}$	-244.884	2.538	-83.058	0.861	-186.161	1.929	-206.406	2.139
2O + H$^+$ + e$^-$ ⇌ O$_{(m)}$ + OH$_{(c)}$	-225.723	2.339	-112.232	1.163	-394.069	4.084	-206.406	2.139
OOH$_{(m)}$ ⇌ O$_{(m)}$ + OH$_{(c)}$	-11.484		-49.669		-157.506		-32.288	
O$_{(m)}$ + OH$_{(c)}$ ⇌ OH$_{(m)}$ + O$_{(c)}$	-19.161		29.175		207.908		N/A	
OOH$_{(m)}$ + H$^+$ + e$^-$ ⇌ H$_2$O$_2$ $_{(m)}$	-72.398	0.750	-6.372	0.066	-39.713	0.412	39.482	-0.409
O$_{(m)}$ + OH$_{(c)}$ + H$^+$ + e$^-$ ⇌ 2OH$_{(m+c)}$	-97.514	1.011	-84.699	0.878	44.169	-0.458	-107.987	1.119
O$_{(m)}$ + OH$_{(c)}$ + H$^+$ + e$^-$ ⇌ O$_{(m)}$ + H$_2$O$_{(c)}$	-154.516	1.601	-157.039	1.628	4.731	-0.049	-122.220	1.267
OH$_{(m)}$ + O$_{(c)}$ + H$^+$ + e$^-$ ⇌ 2OH$_{(m+c)}$	-78.353	0.812	-113.873	1.180	-163.739	1.697	-107.987	1.119
OH$_{(m)}$ + O$_{(c)}$ + H$^+$ + e$^-$ ⇌ H$_2$O$_{(m)}$ + O$_{(c)}$	-154.251	1.599	-111.631	1.157	-193.400	2.004	-76.670	0.795
H$_2$O$_{(m)}$ + O$_{(c)}$ ⇌ O$_{(m)}$ + H$_2$O$_{(c)}$	18.896		-74.583		-9.777		-45.550	
H$_2$O$_{(m)}$ + O$_{(c)}$ + H$^+$ + e$^-$ ⇌ H$_2$O$_{(m)}$ + OH$_{(c)}$	-92.704	0.961	-69.597	0.721	-72.054	0.747	-42.523	0.441
O$_{(m)}$ + H$_2$O$_{(c)}$ + H$^+$ + e$^-$ ⇌ OH$_{(m)}$ + H$_2$O$_{(c)}$	-157.449	1.632	-123.238	1.277	-176.964	1.834	-173.398	1.797
2OH + H$^+$ + e$^-$ ⇌ OH$_{(m)}$ + H$_2$O$_{(c)}$	-214.451	2.223	-195.579	2.027	-216.402	2.243	-187.631	1.945
2OH + H$^+$ + e$^-$ ⇌ H$_2$O$_{(m)}$ + OH$_{(c)}$	-168.602	1.747	-67.355	0.698	-101.714	1.054	-11.206	0.116
H$_2$O$_{(m)}$ + OH$_{(c)}$ ⇌ OH$_{(m)}$ + H$_2$O$_{(c)}$	-45.849		-128.224		-114.687		-176.426	
H$_2$O$_{(m)}$ + OH$_{(c)}$ + H$^+$ + e$^-$ ⇌ 2H$_2$O	-117.260	1.215	-146.831	1.522	-151.032	1.565	-152.069	1.576
OH$_{(m)}$ + H$_2$O$_{(c)}$ + H$^+$ + e$^-$ ⇌ 2H$_2$O	-71.411	0.740	-18.607	0.193	-36.345	0.377	24.357	-0.252

has a more negative Gibbs free energy change associated with it on the Co-N$_{2t}$/C$_g$ active site, it is somewhat comparable to the Gibbs free energy change for the dissociation reaction, -39.753 kJmol^{-1} vs. -37.051 kJmol^{-1} respectively. However, by comparing the Co-O and O-O bond strengths of OOH$_{(ads)}$ for this active site one finds a substantial difference, with values of 133.264 kJmol^{-1} and 171.777 kJmol^{-1} respectively. These results imply, therefore, that the barrier for the dissociation reaction would be somewhat higher than the barrier for protonation and so it can be concluded with relative confidence that both Fe-N$_{2t}$/C$_g$ and Co-N$_{2t}$/C$_g$ are only able to catalyse the 2 e$^-$ reduction of O$_2$ to HOOH.

From Table 4.6 it can also be seen that both of the amorphous active sites are able to catalyse the dissociation of OOH$_{(ads)}$. For Co-N$_{2t}$/C$_a$ it was found that [O$_{(m)}$ + OH$_{(c)}$] was not a stable intermediate, and while attempts were made to place restrictions on the system during optimisation to enforce this geometry no stable structure was found. Indeed during all successful optimisations, the proton quickly transitioned to the metal bound oxygen, resulting in [OH$_{(m)}$ + O$_{(c)}$]. As this active site is also unable to catalyse the reduction of OOH$_{(ads)}$ to HOOH$_{(ads)}$, it is felt that this dissociation/proton transfer reaction dominates, though it is postulated that the barrier for this dual reaction would be relatively high, given the somewhat extensive reorganisation of both the carbon structure and the adsorbed intermediates required. Fe-N$_{2t}$/C$_a$ is able to catalyse the protonation of OOH$_{(ads)}$, though as this reaction has a very small negative Gibbs free energy change, and given the weaker O-O bond compared to the Fe-O bond, 175.922 kJmol^{-1} and 206.776 kJmol^{-1} respectively, it is likely that the dissociation reaction, resulting in [O$_{(m)}$ + OH$_{(c)}$] is favoured.

Both the N$_{2t}$/C$_a$ active sites are capable of reducing the products of the dissociation of OOH$_{(ads)}$ up to their respective limiting potentials; 0.170 V and 0.407 V for Fe-N$_{2t}$/C$_a$ and Co-N$_{2t}$/C$_a$ respectively. Figure 4.12 shows the ESP-on-density maps of the products of OOH$_{(ads)}$ dissociation on these two active sites and from this it is apparent that the ESP is higher on the adsorbed oxygen (regardless of where it is bound) than on the OH$_{(ads)}$. At the limiting potential for these active sites, both the respective protonation reactions are thermodynamically favoured, though given the higher electrostatic potential on the adsorbed oxygen it is felt that the formation of

Fe-N$_{2t}$/C$_a$-[O$_{(m)}$ + OH$_{(c)}$]   Co-N$_{2t}$/C$_a$-[OH$_{(m)}$ + O$_{(c)}$]
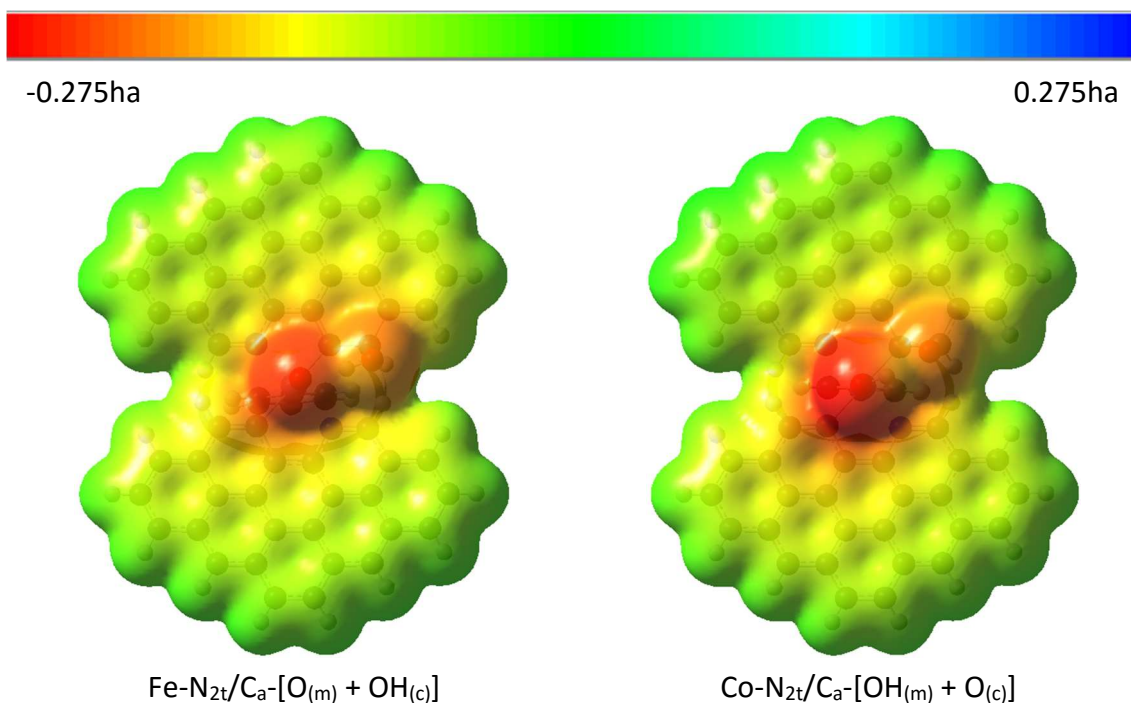
Figure 4.12 - The products of OOH$_{(ads)}$ dissociation on Fe-N$_{2t}$/C$_a$ and Co-N$_{2t}$/C$_a$.

2OH$_{(ads)}$ is likely favoured as proton transfer to adsorbed oxygen likely has a lower activation barrier than the proton transfer to OH$_{(ads)}$.

4.4.4.3 - Third and fourth electron transfer reactions

From Table 4.6, the Gibbs free energy changes for each third and fourth electron transfer reaction for the two N$_{2t}$/C$_a$ active sites can be seen. From this it can be seen that both active sites are capable of reducing 2OH$_{(ads)}$ via either of the two pathways, though the reduction of the carbon bound OH$_{(ads)}$ is thermodynamically favoured on both. Figure 4.13 shows the ESP-on-density maps for 2OH$_{(ads)}$ on both Co-N$_{2t}$/C$_a$ and Fe-N$_{2t}$/C$_a$. The increased electron density surrounding the carbon bound OH$_{(ads)}$ on both active site adds support to the conclusion that its reduction is likely the favoured pathway, resulting in [OH$_{(m)}$ + H$_2$O$_{(c)}$]. As the final reduction reaction is not thermodynamically viable on Co-N$_{2t}$/C$_a$, being 24.315 kJmol^{-1} endergonic. This results in a complete cessation of activity, as OH$_{(m)}$ blocks the metal centre, preventing the adsorption of O$_2$ and its subsequent reduction. However, the reduction of this product to 2H$_2$O is favoured on Fe-N$_{2t}$/C$_a$ up to, and indeed beyond, the limiting potential for the one-electron reduction of O$_{2(ads)}$, U$_{rev}$ = 0.170 V.
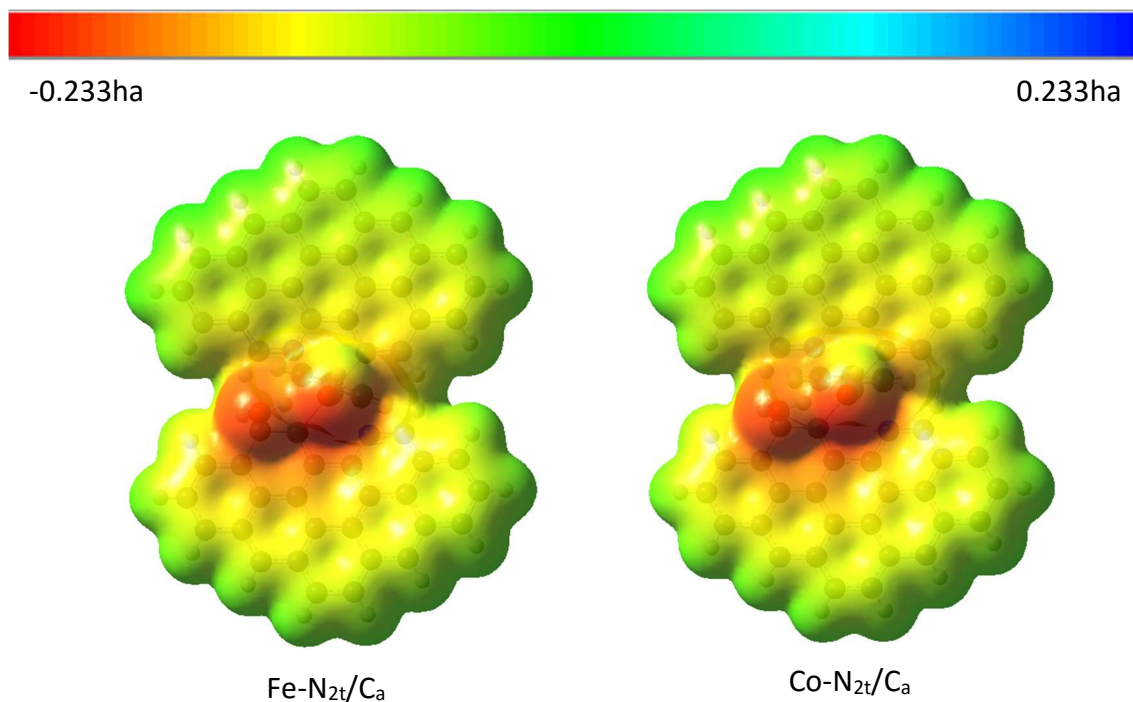
Figure 4.13 - ESP-on-density maps of $2OH_{(ads)}$ on both N_{2t}/C_a active sites.

From these results in can thus be concluded that of the four N_{2t}/C active sites, only $Fe-N_{2t}/C_a$ is capable of reducing O_2 via the direct $4e^-$ reduction pathway, albeit only up to a maximum potential of 0.170 V. Both graphene active sites are capable of reducing O_2 without blocking the surface, up to potentials of 0.183 V and 0.308 V for $Fe-N_{2t}/C_g$ and $Co-N_{2t}/C_g$, respectively, although they are only capable of catalysing the $2e^-$ reduction pathway, resulting in the formation of peroxide.

4.4.5 - N_{2p}/C active sites

From Table 4.7 it can be seen that none of the N_{2p}/C active sites are capable of catalysing the dissociation of O_2, with this reaction being highly endergonic on all four active sites. The reduction of O_2 is thus the only viable reaction post-adsorption, though the potentials at which this reaction is viable are substantially lower than that observed on Pt/C, with one-electron reversible potentials ranging from 0.130-0.488 V. Indeed so low is reversible potential for all of the N_{2p}/C active sites that it is largely expected that this reaction limits the maximum potential for further steps in the reduction chain.

Table 4.7 - Gibbs free energy changes for each N_{2p}/C catalysed reduction reaction and the reversible potentials of those electron transfer reactions.

	Fe-N_{2p}/C_g		Fe-N_{2p}/C_a		Co-N_{2p}/C_g		Co-N_{2p}/C_a	
	ΔG (kJmol^{-1})	E^0 (eV)	ΔG (kJmol^{-1})	E^0 (eV)	ΔG (kJmol^{-1})	E^0 (eV)	ΔG (kJmol^{-1})	E^0 (eV)
$O_2 \rightleftharpoons 2O$	125.895		39.188		172.206		119.030	
$O_2 + H^+ + e^- \rightleftharpoons OOH$	-12.516	0.130	-16.864	0.175	-24.945	0.259	-38.810	0.402
$2O + H^+ + e^- \rightleftharpoons OH_{(m)} + O_{(c)}$	-163.968	1.699	-121.836	1.263	-166.806	1.729	-195.127	2.022
$2O + H^+ + e^- \rightleftharpoons O_{(m)} + OH_{(c)}$	-137.006	1.420	-71.721	0.743	-49.897	0.517	3.466	-0.036
$OOH_{(m)} \rightleftharpoons O_{(m)} + OH_{(c)}$	1.405		-15.669		147.254		161.305	
$O_{(m)} + OH_{(c)} \rightleftharpoons OH_{(m)} + O_{(c)}$	-26.961		-50.116		-116.909		-198.593	
$OOH_{(m)} + H^+ + e^- \rightleftharpoons H_2O_{2\,(m)}$	-73.133	0.758	-25.995	0.269	-48.430	0.502	-16.883	0.175
$O_{(m)} + OH_{(c)} + H^+ + e^- \rightleftharpoons 2OH_{(m+c)}$	-100.853	1.045	-106.393	1.103	-278.608	2.888	-248.609	2.577
$O_{(m)} + OH_{(c)} + H^+ + e^- \rightleftharpoons O_{(m)} + H_2O_{(c)}$	-145.531	1.508	-123.750	1.283	-291.174	3.018	-306.868	3.180
$OH_{(m)} + O_{(c)} + H^+ + e^- \rightleftharpoons 2OH_{(m+c)}$	-73.892	0.766	-56.278	0.583	-161.699	1.676	-50.016	0.518
$OH_{(m)} + O_{(c)} + H^+ + e^- \rightleftharpoons H_2O_{(m)} + O_{(c)}$	-138.330	1.434	-68.638	0.711	-186.833	1.936	-63.458	0.658
$H_2O_{(m)} + O_{(c)} \rightleftharpoons O_{(m)} + H_2O_{(c)}$	19.760		-4.996		12.568		-44.817	
$H_2O_{(m)} + O_{(c)} + H^+ + e^- \rightleftharpoons H_2O_{(m)} + OH_{(c)}$	-97.611	1.012	-74.223	0.769	-63.345	0.657	-23.002	0.238
$O_{(m)} + H_2O_{(c)} + H^+ + e^- \rightleftharpoons OH_{(m)} + H_2O_{(c)}$	-122.530	1.270	-193.069	2.001	-185.628	1.924	-178.980	1.855
$2OH + H^+ + e^- \rightleftharpoons OH_{(m)} + H_2O_{(c)}$	-167.209	1.733	-210.426	2.181	-198.194	2.054	-237.240	2.459
$2OH + H^+ + e^- \rightleftharpoons H_2O_{(m)} + OH_{(c)}$	-162.048	1.680	-86.584	0.897	-88.479	0.917	-36.445	0.378
$H_2O_{(m)} + OH_{(c)} \rightleftharpoons OH_{(m)} + H_2O_{(c)}$	-5.160		-123.842		-109.714		-200.796	
$H_2O_{(m)} + OH_{(c)} + H^+ + e^- \rightleftharpoons 2H_2O$	-135.258	1.402	-152.594	1.582	-185.290	1.920	-200.454	2.078
$OH_{(m)} + H_2O_{(c)} + H^+ + e^- \rightleftharpoons 2H_2O$	-130.098	1.348	-28.752	0.298	-75.576	0.783	0.341	-0.004

The reversible potential for the reduction of $OOH_{(ads)}$ to H_2O_2 $_{(ads)}$ is found to be higher than the one-electron reduction potential of $O_{2(ads)}$ for all but the $Co-N_{2p}/C_a$ active sites, thus it is concluded that $Fe-N_{2p}/C_g$, $Fe-N_{2p}/C_a$ and $Co-N_{2p}/C_g$ catalyse the 2e$^-$ reduction of O_2 directly to peroxide at potentials of 0.130 V, 0.175 V, and 0.259 V respectively. The reversible potential of $OOH_{(ads)}$ on $Co-N_{2p}/C_a$ is found to be lower than that of the $O_{2(ads)}$ reduction reaction, though as neither of the dissociation reactions are favoured, this simply means that peroxide is formed up to 0.175 V, after which the metal centre is blocked by $OOH_{(ads)}$.

4.5 - Conclusions

In this chapter sixteen Co- and Fe-centred $M-N_x/C$ active sites have been computationally modelled to ascertain their activity towards the oxygen reduction reaction and thus their suitability as potential replacements as the cathode catalyst within PEM fuel cells. These active sites were selected based on conclusions drawn from the literature and were felt to represent possible Co- and $Fe-N_4/C$ and $-N_2/C$ moieties resulting from the pyrolysis of metal and nitrogen precursors in the presence of either graphene or amorphous carbon that have been reported to be active towards the oxygen reduction reaction.

An ideal PEM fuel cell cathode catalyst would be able to catalyse four electron transfer reactions at a potential of 1.229 V, the maximum theoretical potential possible for the reduction of O_2. As it has been established within the literature that only the +2 state of $M-N_x/C$ active sites are active towards the ORR (Bikiel et al., 2008), the redox potentials pertaining to the transition from a +2 to a +3 state were modelled, using an axial benzene ligand and a correction factor derived from experimental data, as described in Chapter 3. From this it was found that N_2/C active sites located within graphene were able to achieve redox potentials near or higher than 1.229 V, regardless of the central metal, suggesting that such active sites may be able to catalyse oxygen reduction up to the maximum operating potential of a PEM fuel cell. The redox potentials of the N_2/C_a active sites were found to be lower than their basal plane counterparts, and ranged in value from 0.890-1.323 V. The N_4/C active sites studied did not exhibit such a marked difference in redox potentials between the graphene and

amorphous models, with redox potentials ranging between 0.406-0.732 V across all four N_4/C active sites.

By modelling the +3 state of each active site, and examining the electrostatic potential as a function of the increased charge density upon redox, it was found that the redox potential is linked not only to charge donation to the central metal, but also to the ability of the carbon support to act as an 'electron buffer', an observation supported by the work of others (Liao et al., 2004; Marcotte et al., 2004; Médard et al., 2006).

Twenty one reactions, both chemical and electrochemical in nature and proposed to represent a suitably comprehensive reduction mechanism, were modelled on all sixteen active sites to ascertain the catalytic activity of these M-N_x/C active sites towards the ORR. Of these sixteen only one, Fe-N_{2h}/C_a, displays no activity towards oxygen reduction. The majority of the catalysts investigated are able to partially catalyse the reduction of oxygen, though it is found that this usually results either in the formation of peroxide or surface blocking species. At best, these surface species serve to block secondary active sites, which, it is posited, could promote the reduction of O_2 to peroxide, or adsorb to the metal centre and thus poison the active site.

The most promising active sites, Fe-N_4/C_a and Co-N_4/C_a, are able to catalyse the oxygen reduction reaction up to 0.593 V and 0.559 V, respectively. These two active sites are only able to promote the one-electron reduction of O_2 up to potentials of 0.410 V and 0.473 V, respectively. However, both promote the dissociation of the O-O bond in both $O_{2(ads)}$ and $OOH_{(ads)}$ and so the potential limiting reactions are found to be the protonation of carbon bound oxygen and metal-bound OH respectively. The redox potential of Co-N_4/C_a is high enough that the active site is able to remain in its formal +2 state in the entire potential range of the reduction reaction, though Fe-N_4/C_a is only able to remain in the formal +2 up to 0.406 V and as such reduction can only proceed up to this potential.

Chapter 5 - Discussion and conclusions

In Chapter 3 the ability of platinum to catalyse the reduction of oxygen was described, and the probable sources of the overpotential exhibited by this catalyst identified. Also in Chapter 3, a computational model for the description of Co- and Fe-centred porphyrins, common precursors in the synthesis of $M-N_x/C$ active site, was developed and compared to electrochemical tests to assess its efficacy. It was found that the use of B3LYP with mixed basis sets was capable of describing the redox potential and the preferred oxygen reduction pathway of such compounds, provided an axial ligand and appropriate correction factor were applied.

In Chapter 4 the activities of 16 proposed $M-N_x/C$ active site structures were assessed using the developed methodology. It was found that while these active sites, in general, displayed higher redox potentials than the porphyrins, they suffered from poor activity, stemming from both the low reversible one-electron reduction potentials of the elementary reduction reactions, and the propensity to selectively reduce O_2 to peroxide.

While no active sites modelled within this study presented activity comparable to platinum, a detailed analysis of the results of Chapters 3 and 4 serves to explain how each component of the active site influences its ORR activity and thus provides a signpost towards the identity of highly active, non-precious metal catalysts.

5.1 - Proposed effect of heat treatment on the catalytic activity on porphyrins

From the work presented in Chapters 3 and 4, and from the critical review of the literature in Section 2.6, it is found that the activities of $M-N_x/C$ active sites are a function of two parameters, the redox potential and the lowest one-electron reversible potential of the preferred reduction pathway. Thus heat-treatment of porphyrins must serve to improve these two characteristics to allow for improved catalytic activity.

5.1.1 - Redox potentials

None of the porphyrins investigated in Chapter 3 are able to undergo redox above potentials of 0.675 V, thereby becoming inactive towards the ORR above this range. In Section 4.3, the redox potentials of the proposed $M-N_x/C$ active sites were modelled, and found to be, in general, notably higher than the porphyrin precursors. While investigating why redox potentials varied between the $M-N_x/C$ active sites it was found that increased crossover charge between the equatorial graphene ligand and the central metal correlated to an increased redox potential. This was shown for $M-N_x/C$ active sites in Figures 4.5 and 4.6, and is repeated for the six porphyrins investigated in Chapter 3, in Figure 5.1.

By comparing the ESP-on-density maps of Fe- and $Co-N_4/C_g$, from Figure 4.5, Fe- and $Co-N_4/C_a$, from Figure 4.6 and the six porphyrins, presented in Figure 5.1, one can directly assess how the equatorial ligand serves to affect the redox potential. The most apparent difference between these three figures is the lower electrostatic potential of the additional charge located on the equatorial ligand. While the porphyrin rings in Figure 5.1 accommodate a charge of significant electrostatic potential, it is found that the graphene ligands are more able to stabilise the electron transferred during redox, thus resulting in a lower ESP on the axial ligand. Also, it is noted that cobalt centre is more able to accept charge from the graphene ligands than from the porphyrin ring. From Figure 5.1 it is apparent that the nitrogen atoms of the Co-centred porphyrins are able to accommodate significant amounts of electronic charge, due to the high ESP of the additional charge located around them. However, given the disparity between the ESP-on-density maps of Fe- and Co-centred porphyrin analogues one must conclude that the nature of both the equatorial ligand and the central metal are contributing factors to the achievement of high redox potentials.

Two theories are postulated for the low redox potentials of the Co-centred amorphous active sites. Firstly, as cobalt has a smaller ionic radius than iron, it could be that it is not of sufficient size to allow overlap of the orbitals originating from the N/C atoms immediately surrounding it. While the central 'hole' in which the metal sites certainly increases in size with decreasing redox potentials, the size disparity between
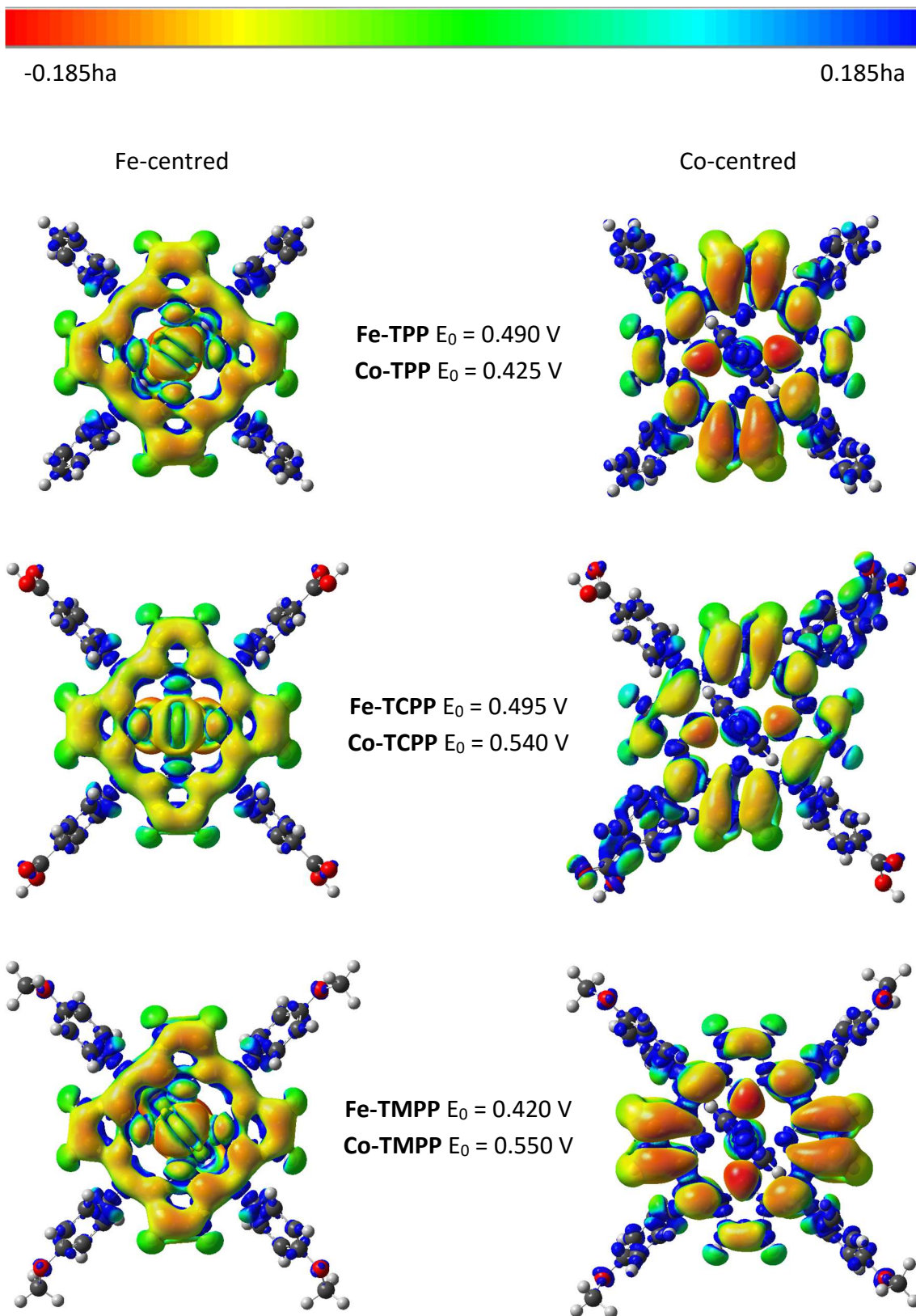
Figure 5.1 - ESP mapped as a function of the change in charge density during +2/+3 redox for each porphyrin investigated in Chapter 3.

the two metal +2 ions is felt to be far too small to cause such a large difference in orbital overlap and thus redox potential. Coupled with this, ESP-on-density maps of the vacant active sites clearly show significant charge occupying the central hole which is comparable, if not higher, than that of the graphene analogue, as shown for the N_{2t}/C active sites in Figure 5.2.

A second postulate, that the redox potential is a function of the HOMO/LUMO gap and the valence orbital levels is preferred (Tai et al., 2013). NBO analysis certainly supports this notion and it is observed that the HOMO/LUMO gap is substantially smaller for those active sites with lower redox potentials. However, this observation is qualitative only as the methodology used to calculate the redox potentials does not allow for detailed exploration of the orbital occupations and the control of partial charges. This is discussed in greater detail in Section 5.3 where the limitations of the method, and suggested improvements to it, are discussed in detail.

Despite the limitations of the methodology employed in this thesis, it is apparent that the inclusion of $M-N_4$ moieties into basal plane graphene results in increased redox potentials. This increase must result from the increased resonance structure of the graphene ligand, allowing for greater stabilization of charge, as described in Section 4.3. Furthermore these results also show that $M-N_2/C_g$ moieties are able to achieve even higher redox potentials, resulting from the lower electronegativity of carbon in comparison to nitrogen which allows for greater charge overlap between the equatorial ligand and the central metal. In addition, the use of cobalt within these graphene-based active sites allows for a more consistently higher redox potential, with all three $Co-N_2/C_g$ active sites having calculated redox potentials of between 1.100-1.135V. Comparatively $Fe-N_2/C_g$ achieve less consistent redox potentials, ranging from 0.890 V to 1.323 V, although it is important to note that these values are higher than the redox potentials for $Fe-N_4/C_g$ and any of the three porphyrins investigated.

The amorphous carbon active sites have notably lower redox potentials, with $Fe-N_4/C_a$ achieving a redox potential comparable to those of the porphyrins, and two of the three $Co-N_2/C_a$ having redox potentials substantially lower. The disruption of the resonant graphene structure is found to result in a decrease in the redox potentials, as

Vacant N_{2t}/C_g Vacant N_{2t}/C_a
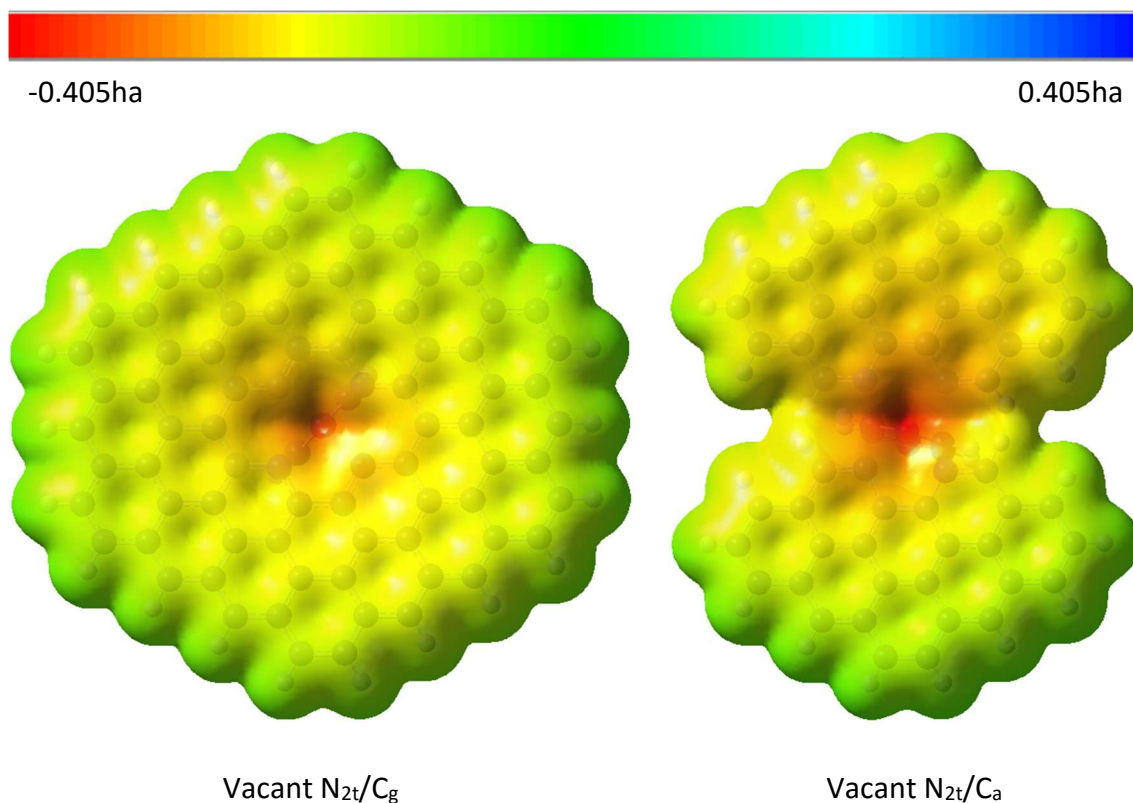
Figure 5.2 - ESP-on-density maps of N_{2t}/C active sites in the absence of a metal centre.

can be seen by comparing the redox potentials of the analogous C_g and C_a sites. However, it is quite possible that the lower resonance of the amorphous carbon equatorial ligands is not representative of reality. Indeed while one would expect there to be variations in the redox potentials between the graphene and amorphous carbon systems, one would not expect either of these two structures to have redox potentials as low as 0.3 V given the experimentally reported activities. Indeed given the conclusions drawn by others regarding experimental characterisation of pyrolysed M-N_x/C systems, namely that performance comparable to that of platinum can be achieved (Herrmann et al., 2009) and that those active sites found in pores developed during pyrolysis with amorphous carbon display the greatest activity (Charreteur et al., 2008), one would expect redox potentials for M-N_x/C_a active sites to be comparable to, or higher than, those for M-N_x/C_g analogues; that they are not is perhaps indicative of an inaccurate computational model. However, this may simply be a limitation arising from the use of a benzene ligand as a model for second layer graphene, which is discussed in greater detail in Section 5.3.2.

5.1.2 - Activities and preferred pathways

From both the experimental and computational work presented in Chapter 3, it is clear that Co- and Fe- centred TPP, TCPP and TMPP are able to promote the $2e^-$ reduction of O_2, to HOOH, but not the more desirable $4e^-$ pathway resulting in the complete reduction to $2H_2O$. However from Sections 4.3 and 4.4 it is apparent that the heat-treatment of porphyrins results not only in variations in redox potentials but shifts in preferred pathways and significant alterations to the one-electron reduction potentials of the elementary reactions. The ability of an $M-N_x/C$ to catalyse the reduction of O_2 can be attributed to a number of synergistic effects, which are themselves a function of both the metal centre and the carbon structure.

5.1.2.1 - O_2 binding and reactivity

When O_2 binds to the central metal it does so via two mechanisms, as shown in Figure 5.3. Firstly an O_2 lone pair interacts with the empty, or partially occupied, $3d_{z^2}$ orbital of the central metal. This is found to occur for all the active sites under investigation, regardless of the central moiety or equatorial ligand. Secondly, charge is transferred from the active site to the O_2 molecule via interaction of the $3d_{yz}$ and π^* orbitals, resulting in a superoxo-like species, O_2^-, with an elongated O-O bond. The extent of charge donation to and from the active site is dependent on the occupations of the metal $3d_{yz}$ and $3d_{z^2}$ orbitals, which are in turn a function of the oxidation state of the metal and the nature of the equatorial and axial ligands. While it is found that the occupation of the $3d_{z^2}$ orbital is near identical regardless of the central metal, it is found that iron has a higher $3d_{yz}$ electron occupation than cobalt, resulting in more significant back-bonding interaction and thus comparatively stronger Fe-O bonds.

By comparing the values presented in Table 3.6 with those for the one-electron reduction of $O_{2(ads)}$ for the $Fe-N_4/C_g$ and $Co-N_4/C_g$ active sites, presented in Table 4.4, it is clear that embedding the N_4 moiety into a graphene sheet has a positive effect on the reduction of $O_{2(ads)}$ to $OOH_{(ads)}$. While the porphyrins are able to reduce O_2 at approximately 0.4 V and 0.6 V, for the Co- and Fe-centred porphyrins respectively, Co-N_4/C_g and Fe-N_4/C_g are able to do so up to potentials of 0.772 V and 0.661 V respectively. This increased reduction potential correlates to an increased partial
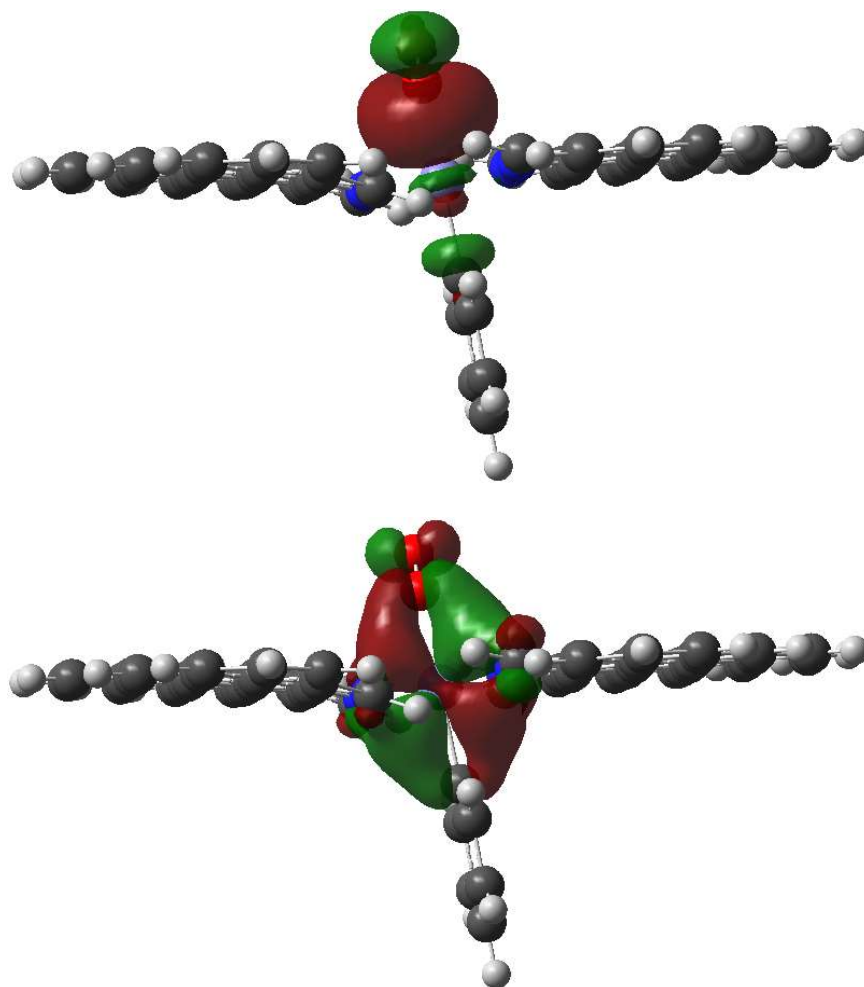
Figure 5.3 - O$_{2(ads)}$ binding interactions with Fe-N$_4$/C$_a$; O$_2$ lone pair donation to the 3d$_{z^2}$ orbital, top, and 3d$_{yz}$ donation to the O$_2$ π* orbital, bottom.

charge on the adsorbed O$_2$, although this additional charge is located on the metal co-ordinated oxygen atom and not, as one may expect, on the terminal oxygen. As donation from the surface to the adsorbed reduction intermediate occurs predominantly via the metal 3d$_{yz}$ orbitals to the O$_2$ π*, it is something of a surprise to note no increase in the O-O bond length. Indeed no discernible difference can be made between the lengths of the O-O bond in porphyrin co-ordinated O$_2$ and when O$_2$ is co-ordinated to an N$_4$/C$_g$ site, instead one notes an increase in the metal-oxygen bond length. These two observations infer that the equatorial graphene ligand actively donates to the metal-oxygen anti-bonding orbital, thus resulting in a greater partial charge on the adsorbed O$_2$.

5.1.2.1.1 - Influence of equatorial ligand

As detailed in Sections 3.4 and 4.4, there exists a trade-off between high redox potentials and high one-electron reduction potentials for O_2. As it has been established that the high redox potentials exhibited by graphene-based active sites in Section 4.3 are due to the ability of the equatorial ligand to stabilise the additional electronic charge, the donation of this charge to a substrate, such as $O_{2(ads)}$, from the graphene ligands can be expected to be more laborious than for the amorphous ligands or porphyrins, which would be evidenced by the formation of weaker metal-oxygen bonds upon O_2 adsorption. Table 5.1 shows the binding strength of O_2 to each investigated active site, from which it can be seen that the adsorption of O_2 is favourable on each of the active sites. M-O_2 bond strengths are higher for Fe-centred active sites than for the Co-centred analogues, and amorphous active sites have a more pronounced interaction than their graphene counterparts; this is the opposite trend to that observed for redox potentials in Table 4.1.

Table 5.1 - Binding strength of O_2 (in kJmol^{-1}) to each active site investigated.

	Co		Fe	
	C_g	C_a	C_g	C_a
N_4	-37.340	-135.853	-60.747	-120.126
N_{2p}	-71.304	-106.232	-92.627	-136.625
N_{2h}	-77.768	-139.134	-92.048	-169.817
N_{2t}	-77.575	-152.835	-88.864	-179.079

Higher binding strengths are indicative of increased back-bonding and thus donation to the O_2 π^* orbital and are thus mirrored by an increase in O-O bond length. The increased donation from amorphous active sites leads to an increased partial charge on the $O_{2(ads)}$ when compared to their graphene-based counterparts and so one may expect all amorphous sites to be capable of reducing $O_{2(ads)}$ at higher potentials. However, in general, this is not found to be the case, with only the amorphous Fe- and Co-N_{2p} and Co-N_{2t} active sites showing higher one-electron reduction potentials than their graphene counterparts.

The electron transferred to the system when modelling the protonation reaction is predominantly located on the $OOH_{(ads)}$, inferring that the equatorial ligand acts as a conduit for electron transfer without actively donating any electron density. However, for those graphene active sites displaying a lower $O_{2(ads)}$ reduction potential than their amorphous analogues, i.e. Fe- and Co-N_{2p} and Co-N_{2t}, it is found that the equatorial ligand actively donates partial charge, with $O_{2(ads)}$ accepting more than one electron during the reduction reaction. As the electronic charge located on the equatorial ligand is highly stable this process likely has a Gibbs free energy cost, which serves to reduce the reduction potential.

However, these active sites are seemingly the exception, not the rule. Why do amorphous active sites display, in general, lower $O_{2(ads)}$ one-electron reduction potentials than their graphene counterparts, despite the more significant charge on the $OOH_{(ads)}$ adsorbed to them? While the active donation of charge from the graphene ligand to $O_{2(ads)}$ is seen to reduce the one-electron reduction potential, the opposite is observed for the amorphous active sites. In Section 4.3 it was concluded that the decreased electron stabilisation capabilities of the amorphous ligand, compared to the graphene ligand, results in comparatively lower redox potentials. While the majority of the electron transferred to the amorphous systems during the reduction of $O_{2(ads)}$ is located on the $OOH_{(ads)}$, some electronic charge is accommodated for by the amorphous ligand. As this electronic charge is not particularly stabilised by this ligand there is a Gibbs free energy cost to accommodate it which serves to reduce the reduction potential.

From these two, somewhat conflicting findings it is postulated that a 'Goldilocks zone' exists for the carbon support, in which an electron transferred during the redox of the active site is able to be somewhat stabilised by the carbon support, and thus able to achieve a relatively high redox potential, though not so stabilised that electron transfer to the adsorbed intermediates becomes laborious.

5.1.2.1.2 - Influence of metal centre

From the results presented in Section 4.4 it is also apparent that the O_2 one-electron reduction potentials of Fe-centred active sites are lower than those of their Co-centred

counterparts. When binding O_2, there is a notable decrease in the partial charge of iron, though no such change is noted for the cobalt centred active sites. NBO analysis shows that, in the +2 state of all the active sites, iron has approximately one electron in the $3d_{yz}$ orbital while the same orbital is doubly occupied for the Co-centred active sites. As the $3d_{yz}$ orbital is responsible for back-bonding interactions, charge is transferred to it from the equatorial ligand upon adsorption of O_2 and subsequently donated to $O_{2(ads)}$ π^* orbital. As the natural state of the Fe-centre is to have $1e^-$ in this orbital it is able to donate this charge to the anti-bonding orbital of O_2. Conversely, the doubly occupied Co $3d_{yz}$ orbital acts as a conduit for charge transfer by forming a bridge between the O_2 π^* orbital and the equatorial ligand, allowing for direct charge transfer from the ligand to the adsorbed oxygen. The increased donor capabilities of Fe results in stronger metal-oxygen bonds compared to the Co-centred analogues, as noted by the results presented in Table 5.1.

Upon reduction of $O_{2(ads)}$, and thus donation of an extra electron, back-bonding interaction decreases, as the already donated charge moves to form a covalent bond with the hydrogen atom. As the Fe-centre donates charge from the doubly occupied $3d_{xy}$ orbital, it returns to a formal $1e^-$ occupation, which results in a decrease in the $3d_{yz}$ orbital energy level. This decrease severs the back-bonding link, thus meaning less partial charge is donated to the $O_{2(ads)}$ during protonation. As the cobalt centre acts as more of a conduit, and no formal charge donation from the Co $3d_{yz}$ orbital to the $OOH_{(ads)}$ occurs, this back-bonding link is maintained and the charge donated is exclusively from the equatorial ligand. Thus the lower one electron reduction potentials exhibited by Fe-centred active sites are a result of the slightly lower charge donation to $O_{2(ads)}$ during the reaction when compared to cobalt.

It is interesting to note the synergistic effect of the metal centre and the equatorial ligand. While Fe-centred $M-N_x/C$ active sites are not able to reduce O_2 at as high a potential as their Co-centred analogues, Table 3.6 shows that Fe-centred porphyrins outperform Co-centred porphyrins for the same reaction. This is found to be due to the charge transferred to the central metal upon redox.

While the central metals of the $M-N_x/C$ active sites do not see a significant change in their orbital occupations upon transition from a +3 to +2 state, there a significant increase in the $3d_{yz}$ orbital occupation of the Fe-centres of porphyrins. While the Fe^{II} centres of the $M-Nx/C$ active sites are high spin, those of the porphyrins are found to be low spin, and so the addition of electronic charge to a partially occupied orbital results in an increase in electron-electron repulsion. Upon donation of this electronic charge via the reduction of $O_{2(ads)}$, this electron-electron repulsion decreases. As this process is exergonic, there is a release of Gibbs free energy which results in a higher reduction potential.

5.1.2.1.3 - Influence of nitrogen

Finally, it can also be seen from Chapter 4 that the N_2/C active sites are not as adept at catalysing the one-electron reduction of oxygen as the N_4/C active sites; with the notable exception of the cobalt-centred amorphous carbon active sites, which are able to achieve broadly similar reduction potentials for this reaction. It is difficult to ascertain the precise cause of this variation in activities as no precise trend can be observed between charge donation to $O_{2(ads)}$ during adsorption and reduction. While $Co-N_4/C_g$ donates more charge to O_2 upon binding than the $Co-N_2/C_g$ active sites, $Fe-N_4/C_g$ donates less than any of the $Fe-N_2/C_g$ sites. Conversely while $Co-N_4/C_a$ donates less charge than any other Co-centred active site, $Fe-N_4/C_a$ donates more than any other Fe-centred active site.

From the ESP-on-density maps shown in Figures 4.5 and 4.6 it is apparent that the nitrogen atoms surrounding the metal centre are less inclined to 'donate' charge to the metal centre during the redox reaction[12], owing to the comparatively higher electronegativity than carbon. This observation leads to the qualitative conclusion that nitrogen atoms in the central moiety act as a 'reservoir', able to accept or donate partial charge as the reaction demands. This would certainly support the observation that the

---

[12] While the ESP-on-density maps show that charge crossover with the central metal occurs, NPA analysis shows that the metal centres do not experience a significant change in partial charge, thus this crossover cannot be formally described as donation. For more detail on this please see Section 4.3.

activity of porphyrins is set by the metal centre and 'fine-tuned' by the substituent groups (Baker et al., 2008), and the broadly similar reduction potentials observed experimentally and calculated in Section 3.3, though confirmation of this observation would require a more in-depth investigation, and likely require the modelling of active sites with a wider spread in nitrogen composition.

5.1.2.2 - O-O bond scission

One of the most important features of a replacement PEM catalyst is the promotion of a 4 e$^-$ reduction pathway. In order for this reaction to occur on an active site, it must be able to promote the scission of the O-O bond of either $O_{2(ads)}$ or $OOH_{(ads)}$. Given the 'end-on' adsorption favoured by both porphyrins and the M-N$_x$/C active sites described in Chapter 4, it is deemed that the dissociation of this bond is unlikely to occur before protonation of $O_{2(ads)}$, given the $\delta+$ charge on the terminal oxygen and the acidic nature of the PEM cathode environment. Thus the ability to promote the dissociation of $OOH_{(ads)}$ over its protonation is deemed to be a critical feature of the ideal active site. In the absence of transition states for the two competing reactions, the preferred pathway is determined by calculating the bond strengths and adopting the assumption that the weaker bond is likely to preferentially dissociate. Table 5.2 gives the bond strengths of the O-OH and metal-oxygen bonds for each active site investigated, alongside the partial charge of the $OOH_{(ads)}$.

Table 5.2 - Metal-oxygen and O-O bond strengths (kJmol^{-1}) of OOH$_{(ads)}$ on each M-N$_x$/C active site.

	OOH$_{(ads)}$ partial charge		O-OH bond strength		M-OOH bond strength	
	C$_g$	C$_a$	C$_g$	C$_a$	C$_g$	C$_a$
Fe-N$_4$	-0.683	-0.674	-202.100	-160.486	-162.712	-166.808
Fe-N$_{2p}$	-0.626	-0.678	-131.004	-103.198	-127.814	-261.631
Fe-N$_{2h}$	-0.655	-0.638	-133.640	-74.031	-141.029	-199.652
Fe-N$_{2t}$	-0.646	-0.666	-138.449	-93.306	-133.264	-206.776
Co-N$_4$	-0.781	-0.715	-190.522	-168.227	-243.756	-215.216
Co-N$_{2p}$	-0.714	-0.764	-176.409	-181.468	-131.030	-183.213
Co-N$_{2h}$	-0.708	-0.750	-175.776	-175.867	-144.316	-188.516
Co-N$_{2t}$	-0.705	-0.772	-171.777	-175.922	-151.768	-188.795

From Table 5.2 it can be seen that the Co-N$_2$/C$_a$ active sites have a higher partial charge and stronger metal-oxygen bonds than their graphene counterparts, though the O-OH bonds are of comparable strength regardless of the ligand type. It is likely therefore that this additional charge is donated back to the metal centre via the oxygen lone pairs, resulting in a metal oxygen bond. This postulate is supported by NBO data showing a more substantial interaction between a lone pair, located on the OOH$_{(ads)}$, and the Co 3d$_{z^2}$ orbital. The lack of significant changes to the O-OH bond strength implies that the π* anti-bonding orbital of OOH$_{(ads)}$ is fully occupied above a particular partial charge. That the Co-N$_4$/C$_g$ active site donates significantly more charge to OOH$_{(ads)}$ than the graphene-based Co-N$_2$ sites and exhibits the highest metal-oxygen bond strength serves to further support this hypothesis.

However, this rather simplistic explanation does not explain the observation that increasing partial charge on the Fe-N$_2$/C results in an increase in both O-OH and metal-oxygen bond strengths. As discussed in Section 5.1.2.1.2, the back-bonding link between the iron centre and O$_2$ is severed during protonation, resulting in a decreased charge transfer and thus a lower OOH$_{(ads)}$ partial charge on Fe-centred active sites when compared to their Co-centred analogues. As the only link now remaining between the iron centre and OOH$_{(ads)}$ is the interaction between an oxygen lone pair and the Fe 3d$_{z^2}$ orbital, any charge donation from the metal centre is via this bond. Thus it can be concluded that increased partial charges on OOH$_{(ads)}$ co-ordinated to M-N$_x$/C active sites serve to strengthen the metal-oxygen bond for all but the N$_4$/C$_g$ active sites.

That the N$_4$/C$_g$ active sites do not correlate with this is the result of the 'reservoir' effect of the nitrogen atoms, as discussed in Section 5.1.2.1.3, and the increased resonance of the graphene ligand, as discussed in Sections 5.1.1 and 5.1.2.1.1. These two factors work to prevent adequate donation from the equatorial ligand to the substrate, and so charge donation from the axial benzene ligand, via the 3dz2 orbital, is found to occur. This serves to increase the metal-oxygen bond strength, though as donation to the anti-bonding orbital is significantly reduced due to the poor interaction of the 3d$_{yz}$ and π* orbitals, the O-OH bond is not weakened accordingly.

Though the comparison of bond strengths allows for an estimation of activation barriers to be made, it does not address the overall feasibility of the reactions. While attempts to ascertain the precise influence of each active site component on the feasibility of the protonation and dissociation reactions were made, it was found to rely heavily on the local electronic structure of the equatorial ligand, the orientation of OOH$_{(ads)}$ and the precise location of the carbon-bound hydroxyl. Furthermore, as stated in Section 4.2, certain adsorption sites were not considered as they were found to contribute towards the de-activation of the active site. Given the limitations of the methodology it is likely that attempting to analyse how the active site composition affects the feasibility of these reactions would be inappropriate, and would likely result in misleading conclusions being drawn. However, a proposed methodology that would allow this analysis is detailed in Section 6.5.

5.2- Stability of M-N$_x$/C active sites within acidic media

As reported in Section 2.6, porphyrins are found to be unstable in acidic media (Chang et al., 2014; Domínguez et al., 2014; Liu et al., 2006; Schilling et al., 2010; Wei et al., 2000; You et al., 2014) and while little work has been performed to directly address their stability, a proposed degradation pathway, shown in Figure 3.4, and the selective reduction to peroxide, suggest that the metal centres are able to act as Fenton's reagents, thereby catalysing the formation of HO· radicals which act to both remove meso-phenyl substituents and eventually cause the decomposition of the macrocyclic ring.

A Fenton reagent is typically an iron salt which is able to promote the one-electron reduction of peroxide, resulting in the formation of hydroxyl free radicals (Goldstein et al., 1993):

$$Fe^{II} + H_2O_2 \rightleftharpoons Fe^{III} + HO\cdot_{(aq)} + HO^-_{(aq)} \tag{5.1}$$

The one-electron reversible potential for the formation of hydroxyl free radical is 0.88 V and it has been shown that a metal centre is only able to catalyse free radical formation if the redox potential of the metal is less than this value (Gubler et al., 2011). As it has been found that hydroxyl free radical attack serves to degrade the structural

integrity of graphene (Feng et al., 2015; Radich & Kamat, 2013; Xing et al., 2014), and that the formation of peroxide is promoted by both porphyrins and $M-N_x/C_g$ active sites, the resilience of a catalyst to free radical attack is thus dependent on the redox potential of the active site.

From Table 3.8, it can be observed that all six porphyrins investigated are capable of catalysing the Fenton reaction, thereby promoting their own degradation. The embedding of these central N_4/C moieties into the graphene plane serves to increase the redox potential, although not enough to prevent the formation of free radicals, as shown in Table 4.1. Conversely, the graphene-based N_2/C active sites are seemingly resistant to free radical formation, with redox potentials ranging from 0.890-1.323 V, although their amorphous counterparts exhibit substantially lower redox potentials, with all N_x/C_a active sites able to participate in the Fenton reaction. The observation that these $M-N_2/C_g$ active sites are more resilient to free radical attack is supported by experimental observations; it has been shown that those active sites prepared at higher temperatures are more stable (Wei et al., 2000), and that the central $M-N_4$ moiety is only stable up to approximately 700 °C (Schilling et al., 2010). Therefore higher pyrolysis temperatures are likely to result in a higher relative abundance of $M-N_2$ active sites.

If it is the case that the amorphous carbon active sites are more representative of degraded graphene-based active sites, then the results presented in Chapter 4 show that degradation results in both a reduction in the redox potential and a decrease in the ability of the carbon support to act as an electron buffer and thus serves to further highlight the importance of the carbon support as an integral component of the active site.

5.3- Limitations of the methodologies used within this thesis

5.3.1 - DFT and NBO analysis

Before addressing the limitations of the methodologies and system sizes used within this thesis, it is essential to consider the limitations of DFT itself. Using a redox reaction as an example; the central metals of each active site are formally stated to have a +2 or +3 charge, which assumes a rigid system where electrons are treated as particles,

although DFT models a 'cloud' of electronic charge. Once the electron density is calculated, a simple one-electron-like Schrödinger equation can be derived and in doing so, electron occupation is assigned to orbitals described by the basis sets. Thus, while a formal view of a redox reaction assigns the reduction and oxidation reactions to the central metal, DFT, by definition, assigns the reduction and oxidation reactions to the entire system. To model a redox reaction the entire system is assigned either a neutral charge for the formal +3 state, or a negative charge for the formal +2 state[13], although the partial charge of the central metal may not change significantly between the two modelled states.

Thus, while the redox reactions formally investigate the +2/+3 system, the partial charge of the metals do not fluctuate exclusively between these two oxidation states, instead they range approximately from +1 to +1.8, dependent on the metal centre and the charged placed on the system. It is interesting to note that when comparing between analogous active sites, the Co-centred systems had a lower partial charge on the central metal than the Fe-centred counterparts, again regardless of oxidation state. Indeed, so stable is this partial charge that the Co centres barely alter between the +2/+3 model systems. This presents a problem when attempting to ascertain why particular active sites have substantially different redox potentials when compared to their structural isomers, i.e. why Co-N_{2p}/C_a has a higher redox potential than the other two Co-N_2/C_a active sites. While it is postulated within Section 5.1.1 that the redox potential of an active site is inherently linked to the HOMO/LUMO gap, this cannot be confirmed by NBO analysis as the metal occupation does not appear to change.

As stated in Section 2.3.4, NBO analysis is only capable of describing formal lone pairs, bonding orbitals and non-bonding orbitals; while other interactions are detailed in the output, limited detail is given. For example, the interaction between the central metal and the nitrogen atoms in the central moiety are only ever given as nitrogen sp^3 hybridized lone pair's crossing over with the empty $3d_{xy}$ orbital of the central metal, not

---

[13] For an active site modelled with an axial ligand. For those initial systems modelled without an axial ligand, the neutral complex correlated to the +2 state, and a positive charge was imposed to model the +3 state.

as covalent bonds, effectively describing very strong van der Waals interactions. While NBO does give details regarding the extent of crossover, its inability to describe this as a bond results in no information being given regarding anti-bonding interactions. In much the same way, oxygen binding is described as being the donation from a lone pair into the partially occupied $3d_{z2}$ orbital and back donation from the $3d_{yz}$ orbital into the O-O π^* orbital. The inability to explicitly describe these interactions as bonds is proposed to be due to the use of an axial benzene group. When O_2 binding to any of the active sites is modelled in the absence of an axial ligand, these bonds are explicitly described. The limitations resulting from the use of the axial benzene are described further in Section 5.3.2.

While DFT and NBO analysis provides accurate geometries and energies, they do not comprise a black box. While attempts could be made to constrain electrons to a more classic 'particle-like' view, doing so could prove to further distort the conclusions drawn from the results. Instead it is postulated that more realistic models of the active sites, perhaps including appropriate axial and equatorial ligand and explicit consideration of solvation, should be sought before attempting to constrain the wavefunction to a more formal model of electron occupation.

5.3.2 - Axial benzene ligand

The use of an axial ligand as a representation of the extended carbon support was addressed in Section 3.3. It was found that attempting to calculate redox potentials without an axial ligand resulted in inconsistent errors in the calculated redox values, whereas the use of an axial benzene ligand underestimated the redox potentials by a consistent amount. Therefore it was found that the use of a correction factor would allow for redox potentials to be accurately assessed. However, in subsequent analysis it was found that the highly covalent interaction between the axial ligand and the metal centre served to obfuscate the exact nature of charge donation to and from adsorbed intermediates.

The highly electronegative nature of the benzene ligand allows more substantial charge donation to the metal centre than might be expected from a more stable, and more distant, graphene-like fragment. Indeed, when attempting to analyse metal-

oxygen bonds, it was found that donation from the oxygen appeared as interaction with the anti-bonding orbital of the axial ligand. It was also found that the d_{z^2} orbital was had a partial $1e^-$ occupation in all systems investigated. It is expected that a more expansive ligand would not donate as significant a charge to the central metal and allow for more accurate electron occupations to be determined. While this may be expected to adversely affect the predicted adsorption strengths of reduction intermediates, and thus reduction potentials, the presence of the axial ligand in all calculations is postulated to cancel out any inferred error, thus allowing for accurate reduction potentials to be calculated. It is felt that the results presented within Chapter 3 support this conclusion.

5.4 - Final conclusions

The original aim of the study was to ascertain the nature of the active sites known to originate from the pyrolysis of metal and nitrogen-containing precursors with carbon and assess the influence of the structural components of M-N_x/C active sites on their ability to catalyse the oxygen reduction reaction. While the exact identity of a highly active M-N_x/C site remains elusive, the work presented within this thesis serves to offer more signposts towards the development of highly active, non-precious metal catalysts.

It is found that the various components of M-N_x/C active sites are somewhat modular, with each influencing the behaviour of the catalyst in various ways. While the analysis techniques used within this thesis prevent the detailed investigation of the reduction of co-adsorbed species, they are detailed enough to elucidate the contributions of each active site component towards the redox potential, oxygen adsorption, one-electron $O_{2(ads)}$ reduction and $OOH_{(ads)}$ dissociation, which are detailed in Section 5.1. In summary:

1. The equatorial ligand acts as the electron 'buffer' for the active site with charge transferred during redox primarily located within it. As a general rule more resonant structures display a greater ability to stabilise charge and thus achieve higher redox potentials. The more stabilised the electron transferred during redox, the more laborious the donation to $O_{2(ads)}$ which results in weaker metal-oxygen bonds. Though graphene-based active sites are shown to have higher one-electron reduction potentials than their

amorphous counterparts, it is proposed that a slightly disrupted graphene structure would allow for relatively high redox potentials while also promoting charge transfer to the adsorbed reduction intermediate, thus allowing for even higher one-electron reduction potentials to be reached.

2. As the nitrogen atoms are a component of the equatorial ligand, they can be thought of as a 'limiter' on charge donation; lower nitrogen content in the central moiety allows increased charge donation to the central metal during redox, thus achieving higher redox potentials, but also allows for the transfer of too significant a partial charge, in turn serving to decrease the one-electron reduction reaction. However, this charge transfer occurs via the $3d_{yz}/\pi^*$ crossover, thus promoting bond scission.

3. The central metal effectively 'sets' the activity, with the equatorial ligand fine-tuning it, in a similar way to that observed with porphyrins (Baker et al., 2008). The double occupation of the Co $3d_{yz}$ orbital allows for a constant back-bonding link to the adsorbed reduction intermediate, allowing for more significant charge transfer to the substrate during the one-electron reduction of O_2 thereby increasing the reduction potentials and promoting O-OH bond scission, thus shifting the reaction to a $4e^-$ pathway. Conversely the single electron occupation of the Fe $3d_{yz}$ orbital, results in a 'set' amount of charge being donated to the substrate, the lack of a constant back-bond results in lower $O_{2(ads)}$ reduction potentials though does potentially also promote O-OH bond scission and generally enable higher potentials to be achieved for the reduction of the dissociated reduction intermediates.

These conclusions serve to improve on the current knowledge base found within the literature. While previous computational studies have investigated the activity of similar M-N$_x$/C active sites, they did not attempt to include the effects of a second graphene layer, nor attempt to model redox potentials of the active sites investigated (Kattel et al., 2013; Kattel et al., 2014; Kattel & Wang, 2013b; Kattel & Wang, 2014; Szakacs et al., 2014). Furthermore, these computational investigations have focussed on the activity of specific active sites structures, without attempting to ascertain the

influence of the metal centre, carbon support or nitrogen/carbon ratios within the central moiety. (Kattel et al., 2013; Kattel & Wang, 2013b).

No computational study that compares the activity of porphyrins to $M-N_x$ doped carbon currently exists within the literature and the observation that highly resonant equatorial ligands serve to improve the redox and one-electron reduction potentials has been alluded to (Kattel et al., 2012; Parvez et al., 2012; Tripkovic & Vanin, 2013; You et al., 2014), but no study that attempts comparison between structures of varying resonance has been found.

The results presented within this work suggest that a highly active site would be comprised of a well-connected, and thus suitably resonant, graphene-like carbon support, incorporating four nitrogen atoms around either a central cobalt or iron atom. This supports the conclusions drawn by Koslowski et al., 2008, that $Fe-N_4$ active sites are highly active towards the ORR, and that graphene embedded $Fe-N_4$ sites are only able to catalyst the 2 e^- reduction pathway (Kattel et al., 2014), though conflicts with the experimental observation that $Fe-N_2$ active sites display greater catalytic activities (Lefèvre et al., 2005; Lefèvre et al., 2002; Médard et al., 2006).

That the conclusions drawn in this thesis both supports and conflicts with the literature suggest that alternative active sites not modelled within Chapter 4 exist. It is plausible that Co- and Fe-centred active sites with a decreased co-ordination to the carbon support, i.e. $Fe-N_2$ sites, are responsible for high ORR activities, though computational modelling supports the notion that active sites within a highly porous, semi-disrupted graphene structure are responsible. Suggested methods to explore the accuracy of these postulates are explored within Chapter 6, along with other suggestions for future work that can build on the conclusions and methodology presented within this thesis.

Chapter 6 - Future work

6.1 - Pore-based active sites

The results presented within Chapter 4, and the conclusions drawn from them in Chapter 5, support the postulate that highly active sites are located within a porous carbon support (Charreteur et al., 2008; Lefèvre et al., 2009) with four embedded nitrogen atoms (Koslowski et al., 2008). While some computational investigations have attempted to model these porous active sites, a number of limitations have been identified.

Though some have modelled a more expansive graphene sheet, both porous and non-porous, the effects of a second graphene layer have always been isolated from the calculations, with layer separations varying from 12-20 Å (Kattel et al., 2014; Kattel et al., 2013; Kattel et al., 2012; Kattel & Wang, 2013b; Kattel & Wang, 2014; Liang et al., 2014; Szakacs et al., 2014; Tripkovic & Vanin, 2013). Within those studies attempting to model porous systems, the active site was located at the junction of two pores, effectively bordering two graphene sheets, as shown in Figure 6.1 (Kattel & Wang, 2013b). However, it is postulated that active sites that are located within the pore itself, possibly bridging two stacked graphene sheets are also catalytically active (Li et al., 2012). Indeed it is felt that by modelling active sites bridging stacked graphene would allow for a more representative model of active sites located in larger pores, which would benefit from being more accessible to reactants.

The comprehensive modelling of pore-based active sites should consider several factors. Firstly, multi-layer graphene has a number of stacking modes and each can strongly affect the electronic properties of the material (Lui et al., 2011). Subhedar et al. (2015), have shown that this stacking mode can be controlled, and thus the electronic properties of the graphene support tuned to best suit the active sites hosted within it. Secondly, while a number of software packages have been utilised in the exploration of M-N_x/C active site activity, each has its limitations.
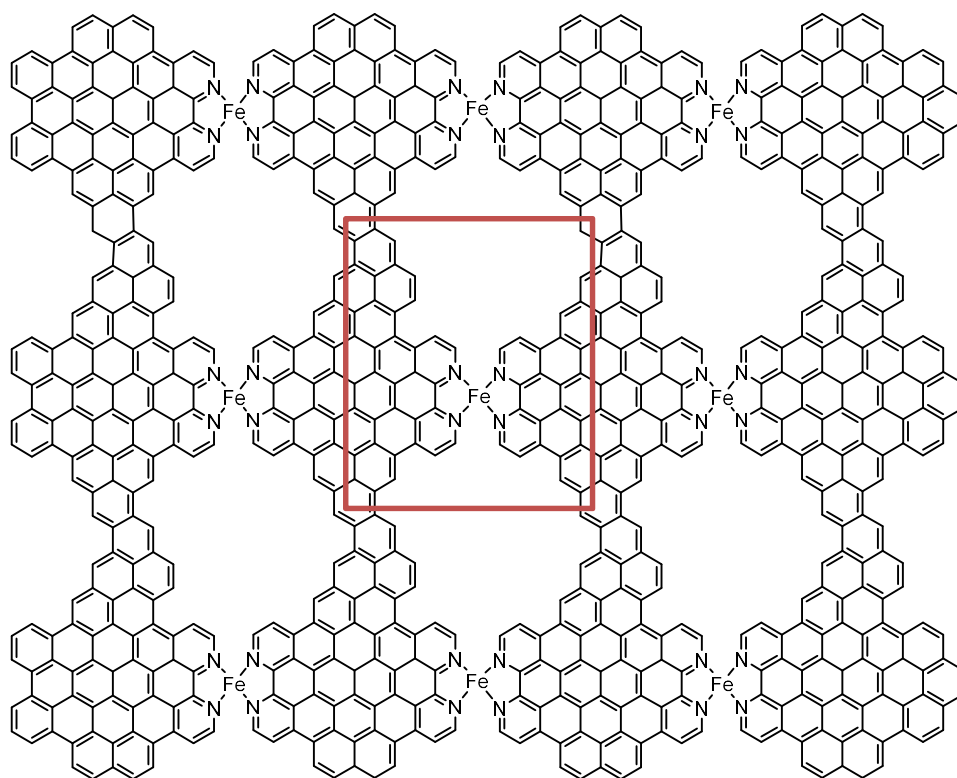
Figure 6.1 - Model of porous active sites utilised by Kattel and Wang, the red box highlights the repeated unit cell, reproduced from (Kattel & Wang, 2013b)

While Gaussian is adept at performing DFT calculations on limited clusters, calculation times increase significantly as the systems investigated increase in size. One possible work around is the use of Gaussians ONIOM methodology, which is able to isolate 'layers' within a system and calculate each at different levels of theory. Utilising this methodology an expansive graphene sheet could be calculated, with a low level, molecular mechanics methodology used to describe the bulk graphene interactions and DFT used to describe the active site and areas of significance. However, caution should be utilised when using this methodology, as breaking cyclic structures is defined as 'incorrect ONIOM partitioning' by the Gaussian user manual (Gaussian Inc, 2009). However, the use of ONIOM partitioning has been reported within the literature for the description of fluorinated graphene and carbon nanotubes to good effect (Osuna et al., 2010). Other software packages utilise plane wave theory to more accurately describe the electronic effects of more expansive 'slabs', with repeated unit cells representing a semi-infinite surface, as shown in Figure 6.1. Such software packages have been utilised extensively for the investigation of graphene-based active sites within the literature

155

(Kattel et al., 2014; Kattel et al., 2013; Kattel et al., 2012; Kattel & Wang, 2013b; Kattel & Wang, 2014; Liang et al., 2014; Szakacs et al., 2014; Tripkovic & Vanin, 2013). The use of the two software packages concurrently would provide a highly powerful analysis tool, allowing for both distant electronic effects and localised molecular interactions to be analysed.

Beyond the modelling of pore-based active sites, these methods could be utilised to investigate the influence of co-doped atomic species, such as nitrogen functionalities likely to be present on the surface (Wei et al., 2000), and surface defects originating from the degradation of graphene by peroxide (Feng et al., 2015).

6.2 - Kinetic modelling

A more detailed investigation of the ORR should also be able to model the kinetics of the reaction over an active site. While it is possible to model activation energies of bond dissociation energies using the method described within this thesis, the inability to accurately describe barriers to protonation renders this exercise futile; without activation energies for competing reactions, such as the protonation and dissociation of $OOH_{(ads)}$, the preferred pathway cannot be determined.

There is a wealth of studies that have attempted to address the calculation of activation barriers for protonation reactions on cathode catalysts (Anderson & Albu, 1999; Anderson et al., 2005; Eberle & Horstmann, 2014; Jinnouchi & Anderson, 2008; Li & Balbuena, 2003; Roman & Groß, 2012; Sidik & Anderson, 2002; Tian & Anderson, 2011; Tripković et al., 2010; Walch et al., 2008; Walch, 2011; Wang & Balbuena, 2004), the best of which utilising a model of a suitably solvated proton. Again these methods vary depending on the software package, with plane wave models able to represent a highly solvated environment by including double layer of water over the entirety of the slab (Tripković et al., 2010; Walch, 2011). Cluster methodologies typically employ a smaller proton donor complexes, ranging from a simple H_3O^+ molecule (Li & Balbuena, 2003) to larger $H-(H_2O)_4^+$ complexes (Tian & Anderson, 2011), the latter of which being a more accurate representation of electro-osmotic drag through the membrane known to occur within PEM fuel cells (Barbir, 2012; Ishikawa et al., 2007).

The use of a proton donor complex allows for transition states of competing protonation and dissociation reactions to be calculated, though consistency should be utilised between all transition state calculations to ensure that the influence of the solvated proton is felt during bond-dissociation reactions. In addition, the use of such a proton donor complex would allow for additional reaction pathways, such as those reactions involving simultaneous protonation/dissociation, to be modelled. Additionally, if a highly representative model of the electrode is used, it is feasible that the CV of a proposed catalyst could be constructed in a similar way to that proposed by Asiri & Anderson (2013), who were able to predict the CV of hydrogen on the Pt(111) surface.

6.3 - Bi-metallic active sites

While the proposed work thus far has focussed on a single metal atom based active site, it is plausible that more active sites could feature multiple iron and/or cobalt atoms, similar to those proposed by Chu & Jiang (2002). These sites would likely benefit from the ability of promote the dissociation of $O_{2(ads)}$ due the availability of two adjacent binding sites. These catalysts could therefore promote selectivity towards the $4e_-$ pathway, reducing the peroxide yield and thus protecting against degradation.

Given the differing properties of Fe and Co, as discussed in Section 5.1, these active sites could utilise the differing features of the two metals, promoting high reduction potentials across the entire reaction. Given the modular nature of the active site, these systems could also utilise varying nitrogen compositions, though a complete study of this would be extremely large.

However, if active sites similar to those proposed by Chu & Jiang (2002), are found to be active towards the ORR, it is likely they are hosted within micropores, or between graphene sheets, and so reactant access would likely be limited. Furthermore, the removal of water from the active site would likely be more laborious than for larger pore-based active sites. It is also postulated that such bi-metallic sites would feature two distinct redox potentials, one corresponding to each metal species present. This mixed redox potential may serve to significantly lower the operating potential or possibly promote free radical formation and thus active site degradation.

6.4 - Synthesis modelling

Although a method for the calculation of the formation energy of an active site has been proposed within the literature (Kattel et al., 2013; Kattel et al., 2014; Kattel & Wang, 2013a; Kattel & Wang, 2014), it is perhaps not a suitable method for ascertaining the feasibility of active site formation at high temperatures. Instead it is postulated that this method attempts to model the stability of an active site, albeit not particularly accurately.

As the $M-N_4/M-N_2$ active site ratio can be controlled by varying synthesis conditions (Lefèvre et al., 2005; Lefèvre et al., 2002; Médard et al., 2006), a computational investigation of the reaction of a variety of metal- and nitrogen-containing precursors with carbon within the 700-1000 °C range would allow for selective synthesis procedures to be developed without resorting to a trial and error experimental method.

Gaussian is particularly adept at describing the interaction of relatively small molecules and is able to impose a variety of conditions, such as temperature, pressure and varying solvents, it seems particularly well suited towards determining the ideal precursor mix and synthesis conditions.

Such a study would likely be incredibly complex and would need to avoid the pitfalls of simply finding conditions suitable to the synthesis of a desired catalyst, but also consider the formation of side-products and their interactions. Indeed while it is unlikely that computational methods could ever provide a complete picture of all the plausible reactions during a complex synthesis reaction, it should attempt to consider the most likely reactions and calculate relative yields of the most likely products.

6.5 - Comprehensive degradation modelling

While Section 5.2 considered the ability of the M-Nx/C active sites and porphyrins modelled within this thesis to act as Fenton's reagents, a number of alternative degradation pathways are proposed within the literature (Banham et al., 2015), though detailed work regarding the stability of active sites is very limited.

Two methods of degradation are proposed, attack by peroxide (Gubler et al., 2011; Gubler & Koppenol, 2012; Lefèvre & Dodelet, 2003; Schulenburg, 2003) and protonation of nitrogen functionalities either within, or close to, the active site (Herranz et al., 2011; Liu, Li, Ganesan, et al., 2009). A detailed investigation into the degradation of the active site should address both postulates and build upon a comprehensive model not only of M-N$_x$/C activity, but also the surface defects and co-doped species likely to be present within the catalyst structure, as identified by a concurrent study into synthesis procedures.

Degradation models should also attempt to model the stripping of metal atoms from the centre of the active site, along with the influence of phenol groups on the central moiety found to form on M-N$_2$/C active sites, as described in Section 4.3. As a reduction in the activity of an M-N$_x$/C catalyst is found to correlate with a loss of iron and cobalt from the catalyst (Lefèvre & Dodelet, 2003), this likely comprises a significant degradation pathway.

6.6 - Concluding remarks

The work within this thesis serves to further the fundamental understanding of how various M-N$_x$/C active site components contribute towards the overall catalytic activity. While none of the active sites investigated within this thesis are capable of competing with Pt/C, currently the best PEM cathode catalyst, in terms of activity, from the conclusions drawn in Chapter 5 it can be stated that a more active catalyst would comprise either cobalt or iron co-ordinated to four nitrogen atoms and located either within a disrupted graphene structure or, as posited by others, within a graphene pore. From experimental observations within the literature it is posited that such an active site would be competitive with platinum. Future work should therefore concentrate on the elucidation of this active site while also considering the stability of such a catalyst within the PEM fuel cell environment.

References

Adzic, R. and Wang, J. 1998. Configuration and site of O_2 adsorption on the Pt (111) electrode surface. *The Journal of Physical Chemistry B*. (111),pp.8988–8993.

Anderson, A. 2002. O_2 reduction and CO oxidation at the Pt-electrolyte interface. The role of H_2O and OH adsorption bond strengths. *Electrochimica Acta*. **47**,pp.3759–3763.

Anderson, A. 2010. Theories for Predicting Reversible Potentials of Reactions on Electrode Surfaces from Internal and Gibbs Energies: Applications to ORR. *ECS Transactions*. **28**(19),pp.1–17.

Anderson, A. and Albu, T. 1999. Ab initio determination of reversible potentials and activation energies for outer-sphere oxygen reduction to water and the reverse oxidation reaction. *Journal of the American Chemical Society*. **121**(50),pp.11855–11863.

Anderson, A. and Albu, T. 2000. Catalytic effect of platinum on oxygen reduction an ab initio model including electrode potential dependence. *Journal of the Electrochemical Society*. **147**(11),p.4229.

Anderson, A., Jinnouchi, R. and Uddin, J. 2012. Effective Reversible Potentials and Onset Potentials for O_2 Electroreduction on Transition Metal Electrodes: Theoretical Analysis. *The Journal of Physical Chemistry C*.

Anderson, A.B. 2012. Insights into electrocatalysis. *Physical Chemistry Chemical Physics*. **14**(4),pp.1330–8.

Anderson, A.B., Roques, J., Mukerjee, S., Murthi, V.S., Markovic, N.M. and Stamenkovic, V. 2005. Activation energies for oxygen reduction on platinum alloys: theory and experiment. *The Journal of Physical Chemistry B*. **109**(3),pp.1198–203.

Anderson, A.B. and Sidik, R. a 2004. Oxygen Electroreduction on FeII and FeIII Coordinated to N4 Chelates. Reversible Potentials for the Intermediate Steps from Quantum Theory. *The Journal of Physical Chemistry B*. **108**(5),p.5031.

Antoine, O., Bultel, Y. and Durand, R. 2001. Oxygen reduction reaction kinetics and mechanism on platinum nanoparticles inside Nafion®. *Journal of Electroanalytical Chemistry*. **499**(1),pp.85–94.

Asiri, H. and Anderson, A. 2013. Using Gibbs Energies to Calculate the Pt (111) Hupd Cyclic Voltammogram. *The Journal of Physical Chemistry C*. (111),pp.17509–17513.

Atkins, P. and De Paula, J. 2012. *Elements of physical chemistry*. Oxford University Press.

Atkins, P. and de Paula, J. 2009. Quantum chemistry: atomic structure *In*: *Elements of Physical Chemistry*., pp. 295–321.

Aydin, M. 2013. DFT and Raman spectroscopy of porphyrin derivatives: Tetraphenylporphine (TPP). *Vibrational Spectroscopy*. **68**,pp.141–152.

Baker, R., Wilkinson, D. and Zhang, J. 2008. Electrocatalytic activity and stability of substituted iron phthalocyanines towards oxygen reduction evaluated at different temperatures. *Electrochimica Acta*. **53**,pp.6906–6919.

Baker, R., Wilkinson, D.P. and Zhang, J. 2009. Facile synthesis, spectroscopy and electrochemical activity of two substituted iron phthalocyanines as oxygen reduction catalysts in an acidic environment. *Electrochimica Acta*. **54**(11),pp.3098–3102.

Banham, D., Ye, S., Pei, K., Ozaki, J., Kishimoto, T. and Imashiro, Y. 2015. A review of the stability and durability of non-precious metal catalysts for the oxygen reduction reaction in proton exchange membrane fuel cells. *Journal of Power Sources*. **285**,pp.334–348.

Barbir, F. 2012. *PEM fuel cells: theory and practice* (R. . Dorf, ed.). Elsevier.

Berná, A., Climent, V. and Feliu, J. 2007. New understanding of the nature of OH adsorption on Pt (111) electrodes. *Electrochemistry Communications*. **9**(12),pp.2789–2794.

Bezerra, C.W.B., et al. 2008. A review of Fe–N/C and Co–N/C catalysts for the oxygen reduction reaction. *Electrochimica Acta*. **53**(15),pp.4937–4951.

Bikiel, D.E., Bari, S.E., Doctorovich, F. and Estrin, D. a 2008. DFT study on the reactivity of iron porphyrins tuned by ring substitution. *Journal of Inorganic Biochemistry*. **102**(1),pp.70–6.

Broglie, L. de 1924. XXXV. A tentative theory of light quanta. *Philosophical Magazine Series 6*. **47**(278),pp.446–458.

Capitano, A., Gabelnick, A. and Gland, J. 1999. Gas phase atomic hydrogen reacting with molecular and atomic oxygen to form water on the Pt (111) surface. *Surface Science*. **419**(2-3),pp.104–113.

Chang, S.T., et al. 2012. Preparation of non-precious metal catalysts for PEMFC cathode from pyrolyzed vitamin B12. *International Journal of Hydrogen Energy*. **37**(18),pp.13755–13762.

Chang, S.-T., Huang, H.-C., Wang, H.-C., Hsu, H.-C., Lee, J.-F. and Wang, C.-H. 2014. Effects of structures of pyrolyzed corrin, corrole and porphyrin on oxygen reduction reaction. *International Journal of Hydrogen Energy*. **39**(2),pp.934–941.

Chao, S., Cui, Q., Bai, Z., Yan, H., Wang, K. and Yang, L. 2014. Varying N content and N/C ratio of the nitrogen precursor to synthesize highly active Co-Nx/C non-precious metal catalyst. *International Journal of Hydrogen Energy*. **39**(27),pp.14768–14776.

Charreteur, F., Jaouen, F., Ruggeri, S. and Dodelet, J.-P. 2008. Fe/N/C non-precious catalysts for PEM fuel cells: Influence of the structural parameters of pristine commercial carbon blacks on their activity for oxygen reduction. *Electrochimica Acta*. **53**(6),pp.2925–2938.

Chen, X., Li, F., Zhang, N., An, L. and Xia, D. 2013. Mechanism of oxygen reduction reaction catalyzed by Fe(Co)-Nx/C. *Physical Chemistry Chemical Physics*. **15**,pp.19330–6.

Cheng, N., Kutz, R., Kemna, C. and Wieckowski, A. 2013. Enhanced ORR activity of cobalt porphyrin co-deposited with transition metal oxides on Au and C electrodes. The ORR threshold data. *Journal of Electroanalytical Chemistry*. **705**,pp.8–12.

Chu, D. and Jiang, R. 2002. Novel electrocatalysts for direct methanol fuel cells. *Solid State Ionics*. **148**,pp.591–599.

Compton, R. and Banks, C. 2007. *Understanding voltammetry*. World Scientific Publishing Co. Pte. Ltd.

Damjanovic, A. and Brusic, V. 1967. Electrode kinetics of oxygen reduction on oxide-free platinum electrodes. *Electrochimica Acta*. **12**(August),pp.615–628.

Domínguez, C., et al. 2014. Effect of transition metal (M: Fe, Co or Mn) for the oxygen reduction reaction with non-precious metal catalysts in acid medium. *International Journal of Hydrogen Energy*. **39**(10),pp.5309–5318.

E. D. Glendening, J, K. Badenhoop, A. E. Reed, J. E. Carpenter, J. A. Bohmann, C. M. Morales, C. R. Landis, F.W. 2013. NBO6.

Eberle, D. and Horstmann, B. 2014. Oxygen Reduction on Pt(111) in Aqueous Electrolyte: Elementary Kinetic Modeling. *Electrochimica Acta*. **137**,pp.714–720.

Eichler, A. and Hafner, J. 1997. Molecular Precursors in the Dissociative Adsorption of O_2 on Pt (111). *Physical Review Letters*. **79**(22),pp.4481–4484.

Elbaz, L. and Garzon, F.H. 2013. Increasing the site density of non-precious metal catalysts in fuel cell electrodes. *Journal of Electroanalytical Chemistry*. **700**,pp.65–69.

Faubert, G., Lalande, G., Cote, R. and Guay, D. 1996. Heat-treated iron and cobalt tetraphenylporphyrins adsorbed on carbon black: physical characterization and catalytic properties of these materials for the reduction of oxygen in polymer electrolyte. *Electrochimica Acta*. **41**,pp.1689–1701.

Feng, Y., Lu, K., Mao, L., Guo, X., Gao, S. and Petersen, E.J. 2015. Degradation of 14 C-labeled few layer graphene via Fenton reaction : Reaction rates , characterization of reaction products , and potential ecological effects. *Water Research*. **84**,pp.49–57.

Flyagina, I.S. 2014. Theoretical and Experimental Investigation of Alternative Cathode Catalysts for Proton Exchange Membrane Fuel Cells. PhD Thesis, University of Leeds.

Ford, D., Xu, Y. and Mavrikakis, M. 2005. Atomic and molecular adsorption on Pt (111). *Surface Science*. **117**(14),p.6737.

Ford, D.C., Nilekar, A.U., Xu, Y. and Mavrikakis, M. 2010. Partial and complete reduction of O_2 by hydrogen on transition metal surfaces. *Surface Science*. **604**(19-20),pp.1565–1575.

Foresman, J. and Frisch, A. 1996. *Exploring chemistry with electronic structure methods*, Gaussian Inc. Second Edition.

Gaussian Inc 2009. *Gaussian09 User's Reference*. Gaussian Inc.

Goldstein, S., Meyerstein, D. and Czapski, G. 1993. The Fenton reagents. *Free Radical Biology and Medicine*. **15**(Ii),pp.435–445.

Gómez–Marín, A. and Schouten, K.J.P. 2012. Interaction of hydrogen peroxide with a Pt (111) electrode. *Electrochemistry Communications*. **22**,pp.153–156.

Groß, A., Eichler, A. and Hafner, J. 2003. Unified picture of the molecular adsorption process: O_2/Pt (111). *Surface Science Letters*. **539**(1-3),pp.L542–L548.

Gubler, L., Dockheer, S.M. and Koppenol, W.H. 2011. Radical (HO●, H● and HOO●) Formation and Ionomer Degradation in Polymer Electrolyte Fuel Cells. *Journal of the Electrochemical Society*. **158**(7),p.B755.

Gubler, L. and Koppenol, W.H. 2012. Kinetic Simulation of the Chemical Stabilization Mechanism in Fuel Cell Membranes Using Cerium and Manganese Redox Couples. *Journal of the Electrochemical Society*. **159**(2),p.B211.

He, Q., et al. 2012. Molecular catalysis of the oxygen reduction reaction by iron porphyrin catalysts tethered into Nafion layers: An electrochemical study in solution and a membrane-electrode-assembly study in fuel cells. *Journal of Power Sources*. **216**(null),pp.67–75.

He, Q. and Mugadza, T. 2012. Mechanisms of Electrocatalysis of Oxygen Reduction by Metal Porphyrins in Trifluoromethane Sulfonic Acid Solution. *International Journal of Electrochemical Science*. **7**,pp.7045–7064.

Herranz, J., et al. 2011. Unveiling N-Protonation and Anion-Binding Effects on Fe/N/C Catalysts for O2 Reduction in Proton-Exchange-Membrane Fuel Cells. *Journal of Physical Chemistry C*. **115**,pp.16087–16097.

Herrmann, I., Kramm, U., Fiechter, S. and Bogdanoff, P. 2009. Oxalate supported pyrolysis of CoTMPP as electrocatalysts for the oxygen reduction reaction. *Electrochimica Acta*. **54**,pp.4275–4287.

Hoogers, G. 2002. *Fuel cell technology handbook*. CRC Press.

Ikeda, T., Boero, M., Huang, S.-F., Terakura, K., Oshima, M. and Ozaki, J. 2008. Carbon Alloy Catalysts: Active Sites for Oxygen Reduction Reaction. *The Journal of Physical Chemistry C*. **112**(38),pp.14706–14709.

Ishikawa, Y., Mateo, J., Tryk, D. and Cabrera, C. 2007. Direct molecular dynamics and density-functional theoretical study of the electrochemical hydrogen oxidation reaction and underpotential deposition of H on Pt (111). *Journal of Electroanalytical Chemistry*. **607**(1-2),pp.37–46.

Jacob, T., Muller, R.P. and Goddard, W.A. 2003. Chemisorption of Atomic Oxygen on Pt(111) from DFT Studies of Pt-Clusters. *The Journal of Physical Chemistry B*. **107**(35),pp.9465–9476.

Jasinski, R. 1964. A new fuel cell cathode catalyst. *Nature*. **201**,p.1212.

Jensen, K.P. and Ryde, U. 2004. How O2 binds to heme: reasons for rapid binding and spin inversion. *The Journal of Biological Chemistry*. **279**(15),pp.14561–9.

Jinnouchi, R. and Anderson, A.B. 2008. Aqueous and Surface Redox Potentials from Self-Consistently Determined Gibbs Energies. *The Journal of Physical Chemistry C*. **112**(24),pp.8747–8750.

Kattel, S., Atanassov, P. and Kiefer, B. 2014. A density functional theory study of oxygen reduction reaction on non-PGM Fe-Nx-C electrocatalysts. *Physical Chemistry Chemical Physics*. **16**,pp.13800–6.

Kattel, S., Atanassov, P. and Kiefer, B. 2013. Catalytic activity of Co-N(x)/C electrocatalysts for oxygen reduction reaction: a density functional theory study. *Physical Chemistry Chemical Physics*. **15**(1),pp.148–53.

Kattel, S., Atanassov, P. and Kiefer, B. 2012. Stability, Electronic and Magnetic Properties of In-Plane Defects in Graphene: A First-Principles Study. *The Journal of Physical Chemistry C*. **116**(14),pp.8161–8166.

Kattel, S. and Wang, G. 2013a. A density functional theory study of oxygen reduction reaction on Me–N4 (Me = Fe, Co, or Ni) clusters between graphitic pores. *Journal of Materials Chemistry A*. **1**,p.10790.

Kattel, S. and Wang, G. 2013b. A density functional theory study of oxygen reduction reaction on Me–N$_4$ (Me = Fe, Co, or Ni) clusters between graphitic pores. *Journal of Materials Chemistry A*. **1**,p.10790.

Kattel, S. and Wang, G. 2014. Reaction Pathway for Oxygen Reduction on FeN4 Embedded Graphene. *The Journal of Physical Chemistry Letters*. **5**,pp.452–456.

Kieber-Emmons, M.T., Li, Y., Halime, Z., Karlin, K.D. and Solomon, E.I. 2011. Electronic structure of a low-spin heme/Cu peroxide complex: spin-state and spin-topology contributions to reactivity. *Inorganic Chemistry*. **50**(22),pp.11777–86.

Kim, S.Y., Lee, J., Na, C.W., Park, J., Seo, K. and Kim, B. 2005. N-doped double-walled carbon nanotubes synthesized by chemical vapor deposition. *Chemical Physics Letters*. **413**(4-6),pp.300–305.

Koch, W. and Holthausen, M.C. 2001a. *A Chemist's Guide to Density Functional Theory* [online] Second Edi. Weinheim: Wiley-VCH.

Koch, W. and Holthausen, M.C. 2001b. *A Chemist's Guide to Density Functional Theory* Second Edi. Weinheim: Wiley-VCH.

Koslowski, U.I., Abs-Wurmbach, I., Fiechter, S. and Bogdanoff, P. 2008. Nature of the Catalytic Centers of Porphyrin-Based Electrocatalysts for the ORR: A Correlation of Kinetic Current Density with the Site Density of Fe−N4 Centers. *The Journal of Physical Chemistry C*. **112**(39),pp.15356–15366.

Kua, J. and Goddard, W.A. 1998. Chemisorption of Organics on Platinum. 1. The Interstitial Electron Model. *The Journal of Physical Chemistry B*. **102**(47),pp.9481–9491.

Lalande, G., Cote, R., Guay, D. and Dodelet, J. 1997. Is nitrogen important in the formulation of Fe-based catalysts for oxygen reduction in solid polymer fuel cells? *Electrochimica Acta*. **42**(9),pp.1379–1388.

Larminie, J., Dicks, A. and McDonald, M. 2003. *Fuel cell systems explained*. Chichester: Wiley.

Leach, A. 2001. *Molecular modelling: principles and applications*.

Lee, K., Zhang, L., Lui, H., Hui, R., Shi, Z. and Zhang, J. 2009. Oxygen reduction reaction (ORR) catalyzed by carbon-supported cobalt polypyrrole (Co-PPy/C) electrocatalysts. *Electrochimica Acta*. **54**(20),pp.4704–4711.

Lefèvre, M. and Dodelet, J.-P. 2003. Fe-based catalysts for the reduction of oxygen in polymer electrolyte membrane fuel cell conditions: determination of the amount of peroxide released during electroreduction and its influence on the stability of the catalysts. *Electrochimica Acta*. **48**(19),pp.2749–2760.

Lefèvre, M., Dodelet, J.P. and Bertrand, P. 2005. Molecular oxygen reduction in PEM fuel cell conditions: ToF-SIMS analysis of Co-based electrocatalysts. *The Journal of Physical Chemistry B*. **109**(35),pp.16718–24.

Lefèvre, M., Dodelet, J.P. and Bertrand, P. 2002. Molecular oxygen reduction in PEM fuel cells: Evidence for the simultaneous presence of two active sites in Fe-based catalysts. *Journal of Physical Chemistry B*. **106**,pp.8705–8713.

Lefèvre, M., Proietti, E., Jaouen, F. and Dodelet, J.-P. 2009. Iron-based catalysts with improved oxygen reduction activity in polymer electrolyte fuel cells. *Science*. **324**(5923),pp.71–4.

Li, T. and Balbuena, P. 2003. Oxygen reduction on a platinum cluster. *Chemical Physics Letters*. **367**,pp.439–447.

Li, W., Wu, J., Higgins, D., Choi, J. and Chen, Z. 2012. Determination of iron active sites in pyrolyzed iron-based catalysts for the oxygen reduction reaction. *ACS Catalysis*. **2**,pp.2761–2768.

Li, X., Popov, B.N., Kawahara, T. and Yanagi, H. 2011. Non-precious metal catalysts synthesized from precursors of carbon, nitrogen, and transition metal for oxygen reduction in alkaline fuel cells. *Journal of Power Sources*. **196**(4),pp.1717–1722.

Liang, W., Chen, J., Liu, Y. and Chen, S. 2014. Density-Functional-Theory Calculation Analysis of Active Sites for Four-Electron Reduction of O_2 on Fe/N-Doped Graphene. *ACS Catalysis*. **4**,pp.4170–4177.

Liao, M.-S., Kar, T., Gorun, S.M. and Scheiner, S. 2004. Effects of peripheral substituents and axial ligands on the electronic structure and properties of iron phthalocyanine. *Inorganic Chemistry*. **43**(22),pp.7151–61.

Liu, G., Li, X., Ganesan, P. and Popov, B. 2009. Development of non-precious metal oxygen-reduction catalysts for PEM fuel cells based on N-doped ordered porous carbon. *Applied Catalysis B: Environmental*. **93**,pp.156–165.

Liu, G., Li, X. and Popov, B. 2009. Stability Study of Carbon-Based Catalysts for Oxygen Reduction Reaction in Polymer Electrolyte Membrane Fuel Cells. *ECS Transactions*. **25**(1),pp.1251–1259.

Liu, H., et al. 2006. Electrocatalytic reduction of O_2 and H_2O_2 by adsorbed cobalt tetramethoxyphenyl porphyrin and its application for fuel cell cathodes. *Journal of Power Sources*. **161**(2),pp.743–752.

Lui, C.H., Li, Z., Chen, Z., Klimov, P. V., Brus, L.E. and Heinz, T.F. 2011. Imaging Stacking Order in Few-Layer Graphene. *Nano Letters*. **11**,pp.164–169.

Lynch, M. and Hu, P. 2000. A density functional theory study of CO and atomic oxygen

chemisorption on Pt (111). *Surface Science*. **458**(1-3),pp.1–14.

M. J. Frisch, G. W. Trucks, H. B. Schlegel, G.E.S. and M. A. Robb, J. R. Cheeseman, G. Scalmani, V. Barone, B. Mennucci, G. A. Petersson, H. Nakatsuji, M. Caricato, X. Li, H. P. Hratchian, A. F. Izmaylov, J. Bloino, G. Zheng, J. L. Sonnenberg, M. Hada, M. Ehara, K. Toyota, R. Fukuda, J. Hasegawa, M. Ishida, T, D.J.F. 2013. Gaussian09.

Maldonado, S. and Stevenson, K. 2004. Direct preparation of carbon nanofiber electrodes via pyrolysis of iron (II) phthalocyanine: electrocatalytic aspects for oxygen reduction. *The Journal of Physical Chemistry B*. **108**(31),pp.11375–11383.

Maldonado, S. and Stevenson, K.J. 2005. Influence of nitrogen doping on oxygen reduction electrocatalysis at carbon nanofiber electrodes. *The Journal of Physical Chemistry B*. **109**(10),pp.4707–16.

Marcotte, S., Villers, D., Guillet, N., Roué, L. and Dodelet, J.P. 2004. Electroreduction of oxygen on Co-based catalysts: determination of the parameters affecting the two-electron transfer reaction in an acid medium. *Electrochimica Acta*. **50**(1),pp.179–188.

Markovic, N. 1995. Oxygen reduction on platinum low-index single-crystal surfaces in sulfuric acid solution: rotating ring-Pt (hkl) disk studies. *The Journal of Physical Chemistry*. **99**(11),pp.3411–3415.

Maruyama, J. and Abe, I. 2003. Cathodic oxygen reduction at the catalyst layer formed from Pt/carbon with adsorbed water. *Journal of Electroanalytical Chemistry*. **545**,pp.109–115.

Masa, J. and Schuhmann, W. 2013. Systematic selection of metalloporphyrin-based catalysts for oxygen reduction by modulation of the donor-acceptor intermolecular hardness. *Chemistry*. **19**(29),pp.9644–54.

Médard, C., Lefèvre, M., Dodelet, J.P., Jaouen, F. and Lindbergh, G. 2006. Oxygen reduction by Fe-based catalysts in PEM fuel cell conditions: Activity and selectivity of the catalysts obtained with two Fe precursors and various carbon supports. *Electrochimica Acta*. **51**(16),pp.3202–3213.

Michaelides, A. and Hu, P. 2001. Catalytic water formation on platinum: A first-principles study. *Journal of the American Chemical Society*. **123**(18),pp.4235–4242.

Nilekar, A. and Mavrikakis, M. 2008. Improved oxygen reduction reactivity of platinum monolayers on transition metal surfaces. *Surface Science*. **602**(14),pp.L89–L94.

Nørskov, J. and Rossmeisl, J. 2004. Origin of the overpotential for oxygen reduction at a fuel-cell cathode. *The Journal of Physical Chemistry B*. **108**(46),pp.17886–17892.

Osuna, S., Torrent-Sucarrat, M., Solà, M., Geerlings, P., Ewels, C.P. and Lier, G. Van 2010.

Reaction Mechanisms for Graphene and Carbon Nanotube Fluorination. *The Journal of Physical Chemistry C*. **114**,pp.3340–3345.

Parvez, K., et al. 2012. Nitrogen-doped graphene and its iron-based composite as efficient electrocatalysts for oxygen reduction reaction. *ACS nano*. **6**(11),pp.9541–50.

Puglia, C., Nilsson, A., Hernnäs, B. and Karis, O. 1995. Physisorbed, chemisorbed and dissociated O_2 on Pt (111) studied by different core level spectroscopy methods. *Surface Science*. **342**,pp.119–133.

Pylypenko, S., Mukherjee, S., Olson, T.S. and Atanassov, P. 2008. Non-platinum oxygen reduction electrocatalysts based on pyrolyzed transition metal macrocycles. *Electrochimica Acta*. **53**(27),pp.7875–7883.

Radich, J.G. and Kamat, P. V. 2013. Making graphene Holey. Gold-nanoparticle-mediated hydroxyl radical attack on reduced graphene oxide. *ACS Nano*. **7**(6),pp.5546–5557.

Roman, T. and Groß, A. 2012. Structure of water layers on hydrogen-covered Pt electrodes. *Catalysis Today*,pp.1–8.

Sarapuu, A., Samolberg, L., Kreek, K., Koel, M., Matisen, L. and Tammeveski, K. 2015. Cobalt- and iron-containing nitrogen-doped carbon aerogels as non-precious metal catalysts for electrochemical reduction of oxygen. *Journal of Electroanalytical Chemistry*. **746**,pp.9–17.

Schilling, T., Okunola, A., Masa, J., Schuhmann, W. and Bron, M. 2010. Carbon nanotubes modified with electrodeposited metal porphyrins and phenanthrolines for electrocatalytic applications. *Electrochimica Acta*. **55**(26),pp.7597–7602.

Schulenburg, H. 2003. Catalysts for the oxygen reduction from heat-treated iron (III) tetramethoxyphenylporphyrin chloride: structure and stability of active sites. *The Journal of Physical Chemistry B*. (Iii),pp.9034–9041.

Seidel, R.W., Goddard, R., Hoch, C., Breidung, J. and Oppel, I.M. 2011. On the structure of unsolvated free-base 5,10,15,20-tetra(3-pyridyl)porphyrin. *Journal of Molecular Structure*. **985**(2-3),pp.307–315.

Sharifi, T., et al. 2012. Nitrogen doped multi walled carbon nanotubes produced by CVD-correlating XPS and Raman spectroscopy for the study of nitrogen inclusion. *Carbon*. **50**(10),pp.3535–3541.

Shi, Z., Zhang, J., Liu, Z., Wang, H. and Wilkinson, D. 2006. Current status of ab initio quantum chemistry study for oxygen electroreduction on fuel cell catalysts. *Electrochimica Acta*. **51**(10),pp.1905–1916.

Si, Y.J., Xiong, Z.P., Chen, C.G., Liu, P. and Wu, H.J. 2013. A non-precious metal catalyst

for oxygen reduction prepared by heat-treating a mechanical mixture of carbon black, melamine and cobalt chloride. *Chinese Chemical Letters*. **24**(12),pp.1109–1111.

Sidik, R. and Anderson, A. 2002. Density functional theory study of O_2 electroreduction when bonded to a Pt dual site. *Journal of Electroanalytical Chemistry*. **528**(1-2),pp.69–76.

Stipe, B., Rezaei, M. and Ho, W. 1997. Atomistic studies of O dissociation on Pt (111) induced by photons, electrons, and by heating. *The Journal of Chemical Physics*. **107**(16),pp.6443–6447.

Subhedar, K.M., Sharma, I. and Dhakate, S.R. 2015. Control of layer stacking in CVD graphene under quasi-static condition. *Phys. Chem. Chem. Phys.* **17**,pp.22304–22310.

Szakacs, C.E., Lefèvre, M., Kramm, U.I., Dodelet, J.-P. and Vidal, F. 2014. A density functional theory study of catalytic sites for oxygen reduction in Fe/N/C catalysts used in H_2/O_2 fuel cells. *Physical Chemistry Chemical Physics*. **16**,pp.13654–61.

Tai, C.-K., Chuang, W.-H. and Wang, B.-C. 2013. Substituted group and side chain effects for the porphyrin and zinc(II)–porphyrin derivatives: A DFT and TD-DFT study. *Journal of Luminescence*. **142**,pp.8–16.

Tian, F. and Anderson, A.B. 2011. Effective Reversible Potential, Energy Loss, and Overpotential on Platinum Fuel Cell Cathodes. *The Journal of Physical Chemistry C*. **115**(10),pp.4076–4088.

Todorovic, R. and Meyer, R. 2011. A comparative density functional theory study of the direct synthesis of H2O2 on Pd, Pt and Au surfaces. *Catalysis Today*. **160**(1),pp.242–248.

Tripković, V., Skúlason, E., Siahrostami, S., Nørskov, J.K. and Rossmeisl, J. 2010. The oxygen reduction reaction mechanism on Pt(111) from density functional theory calculations. *Electrochimica Acta*. **55**(27),pp.7975–7981.

Tripkovic, V. and Vanin, M. 2013. Electrochemical CO_2 and CO reduction on metal-functionalized porphyrin-like graphene. *The Journal of Physical Chemistry C*. **117**,pp.9187–9195.

UN 1998. *Kyoto Protocol to the United Nations Framework Convention on Climate Change* [online].

Vielstich, W., Lamm, A. and Gasteiger, H. 2003. *Handbook of Fuel Cells, Vol 3: Fuel cell technology and applications: Part 1*. Chichester: Wiley.

Villers, D., Jacques-Bédard, X. and Dodelet, J.-P. 2004. Fe-Based Catalysts for Oxygen

Reduction in PEM Fuel Cells. *Journal of the Electrochemical Society*. **151**(9),p.A1507.

Voggu, R., Das, B., Rout, C.S. and Rao, C.N.R. 2008. Effects of charge transfer interaction of graphene with electron donor and acceptor molecules examined using Raman spectroscopy and cognate techniques. *Journal of Physics: Condensed Matter*. **20**(47),p.472204.

Walch, S., Dhanda, A., Aryanpour, M. and Pitsch, H. 2008. Mechanism of Molecular Oxygen Reduction at the Cathode of a PEM Fuel Cell: Non-Electrochemical Reactions on Catalytic Pt Particles. *The Journal of Physical Chemistry C*. **112**(22),pp.8464–8475.

Walch, S.P. 2011. Effect of Solvation on the Oxygen Reduction Reaction on Pt Catalyst. *The Journal of Physical Chemistry C*. **115**(15),pp.7377–7391.

Wang, Y. and Balbuena, P. 2004. Roles of proton and electric field in the electroreduction of O_2 on Pt (111) surfaces: results of an ab-initio molecular dynamics study. *The Journal of Physical Chemistry B*. **108**(14),pp.4376–4384.

Wei, G., Wainright, J. and Savinell, R. 2000. Catalytic activity for oxygen reduction reaction of catalysts consisting of carbon, nitrogen and cobalt. *Journal of New Materials for Electrochemical Systems*. **129**,pp.121–129.

Xing, W., Lalwani, G., Rusakova, I. and Sitharaman, B. 2014. Degradation of graphene by hydrogen peroxide. *Particle and Particle Systems Characterization*. **31**,pp.745–750.

Xu, J.B., Zhao, T.S. and Zeng, L. 2012. Covalent hybrid of hemin and mesoporous carbon as a high performance electrocatalyst for oxygen reduction. *International Journal of Hydrogen Energy*. **37**(21),pp.15976–15982.

Yang, H., Kumar, S. and Zou, S. 2012. Electroreduction of O_2 on Uniform Arrays of Pt Nanoparticles. *Journal of Electroanalytical Chemistry*,pp.1–9.

Yang, Z., Wang, J. and Yu, X. 2010. Density functional theory studies on the adsorption, diffusion and dissociation of O_2 on Pt (111). *Physics Letters A*. **374**(46),pp.4713–4717.

You, J.-M., Han, H.S., Lee, H.K., Cho, S. and Jeon, S. 2014. Enhanced electrocatalytic activity of oxygen reduction by cobalt-porphyrin functionalized with graphene oxide in an alkaline solution. *International Journal of Hydrogen Energy*. **39**(10),pp.4803–4811.

Yuan, X., Kong, H.-C., He, Y.-J., Ma, Z.-F., Yang, Y. and Li, Q. 2014. Effects of composition on electrochemical properties of a non-precious metal catalyst towards oxygen reduction reaction. *International Journal of Hydrogen Energy*. **39**(28),pp.1–9.

Zhang, H.J., et al. 2014. Pyrolyzing cobalt diethylenetriamine chelate on carbon

(CoDETA/C) as a family of non-precious metal oxygen reduction catalyst. *International Journal of Hydrogen Energy*. **39**(1),pp.267–276.

Zhang, H.-J., Kong, H.-C., Yuan, X., Jiang, Q.-Z., Yang, J. and Ma, Z.-F. 2012. Influence of metal precursors on the catalytic activity and structure of non-precious metal electrocatalysts for oxygen reduction reaction. *International Journal of Hydrogen Energy*. **37**(17),pp.13219–13226.

Zhang, Y.-H., Ruan, W.-J., Li, Z.-Y., Wu, Y. and Zheng, J.-Y. 2005. DFT study on the influence of meso-phenyl substitution on the geometric, electronic structure and vibrational spectra of free base porphyrin. *Chemical Physics*. **315**(1-2),pp.201–213.